Erlebte Wissenschaft

Polymorphism of Cross-Linked Actin Networks

Dissertation
von

Bernd Wagner

E27

TECHNISCHE UNIVERSITÄT MÜNCHEN

TECHNISCHE UNIVERSITÄT MÜNCHEN

PHYSIK DEPARTMENT

LEHRSTUHL FÜR ZELLBIOPHYSIK E27

Polymorphism of Cross-Linked Actin Networks

Bernd Dieter Wagner

Vollständiger Abdruck der von der Fakultät für Physik der
Technischen Universität München
zur Erlangung des akademischen Grades eines
Doktor der Naturwissenschaften (Dr. rer. nat.)
genehmigten Dissertation.

TO ALL WHO ENCOURAGED ME!

*"Self-esteem determines any success
and vice versa!"*

Summary

Biological tissues and cells exhibit unique properties. For that reason there is much interest in such biological materials. The structure and mechanical response of living cells is dominated by the cytoskeleton, a complex meshwork of protein filaments. Three different classes of cytoskeletal biopolymers play an important role for the overall properties of cells cytoskeleton: Actin, microtubule and intermediate filaments. The proper function and precisely balanced interplay between the three cytoskeletal biopolymer filaments and their associated proteins are essential for cells to fulfill their tasks in life. The major component of the cytoskeleton is actin whose function is regulated by a myriad of actin binding proteins. One class of this proteins is able to cross-link single filaments. In cells, there exists a huge "zoo" of cross-linker molecules. Numerous cross-linkers modulate the structure as well as the mechanics of actin networks. A systematic investigation was required to understand the mechanisms cells use to control their cytoskeleton. In this work, the influence of well-defined cross-linking molecules on the elasticity and microstructures of complex composite actin filamentous networks were investigated. These complex biopolymer networks were studied *in vitro* using various microscopical and rheological methods.

Detailed macrorheological measurements proved that the number of sticky entanglement points per filament determine the viscoelastic behavior of pure entangled actin networks in the linear as well as the nonlinear response regime. The maximum force which such sticky entanglement points are able to withstand at a certain shear rate, is about 50 times lower than in case of transient heavy meromyosin (HMM) cross-links.

By adding active HMM cross-links to entangled actin networks at the beginning of the polymerization, the elasticity of the resulting networks is reduced as long as ATP is in excess. The decrease of elasticity of the networks is quantified by the plateau value G_0 of the elastic modulus G' in dependence of the HMM concentration $(G_0 \sim (c_{HMM}/c_{actin})^{-0.3})$. In order to explain the observed effect, a new picture for the mechanism of active cross-linking is proposed: The active cross-linkers act as fast transient "distance keepers" for single filaments comparable to lubricants between entanglement points. As a consequence the mean distance between sticky entanglements in the network decreases with increasing HMM concentration, resulting in a lowered overall elasticity of the networks. Under high shear strains, the observed

hardening behavior turns into strain weakening. This observation is in accordance with recent predictions, which consider filament-filament slippage to be responsible for weakening of actin networks. Furthermore, the glassy worm-like chain model is able to fit the data gained from linear measurements and the resulting fit values support the hypothesis.

Investigating seven synthetic cross-linkers of different length, cloned and expressed in *Escherichia coli*, a clear dependence of the actin network structure on the length respectively molecular weight of the cross-linker could be derived. Furthermore, it was possible to relate the mechanical properties of the resulting networks to the network morphism. Consequently, the mechanical properties of the networks could be reduced to the differently sized cross-linkers. The mechanical properties could again be quantified by the plateau value of the elastic modulus. The onset of the increase in elasticity is related to the beginning of bundling of filaments in the network which happens at a critical cross-linker concentration $R^\star$, where $R = c_{cross-linker}/c_{actin}$. For the smallest cross-linker (3-4 nm in diameter) compared to the proximately next longer one, no difference in the elastic behavior could be resolved. The bundles in the network have only a slightly different stiffness, which is not resolvable anymore. This fact reveals the current resolution limits of the macrorheological measuring method. Consequently, G_0 evaluation is limited to several nanometers in cross-linker length.

The next step in complexity was reached by exposing cross-linked actin networks to depletion forces which simulate the crowded conditions of the cells interior. Using HMM as a model for specific cross-linkers and polyethylene glycol as a depletion agent, it could be demonstrated, that these cross-linkers hinder the unspecific buildup of filamentous actin structures. HMM behaves contrarily to most other cross-linkers molecules. Under influence of depletion forces, HMM traps actin filaments into so-called "asters", which occur as large star-like heterogeneities in the network. In dependence of the HMM and PEG concentration a constraint for an aster phase transition could be derived from microscopic pictures $(\log R \sim 0.3 \cdot c_{PEG6k} \, [\% \, w])$. By combining microscopical results with macrorheological measurements, a complete phase diagram could be obtained. Finally, nonlinear measurements of HMM/PEG actin networks confirmed the dominance of the cross-linker molecules.

Within the scope of this thesis it was shown that actin networks possess a complex polymorphism which depends on cross-linker concentration and cross-linker

architecture. The observed structures of the investigated actin networks range from pure entangled networks without any cross-linkers, via mixed phases with embedded bundles to pure bundled phases. The onset of the mixed phase was determined to be at a molar ratio $R^\star \geq 0.01$ of cross-linker to actin molecules. By the help of microscopical and rheological techniques, it was demonstrated that the architecture of cross-linkers define the network structures and consequently the viscoelastic properties of actin networks. Furthermore, it was shown that specific cross-linkers are necessary to hinder unspecific buildup of filament structures, using polyethylene glycol as a depletion agent to model crowded cell conditions.
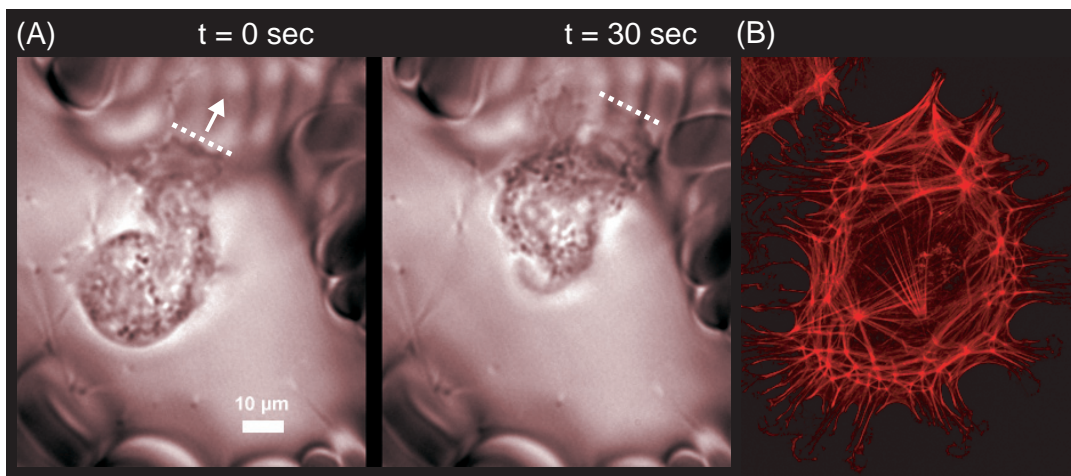
Contents

Introduction

Figure 1: (A) Pictures of a crawling cell (movie recorded with Zeiss Axiovert 200 inverted microscope using 100x immersion oil objective). The cell crawls through human thrombocytes and connective tissue fibres containing environment. The cell body moves with a velocity of 0.8 μm/s and the lamellipodium with 0.5 μm/s. (B) F-actin cytoskeleton in a 2D cultured bovine articular chondrocyte, labeled using phalloidin-FITC (M. Kerrigan, A. Hall and L. Sharp, Membrane Biology Group, School of Biomedical and Clinical Laboratory Sciences).

The smallest devices in organs and biological tissues are cells [Alberts et al., 1995]. They build soft viscoelastic materials (e.g. blood clots) unlike hard, non-biological materials (e.g. steel, concrete) [Boal, 2006]. In life, cells have to fulfill numerous tasks. They are motile and able to crawl (see fig. 1A), they are dividing, contracting and adhere on substrates. Therefore, on the one hand cells have to withstand mechanical strain and on the other hand they have to be able to rearrange and adapt to the environmental conditions on a large range of time scales from seconds to hours. In order

1

to manage these tasks, cells own a complex three-dimensional network of filamentous structures, the cytoskeleton. The cytoskeletons mechanical properties determine the cells mechanical capacities. It is the key unit of the structural organization of cells. The optimal balance of developing robustness versus adaptability is one of the outstanding mechanical properties of the cell cytoskeleton.

One of the three main protein filaments of the cytoskeleton is F-actin [Alberts et al., 1995]. It is prevalent in the cortical regions of the cytoskeleton, defining structures e.g. the lamellipodium, and stress fibres (fig. 1B). Actin filaments are not isolated in the cytoskeleton, but interact with a vast number of actin binding proteins (ABPs). Why do cells require such an enormous diversification of these proteins? According to requirements, the actin filaments in the cytoskeleton need ABPs which are able to build cross-links between single filaments for fortification purpose and simultaneously ABPs which allow for and are able to rearrange the network structure. In cells, transient physical cross-linkers are used instead of permanent chemical ones in order to obtain both properties. Hence, the huge number of diverse cross-links abundant in the cytoskeleton is necessary for the cells shape changing as well as stiffening ability. While in recent years the mechanical properties of *in vitro* α-actinin, human-filamin and scruin cross-linked actin networks were studied [Tempel et al., 1996, Wachsstock et al., 1994, Gardel et al., 2006a, Gardel et al., 2004b], still the influence of many other different cross-linking proteins on actin network properties remains. All these proteins influence the actin networks in a special way but a systematic insight is still missing and up to now a systematic investigation of the influence of cross-linkers on actin network properties is lacking.

Generally, complex F-actin networks exist out of equilibrium due to chemical energy consumption (ATP hydrolysis) used for instance in treadmilling of actin filaments or molecular motor activity (fig. 2). To understand the behavior and properties of complex actin networks of the cytoskeleton *in vivo*, a bottom-up strategy is useful [Bausch & Kroy, 2006]. Using *in vitro* F-actin as a model system for semi-flexible polymer networks mimicking cytoskeletal networks *in vivo*, basic physical and chemical parameters can be isolated to answer the following questions: What is the effect of a single type of cross-linker in dependence of its concentration on the network structure and viscoelastic properties? What are the underlying physical parameters for the observed different morphological structures of actin networks obtained with diverse ABPs (fig. 2)?
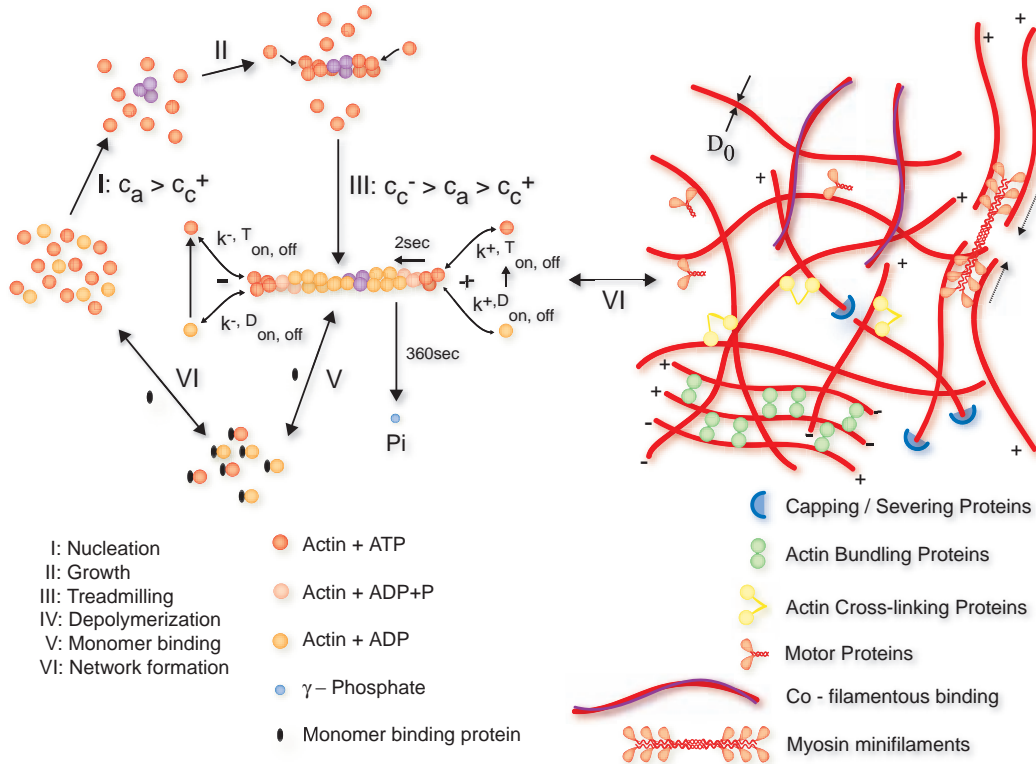
Figure 2: I-V: Polymerization procedure and treadmilling of actin. VI: Supra molecular network structures generated with F-actin and single ABPs. Capping proteins adjust the length of single filaments. Cross-linkers are able to condensate filaments into bundles, or form homogeneous cross-linked networks. Filamentous structures of molecular motors are capable to induce actin filament sliding.

In General, an ABP which is able to cross-link two actin filaments, has a modular archi-

Properties of cross-link		Physical parameters
FLEXIBILITY	Arrangement and	L
	structure of domains	κ_b, κ_s
GLUTINOUSNESS	Structure and	$K_D, k_{on,off}$
	number of ABD	# of ABDs

Table 1: Cross-linker parameterization

tecture. This cross-linker molecules consist out of two actin binding domains (ABD) which are separated and geometrically organized by different numbers of rod domains. Cross-linkers vary (i) in the type of actin-binding affinity (K_D) caused by specific binding domains used and (ii) in the structure, number, and organization of their spac-

3

ing rod domains. Consequently, several parameters determine the effect of a natural cross-linker (binding affinity, on- and off-rate $(k_{on,off})$, length (L) and bending (κ_b) as well as stretching stiffness (κ_s), tab. 1) which can be split in two observable properties: stickiness and flexibility of the cross-linker. For a systematic investigation both parameters have to be studied separately. Yet, the effect of structural rearrangements on the mechanical properties of such cross-linked networks is not fully understood. Thus, one aim of this thesis is to correlate the specific molecular structure of the cross-linker to the resulting network structure and its mechanical response.

In cells, the estimated overall protein concentration ranges between 200-300 mg/ml [Ellis, 2001]. For example, 25 % of the volume of the interior of cells is filled by proteins. Therefrom 10 % are agglomerated in filamentous form (stiff microtubules, semiflexible actin filaments and flexible intermediate filaments) whereas the majority resides in globular form. Hence, the interior of cells is highly crowded and cytoskeletal compartments underlie excluded volume effects, which alter the properties of the proteins. By installing another step of complexity, cross-linkers were investigated under molecular crowding conditions simulated with an important biologically compatible polyether, polyethylene glycol (PEG). Using the model cross-linker heavy meromyosin (HMM) in PEG/actin networks *in vitro*, first answers to the following questions could be obtained: What role do cross-linker molecules play under crowded conditions? What is the impact of molecular crowding on the activity of ABPs? Particularly, are specific cross-linkers tuners of the morphology of filamentous actin networks?

Mechanical forces are important parameters in cell behavior. The question that arises is how cells perceive those forces and how these are transduced into biochemical signals? Although cells are soft biological tissues they exhibit stiffening after straining (e.g. cell spreading). These changes in cell behavior depend on the force distribution within the interior components such as the cytoskeleton. Therefore the study of actin networks under nonlinear conditions is specifically of physical interest. Beside different microscopy techniques micro- and macrorheological methods are suited to solve these issues as demonstrated in this thesis. In combination a detailed microscopic insight of complex *in vitro* biopolymer networks can be attained, which can be the basis for bridging the gap between the different network morphisms and an understanding of cell cytoskeleton properties *in vivo*.

Chapter 1

Materials and their Physical Properties

*"Experience is something you don't have,
unless you could have needed it"*
`nameless`

1.1 Proteins

In this chapter the investigated proteins, used chemicals and beads are introduced. Various physical and chemical parameters like temperature, concentration or pH influence the properties of the relevant materials. Therefore, the most important properties and theoretical descriptions of the following materials are mentioned.

1.1.1 Actin

In all eucaryotic cells actin is the most abundant protein of the cytoskeleton. About 20 % of the overall protein mass of vertebrate skeleton muscular system is comprised by actin [Pollard, 1981]. Even in nonmuscular cells actin makes up five percent by weight of the cellular protein content. In the cytosol of nonmuscular cells actin is highly concentrated (c_a = 0.5 mM) and can be tenfold higher in special cellular structures like microvilli [Lodish et al., 2000].
The polypeptide G-actin consists of 375 amino acids (aa). This globular-shaped protein has a molecular mass M_w of 42 kDa and an absolute volume of 3.3×5.6×5.0

nm [Kabsch et al., 1990] with a minimal mean radius of 2.3 nm. At physiological
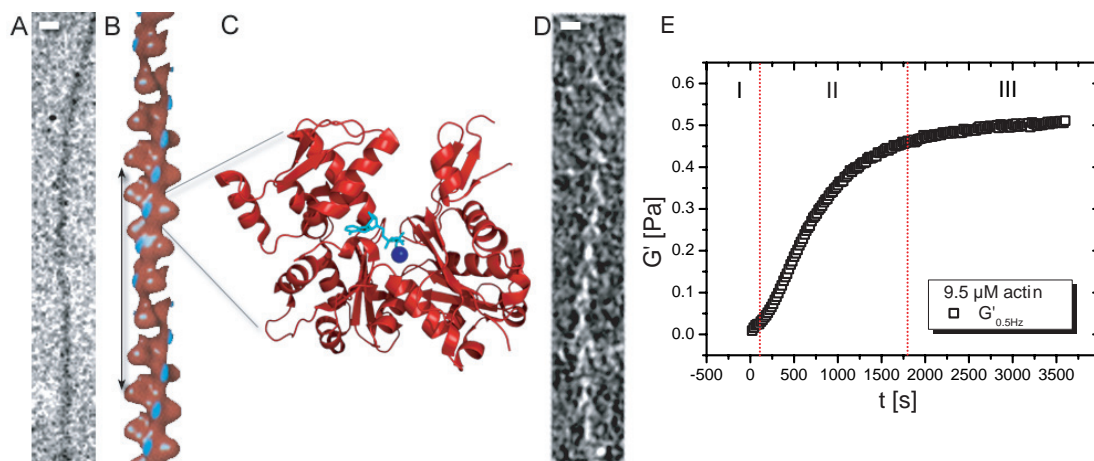
Figure 1.1: (A) *Cryogenic electron microscopy* (cryo-EM) *picture of actin filament with 18k magnification* (*sample preparation see chap. 6.5*). *Scale bar is 10 nm.* (B) *Reconstruction of actin filament from cryo-EM [Donald J. Voet, 2004]. The black arrow indicates the 36 nm long 13 subunit repeat [Ming et al., 2003] of the right-handed double helix.* (D) *X-ray structure of the G-actin monomer* (*backbone in red*) *from Dictyostelium discoideum* (dd). *The globular protein contains an adenosine triphosphate* (ATP, *cyan*) *and a magnesium ion* (*blue*) *[Vorobiev et al., 2003]* (PDB, 1NM1). (D) *Cryo-EM picture* (*sample preparation chap. 6.5*) *of actin filament decorated with heavy meromyosin* (HMM) *indicating the arrow head structure* (*scale bar is 10 nm*). (E) *Polymerization measurement of actin with a macrorheometer* (*chap. 2.2.3*). *The elastic modulus G'* (*defined in chap. 2.2.1*) *is followed over the time of 9.5 μM actin solution.*

conditions and ATP consumption actin assembles in a right-handed double helix with a pitch of 72 nm and a diameter of 7 nm [Bullit et al., 1988]. The actin filament possesses a characteristic 13/6 symmetry [Angelini et al., 2003, Ming et al., 2003]. 13 monomers are raised with 2.75 nm and rotated with 166.15° in six full turns reaching an identical spacial structure each 36 nm (fig. 1.1B). Consequently 364 monomers are built in a 1 μm long filament. In the polymerized state actin is denoted as F-actin. Filaments can reach a total length of up to 100 μm *in vitro*, whereas *in vivo* the filament length is controlled by ABPs. The actin monomers in the filament are oriented and therefore F-actin has two distinguishable ends. The plus (barbed) and minus (pointed[1]) end. On the one hand the polarity of the filaments is a necessary prerequisite for the directed force conduction of motor proteins, and on the other hand influences the polymerization behavior of the monomers on the different ends.

---

[1]the denomination follows from F-actin-myosin complex which appears as arrow heads (fig. 1.1D)

The polymerization process depends on the concentration of actin monomers, single and multivalent ions, temperature [Niranjan et al., 2001] and pH [Zimmerle & Freiden, 1988]. In a deep binding cleft between the four subdomains, the actin monomer is able to bind a magnesium- or calcium-ATP molecule (fig. 1.1C) which stabilizes the actin molecule [Cruz et al., 2000]. If ATP is bound to actin the equilibrium constant is shifted towards polymerization. As in fig. 1.1E, actin starts to polymerize in three successive phases: (I) nucleation, (II) growth and (III) equilibrium phase. In the first phase a seed of three actin monomers has to form.

Below a critical concentration ($c_c = k_{on}/k_{off} \equiv 1/K_D$ with K_D as the equilibrium dissociation constant), the probability of diffusive collision of monomers is to low and polymerization does not happen. Once $c > c_c^+ = 0.1$ μM $\cong 0.004$ mg/ml or $c_c^- = 0.7$ μM $\cong 0.03$ mg/ml at the plus or minus end respectively, nucleation seeds are forming. In the following growth phase monomers are added and the filaments elongate fast. The association rates are directly proportional to the actin concentration in solution $k_{on} \sim c_a$, whereas the dissociation rates k_{off} are not. After attachment of an ATP actin monomer ATP is irreversible hydrolyzed with a half-time of roughly two seconds [Blanchoin & Pollard, 2002]. Phosphate is released with a much lower half-time of about 360 s from the actin monomer [Carlier & Pantaloni, 1986]. The binding affinity of the ADP actin monomer is lower than for ATP containing actin monomers, which results in detachment of ADP actin monomers. The filament elongates further on as long as $k_{on}^{+,T} > k_{off}^{-,D}$ is preserved. But during growth phase, the actin monomer concentration in solution decreases till $c_a < c_c^-$. As a result, the filament depolymerizes at the minus end whereas at the plus end the filament keeps growing. In this way, an equilibrium length of the filaments is regulated which is not a thermodynamic equilibrium since ATP is consumed. The last step is called the treadmilling phase [Wegner, 1976]. Altogether, eight rate constants ($k_{on,off}^{+/-,T}$, $k_{on,off}^{+/-,D}$, the on- and off-rates for ATP and ADP containing actin monomers both for the plus and minus end, see fig. 2) determine this highly dynamical process of assembly and disassembly of actin monomers [Pollard & Borisy, 2003].

1.1.2 Actin Binding Proteins

In the cell, actin interacts with a variety of actin binding proteins. Why does the cell use so many different ABPs? In fig. 2 possible functions of ABPs are depicted. The cell uses these proteins to regulate its elastic behavior over four orders of magnitude

in elasticity from 0.01 to more than 100 Pa and on timescale between 1 ms to some 100 s. All these ABPs cause diversification of actin networks. In the following, the investigated ABPs are summarized.

Gelsolin

The name historically arose from the gel to sol crossover of cytoskeletal actin networks due to actin-gelsolin interaction. The globular protein has a M_w of about 90 kDa and consists of six homologous 15 kDa domains.
As shown in fig. 1.2B, gelsolin possesses three actin binding sites [Bryan, 1988].
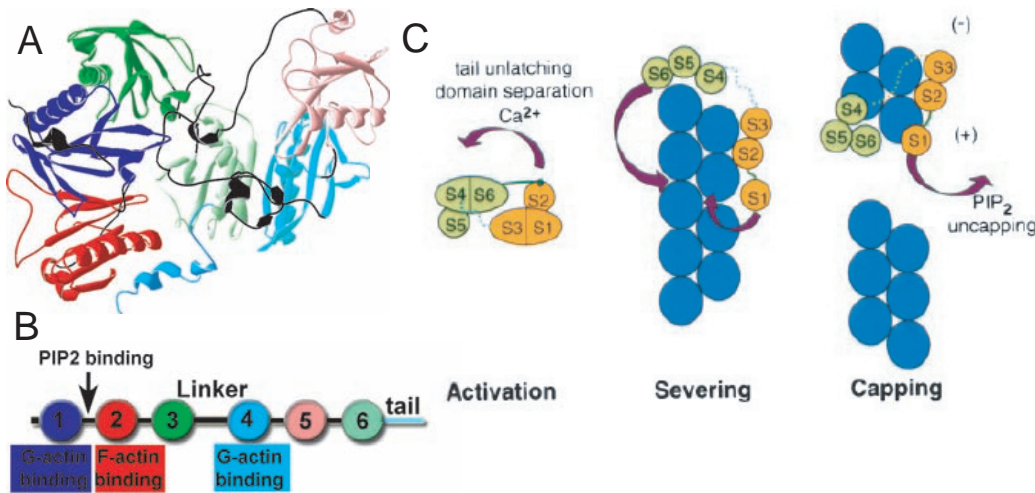
Figure 1.2: (A) *X-ray structure of gelsolin* (*PDB, 2FGH*). (B) *Sketch of the domain arrangement. The colors correspond to the crystal structure above.* (C) *Two functions of gelsolin on F-actin [Sun et al., 1999].*

The F-actin binding domain severs actin filaments if $c_{Ca^{2+}} \gtrsim 1$ μM. Ca^{2+} activates gelsolin so that the tail at the G6 domain unlatches. Consequently, the domains can separate and gelsolin can bind to F-actin. Based on thermal fluctuations, the filament rearranges at the gelsolin position and the filament breaks in two parts, when enough non-covalent bonds were weakened. Hence, the severing process is slower than binding of gelsolin. In addition, gelsolin caps the fast growing +end of actin filaments. The gelsolin cap blocks the filament preventing further growth. The reverse process is regulated by PIP$_2$ (phosphatidylinositol bisphosphate) binding which induces dissociation of gelsolin from the filament [Sun et al., 1999] (fig. 1.2C). Finally, gelsolin facilitates nucleation of actin [Yin & Stossel, 1979].

Figure 1.3: *Two domains of avidin forming a dimer (*cyan *and* blue*). The two biotin molecules are shown in yellow. They interact with the tryptophans # 70,97,110 and phenylalanine # 79 of avidin (*black*) forming the strongest known, non-covalent bond (*PDB*, 1VYO).*

Since the polymerization is pH dependent the actin gelsolin complex forms four times faster at pH 6.0 as at pH 8.0 [Selve & Wegner, 1987]. From EM pictures a simple prediction for the filament length distribution $\langle\, l\, \rangle$ was obtained

$$\langle l \rangle = \frac{R_{A/G}}{370} \mu m \qquad (1.1)$$

with $R_{A/G}$ as the molar ratio of actin to gelsolin molecules [Janmey et al., 1986]. This gauss shaped length distribution evolves and broadens with time (according to the theoretical model of [Coppin & Leavis, 1992]).

Neutravidin

Neutravidin is a conjugate of the avidin (Av) protein. The tetrameric protein has a M_w of 60 kDa and an isoelectrical point of 6.3 (product information, Molecular Probes). Four identical domains with beta-barrel structure form the protein (fig. 1.3). Each domain can bind a biotin[2] molecule. This coenzyme (M_w of 244.3 Da) has the lowest known K_D of non-covalent bonds. In fig. 1.3 binding of biotin by avidin is illustrated. The neutravidin biotin complex is used to bridge two biotinylated reagents, which in this case is biotinylated actin (chap. 6.4). Consequently, neutravidin acts as a cross-linker of actin filaments [Wachsstock et al., 1993], [Xu et al., 1998].

---

[2]former denotations: vitamin B7 or H

Filamins
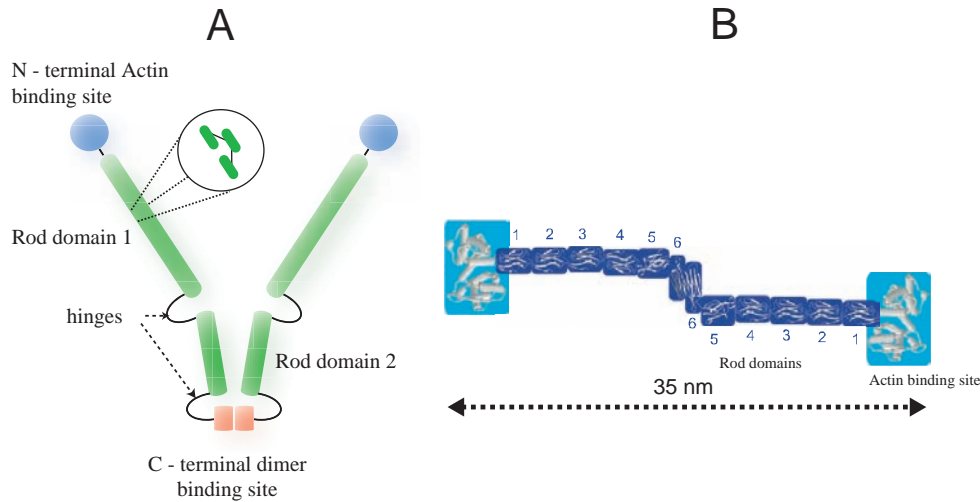
Figure 1.4: Comparison of the structure of ggFln (A) and ddFln (B).

There are a lot of different extended dimeric ABPs of different species which are called filamins[3]. The 280 kDa Filamin of Gallus gallus[4] is denoted as ggFln[5]. ggFln is a V-shaped dimer with a contour length of about 160 nm (see fig. 1.4A), whereas filamin of Dictyostelium discoideum (ddFln) is a more linear, antiparallel shaped dimer of about 35 nm in length (fig. 1.4B)[Fucini et al., 1999]. The K_D of ggFln to actin is 0.5 μM [Limozin & Sackmann, 2002]. ddFln has a similar K_D due to the great homology of the 27 kDa ABD, which is highly conserved also in the ABPs α-actinin, spectrin, dystrophin and fimbrin (human plastin) [Hanein et al., 1997]. 24 Immunoglobuline(Ig)-like fold domain repeats condense into two rods in ggFln. They are bridged together via very flexible chain segments between the 15th and 16th the 23rd and 24th repeat. These flexible parts serve as hinges in ggFln. With the last repeat at the C-terminus ggFln can dimerize [Stossel et al., 2001]. In contrast to ggFln, ddFln has six rod domain repeats. The fifth and sixth domain are involved in the dimerization of the molecule [McCoy et al., 1999]. The fourth repeat can unfold via an intermediate state with a first contour length increase of 14 nm and a second of 16 nm [Schwaiger et al., 2004]. Human filamin has a similar architecture as ggFln. The overall force to unfold individual domains of human filamin is about 50 to 220 pN with

---

[3]dominated corresponding to their filamentous appearance
[4]latin for bankiva chicken
[5]according to the convention of names following [Stossel et al., 2001]
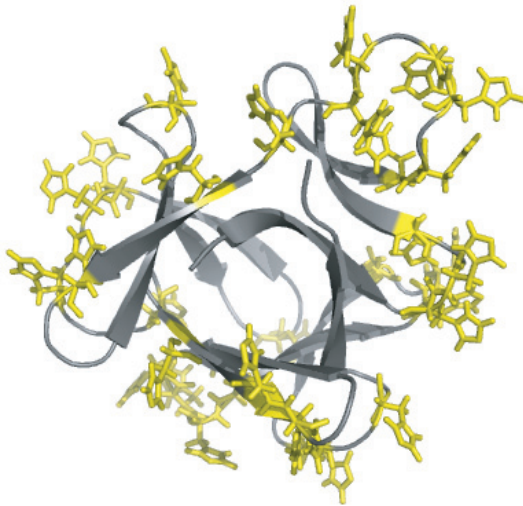
Figure 1.5: *Crystal structure of Hisactophilin (PDB, 1HCD). The backbone is in gray color. Positions of the 31 histidines in the protein are shown in yellow.*

a length increase of around 31 nm. This results in a persistence length l_p[6] of the unfolded polypeptide of 0.33 nm, calculated from the worm like chain model (WLC) [Furuike et al., 2001]. l_p for ddFln is about 0.5 nm. Overall, ggFln is a very flexible ABP. It seems that ddFln is also very flexible but a little bit less than ggFln by comparing the arrangement of domains and l_p.

Hisactophilin

Hisactophilin (hisac) occurs mainly in the submembranous region of amoebae cells [Scheel et al., 1989]. This relatively small protein of 118 residues and a M_w of 17 kDa contains 31 histidines [Scheel et al., 1989], which are directed to the outside of the surface of the barrel like molecule (fig. 1.5). Below a pH value of 7.2, the histidines are positively charged (iso-electrical point of hisac: 7.2) and the hisactophilin is electrostatically attracted to the negatively charged F-actin. Consequently, the high content of histidines is responsible for the high binding affinity to F-actin below pH 7.2 [Schleicher et al., 1995]. For higher pH values the binding affinity vanishes. Moreover, hisac binds to partially charged lipid membranes and mediates coupling of actin to the membrane of cells [Behrisch et al., 1995]. Therefore the hisac molecule is proposed to function as a pH sensor *in vivo* [Stoeckelhuber et al., 1996].

---

[6]chap. 1.4.1

Synthetic Cross-links   Seven synthetic cross-links[7] constructed out of hisac and ddFln domains were used in this work (see tab. 1.1.2).

 In fig. 1.6 four of these recombinant proteins are presented schematically. With these

ABBREVIATION	DESCRIPTION
HisAc-C	Monomeric hisac with a cystein cap at the end
HisAc-woC	Mutant of hisac with exchanged cystein: C49S
HisAc-HisAc	Dimeric hisac, covalently bound via GGS bridge
HisAc-S-S-HisAc	dimeric hisac, bond via a disulfide bridge
HisAc-D5-6	Dimeric molecule: containing 2 hisac as ABDs and domains number 5 and 6 of ddFln
HisAc-D2-6	Dimeric molecule: containing 2 hisac as ABDs and domains number 2 to 6 of ddFln
Biotin-D2-6	Dimeric molecule: containing biotin for Neutravidin binding and domains number 2 to 6 of ddFln

Table 1.1: List of synthetic cross-linkers.

recombinant ABPs the molecular mass and structure of the proteins as well as the binding affinity were varied systematically.

Cortexillins

Cortexillins are required for normal division of cells during mitosis. They suppress ruffling of actin networks and give rise to the bending stiffness of the actin cortex. Therefore they are located in the equatorial region of the mitotic cell [Weber et al., 2000]. No other ABPs from the calponin homology ABD superfamily, which bind to filamentous actin, are co-localized [Weber et al., 1999]. Cortexillin I (CI) is a 51 kDa ABP with 444 aa and a total length of 27 nm (see fig. 1.7 on the left) [Faix et al., 1996]. It dimerizes via a 19 nm long coiled coil [Steinmetz et al., 1998]. The N-terminal calponin-homologous ABD (27 kDa, 4 nm in diameter) has a typical K_D of $2.3 \cdot 10^{-7}$ M [Faix et al., 1996]. The C-terminal tails are about 2-3 nm long and are PIP_2 regulated. It has been shown that on the one hand the C-terminal tail domains are responsible for actin bundling [Stock et al., 1999], on the other hand they have membrane binding capacity [Weber et al., 1999]. If PIP_2 binds to CI the bundling of actin is inhibited.

---

[7]for sequence alignment see fig. 6.6-6.15
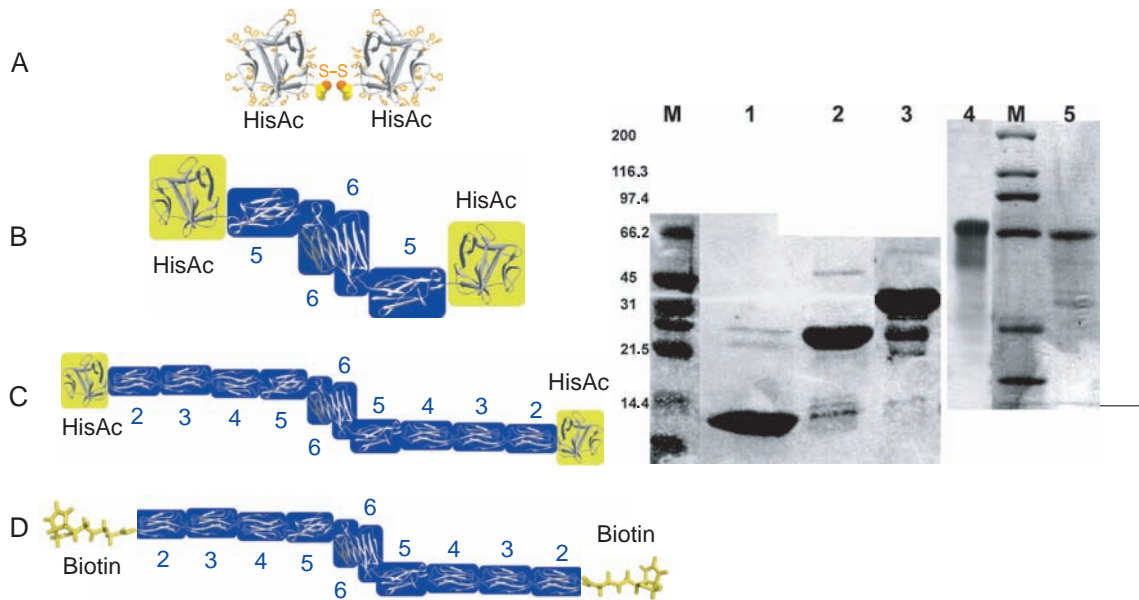
Figure 1.6: Left: lineup of synthetic cross-links and their calculated molecular mass in native state. (A) HisAc-S-S-HisAc (M_w = 27.4 kDa), (B) HisAc-D5-6 (M_w = 72 kDa), (C) HisAc-D2-6 (M_w = 135.4 kDa), (C) Biotin-D2-6 (M_w = 108 kDa). Right: SDS gel of the purified synthetic cross-links. The first line shows the molecular weight of the marker (M), (1) HisAc-C, (2) HisAc-S-S-HisAc, (3) HisAc-D5-6, (4) HisAc-D2-6, (5) Biotin-D2-6.
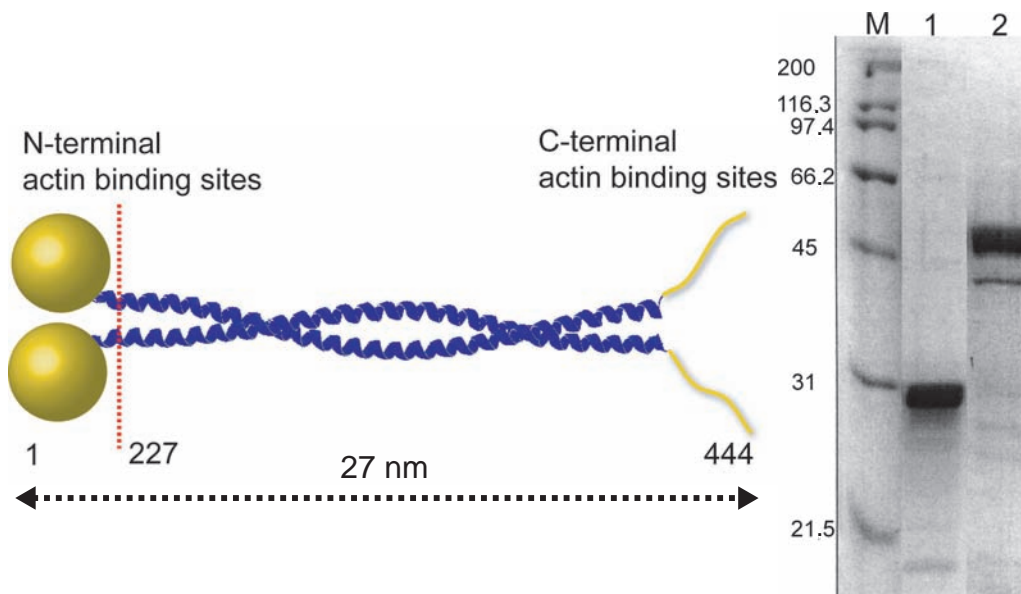
Figure 1.7: Left: structure of Cortexillin I. Right: SDS Gel of purified Cortexillin. The first column shows the M_w of the broad range marker, the second (1) CI227-444 and the third (2) CI1-444.

Myosins

Myosins are common in nearly all eucaryotic cells. There are 17 different classes of the myosin family which follows from sequence alignment (see fig. 1.8I) [Hodge & Cope, 2000]. Members of class II are called conventional myosins, since they were first discovered in muscle tissue. The other myosins are called unconventional myosins because they are expressed from non-muscle cells. Each myosin has a special function. They are used for cargo transport (e.g. vesicles, cell organells or macro proteins), cell movement or they are involved in endocytosis. All myosins are ATPases which convert chemical energy into mechanical energy by hydrolysis of ATP. Therefore, they are also called molecular motors (MM). Some of the MM are able to walk along actin filaments (without detachment for several steps, processive MM) and some are not (nonprocessive MM, e.g. Myosin II) (see. chap. 1.5). Most myosins are homodimeric molecules. The monomer comprises one or two heavy chains (HC) and one to six light chains (LC). The HC has three functional segments. The globular head domain is responsible for force generation and is highly conserved in all myosins. The head is connected via a α-helical neck domain with the tail. The neck domain is responsible for energy conversion and functions as a lever arm [Howard, 2001]. It is stabilized through the LC which encloses the neck. Myosin assembles to dimers by wrapping two α-helical tail domains around each other forming a "coiled-coil" structure. At the end of the tail vesicles or other cargoes can bind.

Myosin II   Myosin II is a 520 kDa dimer and one of the largest known proteins [Wick, 1999]. It has an approximate overall length of 160 nm [Donald J. Voet, 2004] and contains more than 2200 aa in the polypeptide chain (see app. 6.6C). Due to the kink in the coiled-coil (fig. 1.8II,B), myosin II is able to assemble into bipolar filaments (fig. 1.8II,A) dependent on the salt concentration. The backbone of these filaments is formed by the tails whereas the heads stick out to the side (fig. 1.8II,A TEM image [Trinick & Elliott, 1979]). At pH 8.0 and an ionic strength below 200 mM of monovalent ions, the filaments are about 300 nm long and contain 16 to 18 myosin molecules [Reisler et al., 1980]. With a constant ionic strength of 100 mM of monovalent ions the length of the minifilaments can be tuned of a factor 1.3. pH variation between 8.2 and 6.5 triples the number of molecules in the minifilament [Niederman & Pollard, 1975]. *In vivo*, these minifilaments are part of the functional unit of the muscle fiber. Moreover, they are involved in the retrograde actin flow
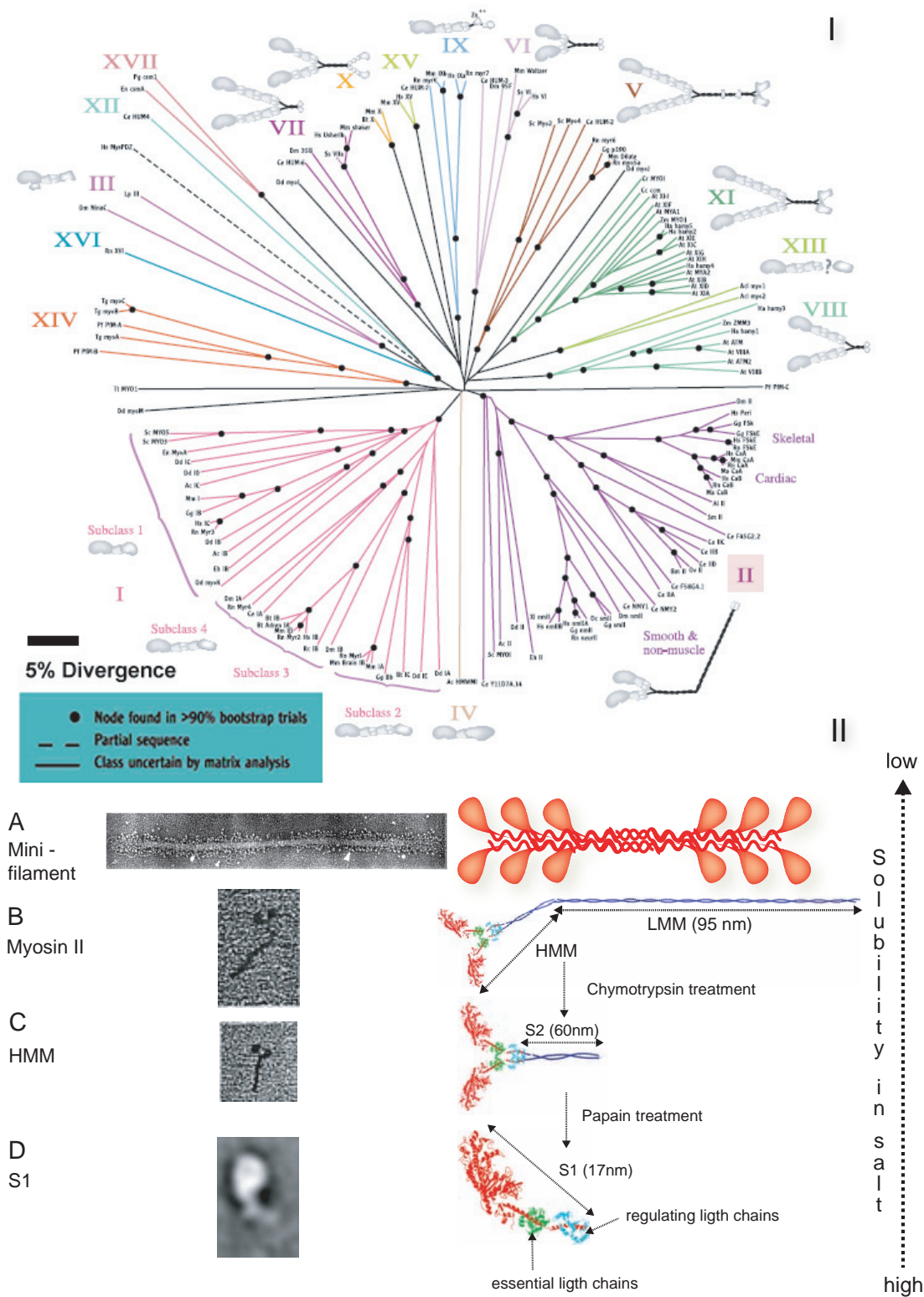
Figure 1.8: (*I*) *Myosin family tree [Hodge & Cope, 2000].* (*II*) *Representation of the myosin II substructures.*

[Medeiros et al., 2006] and cell body translocation [Svitkina et al., 1997] of moving cells or during mitosis [Weber et al., 2000, Weber et al., 1999].

HMM and S1   Myosin II can be enzymatically cleaved into subfragments. After chemotrypsin treatment one obtains heavy meromyosin (HMM) and light meromyosin (LMM), which are depicted in fig. 1.8II,B. The LMM is 95 nm long [Donald J. Voet, 2004] and 2 nm in diameter, which is the coiled-coil from the kink to the tail end. The HMM is a 65 nm long dimer of about 360 kDa. It possesses full enzymatic functionality because it contains the myosin motor heads (metal shadowed EM picture [Lowey et al., 1969], see fig. 1.8II,C), but it is not able to oligomerize into minifilaments anymore, due to the lack of the long tail. HMM can be divided into subfragments by cleaving with papain. The residual of this process is called S1, which is the myosin motor head and S2 which weights 50 kDa. The S1 contains the essential light chain and the regulatory light chain. Its overall polypeptide chain comprises 1128 aa what results in a M_w of 130 kDa and a total length of 17 nm (fig. 1.8II,D. EM picture from http://www.astbury.leeds.ac.uk/gallery/leedspix.html on the left side and corresponding sketch on the right side).

1.2   Accessory Organic Chemical Substances

Polyethers

The most important polyethers are polyethylene glycol (PEG), also known as polyethylene oxide (PEO) or polyoxyethylene (POE). All three names are chemical synonyms[8]. PEG are polymers with $M_w <$ 20 kDa and PEO polymers have a $M_w >$ 20 kDa whereas POE refers to a polymer without a molecular mass restriction.
 Polyethylene glycol is a stable and inert polymer of ethylene oxide, which is often used in clinical applications as well as for food or pharmaceutical products due to its non-toxicity. The polymers are built of long carbon chains of repeating units (fig. 1.9). The number n of the repeating units (M_w = 44 Da) indicate the average molecular weight. Within this work PEG with a M_w of 6 kDa (PEG6k) was used. Over 1 kDa PEG has a wax like appearance and is water soluble. The flexible polymer can be treated as a hard sphere [Tellam et al., 1983] (fig. 1.9 right) with a gyration radius

---

[8]historic development

(H(OCH$_2$CH$_2$)$_n$OH)
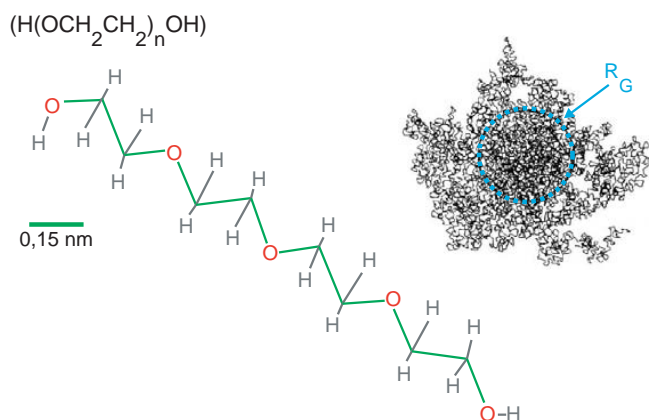
Figure 1.9: *Left side: chemical formula of polyethylene glycol (n = 8). Right side: schematic representation of the PEG polymer chain.*

$R_{g,IC}$ of an ideal chain (IC) [Rubinstein & Colby, 2003]:

$$R_g = \sqrt{\frac{N_K}{6}} \cdot b = 3.0nm \tag{1.2}$$

N_K is the number of Kuhn monomers and b is the Kuhn segment length. For PEG6k N_K is 44 (see. tab. 2.3 [Rubinstein & Colby, 2003]). Including the effect of the self-avoiding swollen coil, $R_{g,IC}$ has to be corrected by a factor of $N_K^{0.1}$. If the polymer is a semidilute solution instead of beeing a diluted one, the polymer size is reduced by a factor of $\left(\frac{c_p}{c_p^*}\right)^{-\frac{1}{8}}$, with c_p as the crossover polymer concentration from the dilute to the semidilute regime [Kulkarni et al., 2000]. Overall the PEG6k has a real chain radius of gyration ($R_{g,RC}$) of 3.7 nm. In a 10 % w/v PEG6k solution the polymer size is reduced roughly by 20 % which results in a total gyration radius of 3 nm. The R_g of 3 nm of PEG6k is comparable to the radius of a single actin monomer (chap. 1.1.1). Furthermore, the PEO218k was used for mimicking large proteins with no specific interactions (see chap. 3.1.2). The PEO with 218 kDa (PEO218k) has a $R_{g,IC}$ of 18 nm and R$_{g,RC}$ of 32.3 nm, which is comparable to the dimensions of an HMM molecule (chap. 1.1.2).

Dyes, Beads and Buffers

Dyes

The dye Tetramethyl rhodamine isothiocyanate (TRITC) attached to phalloidin was used for fluorescence labeling of F-actin. TRITC was purchased and stored as mentioned in [Wagner, 2004].

Beads

Monodisperse colloidal gold particles (0.01 % $HAuCl_4$ suspended in 0.01 % tannic acid from Sigma Aldrich, pnr[9] G-1527) with a mean size of 10 nm in diameter were used for quantitation and 3D alignment of the sections obtained from cryo-EM (see chap. 6.5).

Buffers

Functionality of proteins crucially depends on pH and salt conditions. Therefore different buffer systems were used within this work (see chap. 6.8). For all buffers ultra pure double de-ionized water (ddH$_2$O, filtrated with a Millipore facility) was used. Buffers were degased for 2 h and stored at -20° C in small aliquots.

1.3   Linear Theory of Viscoelasticity

A body of a certain material deforms if exposed to external forces. On the one hand ideal solids show purely elastic behavior whereas perfect fluids are absolutely viscous. On the other hand in real materials often both properties are comprised. Hence they are called viscoelastic. The overall behavior depends on the history of the applied forces and rates. For describing the deformation[10] the distance dl between to adjacent points of a body is changed to dl':

$$dl'^2 = dl^2 + \sum 2 \cdot \gamma_{ij} \cdot dx_i \cdot dx_j \tag{1.3}$$

γ_{ij} is the 3×3 strain tensor, it contains the relative size changes of the body. The symmetrical 3×3 tensor σ_{ij} is called stress tensor. The components of σ_{ij} which act parallel to the areas (i $\neq$ j) of a hypothetical cubic volume element are denoted as shear stresses. Both tensors evolve with time ($\gamma_{ij} = \gamma_{ij}(t)$, $\sigma_{ij} = \sigma_{ij}(t)$). For simplification four assumptions are made, which define the case of simple shear (cf. fig 1.10):

1. only stress differences are considered

2. no normal forces are measurable

---

[9]product number
[10]The description follows basically the theories of [Ferry, 1980], [Landau & Lifschitz, 1966] and [Tschoegl, 1989]
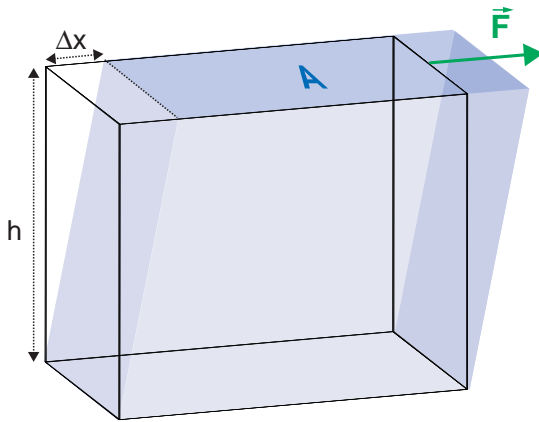
Figure 1.10: *Simple shear of a cuboid volume $V = A \cdot h$ under an applied force $\vec{F}$ parralel to the surface A.*

3. the homogeneous shear field inside the sample solely depends on one single space coordinate

4. the absolute value of the deformation amplitude is small

If a body is sheared between to rigid plate plates, the shear stress τ follows to:

$$\tau = \frac{F}{A} \tag{1.4}$$

with the assumption of the simple shear. The shear strain γ results in the ratio of the deflection of the top surface Δx and the sample height h, which corresponds to the gap width of the two plates.

$$\gamma = \frac{\Delta x}{h} \tag{1.5}$$

Furthermore Hook's law is valid:

$$G = \frac{\tau}{\gamma} \tag{1.6}$$

and G is defined as the young modulus which is constant in case of a purely elastic material. For an ideal fluid τ is directly proportional to the applied shear rate $\frac{d\gamma}{dt}$. The proportionality prefactor then defines the viscosity η of the fluid and one obtains Newton's law for dynamic viscosity:

$$\eta = \frac{\tau}{\dot{\gamma}} \tag{1.7}$$

Since viscoelastic materials exhibit strong time dependencies, it is additionally presumed that the time variation of small deformations $\delta\dot{\gamma}$ is proportional to $\delta\dot{\tau}$. Subse-

quently eq. 1.6 can be rewritten and $\tau(t)$ follows to [Ferry, 1980]:

$$\tau(t) = \int_{-\infty}^{t} dt' G(t - t') \cdot \frac{d\gamma(t')}{dt'} \tag{1.8}$$

with the relaxation modulus $G(t)$ and the creep compliance $J(t)$ which is the inverse of the relaxation modulus:

$$J(t) \equiv \frac{1}{G(t)} \tag{1.9}$$

1.4 Physics of Polymers

1.4.1 Classification of Polymers

Polymers in the liquid state exist as melts or solutions. The physical properties of polymer solutions generally depend on the temperature T, the polymer concentration c and the solvent type. Polymers in good solvents are classified by the polymer concentration into four different regimes (tab. 1.2):
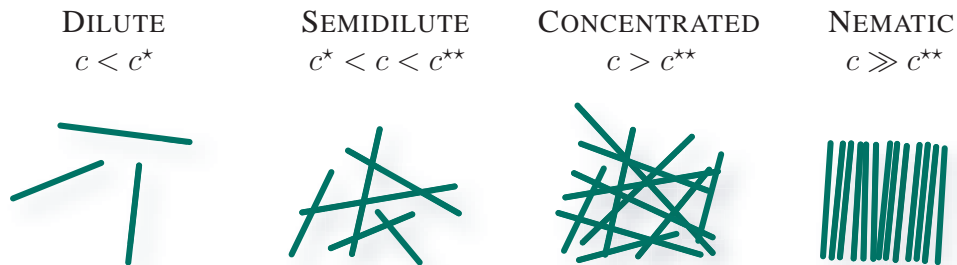
Table
1.2: Classification of polymers solutions. $c^\star$ and $c^{\star\star}$ denote the cross-over concentrations.

1. Dilute solutions: single polymers in solution can move freely due to the large mean distances between them. Therefore the interactions between single polymers are weak and thus can be neglected. Each polymer occupies a space of radius R_g (flexible polymer) or length L (stiff polymer).

2. Semi-dilute solutions: the polymer molecules themselves overlap and start to entangle respectively intersect if the polymer concentration exceeds a critical

value $c^\star$. They still occupy only a small volume fraction.

3. Concentrated solutions: in this regime $(c > c^{\star\star})$ the polymer filaments are isotropically entangled, intersected.

4. Nematic phase: with increasing polymer concentration a nematic phase crossover occurs whereupon filaments arrange in arrays.

The polymer melt is the limit of the infinitely concentrated polymer solution, which contains no solvent molecules anymore.

For further classification of polymers, the contour length L_c, the mean square end to end distance $\langle R^2 \rangle$ and the so called persistence length l_p according to [Doi & Edwards, 1989] are considered (see the three different classes in tab. 1.3).

STIFF POLYMERS	SEMIFLEXIBLE POLYMERS	FLEXIBLE POLYMERS
$l_p \gg L_c$ $\langle R^2 \rangle = L_c^2$	$l_p \approx L_c$ $\langle R^2 \rangle \leq L_c^2$	$l_p \ll L_c$ $\langle R^2 \rangle \ll L_c^2$
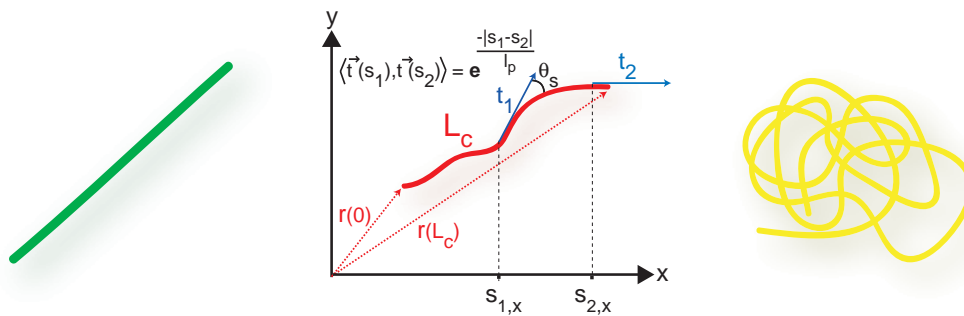
Table 1.3: Classification of polymers by length.

l_p is the length between two points s_1 and s_2, with which the mean correlation $\langle \vec{t}_1, \vec{t}_2 \rangle$ of the tangent vectors t_1 and t_2 has decayed to the 1/e part and is therefore a measure for the stiffness of the polymer.

F-actin belongs to the group of semiflexible polymers with $l_p \approx 17$ μm [Brangwynne et al., 2007], [Gittes et al., 1993], [Goff et al., 2002], [Ott et al., 1993] (obtained through measurements of shape fluctuations of actin filaments) and an average length of $\langle l \rangle \approx 22\mu$m (*in vitro*) [Kaufmann et al., 1992].

1.4.2 Properties of Single Polymers under Force

Mechanical Forces

Mechanical forces act on single filaments if filamentous networks are deformed. For a theoretical description, let $\vec{r}(s)$ be a differentiable space curve. If one considers this curve as an inextensible chain ($|\vec{t}(s)| = 1$) with a contour length L_c and a bending rigidity κ (see fig. 1.11A), then the energy for bending this chain is not purely entropic in origin in contrast to the freely-jointed-chain (FJC) [Doi & Edwards, 1989]. This
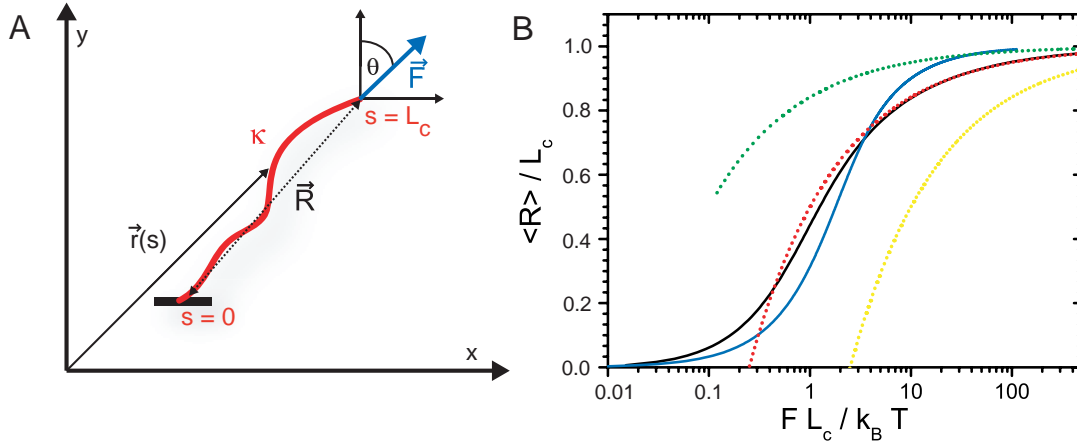
Figure 1.11: (A) *2D illustration of an anchored space curve of contour length L_c and bending rigidity κ.* (B) *The dimensionless mean end to end distance is plotted over the dimensionless force. The black curve is calculated following [Marko & Siggia, 1995]. The blue curve is the FJC [Doi & Edwards, 1989]. The dashed lines are calculated following eq. 1.11 (green: $l_p/L_c = 10$, red $l_p/L_c = 1$, yellow: $l_p/L_c = 0.1$)*

model is known as the worm-like-chain (WLC). For small external applied forces hook's law is valid (linear regime) and the force F is proportional to the extension x:

$$x = F \cdot \frac{\langle \vec{R}^2 \rangle - \langle | \vec{R} | \rangle^2}{k_B \cdot T} \Rightarrow F \sim k \left(l_p, \frac{L_c}{l_p}, \theta \right) \cdot x \qquad (1.10)$$

with the spring constant k. k depends on the angle θ, the contour and persistence length. Since there is no analytical expression for the quadratic mean absolute value of the end to end distance ($\langle | \vec{R} | \rangle^2$) the extension is calculated via a perturbation calculation and series expansion of the difference in eq. 1.10. The spring constant can be calculated if one assumes no rotation of the chain ([Kroy, 1998] p. 27). In cases of stiff rod and flexible chain limit, the simple expressions for k are shown in tab. 1.4.

$$l_p \gg L_c \qquad\qquad l_p \approx L_c \qquad\qquad l_p \ll L_c$$

$$k_s(\theta = 0) = \frac{6 \cdot k_B \cdot T \cdot l_p^2}{L_c^4} \quad k_{sf}(l_p, \tfrac{L_c}{l_p}, \theta) \quad k_f = \frac{3 \cdot k_B \cdot T}{2 \cdot L_c \cdot l_p}$$

Table 1.4: Spring constants for WLC in the linear regime.

For high forces $(F \cdot L \gg k_B \cdot T)$ the mean end to end distance in dependence of the applied force on the polymer can be calculated in the limit of the weakly bending rod approximation (in this case the end to end distance can be identified with the projection of the contour length on a plane) [Kroy, 1998]:

$$\langle R \rangle = L_c \cdot \left(1 - \frac{\coth \sqrt{\frac{F \cdot L_c \cdot L_c}{k_B \cdot T \cdot l_p}}}{2 \cdot \sqrt{\frac{F \cdot L_c \cdot l_p}{k_B \cdot T \cdot L_c}}} \right) \Rightarrow \frac{\langle R \rangle}{L_c} = 1 - \sqrt{\frac{k_B \cdot T}{4 \cdot F \cdot l_p}} \qquad (1.11)$$

In fig. 1.11B the black curve is calculated following [Marko & Siggia, 1995]. For high F, the Marko Siggia formula approaches the WLC for semiflexible polymers. In the low F regime, it converges to the linear approximation of the FJC which equals to the flexible limit of the WLC.

For semiflexible polymers like F-actin the WLC is only a good description for high forces. For small forces $(F \cdot L_c < k_B \cdot T)$ the Marko Siggia formula is the better approximation. For the linear filament length change with tension a third term $(+\frac{F}{K_{tension}}$, with $K_{tension}$ as the elastic stretching modulus) in eq. 1.11 was added considering weak undulations $(|\langle R \rangle - L_c| \ll \langle R \rangle)$ and small elongation of the filaments [Odjik, 1995]. With this formula Liu et al. fitted their stretching experiments of F-actin with a cantilever. The resulting longitudinal stiffness of F-actin was 34.5 ± 3.5 pN/nm. Below 50 pN the length extension was found to be nonlinear with a resultant strain of 0.4-0.6 %. Whereas between 50 pN and the maximal physiological tension ($\approx$250 pN), the filaments can be stretched by 0.3 % [Liu & Pollack, 2002].

Depletion Forces

Entropy can induce attractive forces in many-particle systems. For instance in a binary colloid suspension larg particles experience an attractive force due to the depletion of smaller particles from the volume between the larger ones. If one considers N small colloids as an ideal gas, the entropy ΔS rises with the overlap of the excluded volume

Figure 1.12: *Sketch of two actin filaments bundled together due to depletion forces [Tharmann, 2006]. The filaments are illustrated as cylindrical rods with a diameter 2·R. The green shaded volume which corresponds to the volume gain ΔV is depleted of small colloidal particles with radius r*
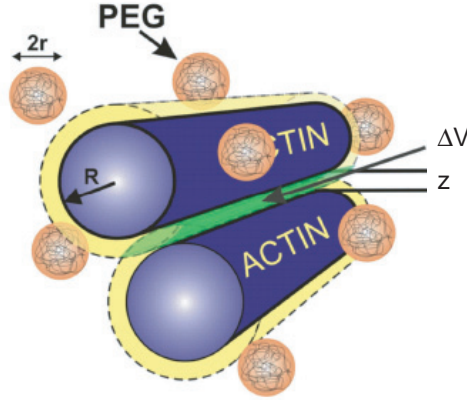
ΔV and consequently the free Energy E_F decreases [Bechinger et al., 1999]:

$$\Delta E_F = -T \cdot \; \Delta S = k_B \cdot T \cdot N \cdot \ln \left(1 + \frac{\Delta V}{V} \right) \tag{1.12}$$

For the large particles this corresponds to an effective attractive interaction with a range of two times r (radius of the small particles). This effect also acts on actin filaments, which are approximated as cylindrical rods (see fig. 1.12). If one takes into account this depletion effect on F-actin filaments, the entropic attraction has to exceed the electrostatic repulsion. In total the gained energy (U_{tot}) is a sum of depletion attraction U_D, electrostatic repulsion $U_{el.stat.}$ and van-der-Waals attraction U_{vdW} [Hosek & Tang, 2004]:

$$U_{tot} = U_D + U_{el.stat.} + U_{vdW} \tag{1.13}$$

By use of an effective pair potential it was possible to take into account all the complex monomer interactions of the polymers from eq. 1.13 [v. Teeffelen, 2004].

1.4.3   Properties of Polymer Networks

Apart from viscous properties, semidilute solutions of actin filaments show elasticity on certain time scales. Therefore, actin networks are an ideal model system for semiflexible polymer solutions with viscoelastic properties. Because of their elongated structure the filaments entangle in semidilute solutions. Surrounding filaments form an imaginary tube (fig. 1.13B) in which a test actin filament fluctuates and reptates. In this tube model of entangled polymer networks [de Gennes, 1979], the mean filament distance ξ is called the meshsize. The maximum amplitude of thermal undulations of an
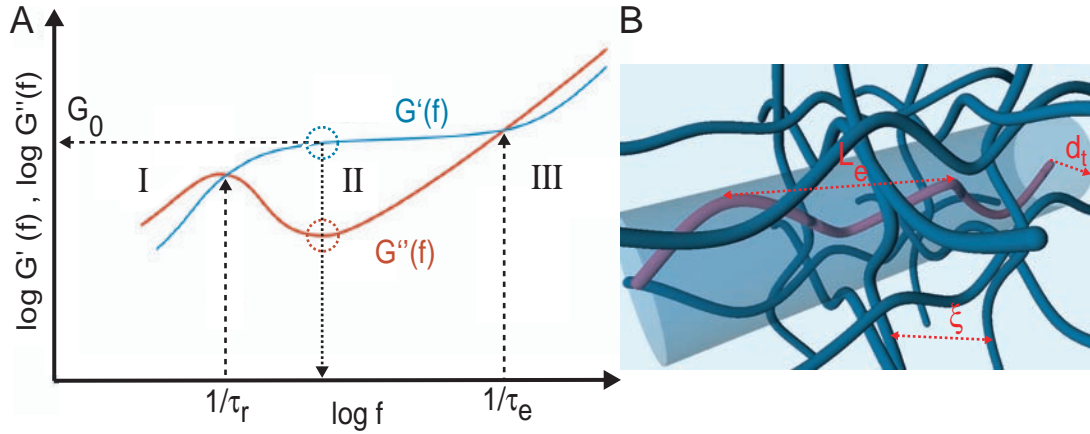
Figure 1.13: (A) Characteristic frequency spectrum of the storage G' and loss modulus G'' (defined in chap. 2.2.1) of a network of semiflexible polymers in solution. (B) Illustration of entangled filaments. The test polymer in its tube (transparent color) is depicted in purple. The entanglement length L_e, meshsize ξ and the tube diameter d_t are shown in red color.

actin filament is denoted as the tube diameter d_t.

$$d_t = a \cdot \xi^{\frac{6}{5}} \cdot l_p^{-\frac{1}{5}} \tag{1.14}$$

The absolute value of $a = 0.32$ was derived in first order from known scaling laws [Hinsch et al., 2007]. Furthermore, the mean distance between two collision points of the test filament with the tube walls is defined as the entanglement length L_e [Odjik, 1983]:

$$L_e = b \cdot d^{\frac{2}{3}} \cdot l_p^{\frac{1}{3}} \Rightarrow L_e \sim \xi^{\frac{4}{5}} \cdot l_p^{\frac{1}{5}} \tag{1.15}$$

with the predicted prefactor of $b = 2^{\frac{1}{6}}$ [Hinsch et al., 2007], $b = 2^{\frac{4}{3}}$ [Morse, 1998a]. Undulations of wavelengths larger than L_e are strongly overdamped. Normally, actin filaments are considered as semiflexible polymers which are only weakly bent. With the assumption of a weakly bending stick, undulating in a viscous fluid, the decay or relaxation time τ_n of the thermally excited undulations of order n, depends on the length L of the rod [Howard, 2001]:

$$\tau_n \simeq \frac{\gamma_d}{k_B \cdot T \cdot l_p} \left(\frac{L_c}{\pi \cdot (n + 0.5)} \right)^4 \tag{1.16}$$

with the drag coefficient γ_d.

In an advanced tube model, the relaxation spectrum of the long wavelength

Figure 1.14: *Calculated relaxation times in dependence of the polymer length following eq. 1.16 with* $\gamma_d = 2 \cdot 10^{-3}$ *Pas. The black arrow indicates the entanglement length* (*corresponding to* $c_a = 9.5\mu M$). *The red shaded area marks the accessible measuring regime for macrorheometry* (*see chap. 2.2*).
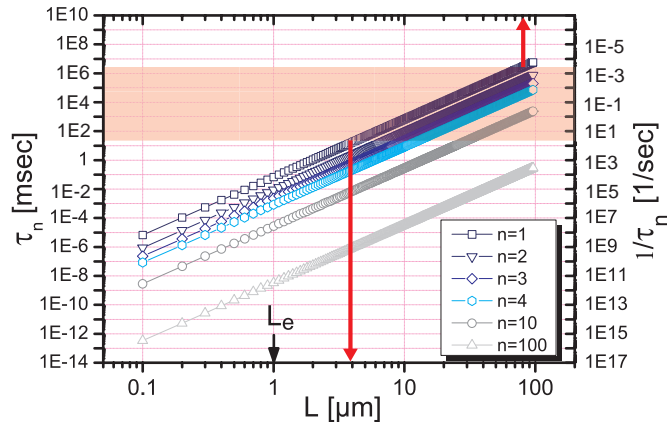
eigenmodes is exponentially stretched. This model, called the glassy wormlike chain (GWLC), is regulated by a single parameter, the stretching parameter ε [Kroy & Glaser, 2007]. It can be interpreted as a barrier height E_F in a free energy landscape. Therefore, ε can be treated as a kind of kinetic "stickiness". In this theory the relaxation time is modified to:

$$\tau_n \rightarrow \tilde{\tau}_n = \begin{cases} \tau_n & (n > L) \\ \tau_n \exp^{N_n \cdot \varepsilon} & (n < L) \end{cases} \tag{1.17}$$

with N_n as the number of interactions per eigenmode wavelength λ_n

$$N_n \equiv \frac{L}{n} - 1$$
$$\lambda_n \equiv \frac{L_c}{n} \qquad\qquad \lambda_n > \Lambda_e$$
$$\Lambda_e \equiv \frac{L_c}{L} \qquad\qquad \Lambda_e \ll L_c, l_p$$

and Λ_e as the interaction length. In fig. 1.13 a typical frequency course of the storage (elastic) modulus G' and the loss (viscous) modulus G'' is shown for such materials. One can classify this theoretical behavior in three distinct regimes. These three regimes are divided by two particular frequencies which correspond to reciprocal crossover times. The reptation time τ_r and the entanglement time τ_e which is defined as follows [Isambert & Maggs, 1996]:

$$\tau_e = \frac{\gamma_d \cdot l_p^{1/3} \cdot d^{8/3}}{k_B \cdot T} \tag{1.18}$$

1. range of internal chain dynamics $(f > \frac{1}{\tau_e})$

on this time scale relaxation processes are only possible inside the tubes. The stress release is determined by the entropic tension of the filament and proceeds therefore mainly perpendicular to the filament contour. Interactions of the tubes do not play a role and consequently the behavior of the polymer solution is determined by the single filament properties. The time dependent mean square deviations of undulations of a single filament could be related to the shear modulus following [Gittes & MacKintosh, 1998]:

$$G(f) \sim f^{3/4} \tag{1.19}$$

This power law could be approved by rheological measurements with microspheres in actin networks for high frequencies $(f > 1000 \text{ Hz})$ [Mason et al., 2000].

2. plateau range $(\frac{1}{\tau_r} < f < \frac{1}{\tau_e})$

Here the G' is approximately constant. The plateau modulus G_0 is defined as G' at the frequency where G'' has a distinct minimum (fig. 1.13A). Confining a filament of contour length L_c in a tube with diameter d_t and a length L_e costs the energy E_F for suppressing the transversal fluctuations of the filament. Each collision of the filament with the tube costs the energy $k_B \cdot T$. The number of polymers in solution is directly proportional to the concentration which is again indirectly proportional to the square of the meshsize. A mere definition of ξ is [Hinsch et al., 2007]:

$$\xi = \sqrt{\frac{3}{n \cdot L_c}} \tag{1.20}$$

Experimentally the following relation for the meshsize and the concentration of actin filaments could be obtained [Schmidt, 1999]:

$$\xi[\mu m] = \frac{0.34}{\sqrt{c_a[\frac{mg}{ml}]}} \tag{1.21}$$

With eq. 1.15 the free energy follows to:

$$E_F \sim \frac{k_B \cdot T \cdot n \cdot L_c}{L_e} \sim \frac{k_B \cdot T \cdot c}{L_e} \sim \frac{k_B \cdot T \cdot c}{\xi^{\frac{4}{5}} \cdot l_p^{\frac{1}{5}}} \sim \frac{k_B \cdot T \cdot c^{\frac{7}{5}}}{l_p^{\frac{1}{5}}} \qquad (1.22)$$

The free energy is directly proportional to the plateau modulus G_0 assuming an affine deformation of the tube in the network [Frey, 2001]:

$$G_0 \sim k_B \cdot T \cdot c_a^{\frac{7}{5}} \cdot l_p^{-\frac{1}{5}} \qquad (1.23)$$

This could be confirmed experimentally for actin solutions with rheological methods [Hinner et al., 1998]. Assuming also an affine deformation of the network, the elastic properties of the polymer solution are scaled down to the properties of a single filament [MacKintosh & Käs, 1995]. Within this theory longitudinal stretching and compression of single filaments between entanglements is responsible for the entropic elasticity of the network and the plateau modulus follows to:

$$G_0 \sim \kappa \cdot l_p^{\frac{2}{5}} \cdot c_a^{\frac{11}{5}} \qquad (1.24)$$

with the bending modulus κ of a single filament (for detailed derivation see [Shin et al., 2004] supporting information, [Wagner, 2004]).

3. terminal regime $(f < \frac{1}{\tau_r})$

τ_r can be interpreted as the time duration which a filament requires for reptating out of its initial tube by diffusion. Therefore τ_r depends directly on the diffused length l and indirectly from the reptation diffusion constant D_r [Morse, 1998b]:

$$\tau_r = \frac{l^2}{\pi^2 \cdot D_r} \sim l^3 \simeq \frac{\eta_0}{G_0} \qquad (1.25)$$

The reptation time can be determined experimentally by measuring the zero shear rate viscosity η_0 obtained from the creep compliance $(J(t)$, see chap. 1.3) [Hinner et al., 1998].

1.5 Enzyme Kinetics of Molecular Motors

Historically, first observations of molecular motors were made in skeletal muscle, which constitutes almost 40 % of the mass of an animal. On top of fig. 1.15 the architecture of skeletal muscle is illustrated. The muscle is made up of bundles of muscle fibres (elongated fibrous cells of 100 μm thickness). The next smaller units are myofibrils, which contain the filamentous proteins. The smallest repeating unit in the myofibril (1-2 μm in diameter) is called the sarcomer (about 2 μm in length) where the actin and myosin filaments are arranged in a parallel way. The exact arrangement of the proteins in the sarcomer is schematically shown in the middle of fig. 1.15. Under ATP hydrolysis the twitching contraction of muscles originates from filaments which slide into each other. Hydrolyzing one mol of ATP ($ATP + H_2O \rightleftharpoons ADP + P_i$) releases a standard free enthalpy ΔG_0:

$$\Delta G_0 = -32.2 \frac{kJ}{mol} = -54 \cdot 10^{-21} J = 13 k_B \cdot T \tag{1.26}$$

At cell like salt conditions ($c_{Mg^{2+}}$ = 1 mM, total ionic strength of 250 mM, pH 7.0, T = 25° C, presence of Myosin and absence of actin) the equilibrium is shifted towards ADP and phosphate. In addition, the lifetime of the ATP hydrolysis is large (between hours and weeks, depending on the temperature). Therefore ATP is a well suited biological temporal energy storage. Assuming a physiological ATP concentration (c_{ATP} = 1mM, c_{ADP} = 1 μM and c_{P_i} = 1 mM) the free enthalpy ΔG follows to:

$$\Delta G = \Delta G_0 - k_B \cdot T \cdot \ln\left(\frac{c_{ATP}}{c_{ADP} \cdot c_{P_i}}\right) \approx 27 \cdot k_B \cdot T \tag{1.27}$$

This energy is consumed in the chemomechanical coupling process of the muscle contraction, where the myosin functions as a molecular motor. Huxley could establish the rotating crossbridge model [Huxley, 1969] for explaining this process. In the bottom of fig. 1.15, the myosin actin interaction is enlarged inside the sarcomer and the cross-bridge model is illustrated (forth rate constants are green, back rate constants red and unlikely processes are drawn in grey [Howard, 2001]). In the following the cross-bridge model of the interaction of myosin heads with an actin filament is explained in detail:

1. At the beginning the myosin head (M) is nucleotide free and bound to the actin filament (A). This is called the rigor state (A*M) which is derived from the latin
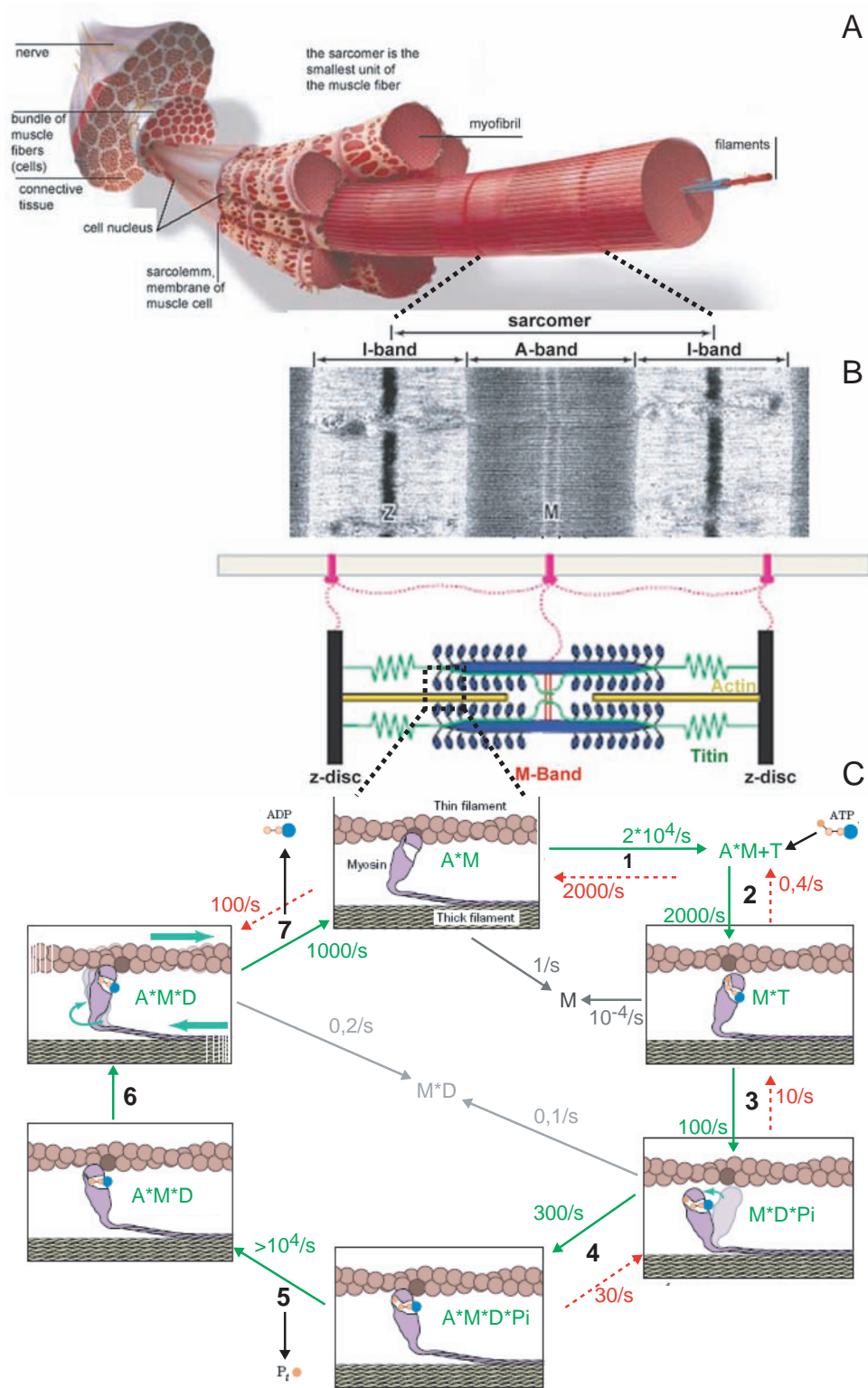
Figure 1.15: (A) Muscle architecture. (B) Electron micrograph of a sarcomeric unit and its schematic illustration [Agarkova & Perriard, 2005]. (B) Rotating crossbridge model.

expression "rigor mortis". The myosin unbinds from the actin filament. In the presence of ATP (T), the myosin head binds one ATP molecule (A*M*T).

2. Binding of ATP catalyzes detaching of the myosin head from the actin filament (M*T), with a high rate constant of 2000 $\frac{1}{s}$. In this state the unbinding of the ATP molecule from the myosin head is very unlikely.

3. ATP is hydrolyzed to ADP and phosphate (M*D*P$_i$) and the tension in the myosin head relaxes which is accompanied by a conformational change of the head. This is referred to as "recovery stroke".

4. Rebinding of the myosin head to the actin filament in the newly reached state happens with a middle rate constant (A*M*D*P$_i$).

5. With the release of P$_i$, a highly strained state is obtained (A*M*D).

6. During the relaxation of this highly strained state the actin filament slides. This corresponds to the so-called "power stroke". Here the working distance δ is defined as the distance which the motor molecule moves forward during the power stroke, while staying bound to the actin filament. For myosin II a mean working distance of 5 nm was measured [Howard, 2001].

7. with the release of ADP the actin myosin complex is again in the initial rigor state and the cycle can restart.

The rate limiting step in this cycle is from the M*T to the A*M*D*P$_i$ state. The overall ATPase rate for fast skeletal muscle myosin at 20° C is 25 1/s. Without actin the rate is 200 fold slower [Bagshaw, 1993]. The ratio of the time which the myosin head stays bound to the actin filament τ_{on} and the overall cycle time τ_{cycle} defines the so-called duty ratio r:

$$r = \frac{\tau_{on}}{\tau_{cycle}} \quad r_{max} = \frac{\delta}{p_d} \tag{1.28}$$

with an upper limit r_{max}. For myosin II the path distance p_d is 36 nm. If r is small the motor can not walk along a filament whereas for larger r the motors are processive (hand over hand model [Yildiz et al., 2003]). For example fast skeletal muscle myosin II has a duty ratio of 0.01-0.02 and reaches therefore *in vivo* a velocity of 6 μm/s [Howard, 2001]. As a theoretical limit for the maximal velocity v_{max} of myosin II:

$$v_{max} = \frac{\delta}{t_{drag}} \tag{1.29}$$

results in about 8 μm/s (with a drag time t_{drag} of 0.6 ms). The probability P_1 that one molecule with a motor head is bound to an actin filament is approximately r:

$$P_1 = 1 - \frac{\tau_{on}^2 + \tau_{off}^2}{\tau_{cycle}^2} \approx r \tag{1.30}$$

Consequently the probability that simultaneously two motor heads are bound to a filament (as it is the case for HMM, fig. 1.8II,B) results to:

$$P_{double} \approx r^2 \tag{1.31}$$

and reaches for fast skeletal muscle myosin II a very low value of $1-4 \cdot 10^{-4}$.

Chapter 2

Methods

"Comprehension means recognizing patterns!"

Isaiah Berlin

2.1 Microscopy

The structures resulting from interaction of filaments and other proteins play a key role in understanding the overall physical macroscopic properties of the samples. Different imaging techniques were used to resolve the structures of the samples.

2.1.1 Fluorescence Microscopy

General Wide-Field Fluorescence Microscopy

Fluorescence microscopy is a common method to visualize small structures like actin filaments with a thickness of about 10 nm − more than one decade below the used wavelength of light. In order to detect single molecules they are labeled with a fluorescent dye. For the excitation of the dye, the microscope was equipped with a mercury-short-arc-reflector-lamp (HXP-R120/45C vis, Osram, Germany). The dye TRITC (chap. 1.2) was excited at a wavelength range of 540-545 nm and the emitted light was observed using a specific filter set (# 15, Zeiss). In case of all actin within the sample was labeled (rhodamine dye, chap. 1.2) only fresh prepared anti oxidation buffer (app. A in [Wagner, 2004]) was used because gradually degradation of this buffer agglutinates the actin network. This artefact hinders investigation of the influence of ABPs. Therefore, the anti oxidation buffer was omitted for samples

which were investigated after 30 min or later in time. Consequently, the investigation time drops to some minutes (min) due to bleaching effects. The signal to noise ratio is improved if not all the actin is labeled within a sample. The so-called reporter filament samples for conventional wide-field 2D fluorescence microscopy were prepared as formerly described [Wagner, 2004].
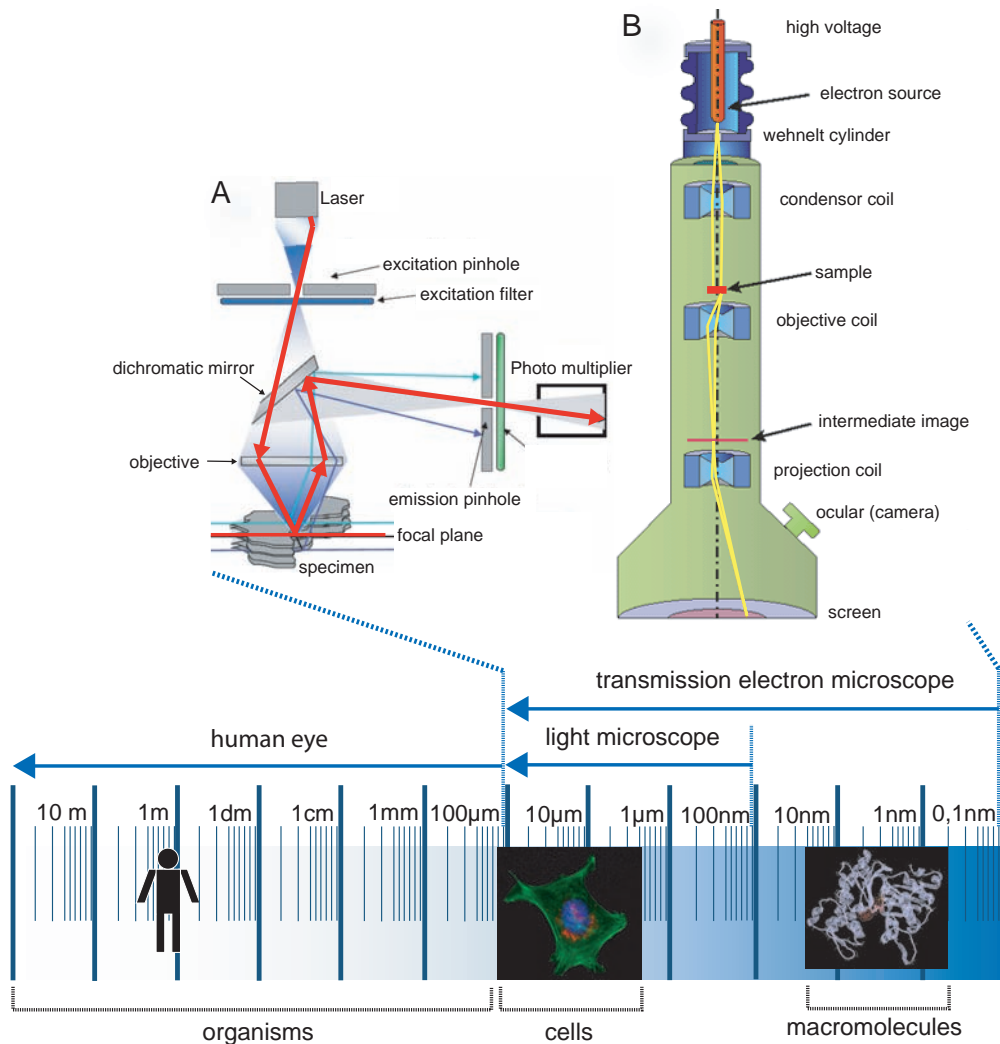
Confocal Microscopy

Figure 2.1: Schematic view of the optical pathway in confocal microscopy (A) and transmission electron microscopy (B). Bottom: length scale

The basic concept of a confocal microscope was originally patented in 1957 by Marvin Minsky. First commercial microscopes emerged in 1987. The confocal microscope (TCS SP5, Leica, Wetzlar, Germany. For a schematic view see fig. 2.1), offers three main advantages compared to the wide-field technique. First, the specimen can be point scanned because a high intensity monochromatic light source (laser) is used and the detection of the emitted light is observed through pinholes. This reduces background fluorescence and increases the signal to noise ratio. Since the emitted light intensity is lower as in common fluorescence microscopy a photomultiplier as a very sensitive detector is required. Secondly, with the possibility of sectioning the sample by varying the focal plane a 3D model can be constructed. Consequently, the real 3D mass distribution is obtained and wrongly interpreted 2D overlays are minimized. Thirdly, the magnification can be varied electronically (zoom) without changing the objective. With the confocal microscope it is possible to examine the samples "alive" contrary to the electron microscope. Time resolved 3D volume fractions of the specimen can be obtained which is essential for the investigation of dynamic processes. Overall, only the limited number of excitation wavelengths and the more harmful high intensive light for cells due to laser employment are the downsides of this method.

Sample Preparation   The sample chambers for confocal microscopy were built out of two glass slides (24 mm) separated by two stripes of parafilm. The lower one was in turn placed with parafilm stripes on a cover slide for stability reasons. Short heating of the chamber glues the glass slides together via the parafilm. The chambers were filled with 50 μl sample volume and sealed with vacuum grease to prevent evaporation. Comparably with macrorheological measurements (chap. 2.2.3), the samples were polymerized for 1h before investigation in the microscope. The sections of the samples were scanned with a scanning frequency between 400 and 1000 Hz, a pinhole size of 95.55 μm and a gain of 800 to 950 using a 63x oil objective (HCS-PL-APO-LS-63x-NA1.4).

Shear Cell   In order to visualize the behavior of actin networks under shear, a small shear setup was designed for the confocal microscope. The underlying principle of this setup is illustrated in fig. 2.2. Using a small piezo ceramic multilayer bender (CMBP04, Noliac, Kvistgaard, Denmark) a simple shear can be applied on the sample. The sample chamber bearing made out of plexiglass was customized to the confocal microscope z-stack table with a circular hole of 35 mm. The changeable bottom circu-
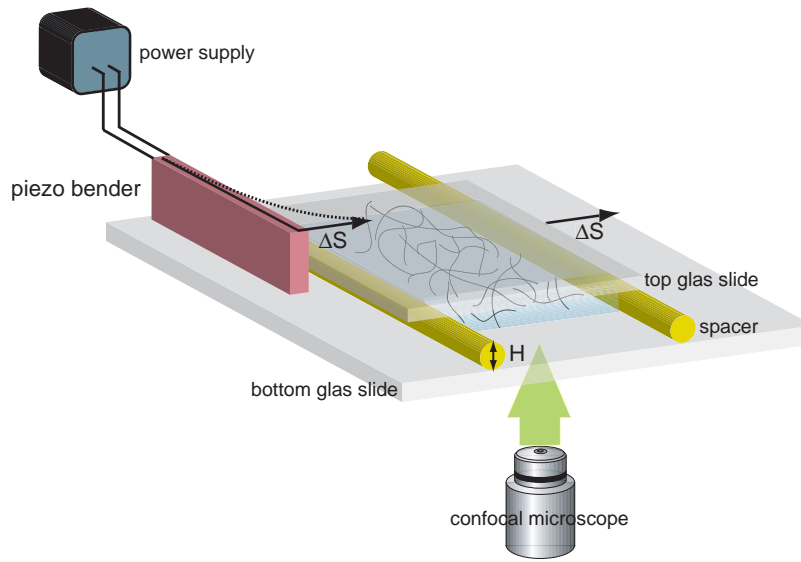
Figure 2.2: Functional design of the shear chamber setup for an inverted microscope.

lar glass slide (40 mm diameter, Thermo Scientific, Menzel, Saarbrücken, Germany) was recessed in the middle of the plexiglass holder and fixed with vacuum grease. The sample was covered with a second quadratic piece of an object slide on top for stabilization reasons. Two standard glass fibers with a diameter of 125 μm ensure a defined gap between the two glass slides. A sample volume of about 25 μl was pipetted through a 2 mm hole in the upper glass slide. Silicon oil (DMS-T05, pnr 63148-6-9, ABCR, Karlsruhe, Germany) with a dynamic viscosity of 5 times of the water viscosity seals the sample. The piezo bender was glued to the upper glass slide with bee wax (pnr 5825.1, Roth, Germany. Melting temperature: 61° C-65° C) which was melted with a soldering iron. Using a DC voltage power supply (PP5-12008, Conrad, Germany), a maximal free stroke of 475 μm can be achieved at 200 V with the piezo bender. Increasing the voltage from 0 to 100 V, a shear of 1.3 μm/V was measured by following the movement of the top glass slide (fig. 2.3A, blue open triangles). The reversed motion exhibits a hysteresis which can be attributed to the piezo bender (red open triangles in fig. 2.2).

In order to size the shear field one can use microspheres embedded in an actin network and follow the motion of beads under forced shear. In fig. 2.3B the results are presented for a cross-linked actin network ($c_a = 9.5$ μM, $c_{neutravidin} = 0.95$ μM). The 1 μm sized fluorescent beads were diluted 1/800 (micro particles GmbH) in the sample. In contrast to the movement of the glass slide, one detects a nonlinear motion of the embedded
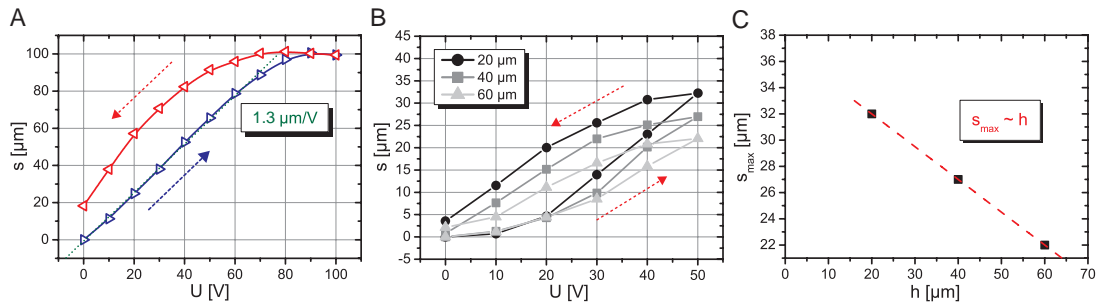
Figure 2.3: (A) *Forced movement of the top cover glas slide and* (B) *of three microspheres on different z planes.* (C) *The maximum shear length of the beads decreases with increasing distance of the top glass slide.*

beads which originate from the actin network. Nevertheless, the beads show the same hysteresis effect for the backward motion. For 20, 40 and 60 μm distance from the top glass slide, the maximum shear distance of single beads decreases linearly as expected (fig. 2.3C). Finally, with the shearing setup it is possible to visualize the shear behavior of single actin filaments and bundled actin networks.

2.1.2   Transmission Electron Microscopy

The samples for transmission electron microscopy (TEM CM-100; Philips, Eindhoven, The Netherlands or JEM-100CX, Jeol, Eching, Germany) were adsorbed (60 s) to glow-discharged, carbon-coated formvar films on copper grids (S160-4 grids, Plano GmbH, Wetzlar). The grids were washed in a drop of distilled water (60 s) before negative staining with 0.8 % uranyl acetate (60 s). Excess liquid was drained with filter paper to the edge of the grid and the grid was subsequently permitted to air dry. Micrographs from the JEM-100CX were recorded on Imago-EM23 films at small defocus. The developed negatives were scanned with a fast high resolution scanner at 1000 dpi (flextight-X5, Hasselblad) resulting in a pixel size of $\frac{254}{X[k]}$Å.

2.2   Rheology

Rheology originated in 1920 and is a coinage from the greek words 'rhei' and 'logos'. It describes the theory of flow behavior of all kind of materials. Rheology includes parts of elasticity and plasticity theory. For a quantitative analysis of the viscoelastic parameters three different rheometers were used. Local properties can be determined with the microrheometer. In contrast, the overall macroscopic properties of the materials can be investigated precisely with macrorheological methods.

2.2.1   Measuring Procedures

Basically three simple measuring procedures can be performed (see tab. 2.1). For

Method	Applied shear	Measured response	Determinant
steady shear	constant shear rate $\dot{\gamma}$	stress τ	flow curve, viscosity η
steady stress	constant stress rate $\dot{\tau}$	strain γ	flow curve
step strain	constant strain γ	stress $\tau(t)$	relaxation modulus $G(t)$
step stress	constant stress τ	strain $\gamma(t)$	creep compliance $J(t)$
oscillatory strain	strain $\gamma(t)$	stress $\tau(t)$	$G'(f)$ and $G''(f)$
oscillatory stress	stress $\tau(t)$	strain $\gamma(t)$	$G'(f)$ and $G''(f)$

Table 2.1: Measuring methods for rheology.

dynamic methods the stress or strain on the sample is periodic in time. Therefore, the measurements result in frequency dependent moduli. For example one can specify a sinusoidal strain and measure the phase shift φ and the amplitude of the response function (stress).

$$\gamma(t) = \gamma_0 \cdot \sin(f \cdot t) \tag{2.1}$$

$$\tau(t) = \tau_0 \cdot \sin(f \cdot t + \varphi) \tag{2.2}$$

By substituting this equation in eq. 1.8 and applying the cosine addition theorem followed by a transformation of variables one obtains:

$$\tau(t) = \gamma_0(G'(f) \cdot \sin(f \cdot t) + G''(f) \cdot \cos(f \cdot t)) \tag{2.3}$$

with the $G'(f)$ and $G''(f)$ as the viscoelastic moduli. With the help of the addition theorem

$$\sin(f \cdot t + \varphi) = \sin(f \cdot t) \cdot \cos(\varphi) + \cos(f \cdot t) \cdot \sin(\varphi) \tag{2.4}$$

eq. 2.2 can be rewritten to:

$$\tau(t) = \tau_0(\sin(f \cdot t) \cdot \cos(\varphi) + \cos(f \cdot t) \cdot \sin(\varphi)) \tag{2.5}$$

Comparison of eq. 2.5 and eq. 2.3 results in the definition of G' and G'':

$$G'(f) := \frac{\tau_0}{\gamma_0} \cdot \cos(\varphi) \tag{2.6}$$

$$G''(f) := \frac{\tau_0}{\gamma_0} \cdot \sin(\varphi) \tag{2.7}$$

G' is the storage and G'' the loss modulus. The theoretical curve for viscoelastic materials (e.g. actin filamentous networks) is depicted in fig. 1.13A.

Nonlinear Behavior of Semiflexible Polymer Networks

Materials such as semiflexible polymer networks in solution show a nonlinear shear response behavior when the shear stress or strain overshoots a critical value. The cytoskeletal biopolymer actin shows distinct nonlinearity crossing a critical strain γ_c. This property is thought to be used in cells for fast adaption of their elasticity to the surrounding environment [Gardel et al., 2006b]. Meanwhile several measuring protocols are established for determination and quantification of this behavior [Semmrich et al., 2008]. Whether shear hardening for actin networks is observable or not, crucially depends on the parameters which are shown in the following table (tab. 2.2):

Four main measuring protocols were established for determination of nonlinearity.

Parameter	Abbreviation
concentration of filaments	c_a
length of filaments	$\langle l \rangle$
cross-linker concentration	$R \equiv c_{cross-link}/c_a$
buffer conditions	I
temperature	T

Table 2.2: Parameters controlling nonlinear behavior.
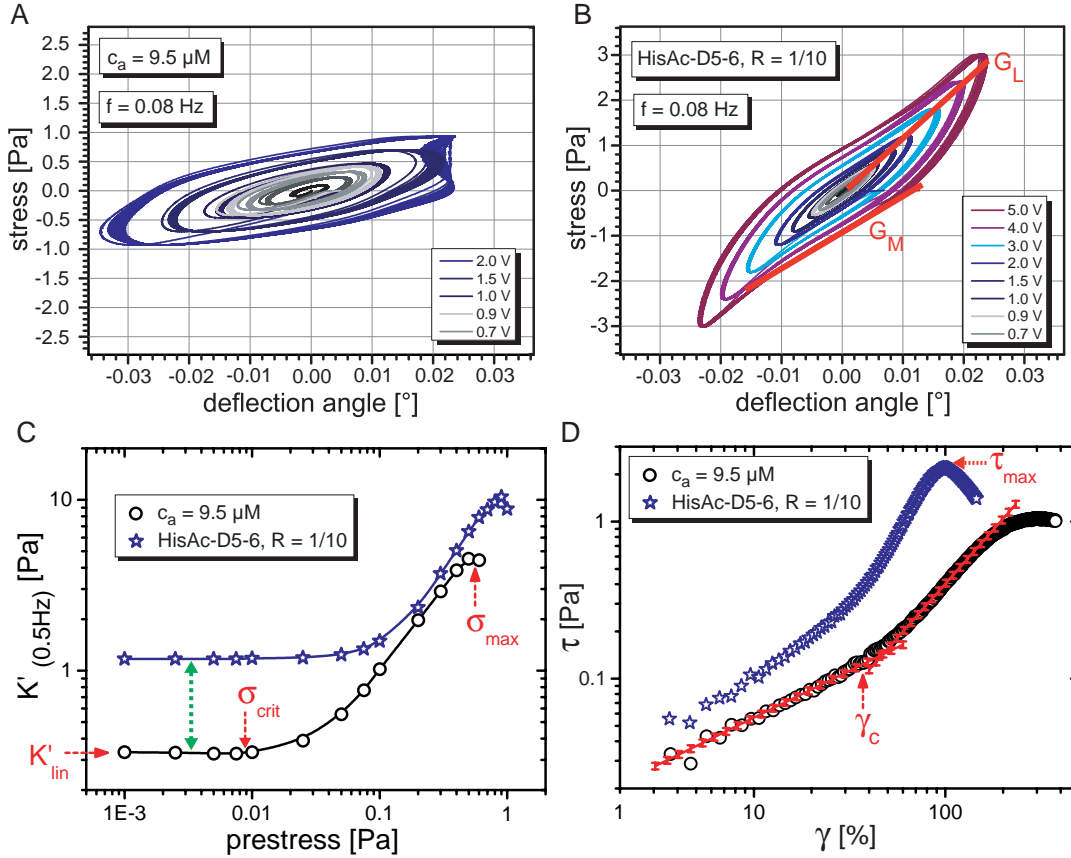
Figure 2.4: (A) Large amplitude oscillatory stress (LAOS) method at a constant frequency for an actin network (c_a = 9.5 μM, $\langle l \rangle$ = 21 μm). The deviation in the left plot at an amplitude of 2 V is an artefact of laser beam detection. (B) Actin network cross-linked with HisAc-D5-6 (R = 1/10). G_M is the tangent and G_L the secant modulus. Both upper measurements were performed with the TDR (torsional rotating disc) rheometer (chap. 2.2.3). The lower two graphs were determined with the commercial MCR rheometer (chap. 2.2.3). Open black circles: c_a = 9.5 μM, $\langle l \rangle$ = 21 μm and open blue stars: HisAc-D5-6 at R = 1/10. (C) Pre-stress method. The small superimposed oscillatory stress was 0.01 Pa. (D) Constant shear rate method with $\dot{\gamma}$ = 12.5 %/s. The maximum stress τ_{max} the sample can withstand is indicated with the leftward pointing arrows.

A standard procedure for various materials is the large amplitude oscillatory shear (LAOS). At a constant frequency, the oscillation amplitude is increased and the resulting strain or stress is measured. As soon as the response function becomes non-sinusoidal the moduli G' and G'' can no longer be calculated with eq. 2.6 and 2.7. In order to exhibit the nonlinear response Lissajous figures are used. For analysis, the applied stress is plotted versus the measured strain (raw data). Exemplarily two Lissajous figures of the raw data (without the correction for the inertia of the plate) are shown for a pure entangled actin solution (fig. 2.4A) and a highly cross-linked network (fig. 2.4B). Whereas perfect elastic materials result in a straight line with a slope corresponding to the spring constant, perfect viscous materials have an ellipsoidal shape and the ellipse axis coincide with the axis of the coordinate system. If the material is viscoelastic, the ellipsoid axis are tilted as long as the response is still in the linear regime. Fig. 2.4A shows that pure actin is perfectly viscoelastic until the applied amplitude gets larger than 1.5 V. The ellipsoids of the cross-linked actin network in fig. 2.4B appear more and more distorted with increasing stress amplitude, indicating a stress stiffening of the network for amplitudes larger than 2 V. With more cross-linkers the networks are getting more elastic what results additionally in a more pronounced stiffening. The elasticity can be evaluated with two parameters. The secant modulus G_L and the tangent modulus G_M. The ratio of both defines the strain stiffening index S [Ewoldt et al., 2007]:

$$G_L \equiv \frac{\tau}{\gamma} \mid_{\gamma=\gamma_{max}} \quad G_M \equiv \frac{\partial \tau}{\partial \gamma} \mid_{\gamma=0} \quad \Rightarrow \quad S \equiv \frac{G_L}{G_M} \tag{2.8}$$

During one measuring point low elastic materials (e.g. non-cross-linked actin fig. 2.4A) soften, resulting in narrowed ellipsoids for each cycle. Restricting the measurement to 2-3 oscillations reduces the softening. In this case, the sampling rate has to be high. For highly cross-linked networks (fig. 2.4B) the softening is negligible since it is smaller as for pure entangled actin networks. The last point can be minimized using the step stress protocol. For that method short stress pulses are applied on the sample and the resulting strain is measured.

The third procedure is the so called prestress method ([Gardel et al., 2004a], [Shin et al., 2004]). It is a combination of two standard protocols (see tab. 2.1). A constant prestress σ superimposed by a small oscillatory stress at a fixed frequency is applied, measuring the differential modulus K'. The prestress is gradually stepwise increased. In fig. 2.4C again the two different networks are compared. K' stays constant

until the prestress exceeds a critical value σ_{crit} and K' rises (red arrows in fig. 2.4C). In the linear regime K'_{lin} is constant and corresponds to G'. Thus, one can clearly distinguish the linear from the nonlinear regime. The highly cross-linked network (blue open stars) shows a higher linear modulus than the pure entangled actin network (black open circles) and is therefore a more elastic material. The maximum prestress the networks can withstand is defined as σ_{max} (fig. 2.4C). σ_{max} conforms well with the obtained maximum stress τ_{max} of the fourth method, the constant shear rate method.

In fig. 2.4D, the nonlinear response can be distinguished from the linear regime by means of larger slope. The critical strain γ_c was obtained from the original stress strain curves. γ_c is the value of the strain where the linear fit on the curve deviates from the original data within a 5 % error bar. Exemplarily these values are illustrated for the pure entangled actin network with the red upward pointing arrows in fig. 2.4D. Similar to the definition of the prestress method a differential Modulus K can be defined:

$$K \equiv \frac{\partial \tau}{\partial \gamma} \qquad (2.9)$$

Since the prestress method takes a long time and pure actin gels are very low elastic gels, viscous flow during the measurements produces artifacts. Therefore the constant shear rate experiment is more accurate for determining of the critical strain. Generally, the best method for analyzing the shear stiffening of actin networks is a steady shear rate experiment. Within this work the nonlinear flow behavior of the various networks were examined with a constant shear rate.

2.2.2 Microrheometer

Cells and the corresponding cytoskeletal polymer networks can be quantitatively analyzed on the μm scale using microrheometry ([Bausch, 1999], [Ziemann, 1994]). Two advantages make the technique of magnetic tweezers (also denoted as active microrheology) to a powerful tool for obtaining local viscoelastic properties of semidilute polymer networks. First, local heterogeneities can be resolved by monitoring several embedded colloidal particles at the same time. Secondly, less additional energy is stored in the sample during the measurement compared to optical tweezers, which use laser light for focusing the particles. Active microrheology based on the magnetic tweezer (MT) setup was used for investigation of *in vitro* actin networks.

The setup is described in detail in [Tharmann, 2006]. The characterization as well as

calibration were done as described in [Wagner, 2004]. The position of the magnetic coils (copper wire with 1.18 mm in diameter and 830 windings per each coil) is fixed with respect to the objective but the cuvette holder can be displaced. This ensures that all observed particles are placed in the center of the magnetic coils. The maximum applicable force with this setup was 5 pN, limiting the use of this technique to materials softer than approximately 10 Pa. Frequency spectra are taken within a frequency range of 2-3 decades depending on the sample stiffness.

Sample Preparation   Monodisperse paramagnetic beads were used as probing particles (4.5 μm in diameter, Dynal M-450, Invitrogen, Karlsruhe, Germany). The beads were diluted in water, vortexed and finally added to the sample before protein addition. Approximately 20 μl sample volume is loaded into a cuvette, made out of teflon covered with a glass slide (8 mm diameter, Schubert Medizinprodukte, Wackersdorf, Germany) and sealed with vacuum grease.

2.2.3   Macrorheometer

Torsional Disc Rheometer

With a self-built, magnetically driven, rotating-disk rheometer (TDR) developed by [Müller, 1991] bulk rheological measurements in the linear response regime were performed. The further improved rheometer was calibrated following [Tharmann, 2006]. All rheological experiments with this rheometer were performed after 2 h of polymerization at $21°$ C temperature. The frequency-dependent moduli $G'(f)$ and $G''(f)$ were detected in a frequency range from 0.001-1 Hz for all samples studied. With the TDR rheometer at low frequencies, drift problems are induced by a small prestress in the linear regime which results from the initiation of the measurment at the beginning. The small prestress results in a banana-like Lissajous figure as it can be seen in fig. 2.5A. During the 8 oscillations the sample underlies a small drift and the banana is displaced to the right. This effect is circumvented by using the Fast Fourier Transformation (FFT) of the sinusoidal strain signals for further calculation of the viscoelastic moduli. If the prestress would be so large that the sample would respond nonlinear, odd harmonics in the FFT of the response signal would appear [Wilhelm et al., 1998]. But only a noticeable second harmonic from the FFT with an amplitude of 10 % of the first harmonic appears for the 1 mHz measurement point (fig. 2.5B).
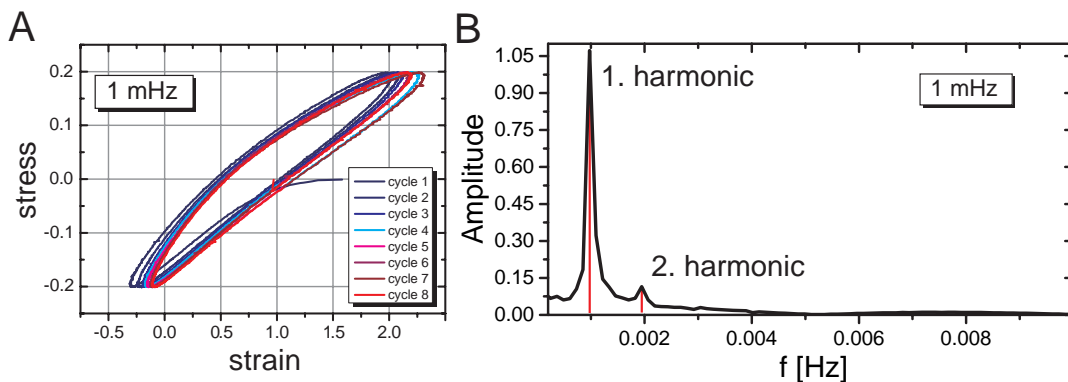
Figure 2.5: Lissajous figure (A) and Fast Fourier Transform (B) for an actin network with sample parameters $c_a = 9.5\,\mu M$, $\langle l \rangle = 21\,\mu m$, measured with the TDR rheometer at a frequency of 1 mHz are shown. The Lissajous figures show a banana-like form. This results in a second even harmonic in the FFT.

Sample Preparation G-actin polymerization was induced by adding 10-fold F-buffer (chap. 6.8). After 2 min of gentle mixing the polymerizing actin was transferred to the sample cuvette. On top of the sample (volume of 400 μl) a phospholipid monolayer of dimystriolphosphatidylcholine dissolved in chloroform was spread in order to prevent denaturation of actin at the air-water interface. After evaporation of the lipid solvent (2 min), the rotating disk was placed onto the sample, and the cuvette was covered with a glass slide to eliminate any evaporation effects.

Physica MCR301

Besides the self-built TDR, a commercial stress-controlled macrorheometer (Physica MCR301, Anton Paar, Graz, Austria, see fig. 2.6) was used within this work. This rheometer generates a torque with an induction motor on an air-beared measuring tool. The angular deflection is measured with an optical rotary position transducer. The minimal torque which the rheometer can apply on a sample was experimentally verified with a 75 %w glycerol solution. In fig. 2.6 the measured G'' (filled square) and the applied torque (M, open and filled circles) are plotted over a frequency range of 0.01-5 Hz. Without the direct strain oscillation technique (DSO) the minimal applicable torque is limited to 0.1 μNm which is indicated by the red dashed line in the figure. With DSO the denoted accuracy of the rheometer is about 0.02 μNm (green dashed line,) [Paar, 2004].

In order to keep the sample volume small all measurements were done with plane plate
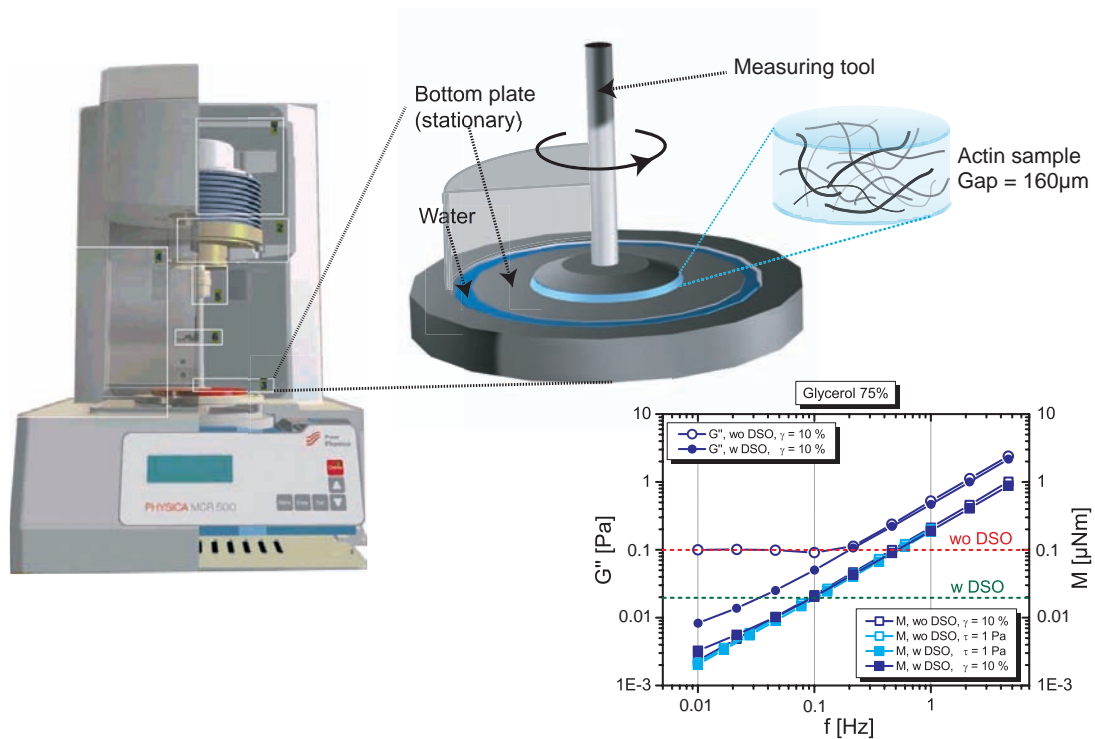
Figure 2.6: Top: schematic sketch of the commercial rheometer MCR301 with a zoom in to the sample. Bottom: measurement of a 75 %w glycerol solution. The minimal applicable torque limit without DSO technique is determined exemplarily. Reaching the limit of 0.1 μNm wrong values for G'' are measured. With DSO technique the G'' can also be determined for frequencies lower than 0.1 Hz. The green line indicates the accuracy of the inertia using DSO mode.

geometry of 50 mm in diameter and a gap width of 160 μm. The smaller cone plate with 25 mm diameter was not used since with this measuring tool unsteady flow in the sample can produce artefacts in the determination of the viscoelastic parameters [Passard et al., 1998].

Cleaning and Calibration Procedure   The temperature was kept constant at 21° C for measurements concerning actin networks. The measuring tool was cleaned with a 2 %v helmanex solution for several minutes followed by ddH$_2$O rinsing for several times and at last wiped with pure ethanol. The bottom plate was cleaned for several times with ddH$_2$O and at last wiped with pure ethanol. No helmanex was used for cleaning the bottom plate because the hydrophobic coating of the stationary bottom plate could be weakened.

Before each measurement the same calibration procedure was performed. First, the driving was equilibrated and the measuring tool was set in the rheometer, adjoining zero point determination. Secondly, when the gap width was reached the moment of inertia of the measuring tool was determined. At last the motor was synchronized. Finally a sample volume of 450 μl was pipetted on the base plate. After polymerizing the sample for 1 h while measuring the G' with an applied stress of 0.01 Pa (or larger if necessary) the further desired experiments were performed.

2.2.4   Comparison of Rheometers

In general, the limitations of an applicable torque are the reasons which rheometer is best suited for the measurements. The MCR301 has an overall accuracy of the applicable torque of 0.02 μNm (fig. 2.6). The TDR excels with a high sampling rate and is limited to low applicable torques by the repelling torsional moment of the retaining coils. In the upper limit of applying high torques on highly elastic samples the MCR301 is the setup of choice as it can produce much higher maximal torques (200 mNm) than the TDR.

In addition to the limitations of the torque further differences concerning the handling of the setups has to be considered. Since the glass sample chamber is fully sealed with a cover slide and vacuum grease and the sample itself is covered by a mono lipid layer evaporation effects are minimal in the TDR. Consequently, the samples can be measured for more than 24 h. Therefore with this rheometer one can measure down to low frequencies below 1 mHz. On the other hand the MCR is much easier to han-
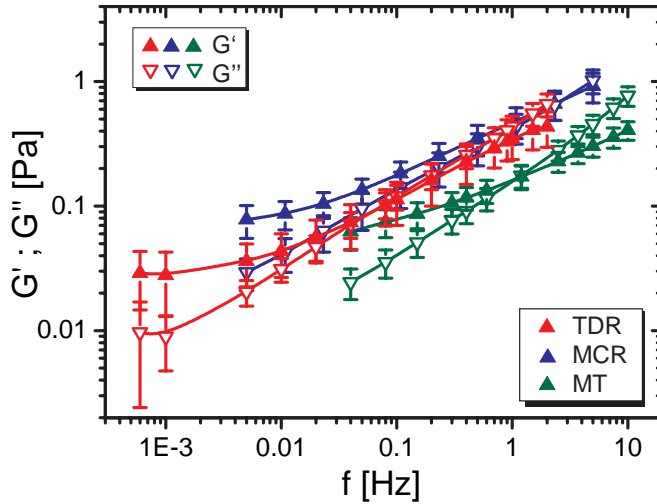
Figure 2.7: *Comparison of the frequency behavior of G' and G'' for the three rheometer setups (MT: green, TDR: red and MCR: blue color). G' (filled upward triangles) and G'' (open downward triangles) are plotted over a range of 0.001-10 Hz. The error bars result from about 20 single measurements for each curve. Measured actin network with the sample parameters c_a = 9.5 μM, $\langle l \rangle$ = 21 μm.*

dle because all possible experimental methods (e.g. tab. 2.1) are programmable with the well developed commercial software. Furthermore rotational experiments are more precisely performable with the MCR because the dimensions of the photodiode limits the measurable amplitude in the TDR.

By means of a pure entangled actin network the results of the viscoelastic frequency behavior measured with the two macrorheometers and the microrheometer are compared. Qualitatively all rheometers measure the same viscoelastic behavior of the same entangled actin networks but the results of the three setups do not overlay for all frequencies within the error bar deviations (fig. 2.7). For better comparison another usual expression for the viscoelastic parameters from eq. 2.6 and 2.7 are defined:

$$\varphi = \arctan\left(\frac{G''(f)}{G'(f)}\right) \quad \phi \equiv \tan\varphi \tag{2.10}$$

with the corresponding dimensionless loss angle ϕ and the absolute value of the shear modulus $|G^*|$

$$|G^*(f)| = \sqrt{G'(f)^2 + G''(f)^2} \tag{2.11}$$

In tab. 2.3 the dimensions of the probing tools of the rheometers are compared for a better understanding of the following arguments. First, the difference between the MT and the MCR is explained considering length scale arguments [Liu et al., 2006, Luan et al., 2008]. The MT constantly delivers a factor of about two lower values as the MCR rheometer (fig. 2.8). All modes of the filaments with length larger than 4.5 μm are not detectable since the probe particle size used in the MT is 4.5 μm in diameter (see tab. 2.3). Those would contribute most to the elasticity in the measurable
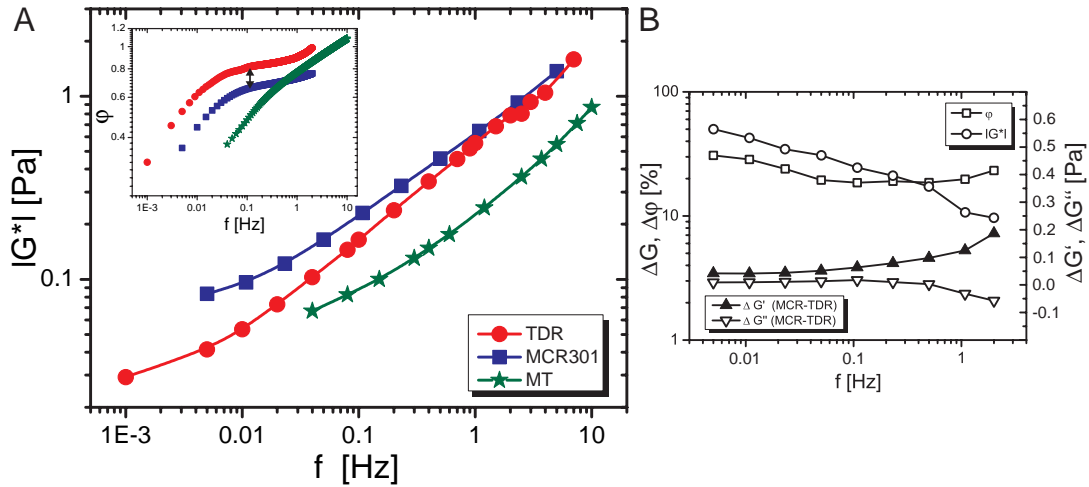
Figure 2.8: The difference of the geometrical setup of the rheometer types in the measured values of $|G^*|$ and φ. All graphs represent the same measured actin network ($c_a = 9.5\,\mu M$, $\langle l \rangle = 21\,\mu m$). (A) $|G^*|$ is depicted over the frequency. In the inset φ is shown over the corresponding f range. (B) The ratios of $|G^*|$ and φ between the two macrohreometers are calculated in percent for frequencies between 0.005-2 Hz.

frequency regime. Therefore, the measured elasticity is lower in the MT compared with the MCR macrohremeter.

Rheometer	r_{probe} [mm]	h_{sample} [mm]	$\frac{r_{probe}}{h_{sample}}$
TDR	6	2	3
MCR	25	0.16	156
MT	0.00225	0.5	0.0045

Table 2.3: Geometric comparison of the probes of the three different rheometers.

In the following, both macrorheometers are compared. Qualitatively the macrorheome-ters measure the same viscoelastic behavior of the sample. This is demonstrated by the similar shape of the phase shift plotted over the frequency for identical samples (fig. 2.8). Quantitatively the self built TDR has an additional constant phase shift of about 30 % and a 50 % deviation in $|G^*|$ for each frequency (fig. 2.8B). The approach of the $|G^*|$ of the TDR to the values of the MCR with increasing frequency originates from the increasing moment of inertia of the probing plate of the TDR. Consequently, a similar factor of two remains in the $|G^*|$ response between the two macrorheome-ters which is somehow difficult to explain. A calibration problem with the calibration fluid can be excluded since both macrorheometers measure the same viscosity for the fluid as an ostwald viscosimetre. For both macrorheometers the probes are disk-like

and the diameter varies by a factor of four (tab. 2.3). Since the gap width of the MCR is variable one chooses a small sample hight in order to obtain a small sample volume. Although the sample hight of the TDR is a factor of ten higher as for the MCR, sedimentation of long filaments in the sample cuvette of the TDR is unlikely on the timescales of several hours. A reduced effective concentration measured with the TDR due to filament absorption on the walls of the glass cuvette can be ruled out. Since a decrease in the measured G_0 of a factor of two would lead to a concentration deficit in the TDR glass cuvette of 40 % following eq. 1.23. Finally the slight difference in the resulting absolute values can be addressed most likely to the entire different buildup of the compared macrorheometers.

Nevertheless, with an inverted oil objective and fluorescence technique one could investigate simultaneously the mechanical parameters and the 3D structures of actin samples in the TDR. Combining microscopy and macrorheology would lead to an entire method for investigation of polymer solutions similar to the magnetic tweezers technique.

Chapter 3

Results and Discussion

[1]

> *"Something is growing - if one continuously thinks about it."*
>
> Henry Ford

3.1 The Number of Sticky Entanglement Points Determines the Viscoelastic Properties of Actin Networks

The cytoskeleton of eucaryotic cells is a complex and dense network of filamentous structures. It participates with its viscoelastic properties in important cellular tasks e.g. cell division or cell motility. Moreover, cells have to adapt to their environments. They have to withstand surrounding pressure or large forces which are transduced to their internal compartments via their membranes. Therefore, the understanding of cell mechanics is of great interest and understanding the mechanical properties of complex actin networks could serve as basis for scaffolds of tissues. Actin filaments – one of the three building blocks of filamentous structures of the cytoskeleton – are an excellent simple physical model system for biopolymer networks. In the cytoskeleton, actin networks have to fulfill two opposed tasks. On the one hand actin networks have to withstand deformations and on the other hand the network has to be adjustable

---

[1]All macrorheological measurements in this chapter were performed with the MCR301 rheometer. If this is not the case it is explicitly noted.

and rearrangeable on different time scales, maintaining the mobility of the cytoskeleton. Therefore, pure entangled *in vitro* actin networks have recently been investigated in great detail [Hinner et al., 1998, Gardel et al., 2003, Claessens et al., 2006b, Semmrich et al., 2008]. A full understanding of pure filamentous systems is needed in order to understand the complex interplay of cytoskeletal filaments and their accessory proteins.

3.1.1 Influence of Filament Length Adjusted by Gelsolin

Several parameters of the constituents and the environment determine the viscoelastic properties of entangled actin networks: the persistence length, which is the material parameter of the filaments (chap. 1.4.1), the filament density and the length of the filaments (see chap. 1.4.3) determine the properties of the entangled network. Additionally, external parameters like salt conditions, pH value, temperature [Semmrich et al., 2008] and force influences the behavior of actin networks. Regarding all these dependencies the question arises whether there is an outstanding important parameter on which the viscoelastic behavior of entangled actin networks can be reduced at constant surrounding conditions. Furthermore, is it possible to quantify this parameter? What can be concluded from this consideration for the behavior of the cell cytoskeleton? By answering these questions one gains a fundamental understanding for biological relevant materials.

 The filament length was varied for three different actin concentrations and the frequency spectrum of the network samples were recorded from 5 to 0.005 Hz. The mean length $\langle l \rangle$ of filaments in actin networks was adjusted with the ABP gelsolin following the relation in eq. 1.1 (chap. 1.1.2). Exemplarily four frequency curves of G' and G'' of entangled actin networks ($c_a = 9.5$ μM) with mean filament length of 2-14 μm are shown in fig. 3.1A. Regarding all actin and gelsolin concentrations, fig. 3.1 B shows that G_0 stays constant for all actin concentrations and filament lengths till the contour length of the filaments is comparable to the entanglement length (see chap. 6.7 for calculated values of L_e with eq. 1.15). At this point G_0 drops below a constant value (fig. 3.1B), which defines the entanglement crossover. The entanglement crossover can be described on the basis of the tube picture which takes into account the semiflexibility of the actin filaments [Hinner et al., 1998]. Deviations of the model for filament lengths larger than 15 μm were not observed in contrast to the results of Hinner. The scattering of the data points can be addressed to the mean error of the macrorheologi-
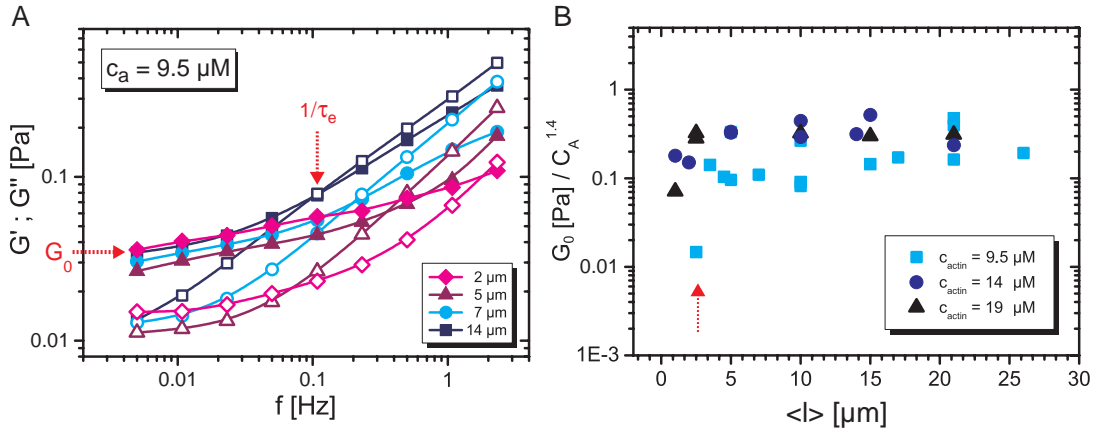
Figure 3.1: (A) Frequency dependence of G' (filled symbols) and G'' (open symbols) for different filament lengths at a constant actin concentration of 9.5 μM. Exemplarily the entanglement time and G_0 (measure for the elasticity of the overall viscoelasticity of the networks) are indicated by the red arrows for filament length of 14 μm. (B) Normalized G_0 (taken from G' at 5mHz, where G'' is smallest within the accessible measuring regime) in dependence of the filament length. G_0 is normalized with the approved scaling law for the c_a dependence (eq. 1.23). The red upward arrow indicates the entanglement crossover [Hinner et al., 1998].

cal measurements of actin networks at the used concentrations.

The second parameter taken from the frequency spectrum is the entanglement time. For $c_a = 9.5$ μM τ_e in dependence of $\langle l \rangle$ is plotted in fig. 3.2A. The observed behavior is the same as for the reptation time. The scaling for both times implicates that the frequency spectrum of actin networks with successive shorter filaments is shifted to larger frequencies. Comparing the ratio of τ_r (values from [Hinner et al., 1998]) and τ_e (from fig. 3.2A) for all filament lengths results in a constant value of $\frac{\tau_r}{\tau_e} \approx 200$. Therefore, the overall properties of the network stay the same, at least as far as the ratio of the dominating length scales is constant. Two important length scales for pure entangled actin networks are basically the filament and entanglement length. In the tube model L_e depends on the meshsize (see eq. 1.15) which in turn is regulated by the concentration (see eq. 1.21). With the ratio of filament length to entanglement length a theoretical number of entanglement points per filament can be introduced:

$$\#_{ep} = \frac{\langle l \rangle}{L_e} \tag{3.1}$$

In fig. 3.2B the loss angle for three actin networks with nearly the same $\#_{ep}$, far above the entanglement transition, is plotted over the frequency. Clearly it is shown, that the
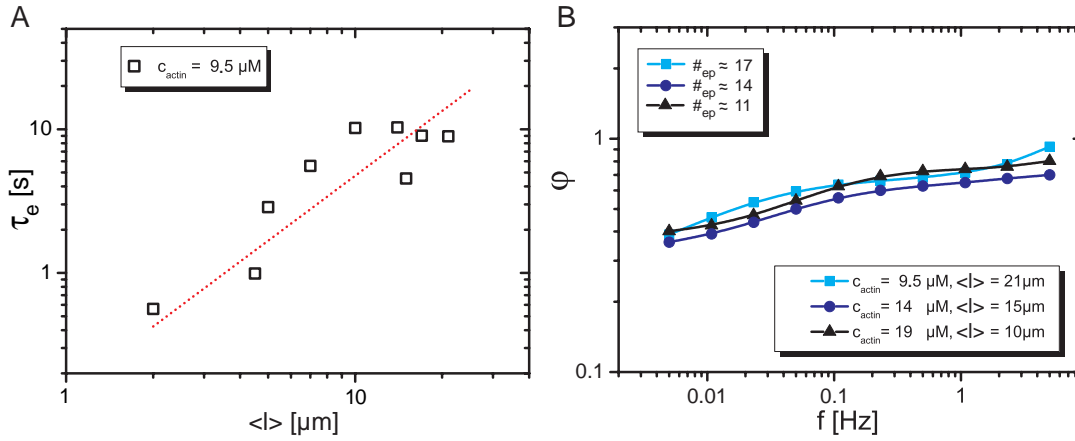
Figure 3.2: (A) *The entanglement time decreases with decreasing* $\langle l \rangle$. *Red dotted line indicates a scaling law of* $\tau_e \sim \langle l \rangle^{\frac{3}{2}}$. (B) *Frequency spectrum of the loss angle for three actin networks with successively increased actin concentration and concomitant reduced filament length.*

viscoelastic behavior does not change. The small differences in $\#_{ep}$ are about a factor of 1.5 which is below the resolution limit of the macrorheological method in the linear regime.

In the linear response regime, the properties of entangled actin networks are not significantly influenced as long as $\langle l \rangle$ exceeds L_e. However, in the non-linear regime, entangled actin networks reveal a hardening behavior [Storm et al., 2005, Janmey et al., 2007]. The occurrence of strain hardening is strongly dependent on the parameters mentioned in chap. 2.2.1 tab. 2.2. In this work constant shear rate experiments ($\dot{\gamma} = 12.5$ %/s) were analyzed for three different actin concentrations with filament lengths from 1 to 26 μm. Exemplarily, stress-strain curves for $c_a = 9.5$ μM with filament lengths from 21-10 μm are shown in fig. 3.3A. The linear response can be distinguished from the nonlinear hardening with the appearance of a steeper slope. After the turning point was reached (maximum stress), the stress decreases again with increasing strain. From this measurements the differential modulus K is obtained by smoothing and derivating the curves (eq. 2.9). For evaluation, the maximum modulus K_{max} (eq. 2.9) is normalized to the smallest length of each actin concentration. K_{max} shows a length dependence (fig. 3.3B). Clearly, a strain hardening crossover occurs between 5-10 μm in dependence of the meshsize. The critical length decreases with increasing actin concentration, resulting in $\langle l \rangle_{crit} \approx 8 \cdot L_e$ independent of the actin concentration. Consequently, every eighth entanglement point can be considered as a quasi cross-linking point, resulting from adhesive contact interactions between two
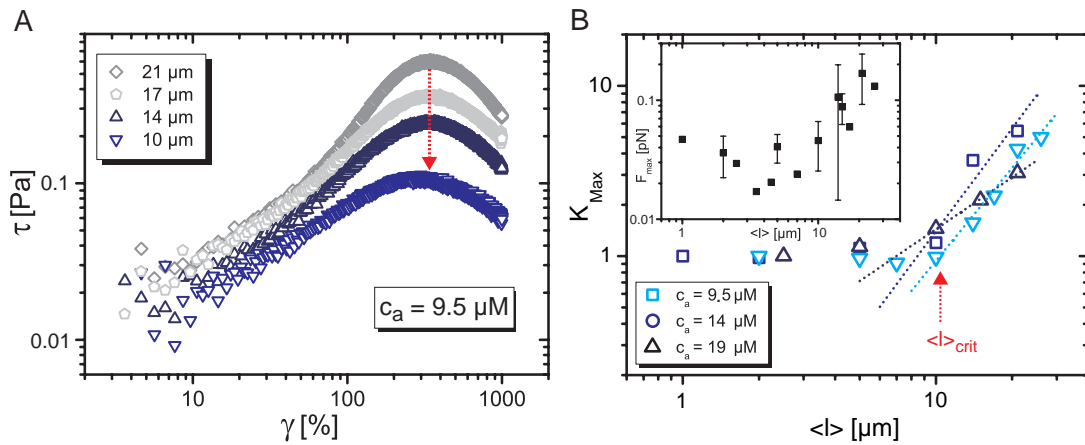
Figure 3.3: (A) *Constant shear rate experiments* ($\dot{\gamma} = 12.5$ %/s). *In the linear regime the stress response is similar for all lengths shown, whereas the strain hardening of the nonlinear response vanishes with decreasing filament length. The concomitant reduced yield stress is indicated by the red arrow. After a maximum* τ *is reached, a network collapse is observed resulting in a reduction of the shear stress with increasing shear strain.* (B) *Normalized maximum nonlinear modulus for three different actin concentrations in dependence of* $\langle l \rangle$. *The red upward arrow points at the strain hardening cross over* (*exemplarily for 9.5 μM*). *In the inset the mean maximum force* (*for all measured actin concentrations*) *was calculated following eq.3.2.*

filaments. Two entangled actin filaments having developed a quasi cross-linking point are considered to be trapped in a polymer-polymer pair-potential minimum with an enthalpic barrier. Accordingly, the decrease of stress at high shear strain, can be reduced to cross-link slippage. This filament-filament slippage in entangled networks presumably results in filament alignment. Recently, with a theoretical model on the basis of the standard tube model with an implemented nonlinear extension, the stress-strain behavior of free-sliding biopolymer networks could be calculated [Fernández et al., 2008]. The catastrophic collapse of the biopolymer networks could be addressed to originate from filament-filament sliding in the network. Free sliding filaments in so-called "hairpin" configured entanglements are not enough to explain the pronounced strain hardening behavior observed for long filaments. In principle, the behavior of filaments in the network under high shear can be visualized experimentally with a shear cell setup of the confocal microscope (chap. 2.1.1). The adhesive interactions between two filaments have been proposed to be of hydrophobic and unspecific character which are incompletely screened by electrostatic repulsion [Kroy & Glaser, 2007]. Indeed, by tuning the physiological relevant parameters as temperature and salt concentration a small energy barrier for the interaction potential in order of $k_B \cdot T$ was found

[Semmrich et al., 2008]. The energy barrier can be overcome with increasing temperature from 21 to 23° C or with decreasing monovalent salt concentration of potassium chloride from 100 to 10 mM at a constant length of 21 μm and $c_a = 9.5$ μM [Semmrich et al., 2008, Semmrich et al., 2007]. Adjusting these conditions, the strain hardening can finally be turned into a strain weakening behavior.

For daily life on cellular level the maximum forces or stresses the cytoskeleton of cells are able to withstand, are of great importance. This maximum stress networks are able to withstand can be derived from nonlinear measurements. In case of entangled actin networks one has to ask: What is the maximum force F_{max} which an entanglement point is able to withstand before two sticky actin filaments detach from each other? This maximum force can be calculated by normalizing the measured maximum pressure on the smallest unit area (within the actin network) and the number of entanglement points:

$$F_{max} = \frac{K_{max} \cdot L_e^2}{4} \tag{3.2}$$

Concerning this, it has to be assumed, that forces are distributed equally on four trapped entanglement points within a mesh of dimension L_e (eq. 1.15) [Tharmann et al., 2007]. Since the differential modulus K is rate dependent the maximum force also depends on the applied shear rate. Forced detaching of two filaments gives rise to the obtained maximum stress [Semmrich et al., 2008, Tharmann, 2006] as in case of cross-linked actin networks [Lieleg & Bausch, 2007].

With HMM as cross-linker molecules a maximum force of 8 pN for all actin and HMM concentrations at a filament length of 21 μm was obtained from nonlinear measurements with a shear rate of 12.5 %/s [Tharmann et al., 2007]. Comparing the 8 pN of cross-linked actin networks with the maximum force of 0.17 pN of the entangled actin networks (inset of fig. 3.3B, 21 μm) the relation: $F_{max,HMM} \approx 50 \cdot F_{max,actin}$ can be derived. The maximum force a cross-linker can withstand is 50 times larger as in case of sticky entanglement points. Therefore, cells use specific cross-linkers to adapt to environmental stress conditions. In conclusion, constant shear rate experiments are an adequate method to investigate the degree of cross-linking in biopolymer networks. In case of pure entangled actin networks, the number of sticky entanglement points per filament could be determined using macrorheological measuring methods.

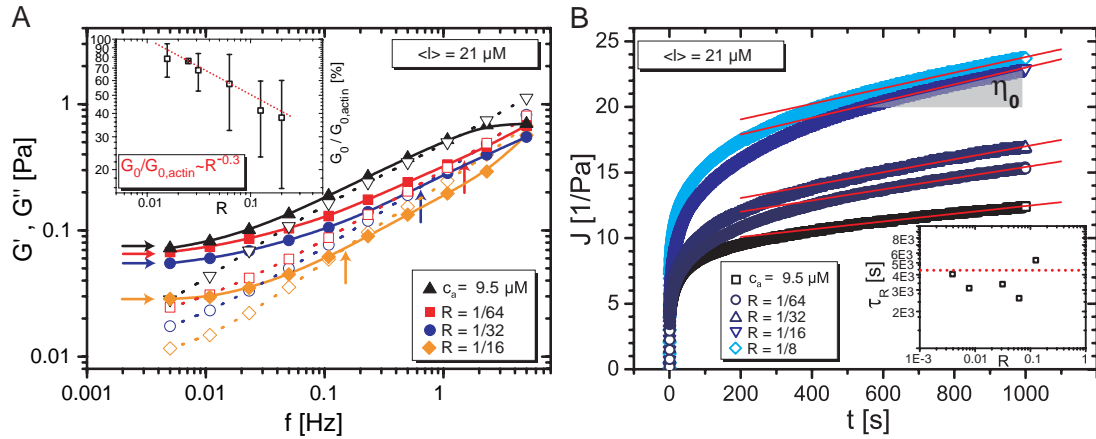## 3.1.2 Regulation of the Number of Sticky Entanglement Points by Active Heavy Meromyosin Cross-Linkers

Figure 3.4: (A) *Frequency spectra of G' and G'' of actin networks under the influence of active HMM as an ATP consuming molecular motor. Filled symbols represent G', open symbols with dashed lines G''. Upward pointing arrows are estimates of $1/\tau_e$. Inset: the decrease of G_0 (in percent) in dependence of R. G_0 is normalized to the values of pure entangled actin. (B) Stress pulse curves for actin networks with active HMM. The zero viscosity was extracted from the slope of these curves for long times. Inset: the relaxation time is not obviously reduced. The red dotted line indicates τ_r for actin without HMM.*

In the previous chapter it was elucidated that a certain amount of entanglement points can be considered as tight transient bonds between two actin filaments. The actin cytoskeleton is involved in the formation of dynamic cellular structures, as for example broad membrane protrusions (lamellipodia), long slender "fingers" (filopodia) or the cleavage furrow which occurs during cell division. Therefore, the actin cytoskeleton has to allow for switching from statical rigidity to dynamical flexibility. How is this mobility of the actin cytoskeleton ensured in cells? One possibility is to reduce the length of filamentous structures to less than the entanglement length. This is accomplished using the ABP gelsolin. The gelsolin concentration in cells can be adjusted resulting in either a gel- or sol-like actin network. Another strategy would be the usage of spacer molecules possessing a small bond lifetime. In actin networks containing active myosin II minifilaments fluidization could be observed [Humphrey et al., 2002]. The fluidization of this active actin networks was explained by diffusive directed motion of the actin filaments induced by the myosin II motor activity. Following this observations the influence of S1 (fig. 1.8, chap. 1.1.2) motor

heads from myosin II was described by enhanced longitudinal diffusion of actin fila-
ments [Liverpool et al., 2001, Liverpool, 2003]. In this model, a small increase in τ_e
and a decrease of τ_r is predicted, whereas G_0 should remain constant. The myosin II
subfragment HMM, introduced in chap. 1.1.2, has still full motor functionality and
can act as a cross-linker. However, the HMM is a very special cross-linker, since the
dissociation constant can be switched from 5 to $5 \cdot 10^{-7}$ M by regulating the ATP con-
centration. Therefore, HMM molecules are able to act as active or passive cross-links
in actin networks. After ATP consumption, a phase transition from sol-like to gel-like
networks can be observed experimentally by macrorheological measurement of the
elastic modulus. During the sol-gel transition in the ATP depletion phase, activated
transport of actin filaments by HMM molecules could be observed within a short time
window [Uhde et al., 2004].

As long as there is an excess of ATP molecules, the addition of HMM is not visibly
altering the network structure, as observed by fluorescence microscopy. No significant
differences to pure entangled actin samples could be resolved and actin filaments are
still organized into isotropically disordered networks. Therefore, at a first glance, it
is surprising that the viscoelastic behavior of active-HMM/actin network at ATP ex-
cess is crucially altered in comparison to pure entangled actin networks. Probing the
frequency behavior of active actin networks, these experiments show a clear depen-
dency of the moduli G' and G'' on the amount of added active motors (fig. 3.4A). For
molar ratios of HMM to actin concentrations R $> 1/64$, the absolute values of the mod-
uli decrease with increasing HMM concentration with respect to pure entangled actin
networks. This results in a changed overall frequency shape (fig. 3.4A). τ_e is shifted
over one decade on timescale towards longer times (arrows in fig. 3.4A). Moreover
the plateau modulus (defined as $G_0 \equiv G'(0.005\mathrm{Hz})$) shows an R-dependence. At the
highest HMM concentrations studied, the plateau modulus G_0 of active actin networks
is reduced to around 50 % of the value measured for pure entangled actin networks
(inset of fig. 3.4A). Since entanglement effects are not considered in the model of
enhanced diffusion [Liverpool et al., 2001], the model is not adequate to describe the
effect of active HMM. Based on the difficult extraction of the reptation time out of
the frequency spectrum, further stress pulse experiments with active actin networks
were performed to yield the zero shear viscosity (chap. 1.4.3, fig. 3.4). With eq. 1.25
the reptation time can be calculated using the measured values of G_0. τ_r obviously
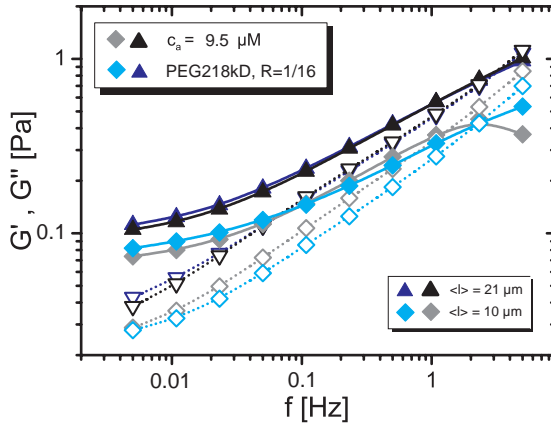varies less than a factor of 2 compared to the pure entangled actin network value (inset

Figure 3.5: *Depletion forces at a constant PEG218k concentration similar to active HMM ($R \equiv c_{PEG218k}/c_a$) do not influence the frequency behavior of G' (filled symbols and solid lines) and G'' (open symbols and dashed lines).*

of fig. 3.4B). These results advert to a more or less unchanged reptation time. If the observed effects are caused by enhanced reptation of the filaments similar to the observations of Uhde et al, it should be visible on timescales larger than 100 seconds after polymerization of the active HMM/actin network for one hour. With ATP in excess the filaments should then move about a distance in the order of their own contour length. Neither movies of fluorescently labeled active HMM/reporter filaments nor fully labeled active HMM/actin networks showed enforced reptation after the polymerization process (labeling of filaments, see chap. 1.2).

In order eliminate possible depletion effects as a reason for the altered viscoelastic behavior of active-HMM/actin networks, large PEG polymers were added to entangled actin networks at excess of ATP. The diameter of PEG218k (chap. 1.2) is comparable to the dimensions of HMM and therefore suited to mimic possible depletion effects of HMM. In contrast to the active-HMM/actin networks of fig. 3.4A the frequency behavior of actin networks with PEG218k is not distinguishable from pure entangled actin networks within the concentration regime used for HMM (fig. 3.5). This shows that depletion effects on the micro-molar range are not responsible for the reduced elasticity of active-HMM/actin networks.

Recently, the decrease of G_0 has been suggested to originate from actively reduced thermal fluctuations of single actin filaments in the network due to HMM activity [Tharmann, 2006]. This explanation fails because the duty ratio of HMM of fast skeletal Myosin II (cf. chap. 1.5) is too small. Moreover, the probability of HMM binding two different actin filaments with its two motor heads is very low and therefore very unlikely (cf. chap. 1.5). Hence, HMM motors are not able to exert their whole motor force of more than 1 pN on two actin filaments.

The scaling law known for entangled actin networks with c_a also holds for active
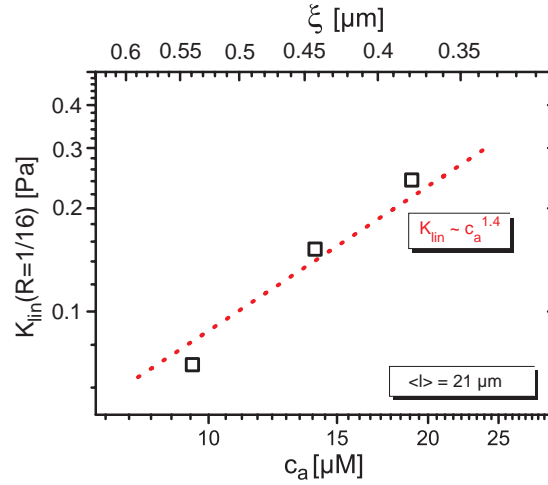
Figure 3.6: *Linear modulus of active HMM/actin networks in dependence of the actin concentration. The known actin concentration dependency in the linear regime is not influenced by active HMM motors.*

HMM/actin networks (fig. 3.6). This is in accordance with the preserved structure of a dense actin filamentous network in the presence of active HMM motors. Considering all arguments up to this point, it is reasonable that the lengths L_e and $\langle l \rangle$ are the key parameters to describe the decrease in G_0 and the increase in τ_e with increasing motor concentration. Combining eq. 1.15 and eq. 1.23 results in the following relation:

$$G_{0,actin} \sim \frac{k_B \cdot T}{\xi^2 \cdot L_e} \tag{3.3}$$

According to the results of fig. 3.6, ξ is assumed to be constant. Using G_0 of the inset of fig. 3.4 and eq. 3.3 it follows:

$$G_{0,active-HMM} \sim G_{0,actin} \cdot \frac{1}{R^{0.3}} \sim \frac{k_B \cdot T}{\xi^2 \cdot L_e \cdot R^{0.3}} \Rightarrow \Lambda_e \sim L_e \cdot R^{0.3} \tag{3.4}$$

with the interaction length Λ_e. From chap. 1.1.2 and eq. 3.4 one can conclude that the number of sticky entanglements per filament is reduced with increasing active HMM concentration:

$$\tilde{\#}_{ep} = \frac{\langle l \rangle}{\Lambda_e} \sim \frac{\langle l \rangle}{L_e} \cdot R^{-0.3} \sim \#_{ep} \cdot R^{-0.3} \tag{3.5}$$

Gathering the results obtained for entangled actin networks with active HMM motors, the following picture can be claimed. First, during the polymerization active HMM motors work as "fast transient distance keepers" respectively "highly dynamic spacers" between two actin filaments. Thus, less sticky entanglement points are produced and the entanglement length is larger in active HMM/actin networks than in pure entangled meshworks. Secondly, HMM motors are not strong enough to completely dis-
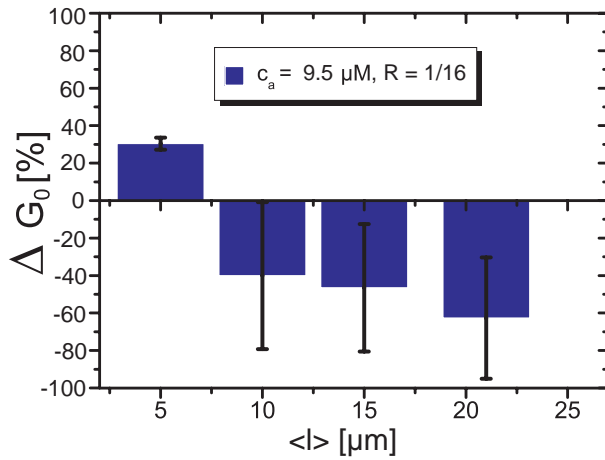
Figure 3.7: *Difference of G_0 ($G_{0,HMM} - G_{0,actin}$) at a constant HMM concentration in dependence of the mean filament length. Black error bars result from several measurements. At a length of 5 μm the resolution limit of the rheological method seems to be reached.*

join entanglement points formed during the polymerization process of actin filaments. However, sticky entanglement points can be weakened by active motors reducing the absolute number of sticky entanglement points in the network and increasing the interaction length. Within this picture, active HMM can be compared to a viscous lubricant between the actin filaments, due to its variety in K_D (in comparison to most ABPs which cross-link actin filaments on long time scales, HMM posses a huge range of K_D for actin, see tab. in chap. 6.6). According to this model, reducing the mean filament length should not influence the effect of active motors on weakening the viscoelastic actin networks, if L_e is kept constant. Thus, the results for G_0 at constant R, and consequently fixed entanglement length, in dependence of the mean filament length verify the proposed picture (fig. 3.7).

The reduction of the entanglement length with increasing active HMM concentration should also influence the nonlinear response regime. What consequences do active HMM molecules have on the nonlinear properties of actin networks? As already introduced in chap. 2.2.1 constant shear rate measurements of pure entangled actin solutions show a strain hardening, once passing a critical strain. Interestingly, active HMM proteins diminish the nonlinear strain hardening (fig. 3.8). With increasing HMM concentration strain hardening disappears, which is accompanied by a reduced yield stress (fig. 3.8). Less force can be transduced in networks with active HMM molecules compared to pure entangled actin networks. The active HMM cross-linkers increase slippage between single filaments in the network resulting in the observed strain weakening behavior. The derivative of the smoothed stress strain curves, K, is shown in the inset of fig. 3.8. The modulus K reveals softening of the linear viscoelastic behavior

Figure 3.8: *Strain hardening of actin networks is reduced by active HMM and vanishes at high HMM concentrations (indicated by the black downward pointing arrow). The measurement was performed with a constant shear rate of 12.5 %/s. Inset: in the linear regime K is reduced comparably to G_0. The strain weakening starts at strain deformations comparable to those in pure entangled actin networks. With increasing active HMM concentration slippage between single filaments is increased (dotted black arrow).*
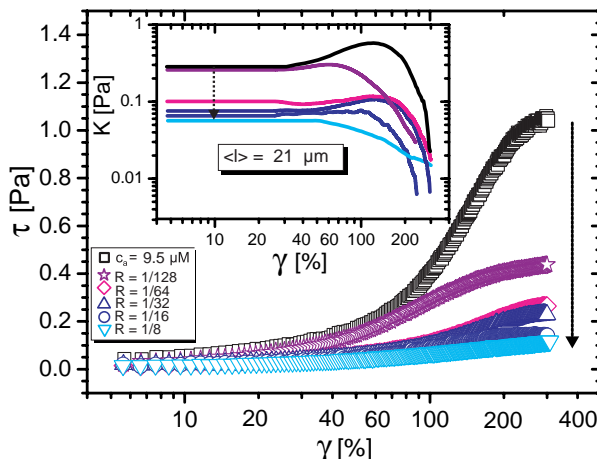
K_{lin} in dependence of the HMM concentration similar to the results of the oscillation measurements (inset fig. 3.8). These observations support the proposed picture of reducing number of sticky entanglements by active HMM.

In fact, cells seem to be able to regulate the stickiness of the actin polymer network using active molecular motors in contrast to other ABPs. Most cross-linker types have similar binding affinities for actin (cf. tab. in chap. 6.6). Therefore, by decreasing the binding affinity, the elasticity can further be reduced in order to maintain the mobility of the cell. The HMM molecule can function from a highly dynamic spacer to a firm cross-link due to its variable binding affinity. In case of active motors acting as lubricants between the actin filaments, they prevent a glassy arrest in the actin polymer networks.

Application of the Glassy Worm-Like Chain Model

In principle, it is possible to test the described picture in the previous subchapter by fitting the data of active-HMM/actin networks (fig. 3.4) with the glassy worm-like chain model introduced in chap. 1.4.3. With this the stickiness parameter ε as well as the interaction length can be extracted. The fits were performed following the GWLC [Kroy & Glaser, 2007, Glaser et al., 2008] with an implemented Maxwell-model for low frequencies. However, for a better interpretation, fits without the implemented Maxwell-model should be performed, in order to decide whether the maxwell-model matters for the HMM containing networks or not.
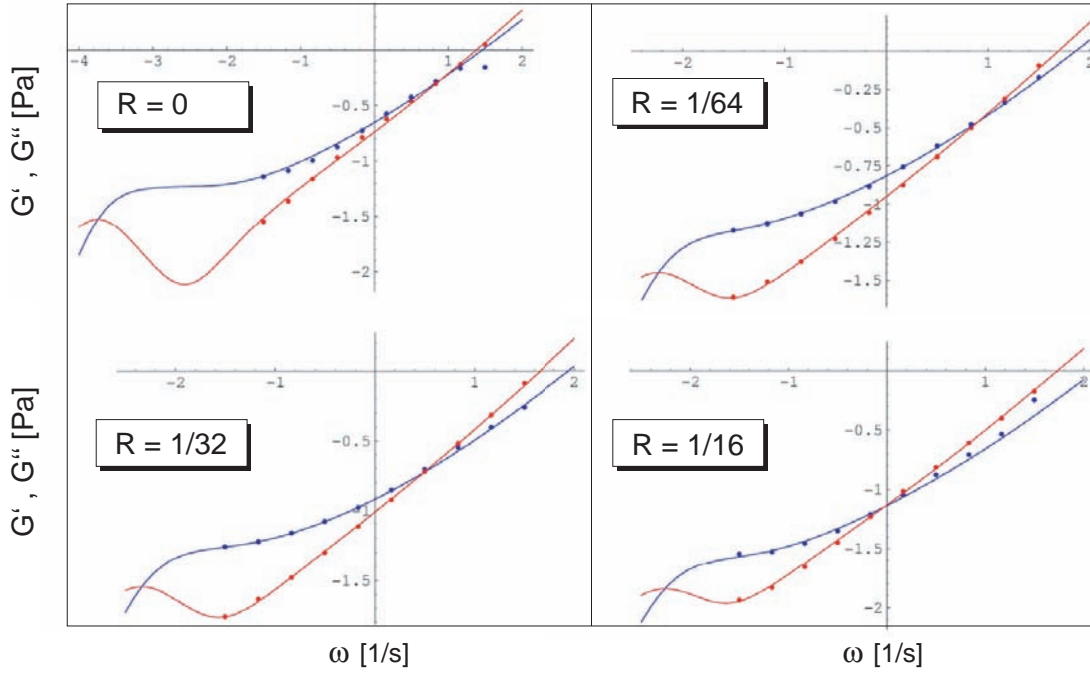
Figure 3.9: Fits to the data of fig. 3.4A with the GWLC model (chap. 1.4.3). The fits were performed by C. Hubert (Institut für Theoretische Physik, Universität Leipzig).

Parameter	R $= 0$	R $= 1/64$	R $= 1/32$	R $= 1/16$
ε	0.23	0.29	0.3	0.35
f_e [fN]	5	15	15	15
ρ [μm^{-2}]	5	4.6	6.7	6.6
L [μm]	8.5	8.3	10.7	15
F	0	$10 \cdot 10^6$	$3.8 \cdot 10^6$	0
η [Pa·s]	1000	41.67	28.57	12.5
Λ_e [μm]	0.51	1.1	2.8	5.1

Table 3.1: Fit parameter resulting form fits of fig. 3.4A using the GWLC model.

Here, the dimensionless parameters F and ε represent the corresponding free energy barriers of the polymer-polymer interaction potential. In General, the euler force $f_e \sim \frac{\kappa}{L^2}$ depends on the length L and the bending modulus κ of a filament [Howard, 2001]. ρ signifies the polymer density in the network (cf. eq. 1.21). The fits result in an increased interaction length with increasing active HMM concentration confirming a decreased network elasticity by the increase of the mean distance between sticky entanglements (tab. 3.1). Furthermore, for the first four fit parameters

senseful values are obtained. The obtained euler force of 15 fN for active HMM con-
taining networks can be compared to filament bucklings of about 2 μm in wavelength.
This lies in the range of the entanglement length for actin networks of the used filament
concentrations. Unfortunately, not all fit parameters are well consistent. For R $= 1/16$
L is too large and F too low and for R $= 0$ the obtained viscosity is too high. Moreover,
the viscosity of the system decreases with increasing HMM concentration. Up to now,
the reasons for this inconsistencies stay uncertain. It could be tested if better results are
obtainable for fixed parameters of actin concentration and filament lengths since these
two parameters are kept constant in the experiments.

3.2   Influence of Cross-Link Architecture on Actin Network Properties

In nature, cells are provided with a huge number of ABPs. Diversity of ABPs is necessary for the functionality of the cell cytoskeleton. Abnormalities and mutations in ABPs cause malfunction of the building blocks of the cytoskeleton and therefore are responsible for disease. Using various methods, mutations of ABPs and their grave influence on the morphism of actin filamentous networks have been investigated so far. Mutations of Espin for example, entail deafness due to malformed actin bundles in the microvilli of sensory cells of the cochlear. The importance of single domains of cross-linking molecules on the morphism of actin networks could be revealed with macrorheological methods. The hinge like domain in hFln is essential for obtaining highly elastic gels under prestress, comparable to the elasticity of cells [Gardel et al., 2006a, Gardel et al., 2006b].

The huge number and diversity of ABPs in nature makes it essential to investigate systematically the influence of the ABPs on actin networks. In general an ABP which is able to cross-link two actin filaments, has a modular architecture. Cross-linker molecules consist out of two actin binding domains which are separated and geometrically organized by different numbers of rod domains. Cross-linkers vary (i) in the type of actin-binding affinity caused by specific binding domains used and (ii) in the structure, number, and organization of their spacing rod domains. Nevertheless, the effect of structural rearrangements on the mechanical properties of such cross-linked networks is not fully understood. Thus, a correlation of the specific molecular structure of the cross-linker to the resulting network structure and its mechanical response is of great importance and the key questions are therefore: is it possible to parameterize cross-linker molecules? How does the cross-link structure influence the network properties? What consequences do the different network morphisms have on the overall properties of cells?

Consequently two parameters determine the effect of a natural cross-linker. The binding affinity and the length or the flexibility. For a systematic research both parameters have to be investigated separately. Although structural arrangements are difficult to quantify, the viscoelastic properties are reliably determinable. In order to solve this task, microscopical methods in combination with macrorheological methods are suited [Shin et al., 2004, Gardel et al., 2004a].

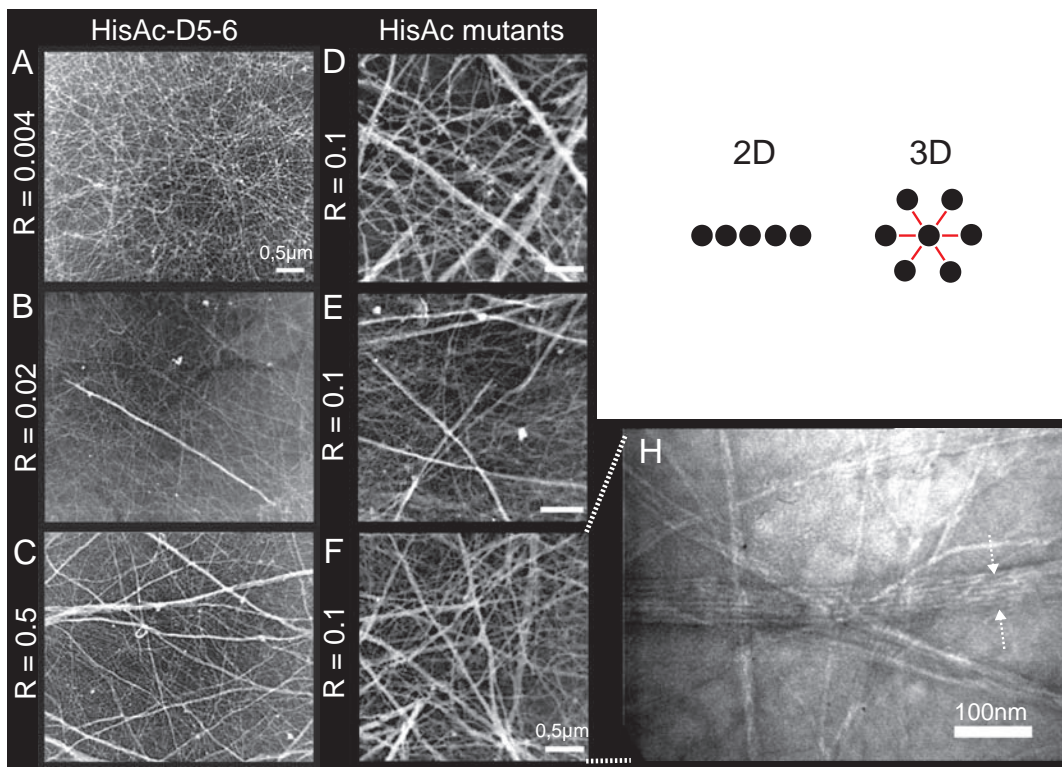### 3.2.1   Synthetic Cross-Linkers Based on Hisactophilin and Filamin

Figure 3.10: (A-C) *TEM pictures reveal a phase cross over from a pure cross-linked to mixed bundled and cross-linked phase for actin* (c_a = 9.5 μM) *HisAc-D5-6 networks* (*white scale bar = 0.5 μm*). (D-F,H) *TEM pictures of HisAc-C* (D), *HisAc-woC* (E) *and HisAc-HisAc* (F, H) *actin networks* (c_a = 9.5 μM). *These three networks have similar structure: embedded straight and stiff bundles in a cross-linked single filament network.*

The structure of networks, cross-linked with ddFln are visualized and compared to the results with networks cross-linked by synthetic cross-linker molecules. Exemplarily for the synthetic cross-linker HisAc-D5-6, electron micrographs show a composite network with a significant number of bundles embedded in an isotropic network of filaments above a concentration of R $\geq$ R* $\approx$ 0.01. The number of bundles increases with increasing concentration of the cross-linker molecules and at concentrations of R $\geq$ 0.1, a percolation of bundles was observed (fig. 3.10A-C). For HisAc-S-S-HisAc, a pure network of bundles was induced at R = 1. Below the transition concentration, a purely isotropic network was observed for all constructs studied.

Two monomeric and two dimeric synthetic cross-links were constructed with mutations in the hisac molecule (see tab. 1.1.2 in chap. 1.1.2). The dimer has a dumbbell
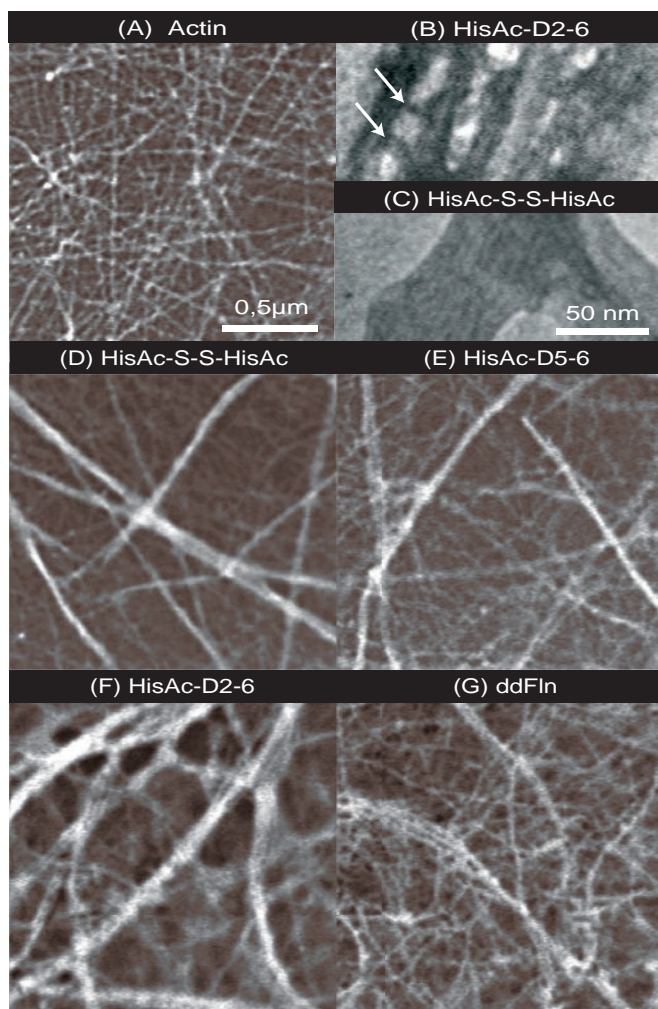
Figure 3.11: *TEM images of cross-linked ($R = 1/10$) actin networks ($c_a = 9.5\ \mu M$, $\langle l \rangle = 21\ \mu m$). Whereas for HisAc-S-S-HisAc (C, D) bundles appear straight and compact, bundles observed in ddFln (G) or HisAc-D2-6 (B, F) cross-linked networks are significantly more curved and appear less dense. White arrows indicate the cross-linkers (B).*

form and therefore has roughly twice the length of the monomeric hisac. Furthermore, the HisAc dimer can be compared to the small rigid ABP fascin in the dimension and binding affinity (cf. tab. 6.6).

 TEM micrographs in fig. 3.10D-F and fig. 3.11D depict that all four cross-links show the same morphological appearance of the actin networks at R = 1/10. A mixed phase is observed, built out of straight bundles which are embedded in an isotropically cross-linked actin network. At a first glance it appears surprising that the monomeric hisac forms bundles. In this special case the architecture of the hisac molecule allows the formation of bundles. More than 30 histidines in the molecule arrange a more or less globular allocation of positive charges. Consequently, the hisac functions like a sticky ball between the negatively charged actin filaments. It is not clear if the dimeric molecule is arranged parallel or transverse to the filaments in the bundles. A zoom

into the straight bundles exposes that about five filaments are aligned in parallel in the bundle (fig. 3.10H), taking into account that the bundle is projected on a flat surface. Hence, seven filaments are estimated to be contained in this bundle assuming a hexagonal packing of the filaments in the bundle in three dimensions (fig. 3.10). Since the diameter of this bundle is about 50 nm the center of the filaments are 16 nm apart. Considering the diameter of a single filament ($D_0 \approx 8$ nm) the resulting free space between the filaments is 8 nm. With a mean diameter of about 3 nm of a monomeric hisac the dimeric hisac has an estimated length of 7 nm which is in good agreement with the calculated spacing in the bundles from the TEM images. Consequently, the hisac dimers probably connect two actin filaments via a transverse bridge.

Polymerizing actin in the presence of ddFln resulted in a mainly isotropically cross-linked actin network. Electron micrographs show that, even at high concentrations of ddFln only a few embedded bundles are present in an isotropic network. The bundles appear loosely packed and significantly curved (fig. 3.11G). These structural observations depict that the elongated cross-linker ddFln is rather ineffective in forming strong bundles of actin filaments. The question arises whether these observations can be related to the extended molecular structure of ddFln. HisAc-D2-6, which contains rod repeats 2-6 of ddFln, was the longest synthetic cross-linker protein used in this study. Addition of HisAc-D2-6 cross-linker molecules resulted in an isotropically cross-linked network with curved and widely packed embedded bundles at high concentrations (fig. 3.11B,F). The shortest cross-linker induced dense and rather straight bundles, whereas all structures observed after addition of the longest construct or of ddFln seemed to be significantly bent and appeared fuzzier in the electron microscope pictures (fig. 3.11G). This increased effectiveness of the shorter constructs in fortifying actin networks can be related to pronounced structural rearrangements, induced by the distinct structures of the cross-linker constructs. For all cross-linker molecules under study, composite network structures were observed in which non-percolating bundles were integrated in an isotropic network below R $\approx$ 0.1. The electron micrographs suggest that the bundle stiffness depends on the cross-linker used, which could be due to the limited number of filaments inside the ddFln cross-linked bundles or an increased flexibility between the bundled filaments cross-linked by ddFln or HisAc-D2-6 [Howard & Ashmore, 1986, Claessens et al., 2006a]. Therefore, one has to understand how the different compliant bundle structures installed in actin networks

affect their mechanical viscoelastic properties.

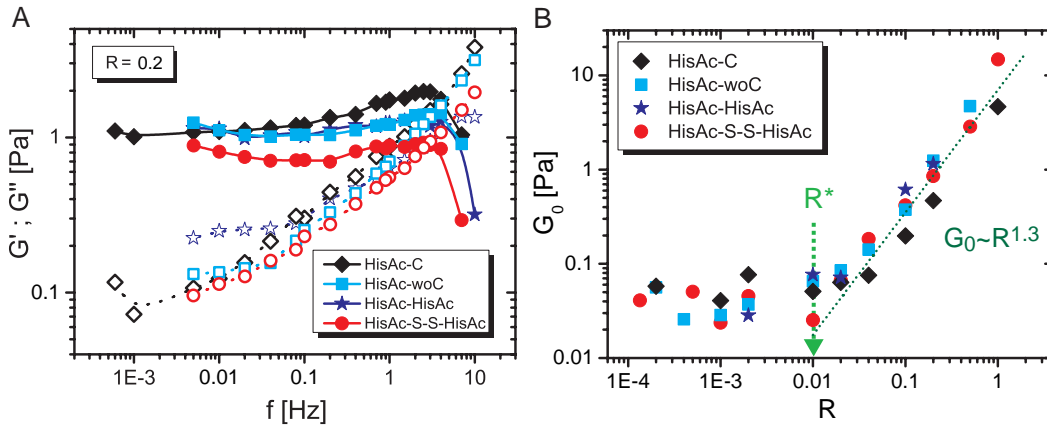Likewise the results of the TEM images, no differences were resolved from mea-

Figure 3.12: (A) *Macrorheological* (TDR) *comparison of the four used hisac mutants at a constant concentration of cross-links and actin* (c_a = 9.5 μM). *The overall appearance of* G' *and* G'' *in dependence of the frequency is similar which is in accordance with the TEM micrographs.* (B) *By evaluation of the elastic modulus* (G *at 5mHz, measured with the TDR macrorheometer*) *over the cross-linker concentration all HisAc mutants show a phase cross over at 0.01 < R < 0.04. The scaling for all four mutants is the same.*

surements of the viscoelastic frequency behavior comparing the monomeric with the dimeric hisactophilin constructs. For R = 1/5 the gels with the hisac mutants are elastically dominated. G' reaches 1 Pa and stays more or less constant over the whole measurable frequency regime (fig. 3.12A). The corresponding concentration dependent G_0 plot of the four hisac mutants enlightens two phases (fig. 3.12B). A first cross-linked phase in which the G_0 stays constant within the resolution of the macrorheometer. In the second regime the elasticity steeply increases with the concentration of the cross-linker. This increase in the elasticity coincides with bundle formation within the actin network. The critical concentration can be extracted from the data points to R > R* ≈ 1/100 which is in good accordance with the electron micrographs. With increasing cross-linker concentration the number of bundles embedded in the network rises. Therefore the macrorheological method is suitable to differentiate morphological differences in *in vitro* cytoskeletal actin networks.

Doubling the length dimension from a monomeric hisac molecule to a dimeric one does not result in resolvable differences. Considering the results of the TEM micrographs from fig. 3.10 it is not surprising that the four mutants result in the same viscoelastic behavior. Consequently, small varieties of the bundles due to the

differences of the dimers and monomers are not resolvable with the macrorheometer.
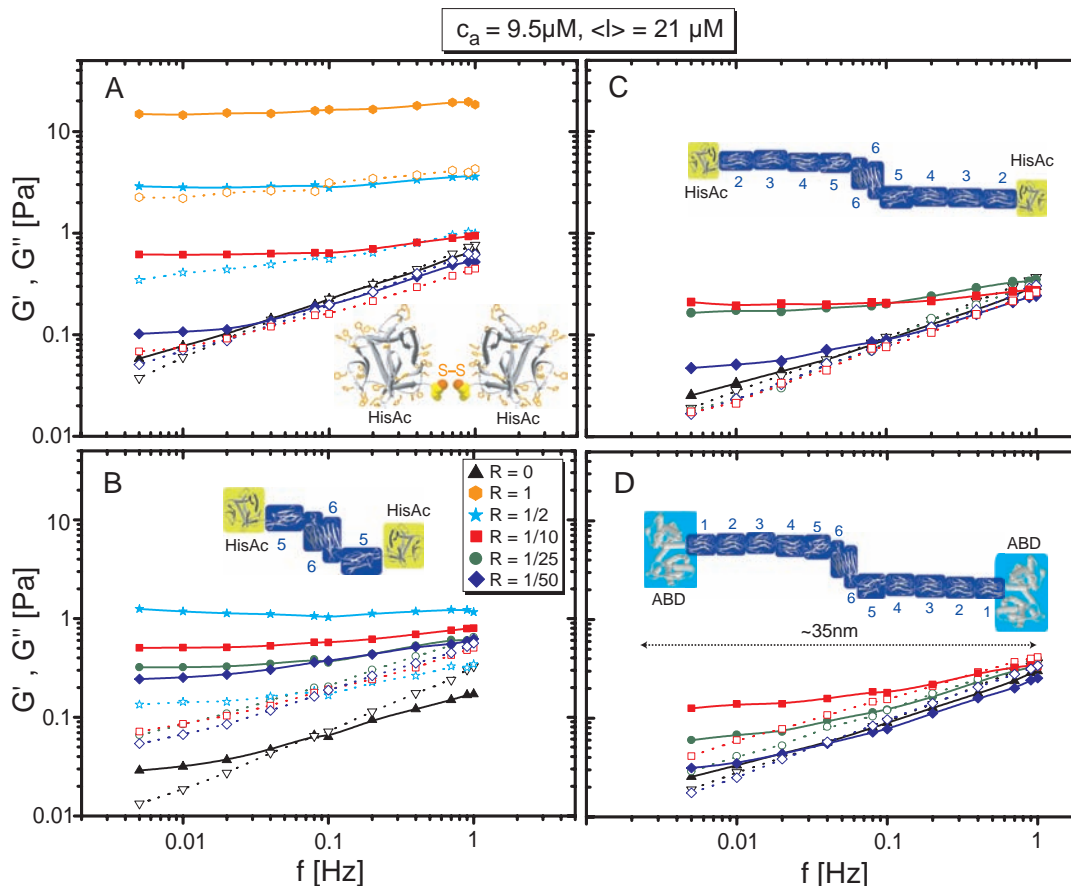

Figure 3.13: $G'(f)$ and $G''(f)$ of cross-linked actin networks measured at different molar ratios in bulk with the TDR rheometer. (A) HisAc-S-S-HisAc. (B) HisAc-D5-6. (C) HisAc-D2-6. (D) ddFln. For all cross-liner molecules, the same concentration ratios are shown. All frequency sweeps show a flattening of G' and a shift in the crossover frequency with increasing R. The insets show schematics of the cross-linker constructs (see fig.1.6) from structural data of single domains.

To test how the extended linear geometry influences actin network strength and to systematically relate the molecular structure of different cross-linking molecules to their mechanical effectiveness, three synthetic chimeric proteins were constructed. In all constructs, hisactophilin was used as the actin-binding domain, and, in two cross-linkers, the length of the spacer region was varied by using different numbers of IgG repeats of ddFln (cf. chap. 1.1.2).

Because it is not possible to obtain a reliable quantification of the structural rearrange-
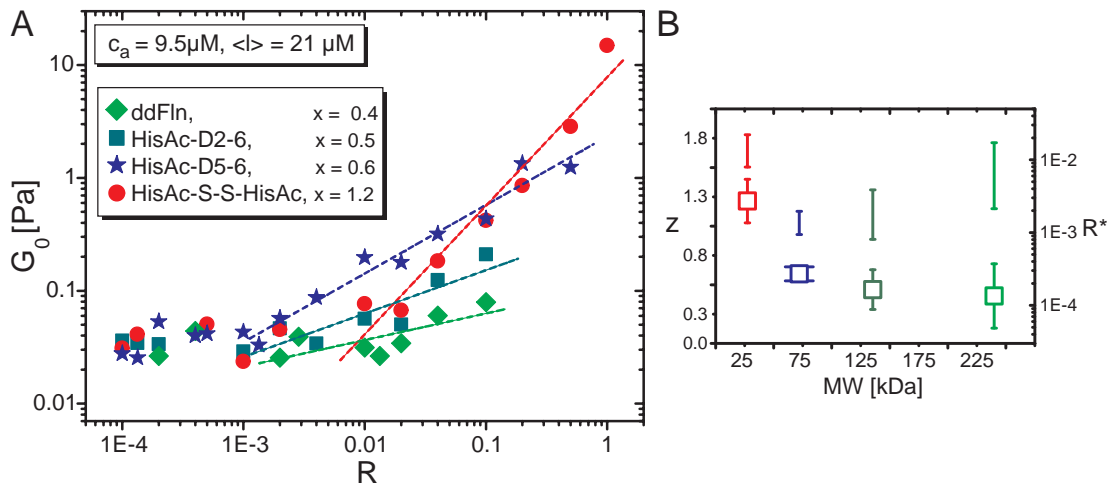
Figure 3.14: (A) Plateau modulus G_0 depends on R for cross-linked actin networks. Above a critical ratio $R^\star$ G_0 increases in all cross-linked actin networks ($G_0 \sim R^z$). (B) Scaling exponent z (squares) and $R^\star$ (bars) in dependence of cross-linker molecular weight (MW). With increasing molecular weight cross-linkers are less effective in network fortification. The error bars were obtained by assuming slightly different threshold values.

ments from electron micrographs, the mechanical effect of the compliant cross-linker ddFln on actin networks was determined. In the linear response regime, ddFln/actin networks show only a weak frequency dependence for the loss and storage moduli, as can be seen in fig. 3.13D. The effectiveness of ddFln in strengthening actin networks was determined by measuring the elastic modulus G_0 at 5 mHz at a given actin concentration. Fig. 3.14A shows that, above a critical concentration of ddFln ($R^\star \approx$ 0.01±0.008), the elastic modulus gently inclines with increasing cross-linker concentration $G_0 \approx R^{0.4\pm0.3}$. Accordingly, the ddFln is not only ineffective at bundling actin filaments but also has only a modest effect on raising the viscoelasticity of these networks. Furthermore, rheological measurements of HisAc-D2-6 showed that, below a transition concentration $R^\star$, the mechanical properties of the network are not affected by the addition of the cross-linker. However, above a critical concentration ($R^\star \approx 0.0023\pm0.0015$), increasing amounts of HisAc-D2-6 resulted in (i) an increase of the viscoelastic moduli, (ii) a flattening of the frequency dependence of the plateau modulus, and (iii) a shift in the crossover frequency (fig. 3.13C). For all concentrations, the HisAc-D2-6/actin networks are predominantly elastic. As can be seen in fig. 3.14, the modest effect of the longest construct on the elastic properties of the network is comparable with that of ddFln. Again, exceeding a critical concentra-

tion, G_0 increases weakly with the concentration of the cross-linker ($G_0 \approx R^{0.5\pm0.2}$). This similarity in mechanical effectiveness is obtained, although the actin-binding domains in ddFln and HisAc-D2-6 are very different, which suggests that the spacing structure of the cross-linker molecules predominantly determines their mechanical effectiveness and not the affinity of the actin-binding domain. This result implies that the mechanical effectiveness should be affected by shortening the spacing domains without modifying the binding domains. Indeed, we observed that a stronger effect on the mechanical properties can be achieved with a decreased number of rod domains. The construct with two rod domains (HisAc-D5-6) already has a significantly stronger effect on the elastic modulus of the network. When the critical concentration ($R^\star \approx$ 0.0015$\pm$0.0005) is passed, a remarkable increase as a function of cross-linker concentration is observed ($G_0 \approx R^{0.6\pm0.1}$, fig. 3.14). For the shortest cross-linker studied, a simple dimer of two hisactophilin molecules chemically fused by a disulfide bridge (HisAc-S-S-HisAc), a high increase in the elastic modulus is observed for $R > 0.01$. Further increase in the cross-linker concentration causes the elastic modulus to change more than two orders of magnitude and scale with $R^{1.2\pm0.2}$. Thus, at concentrations above the critical concentration, a clear dependence of the rheological behavior on the number of rod domains can be observed. Consequently, the structural rearrangements and the mechanical effectiveness differ significantly between the constructs. The increase of the elastic modulus with increasing concentration of cross-linker molecules ($G_0 \sim R^z$) depends on the molecular mass (MW) and thus on the contour length of the cross-linker constructs. The MW dependence can in first order roughly be approximated by a power law: $z \approx MW^{-0.7}$. For the threshold value, $R^\star$, no direct dependence was observable. Considering the moderate effect on the linear mechanical response of the actin network, it may be surprising that living cells use ddFln as a cross-linker. One important aspect could be that cross-linking actin networks by ddFln adds additional compliances to the network that affect the nonlinear response. Indeed, the nonlinear viscoelastic behavior of the networks depends strongly on the structure of the cross-linking molecules (fig. 3.15). For all constructs, the onset of the nonlinear response regime γ_{crit} and the fracture stress τ_{max} was determined at a concentration of $R = 0.1$. As can be seen in fig. 3.15A, γ_{crit} was observed at increasingly higher strains the longer the construct was. Simultaneously, τ_{max}, the stress at which weakening of the network was observed, depends significantly on the studied constructs. The longest cross-linkers were withstanding the largest stresses, attaining a stress up to 3$\pm$0.4 Pa.
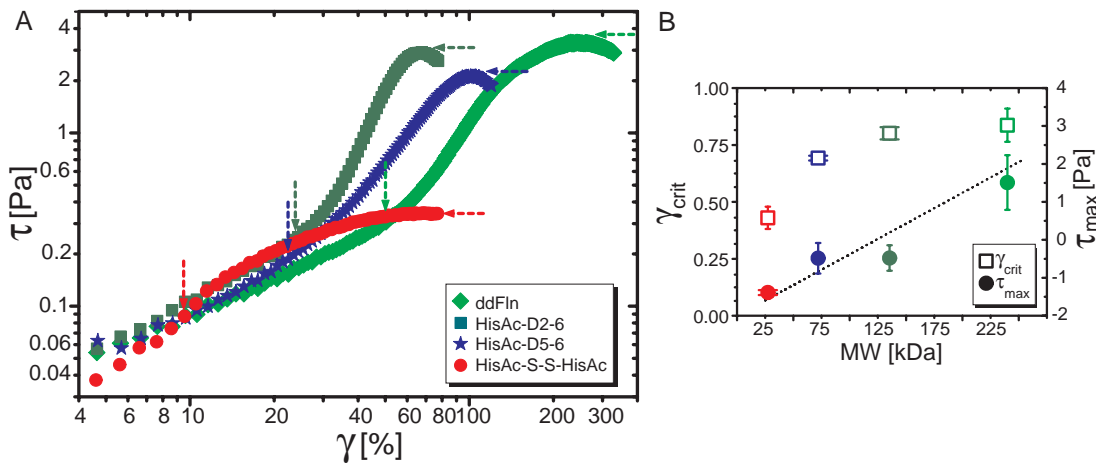
Figure 3.15: (A) Recorded stress-strain dependence of F-actin networks ($c_a = 9.5$ μM with $\langle l \rangle = 21$ μm) with HisAc-S-S-HisAc, HisAc-D5-6, HisAc-D2-6, and ddFln cross-linkers at a constant R = 0.1. Arrows pointing left illustrate the maximal reachable stress τ_{max}, and downward-facing arrows indicate the onset of nonlinearity γ_{crit}. (B) γ_{crit} and τ_{max} are shown over the MW of the cross-linking constructs. The dotted line indicates a linear relation.

In contrast, the shortest cross-linker ruptured first, reaching only 0.6±0.3 Pa. Concomitant with the differences in τ_{max} for each cross-linker, the maximal absolute modulus is increased from 1.1 Pa for the shortest cross-linker to 2.2 Pa for HisAc-D5-6 and 4.5 Pa for HisAc-D2-6. The increase of the γ_{crit} and the maximal obtainable modulus depends almost linearly on the molecular weight and thus the contour length of the constructs, as can be seen in fig. 3.15B.

The systematic variation of the molecular structure of cross-linker molecules shows that the geometry of the cross-linker determines the mechanical network fortification. Short cross-linker constructs result in composite networks in which isolated bundles are embedded in an isotropic network of single filaments. The short cross-linkers are most effective in enhancing the linear viscoelastic properties of actin networks. Longer constructs and ddFln do not result in a significant increase of the linear elastic moduli, which can be attributed to their lower bundling propensity. For all cross-linker constructs studied, two regimes were distinguishable in the linear mechanical response: (i) one regime with no remarkable increase of the viscoelastic moduli and (ii) another regime with an increase of the plateau modulus G_0 correlated with the concentration of cross-linkers. Because the binding affinity is the same for all of the constructs, the differences in the mechanical response of the networks are affected by the num-

ber of rod domains and thus the resulting compliance. The structural transition from a weakly isotropically cross-linked network to a strongly isotropically cross-linked network or to a composite network with embedded bundles depends on the geometrical structure of the ABPs. Because of the relatively lower entropic cost associated with cross-linking two filaments, the longer constructs cross-link filaments already at lower concentrations than the shorter constructs but with an impeded bundling efficiency [Borukhov et al., 2005]. The short-range interaction of shorter constructs results in an increased cooperativity favoring bundling with the transition occurring at higher concentrations. It is important to point out that, although the binding constants of all constructs are kept constant, the molecular structure sensitively affects their effectiveness in bundling, which requires simultaneous binding of both actin-binding domains and therefore may be easiest for the shortest construct. For the almost covalent and rigid cross-linker scruin, the observed increase of the moduli of $G_0 \approx \mathrm{R}^2$ and its observed transition at $\mathrm{R}^\star = 0.01$ are in excellent agreement with the shortest cross-linker in the present study [Shin et al., 2004]. Depletion forces induce a direct transition from an isotropically cross-linked network to a pure bundle phase, in which the moduli increase as $G_0 \approx \mathrm{R}^{3.5}$ [Tharmann et al., 2006]. These results suggest that the increase of the moduli as a function of concentration in the second regime can be understood as a measure of the bundle propensity that dominates the mechanical effectiveness. Furthermore, it is important to keep in mind that not only the number of rod repeats but also their structure and the degree of dimerization determine the compliance of a cross-linker molecule. For example, in α-actinin, the spacing domain is composed of four repeats (based on a triple-stranded, coiled-coil α-helix called spectrin domain), which are completely dimerized, resulting in a presumably rigid rod of a contour length of ≈ 36 nm. This cross-linker increases the linear elastic modulus of cross-linked networks quite effectively: $G_0 \approx \mathrm{R}^{2.4}$ [Tempel et al., 1996] or $G_0 \approx \mathrm{R}^{1.7}$ [Tseng & Wirtz, 2001], and, for different long isoforms of α-actinin, significant differences in bundling propensity were observed [Meyer & Aebi, 1990]. In addition, the nonlinear response regime of actin networks is drastically affected by cross-linker proteins [Gardel et al., 2004a, Xu et al., 1998]. Once a critical strain is passed, further increase of the strain on actin/cross-linker networks results in a stress hardening. Whereas ddFln cross-linked networks harden by a factor of 10, the shortest cross-linker construct results only in a modest hardening response, almost comparable with pure actin networks, before weakening of the network was observed. The structure

of these networks and the increased compliance of the longer cross-linkers allow the network to withstand higher shear stresses. Consistently, the critical strain γ_{crit}, upon which a nonlinear response occurs, is linearly dependent on the MW of the cross-linker constructs (fig. 3.15B). The fracture stress depends on the force redistribution inside the network, which was observed to depend on the MW and thus the length and compliance of the cross-linkers. Because the binding affinity is kept constant between the constructs, the measured differences have to be attributed to structural differences of the cross-linkers and the resulting networks. Recently, it was shown that a small difference in the molecular structure of human filamin isoforms has significant effects, especially in the nonlinear response of cross-linked networks. Hinged filamins reached fracture stresses of 10-30 Pa, which were 10-fold higher than for non-hinged filamins [Gardel et al., 2006a].

In sum, on the basis of well defined synthetic constructs, it was possible to correlate the macroscopic mechanical behavior of cross-linked actin networks with the structure and geometry of actin cross-linking proteins. The observed dependence of the linear elastic properties and the phase behavior on the molecular structure exemplifies how single-molecule properties affect the macroscopic behavior of networks.

3.2.2 Variation in the Number of Actin Binding Domains in Cortexillin I Constructs

The influence of an increased number of spacing domains in a cross-linker molecule which enlarges the dimension of the cross-linker, expresses itself in the formed actin network phase. Here, the number of the actin binding domains in a cross-linker molecule is varied with the two constructs of Cortexillin I, which are described in detail in chap. 1.1.2. Macrorheological experiments were performed and the measured viscoelastic properties are related to the microstructure of the built actin networks.

In fig. 3.16 the influence of the two cortexillin I constructs on the actin networks are compared. From TEM picture analysis it is known that both constructs are able to form actin bundles [Stock et al., 1999]. Comparing the structures formed at R $\geq$ 0.2 confirms this result (fig. 3.16A-B). Since quantification of electron microscope pictures remains difficult, macrorheological analysis was performed to elucidate differences of the two cross-linker constructs.

The frequency spectrum in the linear response regime of both cortexillin I cross-linkers
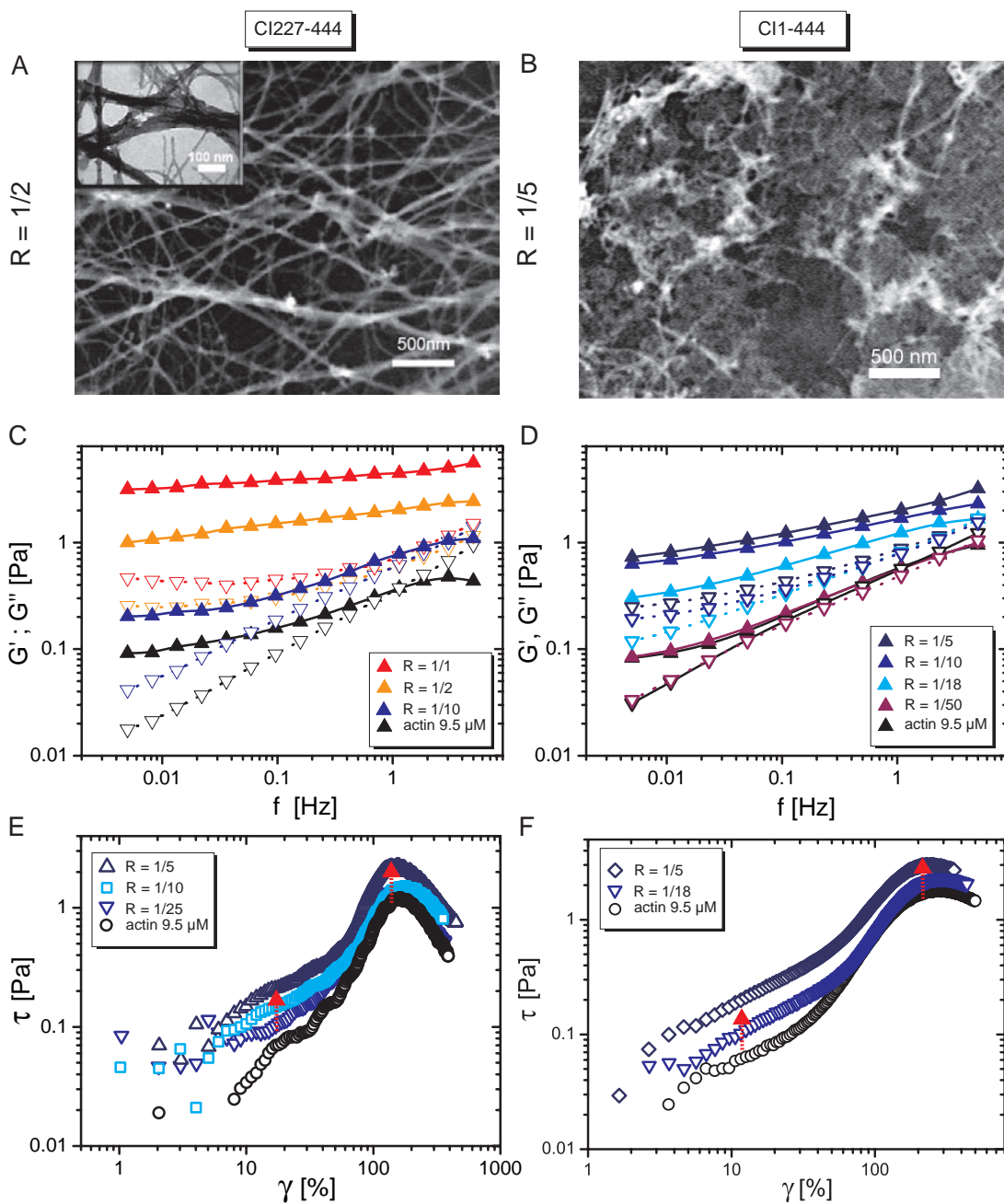
Figure 3.16: (*A, B*) *TEM micrographs reveal structural differences for high concentrations which are in accordance with rheological data.* (*C, D*) *Viscoelastic frequency behavior of cortexillinI/actin networks. G' becomes more flat with increasing R.* (*E, F*) *Constant shear rate experiments* ($\dot{\gamma} = 12.5$ %/s). *Strain hardening is enhanced for both cortexillin I constructs* (*indicated by red upward pointing arrows*).

show an increase in elasticity with increasing cortexillin concentration (fig. 3.16C,D). For the highest R used (CI227-444), G' is nearly constant over the whole frequency range and G'' reveals a minimum at about 0.03 Hz (fig. 3.16C). Plotting the G_0 over R reveals the differences in bundling ability of the cortexillin I constructs (fig. 3.17A). Similar to the hisac mutants the increase of G_0 happens at a critical concentration R $> R^* \approx 0.01$ which is the transition to the bundle phase. In this regime, G_0 increases nearly linearly with the concentration of cortexillin I. Both molecules enhances the elasticity in the same way in the bundle phase till the concentration exceeds R > 0.2 where $G_0 \approx 1$ Pa. Beyond this point, the elasticity of the actin networks drops down with the used full length CI1-444 whereas the circumcised CI227-444 with the missing two ABDs is able to rise the elasticity further up to 6 Pa.

Since cells are generally prestressed [Trepat et al., 2008] their cytoskeleton always underlies a sort of stress. Consequently, cortexillin/actin networks in the cleavage furrow of dividing cells experience large forces. Therefore it is important to investigate the nonlinear properties of cortexillin/actin networks *in vitro*. The constant shear rate experiments for both cortexillin I constructs are presented in fig. 3.16E and F. Both cortexillins enhance the elasticity in the linear regime and increase the maximum stress which the networks can withstand in the nonlinear response (fig. 3.16E and F). Extracting the critical strain from this stress strain curves confirms the results similar to the G_0-R-dependence of the linear measurements (fig 3.17). γ_{crit} reaches the same
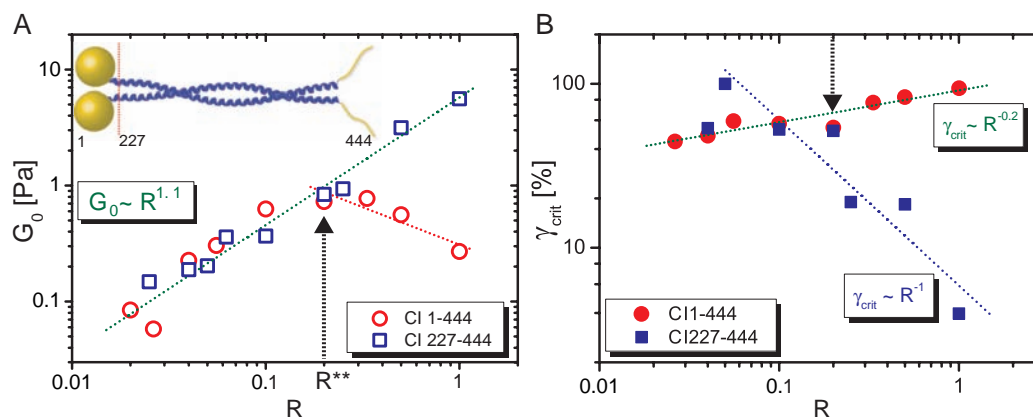

Figure 3.17: (A) *In the bundle dominated regime both cortexillin I constructs exhibit the same scaling behavior with R. While CI227-444 builds successively stronger gels, G_0 of drops down at $R^{\star\star} > 0.2$ for the whole cortexillin I. (B) From evaluation of stress-strain curves a contrary concentration dependence of the critical strain is obtained for $R^{\star\star} > 0.2$ indicated by the black downward pointing arrow.*

values at low values of R, for both constructs (fig. 3.17B). Above R > 0.2 the critical strain for the CI227-444 decreases linearly whereas γ_{crit} for CI1-444 slightly rises with R. The same relation of γ_{crit} of CI227-444 was found for pure bundled actin networks with the ABP fascin [Lieleg et al., 2007], indicating a pronounced bundle phase. The bundling ability of CI227-444 is in accordance with the observations made from TEM micrographs. The TEM pictures showed that the C-terminal binding domains are responsible for the bundling activity of the cortexillin I [Stock et al., 1999]. Since the CI227-444 lacks the N-terminal domain the results of the network structure is in agreement with the obtained macrorheological data. In contrast hereunto, the critical strain for the CI1-444 slightly rises to about 90 %, which is about a factor of three larger as for pure entangled actin networks (cf. fig. 2.4D). In pure entangled actin networks the dominating length scale is the entanglement length. With addition of cross-linkers to the actin network the dominating length scale parameter of the deformation mode of filaments and bundles in the network is the cross-linker distance l_c. Since the critical strain is proportional to l_c, this parameter has to increase with increasing concentration of the cross-linker.

$$\gamma_c \sim l_c \sim l_e \cdot R^{-y} \tag{3.6}$$

This assumption is senseful because the cortexillin/actin networks are composite networks of bundles which could be considered as cross-linked (minimum in G'' at high R, fig. 3.16C). Futhermore, G_0 increases with increasing R if the average distance between the ABPs is assumed to be constant in an actin network with a certain concentration:

$$G_0 \sim R^z \tag{3.7}$$

At last the bundling degree of the composite networks is quantified with the bundling exponent x. In general the bundling exponent could be verified by bundle thickness analysis from electron microscope pictures of the cortexillin/actin networks. The exponents of G_0 and γ_c are associated with the bundling exponent x, assuming an intermediate coupling of the bundles in the network and a non-affine bending of the bundles [Lieleg et al., 2007] in the following equation:

$$x = 0.5y - 0.25z \tag{3.8}$$

Taking the values for y and z from fits to the data of fig. 3.17, x can be calculated. In the following table the results for x, y and z are shown for CI227-444: the results

	x	y	z
CI227-444	0.25	1	1.1

Table 3.2: Scaling exponents of cortexillin I.

for the CI227-444 are similar to fascin/actin networks, where the bundle thickness grows with an exponent of 0.27. This leads to the interpretation that CI227-444/actin networks have a high bundling degree and the bundles are coupled in a certain way. From bending fluctuation analysis of the bundles, comprised in emulsion droplets, the coupling of the bundles can be quantified [Claessens et al., 2006a]. For the observed decrease of G_0 of the CI1-444/actin networks the following possible interpretations are conceivable. The elasticity of the network decreases if the bundles are weakly coupled and the increase of the distance between bundles is not compensated by the increased bundle stiffness. Or, a macroscopic phase separation takes place and the bundles are condensed to an inhomogeneous network, in which the dominating length scale is the distance between large bundle agglomerates. If those bundle agglomerations are weakly interconnected among each other the whole network elasticity is lower as for the composite network which is on the whole homogeneous. Such effects could be utilized in cells during cell division. In the cell, cortexillin is expressed during mitosis near the equatorial region [Weber et al., 2000, Weber et al., 1999]. If the cell increases the concentration of cortexillin I the presence of the cross-linker leads to an arrangement of the dense network of single actin filaments and gives rise to the bending elasticity of the actin cortex. This arrangement could be thought to be a prerequisite for the separation of the actin cortex in this region of the cell.

Overall, with the macrorheological method it was possible to determine quantitatively the cortexillin concentration dependent behavior of the built actin networks and enlighten the influence of the lacking N-terminal binding domains in the CI227-444 in comparison to the whole CI1-444 molecule.

3.2.3   Macrorheological Comparison of the Influence of Different Cross-Linkers on Actin Network Elasticity

The elasticity of actin networks can be tuned with the actin concentration and the amount of added ABPs. Keeping the actin concentration constant, the elasticity of the cross-linked actin networks show astonishing similarities in dependence of cross-linker

concentration added. Beside the flexibility and dimension of a cross-linker molecule its binding affinity to actin filaments is another characteristic parameter which in turn determines the properties of cross-linked actin networks. Although all wild-type cross-linkers have a different architecture, the binding affinities to actin filaments is similar. The dissociation constant K_D lies in the range of 0.1-10 μM (cf. tab. 6.6). In the following the four wild type ABPs cortexillin I, ddFln, ggFln and fascin as well as the hisac-woC mutant and HMM/networks are compared. The calculated association energies ΔG in tab. 6.6 for the six cross-linkers lie in the range of 12-16 $k_B \cdot T$. This is only a factor two lower as for the firmest known complex of biotin and avidin. Therefore the comparison of these six ABPs is reasonable. As a measure for the elasticity of
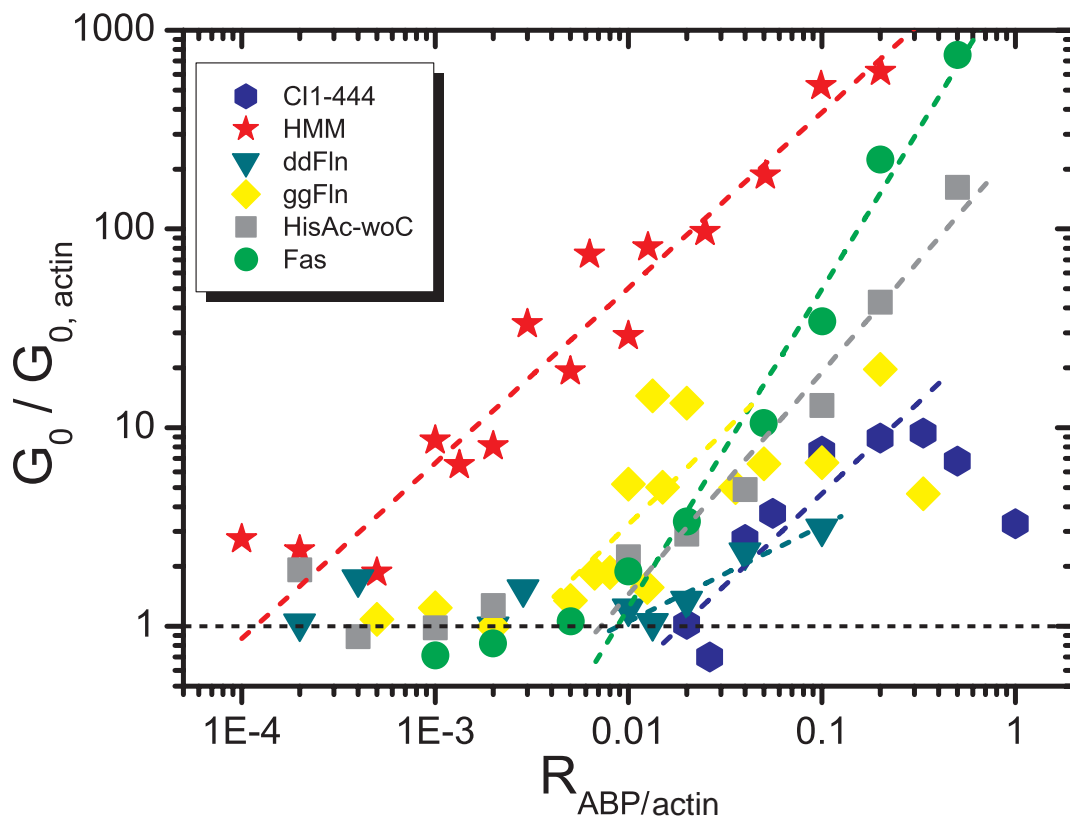
Figure 3.18: *Comparison of the normalized* G_0 *plotted over R for six different cross-linkers. Four regimes can be distinguished. With increasing cross-linker concentration the actin network traverses from an entangled, via a cross-linked and mixed to a purely bundled actin filament dominated phase. At the highest R, the molecular properties of the cross-linker determines whether a purely bundled phase or an heterogeneous network emerges. (Fascin data points by courtesy of O. Lieleg)*

the resulting cross-linker/actin networks G_0 normalized on the actin concentration is

used. In fig. 3.18 G_0 is plotted over four decades of cross-linker concentration. The six cross-linker/actin networks stride on two paths the phase diagram resulting in four distinguishable phases divided by critical concentrations R^*. The HMM, which originates from enzyme digestion of myosin II, increases the elasticity of the actin networks for $R^*_{HMM} > 1/2000$, whereas all other actin networks still follow the same path. Apart from HMM/actin networks, all other cross-linkers increase the elasticity if the concentration overshoots $R > R^*_B \approx 1/100$, where the beginning of the bundle phase transition is located. Only from this G_0 analysis, one can state that HMM molecules are not able to form bundles within actin networks. Rising the concentration again one decade two possible pathways are left. First, for small and rigid cross-linkers the network separates into a pure bundle phase, like it is observed for fascin and hisac-woC and secondly a disordered actin filament agglomeration phase, like for the cortexillin I. With the different ABPs cells have the possibility to adjust the stiffness of their actin containing cytoskeleton over three orders in magnitude in dependence of the cross-linker concentration. Expressing a small amount of isotropically cross-linking molecules needs only a tenth of the amount of cross-linkers which fortify the network by inducing bundling of filaments. The stiffer the bundles, the higher the overall network elasticity. This task is best accomplished with the small, stiff and rigid dimeric fascin molecule. Although unlike larger and more flexible as fascin, GgFln is also very effective in fortifying the actin network in the middle of the concentration regime. Comparing the measured elasticity with microscopic pictures one can deduce that the rise in G_0 at $R \approx 0.01$-0.025 occurs due to bundle formation. Again a composite networks of filaments and bundles is responsible for the observed elasticity of ggFln/actin networks. For large ggFln concentrations ($R > 0.03$) the elasticity of the network increases only slightly further. Whereas the networks phase separate in a pure bundle phase with fascin as cross-linker, the network structure gained with ggFln remains trapped in a non-equilibrium state, where bundles branch, resulting in a broad bundle thickness and meshsize distribution [Schmoller, 2008]. The observed dependence of the linear elastic properties and the phase behavior on the molecular structure exemplifies how single-molecule properties affect the macroscopic behavior of networks. Differences in the elasticity turns out to be of structural origin of the ABP which is derived from the known overall network structures observed by the help of microscopy techniques (fig. 3.19). Beside the concentration of the cross-linker, its flexibility and glutinousness determines the observed phase diagram. Because the mechanical properties of
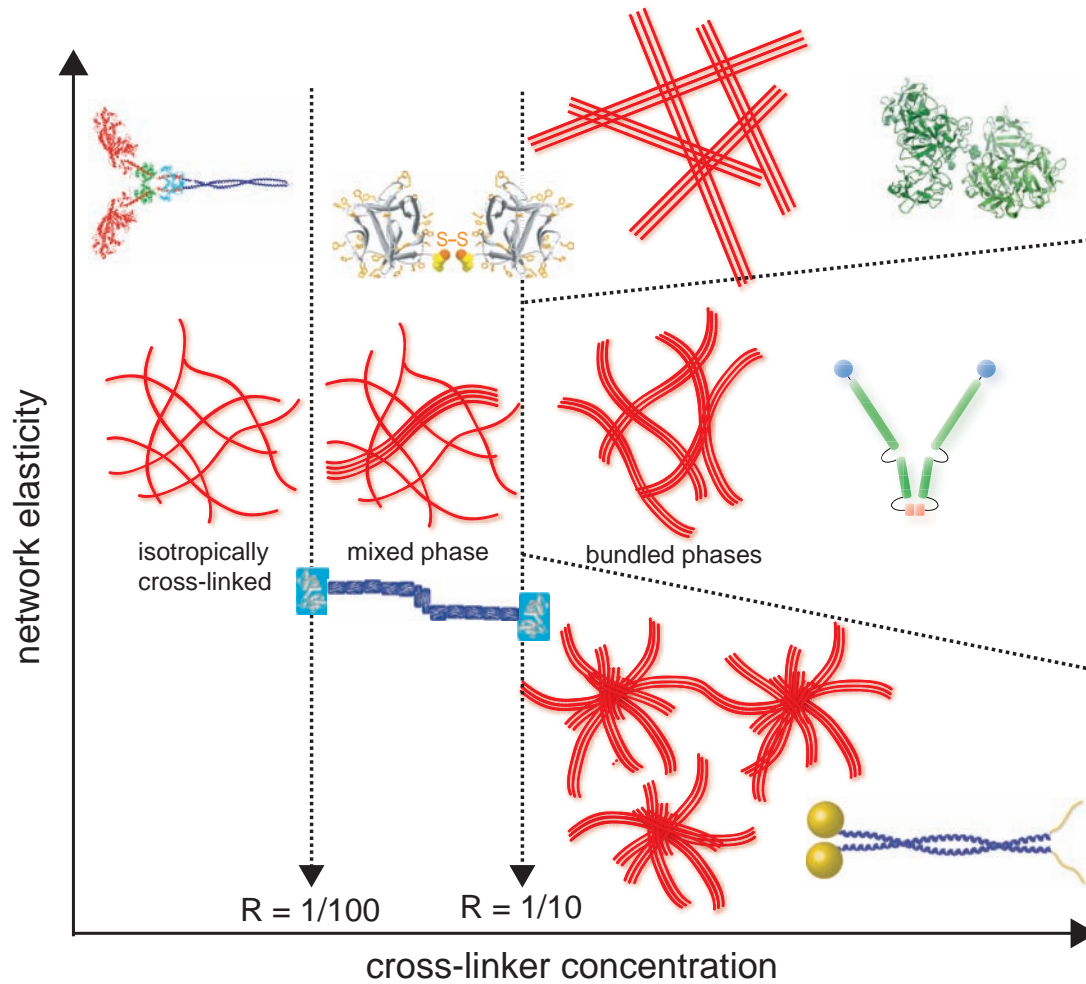
Figure 3.19: Morphological phase diagram of actin networks. The network elasticity varies in dependence of the cross-linker concentration and the structural properties of the used cross-linker. Two phase boundaries are obtained at critical concentrations of the cross-linker. For $R^\star > 0.01$, actin networks are in the composite bundle and single filament phase and for $R^{\star\star} > 0.1$ most cross-linkers have totally bundled the actin filaments. With varying flexibility and glutinousness the cross-linkers drive actin structures in different morphological phases.

some single ABP molecules (e.g. rod domain of ddFln [Schwaiger et al., 2004]) are well studied, a bottom-up strategy appears to offer the promise of bridging the gap between the understanding of properties of single molecules and complex materials. Still a relation between the number of bundles in the network and the absolute elasticity is lacking. So far, analytical theories fail to describe composite networks due to the lack of information about the stress distribution over the heterogeneous structural elements [Heussinger & Frey, 2006]. Recently introduced mesoscopic simulations of such networks appear to offer the promise of quantitatively describing the underlying physical principles [Head et al., 2003, Wilhelm & Frey, 2003].

Overall, with the variation of concentration and architecture of ABPs, cells have access to a huge range of elasticity of their actin cytoskeleton. Finally, the morphological differences of actin networks are resolvable with macrorheological methods down to 300 nm which are common distances of ABPs in the network at the highest measured concentrations of the phase diagramm. For the resolution of smaller inhomogeneities microrheological methods are able to gather further information.

3.3 Cross-Linked Actin Networks under the Impact of Depletion Forces – Specific Cross-Links Hinder Unspecific Buildup of Filamentous Structures

[2]

 In biological tissues crowding is a common phenomenon. Especially cellular environments and the interior of cells generally underlie crowding effects. For example 25 % of the volume of the interior of cells is filled with proteins. Therefrom 10 % are agglomerated in filamentous form whereas the large part resides in globular form. The estimated overall protein concentration in cells ranges between 200-300 mg/ml [Ellis, 2001]. Molecular crowding causes excluded volume effect, which is responsible for several alterations of the properties of biological macromolecules: up to ten fold slow down of diffusion rates, crowding induced protein association, enhancement of protein folding and aggregation as well as enhancement of chaperonin action. In general, depletion forces are forces generated by the gain of excluded volume. Depletion forces developed by PEG polymers, alter the properties of filamentous actin e.g. the polymerization rate and the extent of polymerization [Tellam et al., 1983]. Furthermore depletion forces induce bundling of actin solutions [Hosek & Tang, 2004]. The phase separation in dependence of the depletion agent was already predicted in 1993 [Madden & Herzfeld, 1993]. Alterations on the structure and the viscoelastic properties could be quantified with a simple model consisting of actin filaments and PEG6k solutions [Tharmann et al., 2006]. In cells the actin cytoskeleton does not exist isolated, but interacts with hundreds of macromolecular proteins. Since biological macromolecules like ABP have evolved to function in crowded conditions, depletion forces are not negligible if cellular conditions want to be simulated for the actin cytoskeleton. Still numerous questions have to be addressed. What role do cross-linker molecules play under crowded conditions? What is the impact of molecular crowding on the activity of ABPs? Are specific cross-linkers tuners of the morphology of filamentous actin networks?

---

[2]For all following measurements in this chapter, the length of the single actin filaments were controlled with gelsolin to a mean length of $\langle l \rangle = 21$ μm using eq. 1.1. For different cases it is explicitly mentioned.

3.3.1   Polymerization and ATP Depletion of HMM/PEG-Actin Networks

To address the posed questions from above the ideal cross-linker HMM was used to investigate the influence of depletion forces on cross-linked actin networks. In 1990 it was found that antiparallel filaments in bundles of actin produced by 0.3 %w/v methyl cellulose slide together due to active HMM molecules [Takiguchi, 1990]. Since methyl cellulose contributes in an additive way on the mechanical properties of actin networks [Köhler et al., 2008], the uncritical PEG6k was used to simulate the crowding effect. The mechanical response of pure highly concentrated PEG6k in comparison to pure entangled actin networks is negligible. In fact a 22 %w PEG6k solution has at least a one decade smaller G'' over the measured frequency regime and a not measurable elasticity. The appearance of the rigor state of the HMM motors are detectable due to a
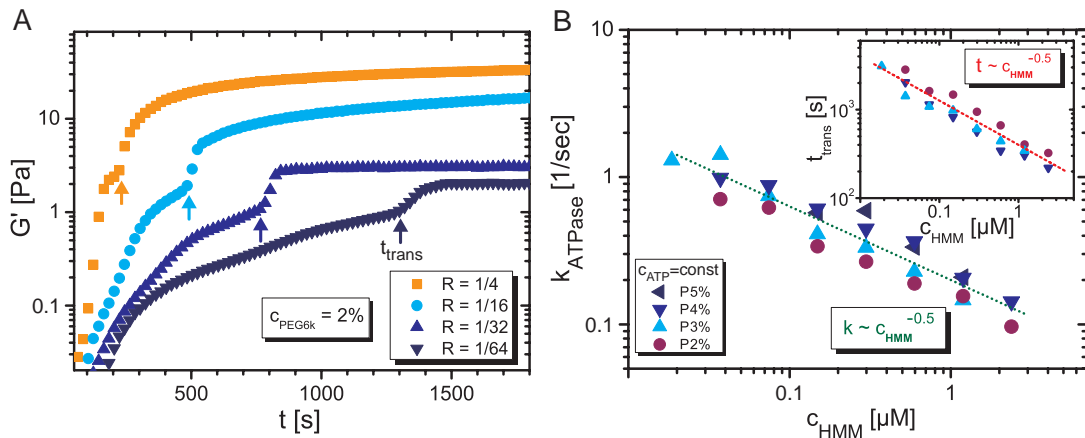
Figure 3.20: (A) *Polymerization curves for PEG/HMM actin networks with $c_a = 9.5 \ \mu M$. The upward pointing arrows indicate the transition time which is used to calculate the ATPase rate.* (B) *ATPase rate plotted versus HMM concentration. PEG has only a marginal influence on the ATPase rate. The rate depends on the HMM as well as ATP concentration. In the inset, the transition time shows a nonlinear decrease with increasing HMM concentration.*

sudden increase in G' at a time t_{trans} during the polymerization (fig. 3.20A). Extracting t_{trans} from polymerization curves and using the following equation [Keller, 2003]:

$$k_{ATPase} = \frac{c_{0,ATP}}{c_{HMM} \cdot t_{trans}} \tag{3.9}$$

The ATPase rate k_{ATPase} was calculated for PEG6k concentrations of 2 to 5 %w in dependence of the HMM concentration (fig. 3.20B). For a fixed ATP concentration in

the sample solution (which originates from the ATP containing G-buffer) the ATPase rate does not decrease linearly with increasing HMM concentration. For concomitant large HMM and small initial ATP concentrations the binding sites for ATP is hindered by ADP in the HMM molecules and prolonged association on the filaments, resulting in decelerated ATPase rate. Astonishingly, the presence of PEG6k has only a marginal influence on the ATPase rate of HMM. The absolute values for the transition times are comparable to values for solutions without PEG6k [Keller, 2003].

For PEG/HMM actin networks with $c_{PEG6k} = 6,7\,\%\,w$ and R $> 1/64,128$ the poly-
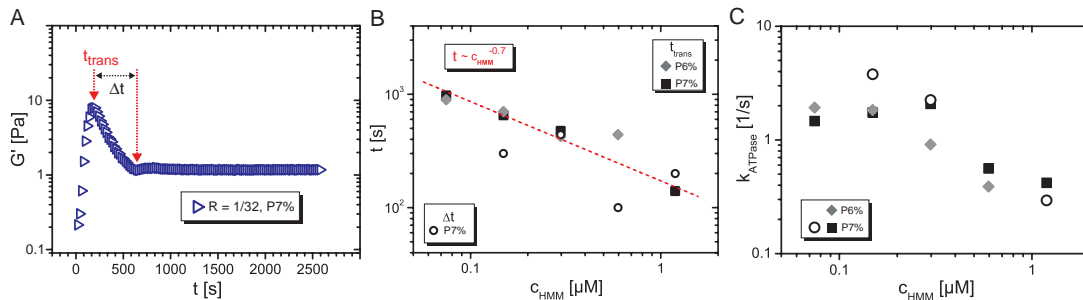
Figure 3.21: (A) *Polymerization course for a PEG/HMM actin network beyond the phase transition boundary shows a nova like behavior.* t_{trans} *is defined in analogy to the definition in fig. 3.20A. The red arrows indicate the crossover time which is the time difference between elasticity breakdown and steady state.* (B) *Transition and crossover time in dependence of* c_{HMM} *for two PEG concentrations.* (C) *Although the time course of the rigor transition of* G' *is inverted for PEG6k concentrations* $> 6\,\%\,w$, *the ATPase rate has the same values as for 2-5 %w PEG6k.*

merization runs a special course with time (e.g. fig. 3.21A). Initially the G' evolves very fast like for all other actin networks under depletion forces. But instead of running into a plateau value, the measured G' descends suddenly at a time t_{trans} before it equilibrates. This nova-like burst of G' is indicated by the red downward pointing arrow (fig. 3.21A). What is responsible for this special polymerization behavior and how can it be explained at a molecular level? In fig. 3.21B, t_{trans} reveals a decrease with increasing HMM concentration. The nova-like event happens earlier at high motor concentrations. The time difference Δt between t_{trans} and the beginning of equilibrium ranges between 100-400 s. In analogy to the rigor transition at 2-5 % PEG6k the ATPase rate was calculated with the values of fig. 3.21B. Comparing the ATPase rate of fig. 3.20B with the values in fig. 3.21C shows that only the time course of G' is inverted but the rates stay the same. What is the reason for the observed behavior and is it possible to explain the effect on the micrometer scale? In some *in vitro* Biopoly-
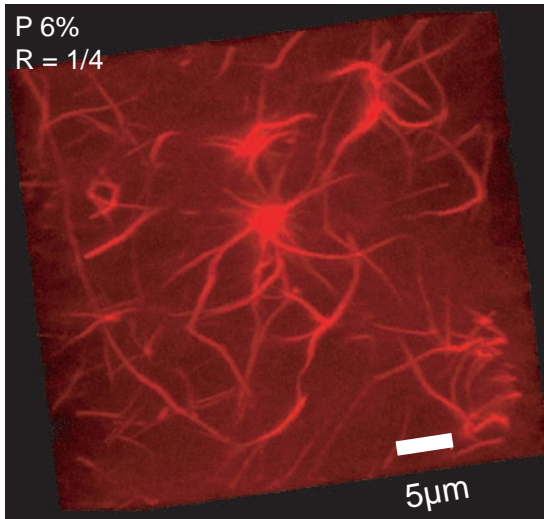
Figure 3.22: (*A*) *3D fluorescence image (white scale bar 5 μm). Example of an aster consisting out of actin filaments (c_a = 9.5 μM) formed at high PEG6k and HMM concentrations.*

mer systems similar effects have been observed. Generally star-like shapes of filament arrangements, so-called asters, are abundant *in vivo* as well as in different *in vitro* systems of stiff biopolymers in the presence of molecular motors in single or filamentous form. For example nova-like light intensities during aster formation in myosinII fascin-bundled actin networks in a special concentration regime $(1/14 < R_{myosinII/actin} < 1/7$ and $R_{fascin/actin} > 1/14)$ could be observed [Bakouche et al., 2006]. Another example is actin filament sliding in the presence of methyl cellulose resulting in filament agglomerations at certain concentrations of active HMM $(R_{HMM/actin} > 1/16$ and $c_{methylcellulose} = 0.3 \,\%\,\text{w/v})$ [Tanaka-Takiguchi et al., 2004].

In HMM/PEG networks during the transition from the maximum G' to the equilibrium G' value, ATP is completely depleted. Most of the HMM molecules are already in rigor state. Only a few HMM molecules still convert ATP and are in active state. Two possible scenarios are conceivable: active transport of filaments [Uhde, 2004, Tanaka-Takiguchi et al., 2004] or a trapped, out of equilibrium polymerization state, after complete ATP consumption. Both possibilities end up in networks which contain large aster inhomogeneities. Those networks show low overall network elasticity if the aster assemblies are not interconnected. In fig. 3.22 a large aster inhomogeneity is shown exemplarily for large PEG6k and HMM concentrations. To decide whether during Δt filament sliding happens or not, fluorescent microscopy movies need to be recorded.

Similar to the observation in the myosinII/fascin actin networks or the HMM/methylcellulose actin networks, the nova like G' evolution of the HMM/PEG

networks show that a concurrently high enough bundle thickness (which determines the bundle stiffness of the filaments) and a certain active cross-link density are prerequisites for aster formation and filament sliding. The relation of bundle stiffness and motor/active cross-link density is restricted to a small regime for observing these effects. For the active-HMM/PEG actin networks the bundle thickness to line density ratio for occurring G' novas is: $\frac{D_B}{\rho_l} > 0.5$ (6-7 %w conforms to a bundle thickness of about 100 nm [Tharmann, 2006] and R = 1/64 results in a theoretical line density of HMM molecules of 180 nm).

Since the binding affinity of HMM is largest without ATP these measurements were repeated with complete absence of ATP in the solution (in F- as well as in G-buffer, see tabs. chap. 6.8). With lacking ATP in the sample G' evolves fast till it shows a
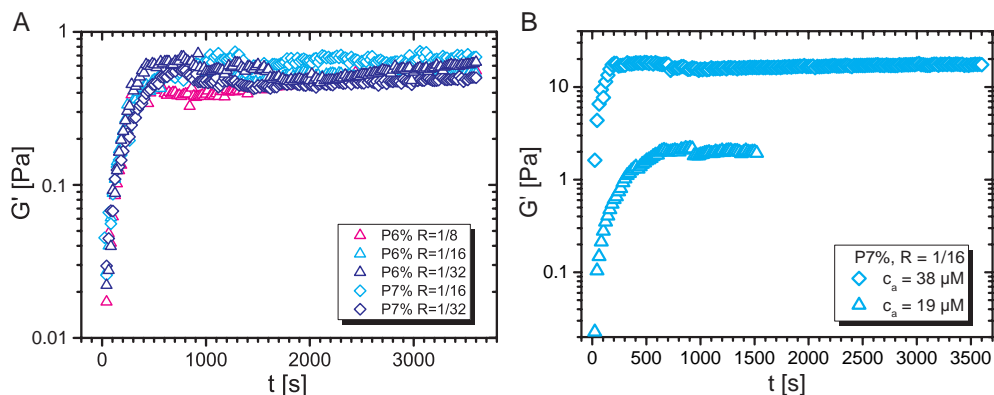
Figure 3.23: Polymerization behavior of mixed PEG/HMM actin networks: (A) *without ATP in the sample solution,* (B) *for high actin concentrations with ATP, at constant HMM and PEG6k concentrations. All concentrations of HMM and PEG6k show no obvious nova like G bursts.*

distinct kink during the time when novas occurred in the presence of ATP (fig. 3.23A). If one imagines that at these PEG6k and HMM concentrations (see fig. 3.23) the formation of aster-like structures leads to a nonpercolation transition of bundles in the whole network system, the missing interconnections of the asters would lead to a decreased elasticity of the material. As soon as filaments are polymerized long enough they are trapped with HMM in aster structures before they can form longer bundles. Consequently the elasticity never increases up to higher values. For pure cross-linked HMM/actin networks as well as for pure PEG/actin networks the maximum elastic modulus is shifted to lower HMM concentrations with increasing actin concentration [Tharmann et al., 2007, Tharmann et al., 2006]. Therefore one can assume that the phase boundaries in the composite HMM/PEG actin networks are postponed equally

to lower $R_{HMM/actin}$ and c_{PEG6k} with increasing actin concentration. In fact for actin concentrations of $c_a = 0.8$ and 1.6 mg/ml the nova like evolution of G' was not observed at R = 1/16 and $c_{PEG6k} = 7\%$w and G' increased steadily running into a constant value in contrast to 0.4 mg/ml at the same HMM and PEG6k concentration (fig. 3.23B).

3.3.2   Morphology of Passive HMM/PEG-Actin Networks

Pure HMM/actin networks are known to form an isotropically cross-linked phase. Furthermore, PEG/actin networks form bundles of actin filaments, where the bundle thickness increases with increasing PEG concentration. In the cytoskeleton cross-linkers are exposed to depletion forces due to molecular crowding. Therefore it is of interest to resolve the structures of HMM cross-linked actin networks under the influence of depletion forces induced by PEG. Are there different structures beside cross-linked and bundled networks observable for composite HMM/PEG actin networks? For example in nature, dynamic aster structures made out of microtubules are found in mitotic and meiotic spindles of cells [Barton & Goldstein, 1996]. With dark field microscopy aster formation was observed *in vitro* with stabilized microtubule and multi-headed kinesin motors at 1.4 mM ATP and 0.6 mM GTP [Nédélec et al., 1997]. Also, rapid formation of aster-like assemblies of actin filaments with myosin II could be observed in contracting fibroblasts, due to the treatment with cytochalasin D, [Verkhovsky et al., 1997]. Are similar structures observable with a simple basic composite material made out of a non-processive cross-linker and bundled actin filaments *in vitro*? Which role do specific HMM cross-linkers play under crowded conditions in actin networks? For this purpose the structure of composite HMM/PEG actin networks are enlightened with several microscopy techniques.

 Phase contrast pictures were made of mixtures of HMM/PEG actin networks. The HMM concentration was varied from R=1/1024 up to 1/4. For each HMM concentration the PEG concentration was adjusted from 2-10 %w. Three main observations could be made. First, beside the already known structural morphologies like isotropically cross-linked actin networks and bundled actin networks so-called asters were found for a critical concentration of HMM. For each HMM concentration the critical value depends on the PEG6k concentration. Secondly, for $c_{PEG6k} = 4\%$w and R < 1/32 as well as for $c_{PEG6k} = 6\%$w and R < 1/64 no bundled actin filaments could be observed, whereas without HMM actin networks (containing 4-6 %w PEG6k) are clearly in the bundled phase. At last, for high PEG6k concentrations $c_{PEG6k} > 8\%$w
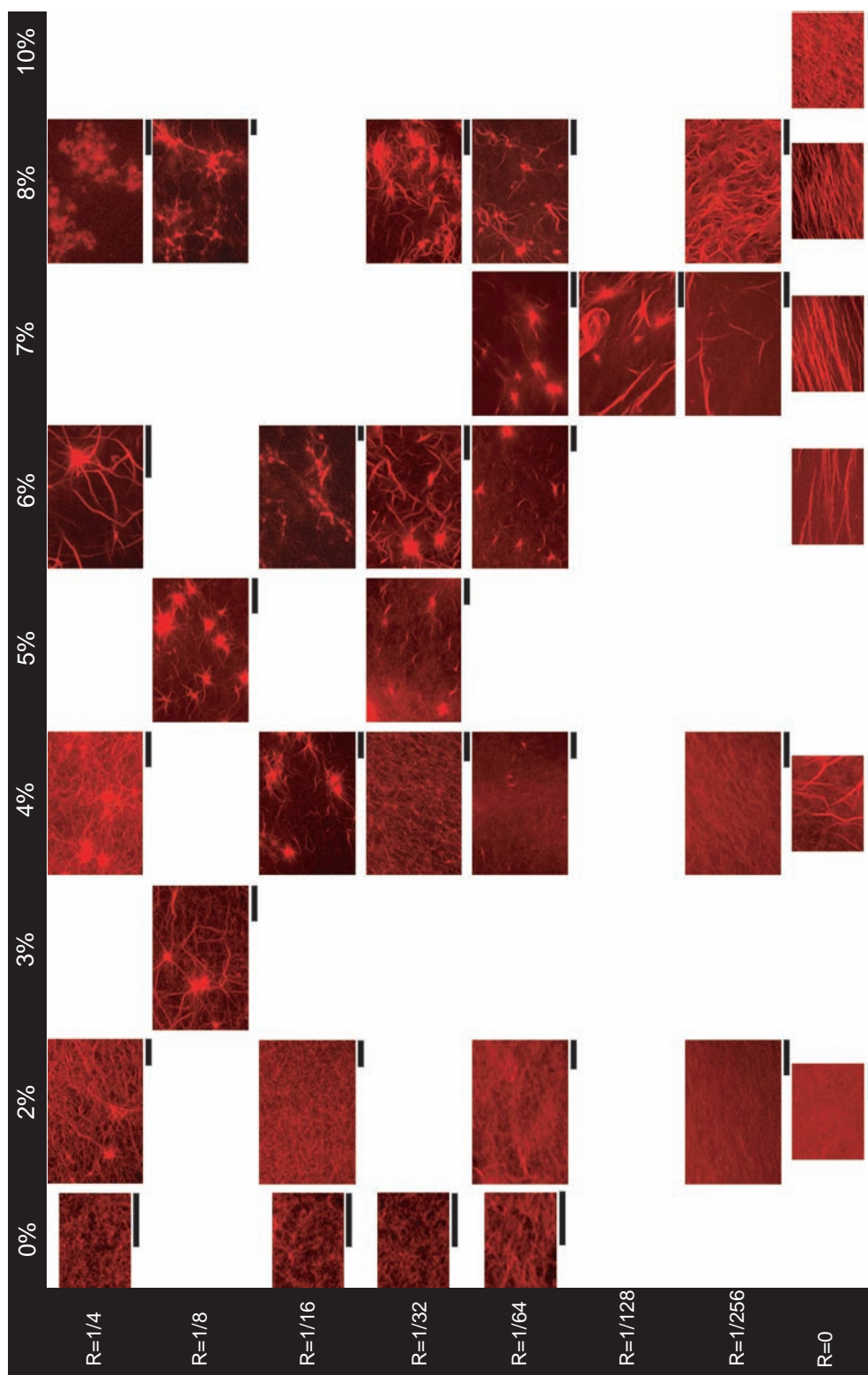
Figure 3.24: Fluorescence images, recorded with the confocal microscope (see chap.2.1.1) of cross-linked (HMM) actin networks (c_a = 9.5 μM) under depletion forces (PEG6k) arranged in a phase diagram. Scale bars represent 10 μm.

with simultaneous high HMM concentrations protein agglutination was observed finally ending up in a macroscopic phase separation.

To enhance the obtained phase diagram, fluorescence images with the confocal microscope (chap. 2.1.1) were recorded. In fig. 3.24 the whole phase diagram for an actin concentration of 9.5 μM is imaged. From the arranged phase diagram a clear aster crossover can be observed. The boundary paces the diagram from $c_{PEG6k} = 2$ %w and R=1/4 to $c_{PEG6k} = 8$ %w and R=1/256.

The difficultly resolvable structures below the aster transition were enlightened by
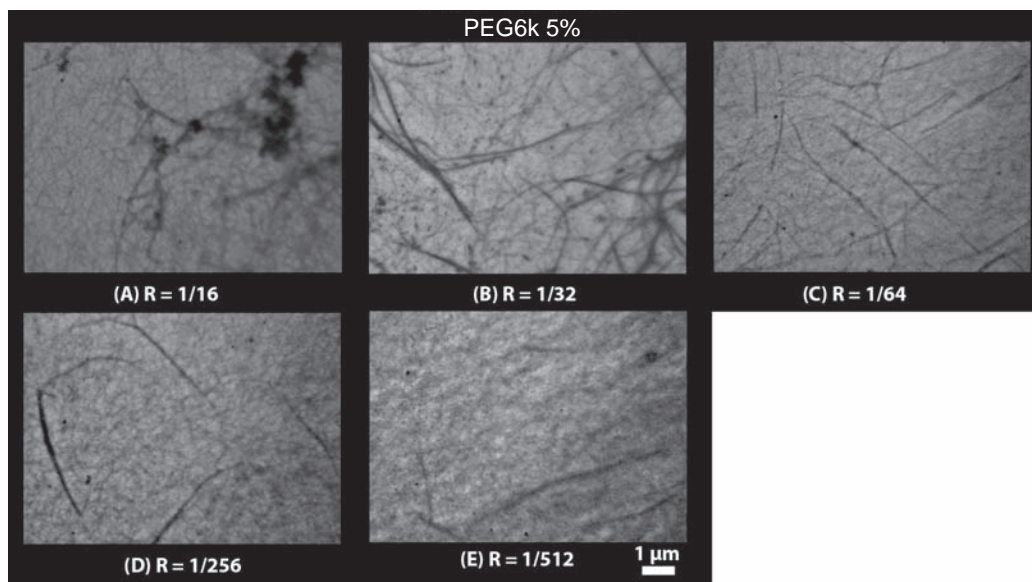
Figure 3.25: EM pictures of actin networks ($c_a = 9.5$ μM) cross-linked with HMM at a constant depletion force. With rising HMM concentration the number of bundles is increased.

TEM images in this concentration regime. Fig. 3.25 shows a mixed phase. Cross-linked actin networks containing a certain amount of actin bundles are observed at a constant PEG6k concentration of 5 %w. With increasing HMM concentration the number of bundles increases. For R $\geq$ 1/32 asters occur. Interestingly the onset of the bundle crossover, seems to depend on the HMM concentration. From this pictures it seems that at a fixed PEG concentration the aster density is controlled by the HMM motor concentration. Without any HMM molecules the bundle crossover was determined for this actin concentration to occur between 2-4 %w.

In sum all observations of the three imaging techniques are condensed to a fully illustrated phase diagram (see fig. 3.26) which describes the two created morphological structures of the composite HMM/PEG actin networks. The orange shaded mixed
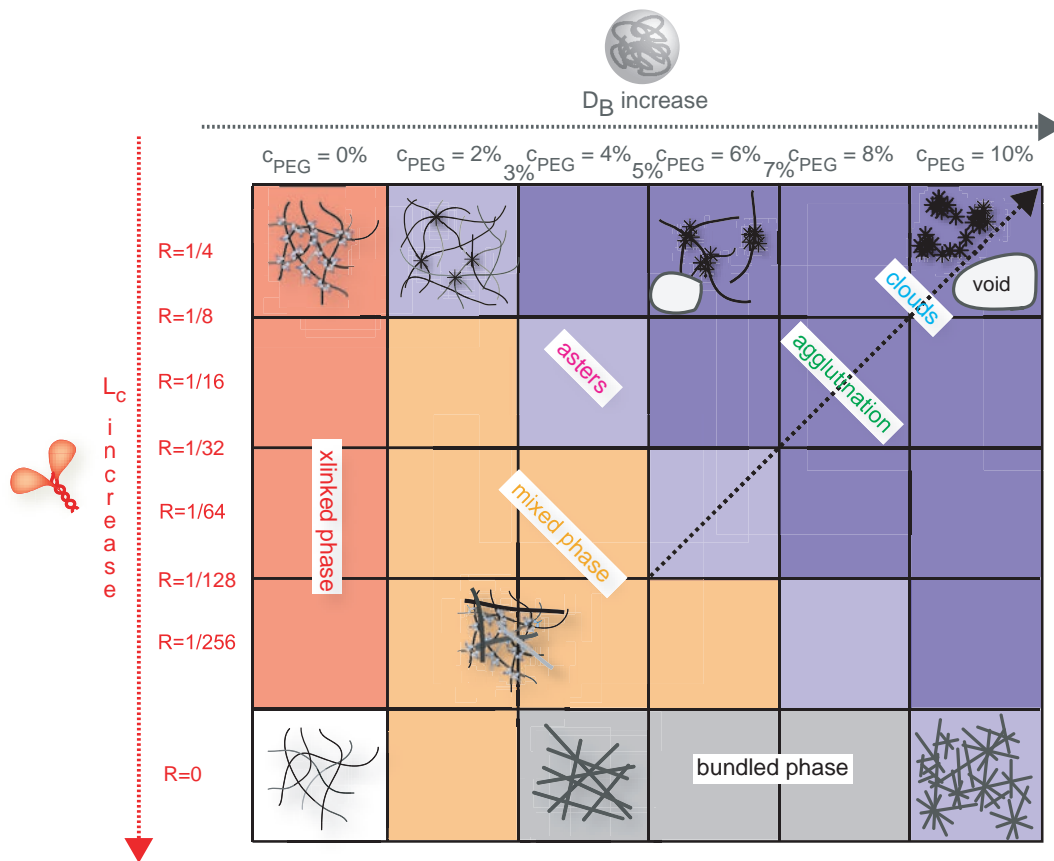
Figure 3.26: Illustration of the observed phase diagramm for the HMM/PEG actin networks. The black arrow depicts the direction of the aster growth in the phase diagram.

phase and the aster phase (blue shaded area). From the obtained pictures (figs. 3.24, 3.25), the aster transition can be parameterized by the following equation:

$$\log R \sim 0.3 \cdot c_{PEG6k}[\%w] \tag{3.10}$$

With increasing HMM and PEG concentrations enlarged voids in the gel solution appear. This implies an aster growth which is indicated with the black arrow in fig. 3.26. Thus the question arises, whether the number density and size of asters really do increase with increasing HMM and PEG concentration in the aster phase. Since quantification of the number of asters or aster size in dependence of the HMM and PEG concentrations is a difficult and elaborate task, macrorheological methods first were applied in order to extract the mechanical response of the networks.

3.3.3 Rheology of Passive HMM/PEG-Actin Networks

Linear Response of Passive HMM/PEG-Actin Networks

For quantification, macrorheological experiments were performed with the HMM/PEG actin networks at the same actin concentration of 9.5 μM as used for the structural investigations. After ATP depletion HMM strongly binds to actin filaments (rigor state), acting as passive cross-linker molecules and forming highly viscous gels with pronounced strain hardening ([Tharmann, 2006, Tharmann et al., 2007, Luan et al., 2008]). The viscoelastic properties of this isotropically cross-linked actin networks are dominated by a single length scale parameter, the cross-linker distance l_c. This parameter decreases with increasing HMM concentration [Tharmann et al., 2007]. In this case, entropic stretching of filaments between two cross-linking points dominates the elastic behavior, following the scaling law in eq. 1.24. Further it is already known that depletion forces bundle actin filaments (chap. 1.4.2). The mechanical properties of networks of bundled actin filaments produced with depletion forces depend on the degree of cross-linking and the bundle thickness D_B [Tharmann et al., 2006]. Both observations give rise to the question if there are similar dominating length scale parameters in composite HMM/PEG actin networks.

For a better interpretation, the absolute shear modulus and the apparent loss angle φ are shown in the following figure (3.27) on the left and on the right side, respectively. In order to understand the viscoelastic properties of the composite
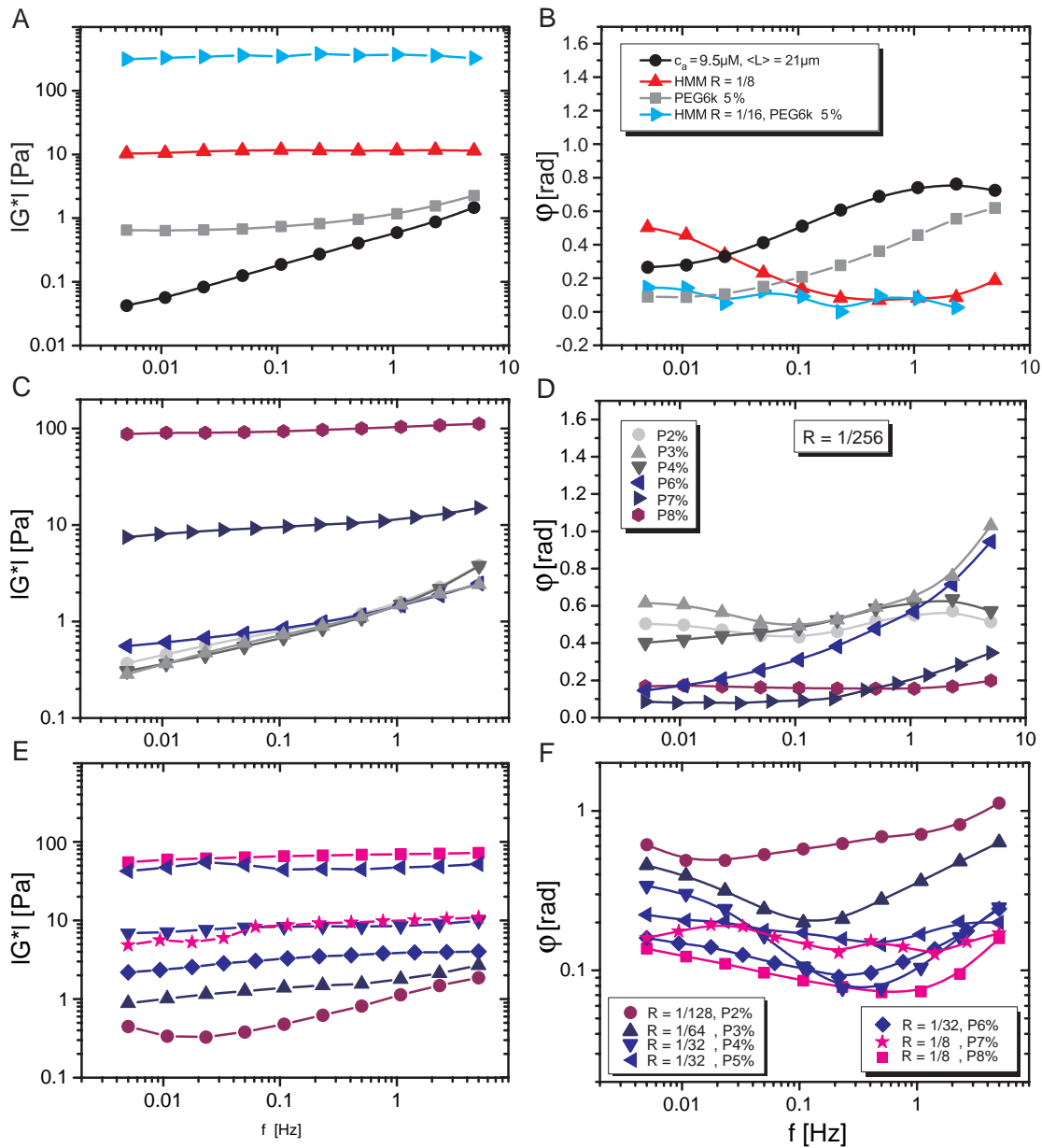
Figure 3.27: (A, C, E) *Frequency spectrum of the absolute value of the shear modulus.* (B, D, F) *corresponding loss angle plotted over the frequency.* (A, B) *Comparison of an entangled* (c_a = 9.5 μM), *bundled* (c_{PEG6k} = 5 %w), *cross-linked* ($R_{HMM/actin}$ = 0.125) *and composite HMM/PEG actin network* (c_{PEG6k} = 5 %w, $R_{HMM/actin}$ = 0.0625). (C, D) *Impact of PEG at constant HMM concentration.* (E, F) *Examples for different phases produced by PEG/HMM actin networks.*

HMM/PEG actin network the viscoelastic behavior of the single components are compared (fig. 3.27A, B). The common linear frequency response of pure entangled actin slightly decreases with decreasing frequency and the loss angle shows the typical horizontal s-shape (black dots, fig. 3.27A). Under the influence of 5 %w PEG6k the shear modulus runs into a constant value and φ is lower as for the actin network, going nearly to zero for frequencies lower than 0.1 Hz (grey squares). These observations are typical for filaments under PEG6k concentrations larger than 4 %w because filaments in the network are bundled. Cross-linked actin networks with HMM have a totally flat shear modulus in their frequency spectrum. φ has a minimum at 0.7 Hz with an adjoining rise towards low frequencies reaching the maximum value at 0.005 Hz (red upward pointing triangles). The minimum in the frequency spectrum of φ is related to the HMM molecule unbinding from the filament [Tharmann et al., 2007, Lieleg & Bausch, 2007]. In General, this minimum reflects a clear fingerprint for cross-linker unbinding in the networks. In case of HMM/PEG actin networks this minimum shows the finite association constant of the HMM cross-linker. Finally, the composite PEG/HMM actin network is elastically dominated for all frequencies (cyan right pointing triangles). Consequently, the loss angle is constantly lower as 0.2 over the whole frequency spectrum. Even unbinding of the HMM molecules does not dominate any longer. In sum, with every step of further complexity the $|G^\star|$ at 5 mHz rises roughly at least one decade in absolute value (fig. 3.27A).

Increasing the PEG6k concentration from 2-8 %w at constant HMM concentration, one can observe the bundle crossover taking place between 4 and 6 %w. The effect is clearly visible in the frequency behavior of the loss angle (blue left pointing triangles in fig. 3.27D). The slight minimum resulting from HMM cross-linker unbinding (R = 1/256) is first smeared out with increasing PEG6k concentration till bundles start to dominate the viscoelastic behavior. Here, the loss angle lies below 0.2 over the whole frequency range, which is similar to values of the cytoskeleton. From measurements on varying cell types with different experimental methods it was obtained that the loss angle nearly stays constant in a range of 0.2-0.4 for lower frequency decades [Trepat et al., 2008]. This implies that composite HMM/PEG actin networks, used as an *in vitro* basic simple model system, mimick in principle cytoskeletal networks.

In fig. 3.27E and F the HMM and PEG concentration is increased simultaneously in the actin networks. With increasing HMM concentration the minimum of the loss angle gets more pronounced. Additionally, with increasing PEG6k concentration the mini-

mum broadens which indicates bundling domination and suppressed HMM unbinding events. Interestingly $|G^\star|$ does not overshoot a certain value. The strongest gels which are formed have certain PEG and HMM concentrations (R = 1/4, 1/8 and $c_{PEG6k} = 4$, 5 %w, figs. 3.28, 3.29).

Therefore the elasticity of these gels is evaluated with the parameter G_0 plotted versus PEG6k concentration as a series of different R values[3]. An effective bundle transition and points of the maximum G_0 can be extracted from fig. 3.28A for all PEG concentrations. The bundle transition is determined as the crossover from a slight to a steep increase of G_0 with increasing PEG concentration. The steep slope of G_0 for R
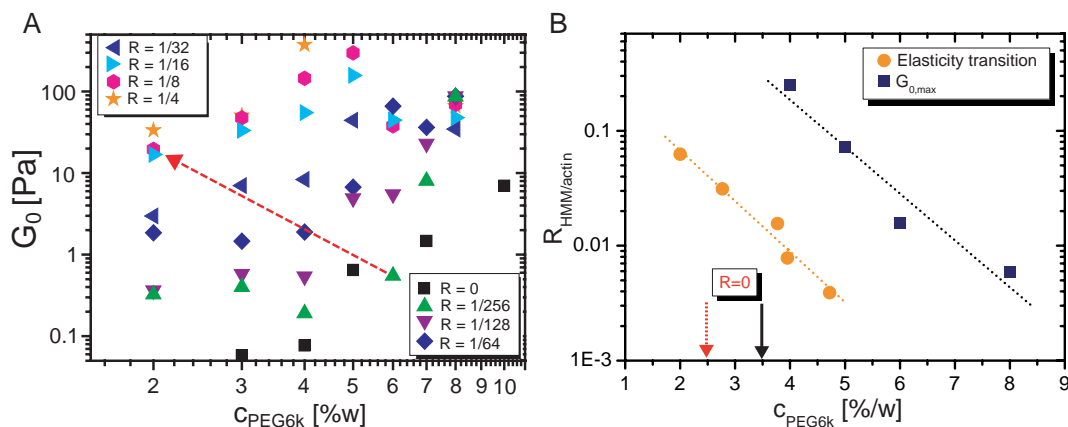
Figure 3.28: (A) G_0 *values (at the minimum position of G'') shown for all HMM concentrations in dependence of the PEG concentration. The elasticity crossover of the pure PEG actin networks is shifted with varying HMM concentration, indicated with the red arrow.* (B) *points for the elasticity cross over and the maximum elasticity for each PEG6k and HMM concentration. The red dashed arrow depicts the transition for R = 0 [Tharmann et al., 2006]. The black arrow illustrates the assumed transition from* (A), *which is in accordance with the microscope pictures of chap. 3.3.2.*

= 1/256 sets in at 5 %w (green upward pointing triangles fig. 3.28A). With more and more HMM molecules in the network this onset is shifted to lower PEG6k concentrations. Concomitantly, with rising R the absolute value of G_0 increases and consequently the transition from a flat regime of G_0 to a steep slope is shifted up and to the left (red arrow in fig. 3.28A). The crossover contains a large uncertainty at low PEG6k and concomitant high HMM concentrations. This uncertainty results from the highly error-prone beginning of the steep slope for R > 1/16. Plotting the points of maxi-

---

[3]G_0 is the value of G' at the frequency where G'' is minimal similar to the definition in chap. 1.1.2, fig. 3.28

mum G_0 value (navy squares) and bundle transition points (orange dots) for every R in a phase diagram one remarkable observation can be stated (fig. 3.28B). Instead of shifting the transition from the initial value of about 3 %w (arrows in fig. 3.28B) it sets in at the doubled PEG6k concentration in the presence of HMM molecules with a concentration of R = 1/256. For outstanding R values (R ≤ 1/128) bundling by depletion forces is hindered by the specific HMM cross-linker molecule. This implies that although depletion forces are acting on actin filaments, the whole actin network is dominated by big HMM proteins. Interestingly the extracted bundle transition of fig. 3.28B follows nearly the same scaling as the transition for the maximum G_0, only shifted downwards to 0.4-4 Pa.

The outstanding benefit of the macrorheological method is that the viscoelastic behavior of the networks as well as the phase transition can be determined using the obtained elasticity of the network samples as a measure. In combination, microscopical and rheological methods are able to describe a full phase diagram of PEG/HMM actin networks (fig. 3.29). The different morphological appearances, e.g. asters (fig. 3.22), and the resulting viscoelastic properties are represented with distinct symbols in the graph. Accordingly, by implementing complex bundle structures elasticity of actin networks are boosted by a factor of 10-100. Networks with the highest elasticity were observed for R =1/4, 1/8 and c_{PEG6k} = 4, 5 %w. Since the measured elasticity for those two concentrations are similar to fascin actin networks at the same actin concentration [Lieleg et al., 2007], the question arises if cross-linked bundles percolate through the network. From microscope pictures it appears possible in this case, that asters are interconnected throughout the whole network. These observations are a hint for dominance of a certain length scale parameter in respect to the elastic properties. Above the aster transition two possibilities are left: first, the bundle thickness and the mean distance between cross-linked intersection points of bundles are the important length scales. Or secondly, the mean distance between larger inhomogeneities like asters is responsible for the elastic property of the network. In the last case the elasticity is lower as for the first case, when the mean distance is increased with increasing HMM or PEG concentrations.

Converting the PEG6k concentration values from %w unity to mol/l (taking a density of 1.08 mg/ml for a PEG6k solution of 40 %w and a mean molar mass of 6000 Da) the following scaling law from a fit to the data points of fig. 3.30 is obtained:

$$c_{HMM} \cdot c_{PEG6k}^3 \sim 10^8 \cdot c_a^4 \Rightarrow c_{HMM}^{\frac{1}{4}} \cdot c_{PEG6k}^{\frac{3}{4}} \approx 100 \cdot c_a \qquad (3.11)$$
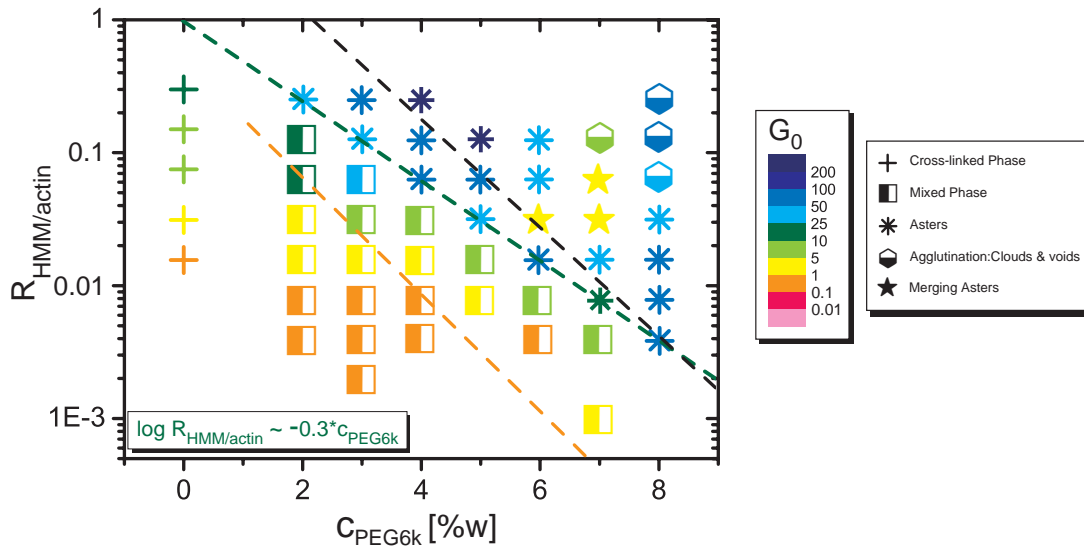
Figure 3.29: Phase diagram of PEG/HMM actin networks. The macrorheological data is combined with structural observations of phase contrast, fluorescence and TEM microscopy (see fig. 3.24). The phase transitions are indicated with the scaling laws corresponding to fig.3.28. A clear phase transition (indicated by a green dashed line) occurs from cross-linked and bundled actin networks to complex and inhomogeneous structures, so-called asters. The elasticity transition is depicted with an orange dashed line and the maximum elasticity crossover is represented by a black dashed line.
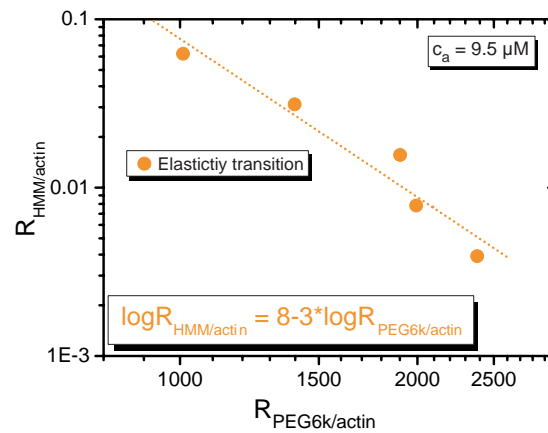
Figure 3.30: *Rescaled logarithmic plot of fig.3.28B. The molar ratios of the PEG6k to actin concentrations were calculated using a PEG6k density of 1.08 mg/ml. The dotted line represents a fit to the data points.*

This can be done because up to this transition the structure of the actin networks is very homogenous. Comparing the known bundling crossover for natural occurring ABPs (see fig. 3.18) which happens at $c_{ABP} \approx 0.01 \cdot c_a$ (cf. fig. 3.18) with the obtained constraint for the unspecific one, it turns out that specific cross-linkers are several orders of magnitude more effective in bundling of actin filaments as unspecific ones. Consequently, cells need only a small amount of specific cross-linker molecules to equalize the unspecific depletion forces. A small amount of ABPs, which have considerably small on and off rates, are enough for cells to escape from molecular crowding catastrophe of their cytoskeletal filaments.

Nonlinear Response of Passive HMM/PEG-Actin Networks

Often cells are exposed to large stresses originating from interactions with their environment. Cells spontaneously respond to extracellular elasticity or develop tension on substrates *in vitro* [Wrobel et al., 2002, Bischofs & Schwarz, 2003]. Therefore the cytoskeleton of cells is responsible for cell mechanics and is involved in mechanosensing ability of cells [Weitz, 2004]. Consequently, the influence of high forces on actin networks is of great interest. In order to withstand high forces, the actin cytoskeleton is cross-linked. Under the impact of molecular crowding, a small amount of specific cross-linkers are used to fortify the actin networks at low forces in the linear response regime. What properties do composite HMM/PEG actin networks show for large applied strains?

From constant shear rate experiments K is derived following eq. 2.9. At a constant PEG6k concentration of 5 %w, two observations are made (fig. 3.31A): the linear part of the modulus rises with increasing HMM concentration accrodingly to G_0. Surprisingly the hardening behavior (which sets in at about 10 % strain) simultaneously turns into strain weakening. This behavior was also observed in bundled fascin/actin networks [Lieleg et al., 2007]. To decide whether an increased bundle stiffness or a decreased cross-linker distance is responsible for the observed strain weakening microscope pictures have to be considered. Furthermore, for the composite HMM/PEG actin network a mixture of both possibilities is conceivable similar to α-aktinin/actin networks [Lieleg, 2008]. Regarding the TEM pictures of fig. 3.25 one can conclude that bundles dominate at this PEG6k concentration the mechanical response. At high HMM concentrations large bundle clusters occured. Consequently the strain weakening could originate from cross-linker breakage between bundles and filaments or from
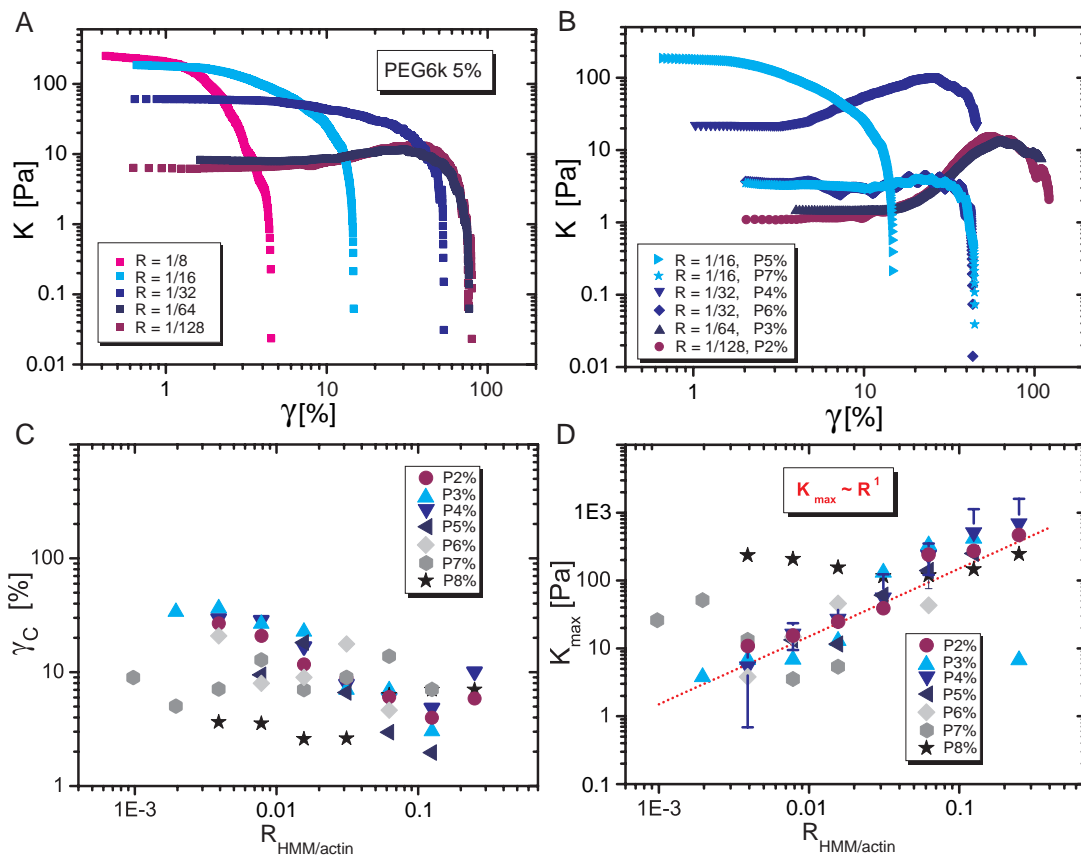
Figure 3.31: (A) Constant shear rate experiments ($\dot{\gamma} = 12.5$ %/s) with a constant PEG6k concentration and varied HMM concentrations. (B) Example curves for the different phases of fig. 3.29. (C) Critical strain and (D) maximum K, extracted from the constant shear rate experiments for all HMM and PEG concentrations. For the most PEG/HMM actin networks one could observe a linear relation of the maximum K in dependence of the HMM concentration, depicted by the red dotted line. In case of strain weakening, the maximum K modulus coincides with the linear K modulus.
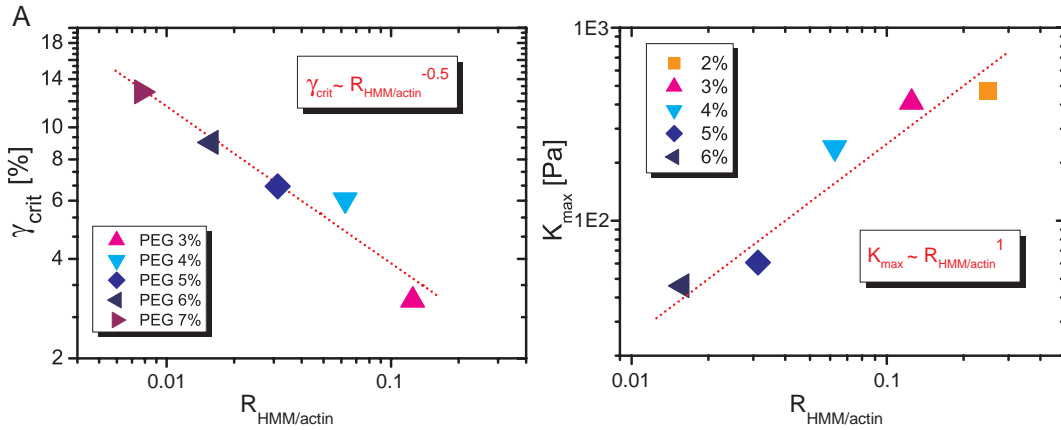
Figure 3.32: For successively increased R and concomitantly decreased PEG6k concentration γ_{crit} decreases with $R^{-0.5}$ (A), whereas the K_{max} scales linearly with R (B).

breaking of interconnections between large bundle clusters. Plotting K versus strain (fig. 3.31B) for low PEG and HMM to high PEG and HMM concentrations, networks of the mixed phase show a clear strain hardening (c_{PEG6k} = 2-4 %w and R = 1/128-1/32). In this phase the filaments in the networks still can be stretched between cross-links before they unbind or break. Also, bundles barely occure which have a higher flexibilty and for which bending is energetically unfavorable. Across the aster transition, for medium PEG6k concentrations (c_{PEG6k} = 5 %w and R = 1/16) a high linear elasticity is obtained with concomitant strain weakening behavior. For high PEG6k concentrations and HMM concentrations above the aster line (c_{PEG6k} = 6-7 %w and R = 1/16-1/32) the aster dominated structures have a lower linear elasticity as the bundled structure. They do not show a hardening behavior in comparison to the mixed phase, which seems to be cross-link dominated.

Moreover, the critical strain was derived from constant shear rate experiments by a linear fit on the low strain regime and extracting the value at the point where the stress strain curve deviates more than 10 % from the linear fit. For PEG6k concentrations of 2-5 %w the critical strain decreases with increasing HMM concentration (fig. 3.31C). With exceeding PEG6k concentration of 6 %w γ_{crit} stays more or less constant. A similar observation is also made for the maximum K modulus (fig. 3.31D).

On the aster line of the phase diagram (fig. 3.29) K_{max} and γ_{crit} show distinct scaling behaviors in dependence of the HMM concentration (see fig. 3.32). While a linear increase with R of K_{max} (fig. 3.32B) is obtained, γ_{crit} decreases with increasing R (fig. 3.32A). Pure bundled actin networks formed with fascin show a linear

decrease of γ_{crit} with the fascin concentration [Lieleg et al., 2007], contrary to the aster dominated PEG/HMM actin networks which reveal a weaker dependence of γ_{crit} with HMM concentration. Moreover a decrease of γ_{crit} with HMM concentration of isotropically cross-linked actin networks with an exponent of -0.4 were reported [Tharmann et al., 2007]. Again this dependence reflects that the PEG/HMM actin networks are dominated by the HMM cross-linker which is signified with the aster structures. In accordance, the distance between cross-links is still dominating the elastic response below the aster transition.

All in all, the macrorheological and microscopical analysis complementary quantify the mesoscopic structures of actin networks which determine the mechanical properties.

Theoretical Predictions

A phase diagram for the concentration of active molecular motors in dependence of the filament density for semidilute solutions has already been predicted [Liverpool & Marchetti, 2003]. In this study the filaments are modeled as fuzzy rods with a much larger length than their diameter. Four phases are proposed by the model. An isotropic, bundled, oriented and the combined bundled and oriented phase. For small filament concentrations the symmetry breaking structures like bundles and asters occur consecutively with increasing motor concentration. At a certain medium filament density a direct transition from the isotropic to the oriented bundle phase takes place. For high filament concentrations, filaments first are oriented before they form oriented bundles with increasing motor density. Similar to the predictions of Liverpool et al, microscope pictures of the HMM/PEG actin networks show that HMM cross-linkers determine the beginning of the aster phase. Whereas the model proposes an oriented bundle phase such structures were not observed in the composite HMM/PEG actin networks. Moreover, in contrast to the model of Liverpool et al, in this work the filament density was kept constant and depletion forces were varied. In dependence of depletion forces the proposed aster phase is shifted. Therefore, further simulations have to be performed in order to test the measured results of the phase diagram in fig. 3.29.

Chapter 4

Conclusion

"Nature does nothing uselessly.
`Aristotle (384 BC - 322 BC)`

In the previous chapter the influence of the specific cross-linker HMM on actin networks under depletion forces was studied. It turned out that specific cross-linkers are used within the cells cytoskeleton to hinder an unspecific buildup of network structures. Now the question arises whether different cross-linkers fulfill other tasks when acting in crowded conditions in actin networks. In conclusion to the results of chap. 3.2, again the architecture of the numerous cross-linkers should make differences in the morphism of actin networks under depletion forces. In first experiments, ggFln was used to show if a different mode of action appears with cross-linker of distinct diverse architecture.

HMM as well as ggFln are big and heavy molecules. In contrast to the HMM, ggFln is not able to work as an ATPase. Although both molecules have a similar binding affinity in the absence of ATP (cf. tab. in chap. 6.6), they own a distinct different structure. HMM is Y-shaped and dimerizes via a 60 nm long, stable coiled-coil (chap. 1.1.2). ggFln is 160 nm in contour length, V-shaped and dimerizes via one of the 24 Ig-fold domains (chap. 1.1.2).

As shown in detail in chap. 3.2, the structure of cross-linkers determines the morphism of actin networks. Therefore it is of interest to investigate whether distinct cross-linker architectures also differentiate network structures under crowded conditions or not. Since ggFln is known to build a pure bundle phase at high concentrations (chap. 3.2.3, [Schmoller, 2008]), ggFln can be used to relate the effect of depletion forces on cross-linked actin networks to pure bundle structures occurring in cells.
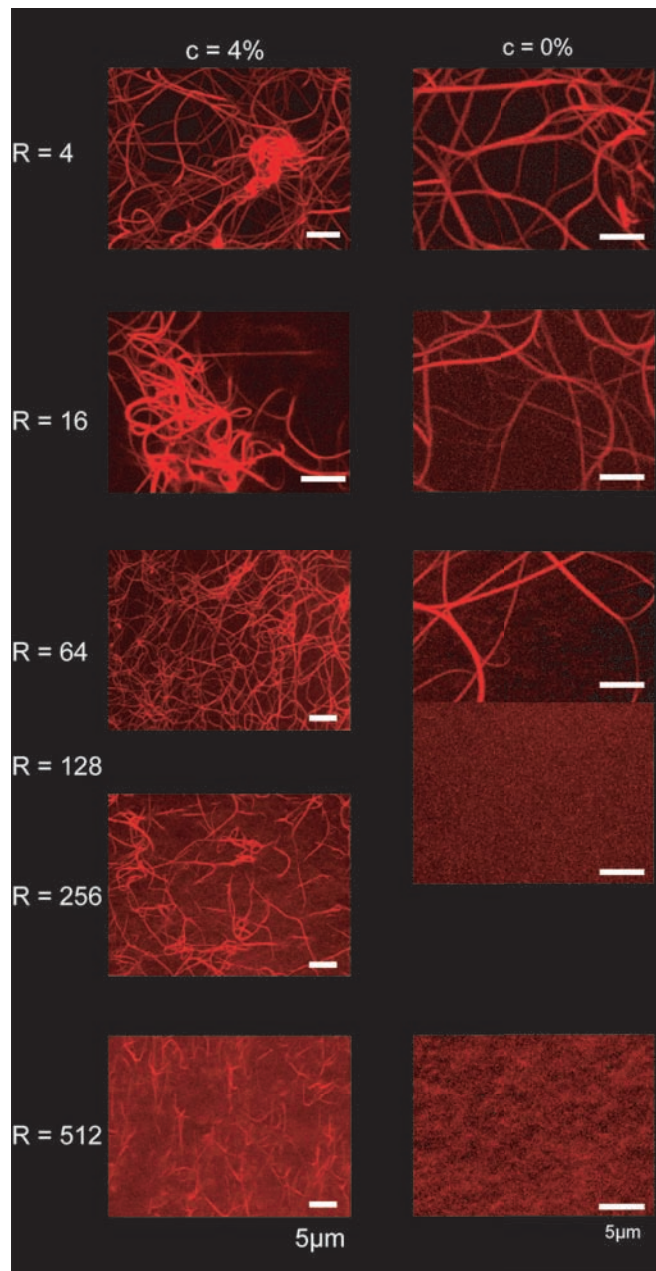
Figure 4.1: *Addition of 4%w of PEG6k to ggFln/actin networks (9.5 μM) sets the bundling crossover one decade down, below R = 1/512. For R > 1/32 large heterogeneities occur. Filamin bundle agglutination into "wool-knots" is observed. The white scale bars represent 5 μm. The bundle efficiency of ggFln is increased by the depletion forces.*

In fig. 4.1, confocal images of pure ggFln/actin networks exhibit a bundling crossover between R = 1/128-1/64. The bundling transition for pure filamin/actin networks was determined with differential interference contrast microscopy and polarization microscopy at R = 1/70 and c_a = 11.9 μM [Hou et al., 1990], which is in good agreement with the presented pictures (fig. 4.1). By addition of 4 %w PEG6k, the bundling crossover is shifted to values below R = 1/512 (fig. 4.1). The results of the pictures in fig. 4.1 are in contrast to the ones obtained with PEG/HMM actin networks (chap. 3.3). Under the influence of constant depletion forces, bundles in the network get more bent and form so-called wool knots with increasing filamin concentration. Further measurements are necessary to determine the phase transition of the wool knots in the whole phase diagram in dependence of the PEG6k concentration. From this preliminary results it can be stated, that in case of the floppy cross-linker ggFln the depletion forces act in an additive way.

In summary, the Y-shaped rigid HMM molecule hinders unspecific buildup of bundle structures, whereas bundle efficiency of the more flexible and V-shaped ggFln is enhanced by depletion forces. Furthermore, it was already shown that the rigid and small dumbbell-shaped fascin cross-linkers dominate the viscoelastic properties and the structure of fascin/PEG actin networks at 4 % PEG6k [v. Olshausen, 2007]. All these observations strengthen the predicted statement.

During evolution, the architecture of cross-linker molecules were optimized to function under crowded conditions in the cells interior. Hence, it is obvious that the cross-linker architecture determines actin network morphism in presence of depletion forces. In relation to the interior of cells, this connotes that already a small amount of cross-linker molecules like ggFln are enough to bundle the actin filaments in order to increase elasticity of the cytoskeletal actin network. Therefore, using cross-linkers with distinct architectures allows living cells to deal economically with material resources.

Chapter 5

Outlook

*"We are still standing in front of the door,
behind great answers are waiting."*
Arthur Schnitzler

Beside the cell cytoskeleton being highly elastic and stiff, the cytoskeleton has to be flexible and adjustable to surrounding pressure as well as internal forces. Therefore mobility between filaments is required. Mobility is accomplished using treadmilling of actin filaments, or molecular motors which interact with cytoskeletal filaments. For example the ATPase myosin II is able to assemble to thick filaments under physiological conditions (chap. 1.1.2). Myosin II filaments can be considered as a physical model system for stiff rods (cf. chap. 6.1). Thus, they are supposed to be well suited to investigate the influence of stiff rods on a network composed out of semiflexible polymers. With composite networks of myosin filaments and actin filaments it would be possible to determine the number of stiff myosin filaments in the network. The motivation of studying such materials could be to obtain a relation between the total number of stiff filaments and the absolute elasticity of the whole network, since such an elementary correlation is still lacking.

Especially during cell division the cytoskeleton has to reorganize. A contractile ring of actin filament structures is observed at the stage of mitosis. There, myosin II filaments as well as the cross-linker cortexillin I are co-localized within the actin network. Still, there is much to find out since composite myosinII/cortexilinI/actin networks have yet to be investigated in detail. Studies of such networks could prove useful to exhibit the principle mechanisms and the origin of contractility during cell contraction and cell division.
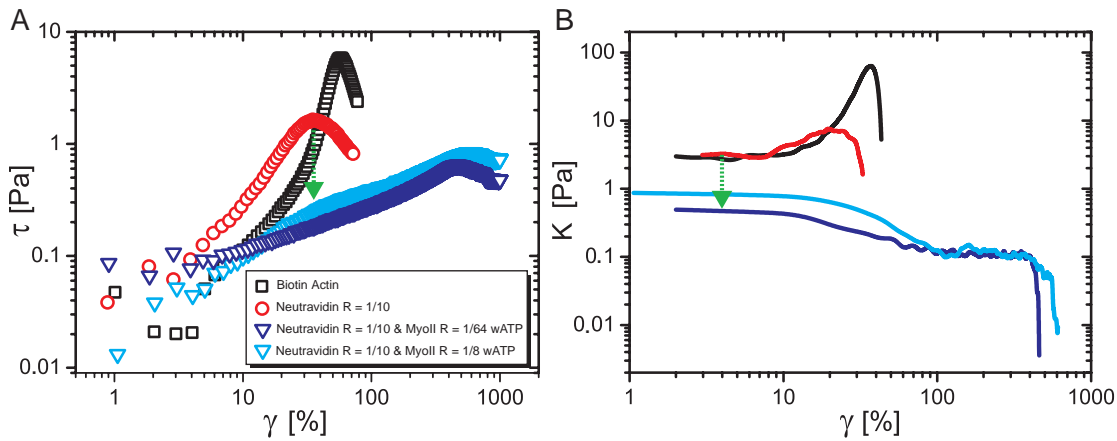
Figure 5.1: (A) *Actin networks with neutravidin cross-linkers are less elastic with active myosin II filaments.* (B) K_{lin} *is decreased and one observes a strain weakening* (*indicated by the green downward pointing arrow*)*. The modulus* K *is derived from this experiments following eq. 2.9*

If myosin II filaments act in bundled actin networks they fluidize the whole network [Humphrey et al., 2002]. This can be observed by performing constant shear rate experiments. K in dependence of strain illustrates the decrease of elasticity in the linear regime with active filaments acting in the network (fig. 5.1B). Bundled and crosslinked neutravidin actin networks strain harden while being sheared (red curve). With addition of myosin II, present already from the beginning of the polymerization process under ATP excess, no strain hardening can be observed (blue curves). The strain weakening behavior implies that cross-link points between bundles or filaments are not formed due to the presence of active motor heads of the myosin filaments embedded between actin bundles and filaments. Consequently, active myosin II filaments are responsible for the strain weakening behavior of the bundled actin network. In comparison to pure entangled actin networks with active HMM (chap. 3.1.2) the more complex system of fig. 5.1 shows the same rheological behavior while performing constant shear rate experiments. The principles learned from these studies are central to gain a deeper understanding of the cells cytoskeleton. Hence, one can state that one possibility for cells is adjusting the ATP concentration in order to switch their cytoskeletal actin networks from highly elastic to fluid gels.

The macrorheological method probes in both cases a lower elasticity of the sample according to a lower cross-link point density compared to the networks without molecular motors being present already in the beginning of the polymerization. Un-

fortunately, direct filament transport or reorganization of networks during polymerization under ATP consumption are not observable by macrorheology since such effects averages in the overall elastic modulus. Optical microscope techniques are better suited to do this. Recently, microtubules (MTs) were used as micromechanical probes in active myosinII/actin networks using bending fluctuations of MTs for analysis [Brangwynne et al., 2008]. Such elaborate approaches are especially useful to resolve the fascinating behavior of active biopolymer networks. For example with two-color labels, recorded fluorescent movies could give information about the velocity of structural reorganizations. Statistical evaluations could exhibit the underlying mechanism of the occurring rearrangement processes. Still a model for stress and tension relaxation in such complex biopolymer networks is missing. First three-dimensional numerical simulations model the spontaneous formation of stress fibres with active cross-link formations in cytoskeletal actin networks [J. A. Åström et al., 2008].

By addition of cortexillin I cross-linkers to active myosin II/actin networks one could create a basic simple model system for cytoskeletal contractile ring structures *in vitro*. The general molecular principle learned could enlighten the contractility in actin networks. It seems to be straight forward answering following questions with already established methods: Are there certain concentration regimes necessary for allowing active transport of filament and bundle structures in cross-linked actin networks? In which way do these parameter regimes depend on molecular structures of the used cross-linker types?

As already known, the length of myosin II filaments depend on pH value and mono as well as divalent salt concentrations (chap. 1.1.2). From first electron micrographs it is shown that at low pH value the bundle structures in the composite myosinII/cortexillinI/actin-networks are shorter and less bend in contrast to high pH value (fig. 5.2A). Analyzing the TEM pictures results in a pH dependence of the length of the bundle structures in the working range of living muscle cells. With increasing pH, the bundle length almost doubles (fig. 5.2B). At pH 8, the rigor transition in active myosin filament is fast, reaching an elasticity of about 20 Pa, whereas at pH 6 ATP depletion is slower and the overall network elasticity is about ten times lower (fig. 5.2C). From this measurements, the crossover time for the rigor state could be obtained in dependence of the pH value. An interesting question to answer is in which way do differently large myosin filaments influence the buildup of actin bundles during polymerization? Instead of using cortexillin I, α-actinin could be used for cross-linking of
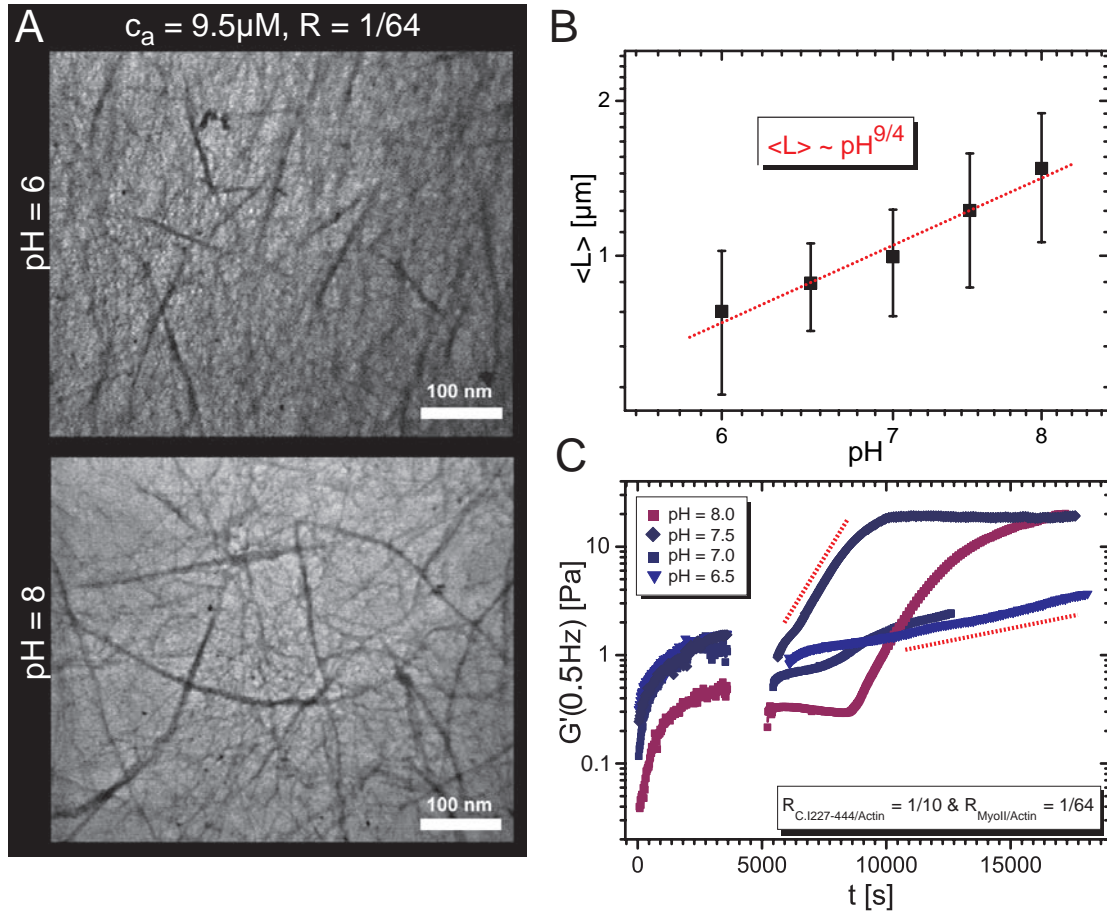
Figure 5.2: (A) TEM micrographs: comparison of cross-linked actin networks with myosin II concentration of 0.15 μM and CI1-227 concentration of 0.95 μM in Hepes buffer at pH 6 (top) and pH 8 (bottom). At low pH the embedded bundles in the network appear shorter and more straight in contrast to high pH value. (B) Mean length of the bundles in dependence of pH value. (C) For pH < 7.5 the crossover to rigor state of myosin II is decelerated. Are larger myosin II filaments responsible for greater tension in cross-linked actin networks? Moreover, do actin bundles grow bigger during polymerization?

actin filaments, since α-actinin is an important cross-bridging molecule in the z-disc of muscle cells. Results from such active myosinII/α-actinin/actin networks could be compared to experiments of live cardiac myomuscle cells (Lappaleinen Lab, Institute of Biotechnology, University of Helsinki in Finland).

Instead of increasing the complexity based on one biopolymer system, particularly mixtures of different biopolymers with various flexibility are materials of great importance since such mixtures are again simple model systems of the cytoskeleton. For example it remains a challenging endeavour to investigate mixtures of microtubules and actin networks and determining their physical properties. From theoretical calculations, segregation of mixtures of filaments with different stiffness due to depletion effects is already predicted [Kulp & Herzfeld, 1995].

Pursuing the bottom-up strategy for modeling of the cell, further basic studies have to be made. Still most basic model systems remain at a rudimentary level concerning the understanding of essential principles. Further essential cellular mechanisms have to be revealed before ultimately all pieces of the puzzle can be overall joined to a model for the functional unit of life. Up to this day new discoveries in complex mimicked cytoskeletal networks can be achieved by existing and established microscopical as well as micro- and macrorheological methods. Nevertheless, new and innovative measuring methods are necessary in order to obtain higher force, length or time resolutions for approaching single molecular level in the huge framework of protein assemblies.

Chapter 6

Appendix

6.1 Properties of Myosin II Filament Solutions

Bipolar filaments of myosin II (introduced in chap. 1.1.2), herein referred to as myosin filaments, are investigated with electron microscopy and rheological methods in order to address the following questions: What are the viscoelastic properties? At which concentrations do transitions occur from the dilute to the semi-dilute and the concentrated regime? Do myosin II filament solutions reveal any elastic response which could be detected by macrorheology?

First, basic structural investigations are presented. The images displayed and evaluated were obtained by electron microscopy (recorded with the JEM, see chap. 2.1.2). Afterwards the macrorheological results are discussed in detail within the context of the structural dimensions of the myosin II filamentous networks.

Characterization of Myosin II Filaments in Solution with Electron Microscopy

Dense myosin filament solutions appear to be similar to a mikado play: The rod-like filaments are randomly distributed intersecting each other (fig. 6.1, cf. simulation in the inset of fig. 6.5A). Single filaments are straight and have a mean length of about 600 ± 150 nm and a diameter of 30 ± 10 nm (fig. 6.2A). The mean distance between two parallel filaments $\chi_{MyosinII}$ decreases with the concentration. Since $\chi_{MyosinII}$ is in the range of the filament length (fig. 6.2A,B), resulting filament solutions are better described as a mikado like network of rods, than as a web-like network of long fil-

Figure 6.1: *TEM micrograph of myosin filaments arranged in a network of straight rods on the two dimensional plane.*
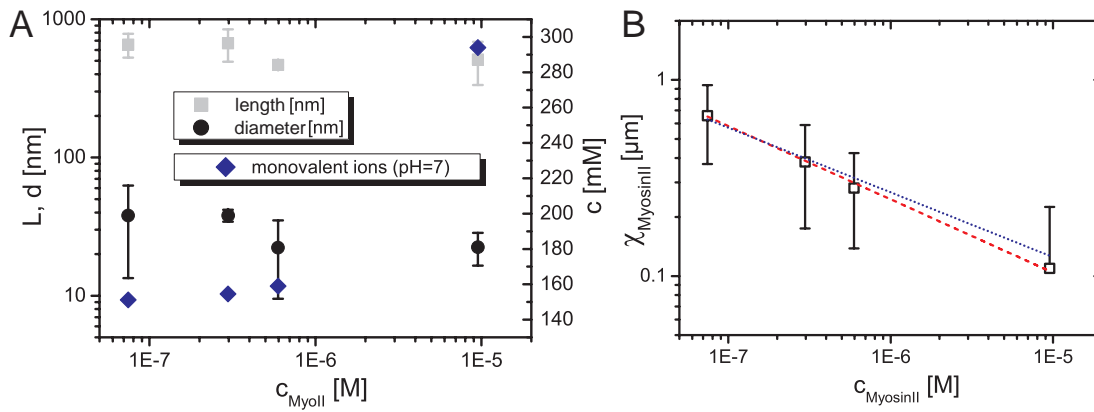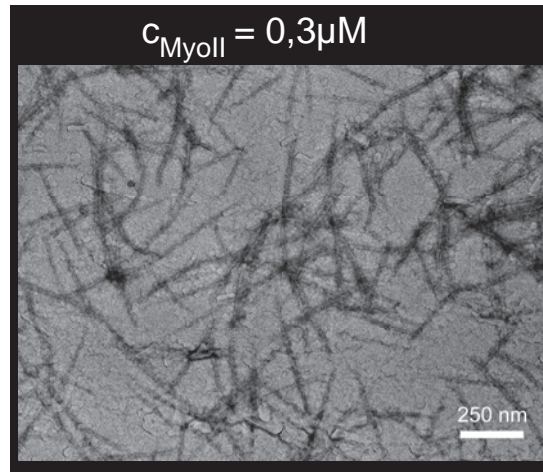
Figure 6.2: *All results in both graphs originate from pictures recorded with the JEM-100CX (see chap. 2.1.2). (A) The graph shows the dimensions of the myosin II filaments in dependence of the concentration obtained from TEM micrographs. The ratio of the length and the diameter $\frac{L}{d}$ of the filaments stays roughly constant and reaches a factor of about 20. (B) Average distance of parallel myosin filaments in dependence of the concentration. The red dashed line is a best fit with resulting exponent of -0.4 and the blue dotted line a fit with fixed exponent -0.5.*

aments (cf. actin). Similar to the meshsize of actin networks (cf. eq. 1.20) the blue dotted line indicates an one over square root dependence of $\chi_{MyosinII}$ on the myosin concentration ($\chi_{MyosinII} \sim \frac{1}{\sqrt{c_{MyosinII}}}$) whereas the red dashed line is a fit on the data with a resulting exponent of -0.4. For concentrations smaller than 70 nm $\chi_{MyosinII}$ is larger than the mean length of the filaments. Consequently, contacts between filaments are rather unlikely. Hence, one can state the crossover from the dilute to the semidilute concentration regime $c^\star$ to be between 40 and 70 nM. One has to keep in mind that the experimentally determined $c^\star$ results from a three dimensional solution which has collapsed on a two dimensional EM grid. Theoretically $c^\star$ for 600 nm long rods in three dimensions is calculated to be [Doi & Edwards, 1989]:

$$c^\star = \frac{1}{L^3} = 4.6 \cdot 10^{18} \frac{1}{m^3} = 7.7 \cdot 10^{-9} \text{M} \qquad (6.1)$$

The crossover concentration $c^{\star\star}$ from the semi-dilute to the concentrated regime of rods with a length of 600 nm and a diameter of 30 nm is calculated as:

$$c^{\star\star} = \frac{1}{d \cdot L^2} = 9.2 \cdot 10^{19} \frac{1}{m^3} = 1.5 \cdot 10^{-7} \text{M} \qquad (6.2)$$

A 600 nm long filament contains about 32-56 myosin II molecules [Reisler et al., 1980, Peppe & Drucker, 1979] and the crossover concentrations result to $c^\star = 0.25\text{-}0.44\ \mu\text{M}$ and $c^{\star\star} = 4.9\text{-}8.6\ \mu\text{M}$. The experimentally determined $c^\star$ from the EM pictures is 3-6 times lower than the calculated $c^\star$ due to the loss of one dimension.

Rheology of Myosin II Filament Solutions

Using the MCR macrorheometer, solutions of myosin II in Hepes buffer at pH 7.0 (chap. 6.8) were investigated in a concentration regime spanning more than three orders of magnitude from 10 nM to 40 μM. The viscoelastic parameters G' and G'' were measured in dependence of the frequency while applying torque of 0.25 μNm. The myosin II filamentous network solutions show an increase of the elastic modulus with increasing concentration (fig. 6.3A). Due to the inertia of the measuring plate, values of G' and G'' at frequencies larger than 0.7 Hz do not originate from the sample. For these frequencies the inertia of the measuring tool is too large and the values for G' decrease suddenly whereas G'' increases (fig. 6.3A and B). The elastic modulus G_0 extracted from the frequency dependence of G' is normalized in fig. 6.3C on the pure
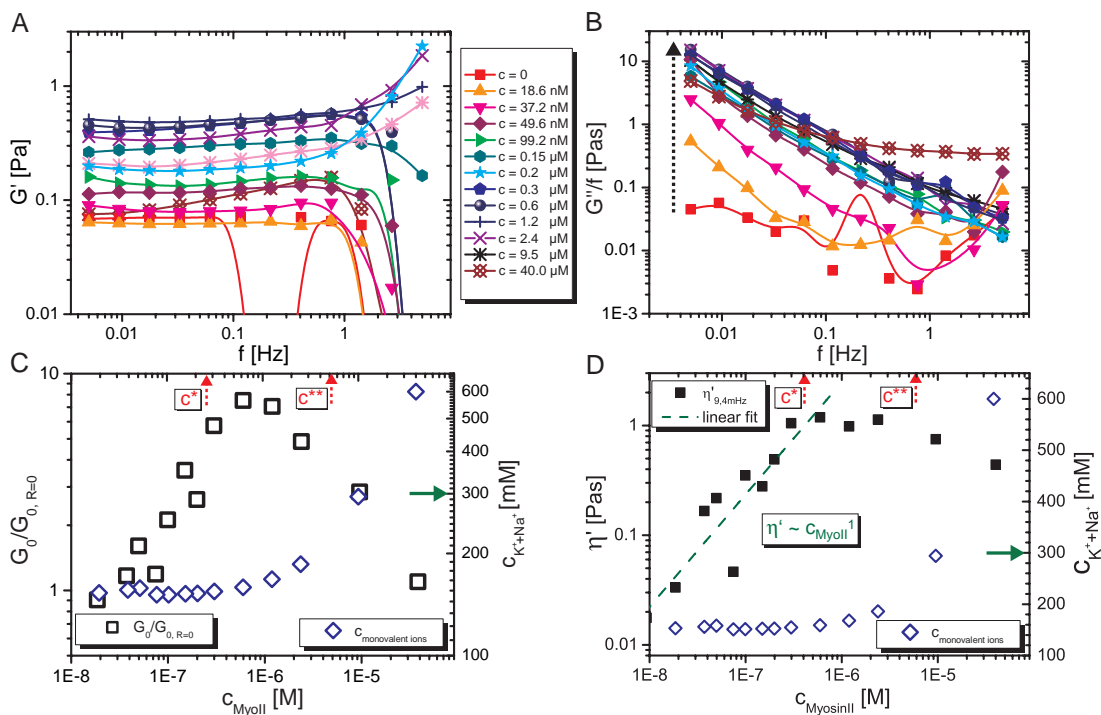
Figure 6.3: (A). G' of myosin II in solution with Hepes buffer at pH 7. (B) G'' divided by the frequency shows a decrease with increasing frequency if filaments are present in the solution. (C) G_0 and the monovalent ion concentration (the concentrations of K^+ and Na^+ were summed up) in dependence of the myosin II concentration. In the dilute and semidilute regime, the elasticity increases till the solution of the filaments becomes concentrated ($c_{MyosinII} > 2$ μM). If the monovalent salt concentration exceeds 300 mM (green rightward pointing arrow) the solution is purely viscous due to the nonformation of the filaments. (D) G''/f reveals the crossover from the dilute to the semi-dilute filamentous regime, in accordance with the calculated value of $c^\star$ (red upward pointing arrow). The green dashed line depicts the linear increase of the viscosity in dependence of the myosin II concentration in the dilute regime as predicted by [Doi & Edwards, 1989].
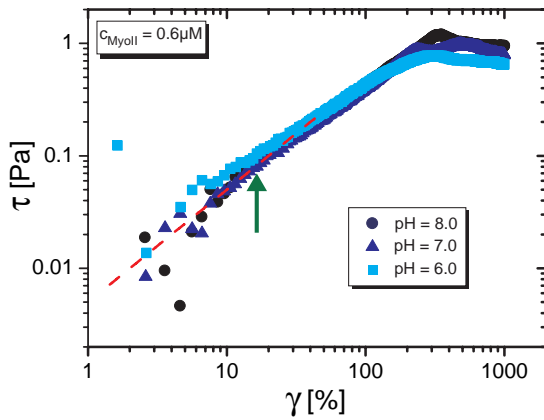
Figure 6.4: *Constant shear rate experiment ($\dot{\gamma}$ = 12.5 %/s). The flow behavior of the myosin II filament solution shows no strain hardening. The semi-dilute filaments shear weaken exceeding a strain of about 20 % (green upward pointing arrow). Moreover, no dependency on the pH value is resolvable. The red dashed line depicts a simulation with linear scaling.*

buffer solution. At a concentration of 1-2 μM the elastic response is maximal. This concentration can be referred to as the crossover to a concentrated filament solution [Doi & Edwards, 1989] but is about three times lower than $c^{\star\star}$, which was calculated in the previous chapter.

Since the myosin II stock solutions has a high monovalent ion concentration, the concentration of monovalent ions in the sample solution is increased with increasing myosin concentration. Exceeding 300 mM of monovalent ions in the sample solution (depicted by the green rightward pointing arrow in fig. 6.3C) the myosin II molecules are not able to form filaments and the solution stays purely viscous. In fig. 6.3B G'' divided by frequency decreases linearly with frequency for all solutions containing filaments. With increasing filament concentration G''/f increases (black upward pointing arrow in fig. 6.3B). The concentration dependence of the real part of the viscosity $\eta' \sim G''/f$ (fig. 6.3D) reveals a crossover from the dilute to the semi-dilute regime at about 0.3-0.6 μM which is in accordance with the theoretical prediction. Following the theoretical model of [Doi & Edwards, 1989] the viscosity of a dilute or semi-dilute solution of rigid rods increases linearly with increasing concentration. The fit on the concentration dependence of η' supports the prediction (depicted by the dashed green line in fig. 6.3D).

From the linear response measurements shown in fig. 6.3 it is not clear if the myosin II filaments hold tight contact among each other. The flow behavior of the filament solutions is exhibited by performing constant shear rate experiments. The recorded stress response depicted in fig. 6.4 stays linear till the strain exceeds about 20 %. For higher strains the myosin II filamentous solution reveals shear thinning in contrast to mesh-like actin networks. According to the results shown in fig. 6.4, the filamentous solutions are considered to be not cross-linked.

Wilhelm et al simulated a network of stiff rods similar to a mikado play
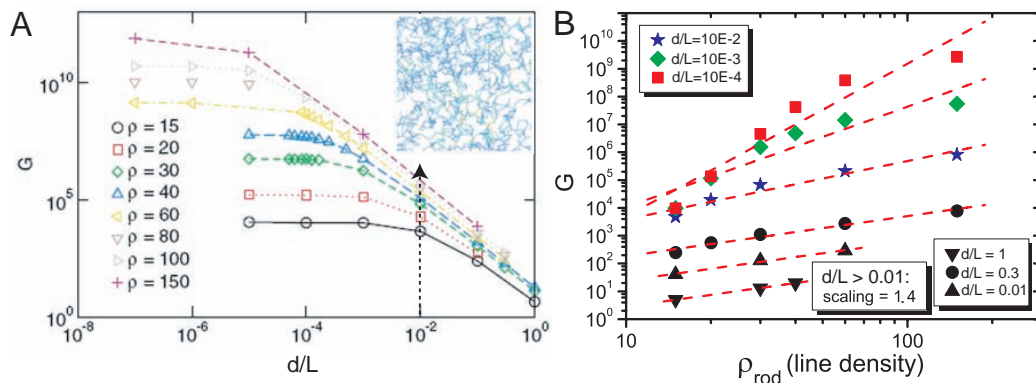
Figure 6.5: (A) *Simulated mikado play with stiff rods resulting in an elasticity G of the network in dependence of the diameter to rod length ratio (ϱ) [Wilhelm & Frey, 2003]. (B) Extracted values for distinct ϱ-values in the range of the myosin II filament dimensions obtained in fig. 6.2. A mikado like network of cross-linked stiff rods scales with 1.4 or higher above the percolation transition.*

[Wilhelm & Frey, 2003]. At each intersection point stiff cross-links are present and the calculated elasticity of the networks depends indirectly proportional on the diameter to rod ratio $\varrho \equiv \frac{d}{L}$ for $\varrho > 10^{-4}$ (fig. 6.5A). For $\varrho > 10^{-2}$ the concentration dependence of the elasticity is predicted to scale with an exponent of 1.4 (fig. 6.5B, for myosin filaments at pH 7 in Hepes buffer the line density ϱ is approximately 0.05). Since the filaments are expected not to be cross-linked at the intersection points, it is not surprising that the elasticity does not scale with the predicted scaling factor of 1.4. In order to test the predicted scaling law, filaments cross-linked with glutaraldehyde could be used as a model system. With this networks one could answer the question whether the resulting networks are dominated by enthalpic bending of the stiff rods or not. The results could be compared to cross-linked networks containing the more flexible actin filaments.

In muscle cells myosin filaments are packed into hexagonal structures with the protein myomesin [Agarkova & Perriard, 2005]. Therefore myomesin could be an interesting protein for future experiments. Using the biological relevant myomesin for bundling the myosin filaments, small active contraction units could be emulated *in vitro*. Those active contraction units in the presence of actin networks could be implemented in vesicles simulating a contracting muscle cell *in vitro*.
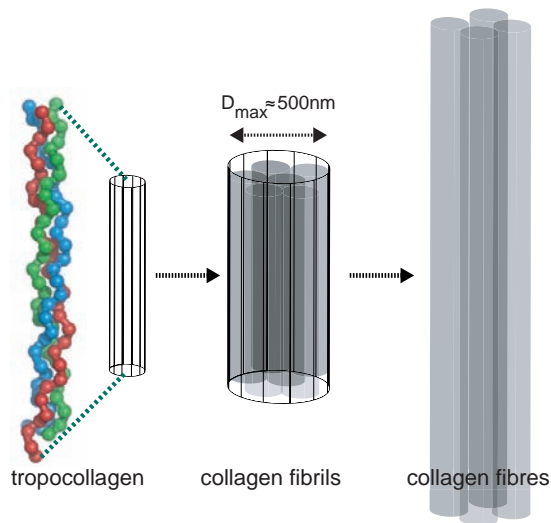
Figure 6.6: *Collagen fibre formation in two steps out of tropocollagen units. The collagen fibrils are self-assembled from 300 nm long tropocollagen subunits. The fibrils reach several μm in length and are about 500 nm thick. The collagen fibres form cross-links among themselves via lysin residues.*

6.2 Comparison of Viscoelastic Properties of Agarose, Collagen, Nucleoporin and Actin Gels

At the beginning of this chapter, the occurrence and general properties of the used materials, collagen, agarose and NSP1 are described followed by a subchapter which elaborates on the source and sample preparation for macrorheological experiments. Finally, the results of the experiments are compared altogether and discussed in the context of the physical properties of cells and cell environments.

Collagen

Occurrence in Nature and Physical Properties

Collagen is the main protein of the connective tissue of mammals with 28 gene families known. About 25 % of the mammalian organism protein content consists of collagen. 90 % of the human collagen belongs to the type I family. Type I collagen occurs in tendon, skin, artery walls, myofibrilla, organic parts of the bones and teeth as well as in scar tissue.

In order to generate these materials, collagen forms fibres. The buildup of the collagen fibres is divided in two steps. First, three polypeptide strands, each wound left-handed, are twisted around each other (similar to coiled coil formation) forming a right handed triple helical structure, the so called tropocollagen. Tropocollagen is 300 nm long. It is 1.5 nm in diameter and is the subunit of the collagen fibrils. These are bundles ba-

sically self-assembled from tropocollagen units (fibril genesis). In the collagen fibrils the tropocollagen units are shifted 67 nm against each other what can be observed as cross stripes in metal shadowed electron microscopy pictures. Overall the collagen fibrils can reach several μm in length and a maximal diameter of 500 nm. The collagen fibrils themselves bundle together forming collagen fibres (see fig. 6.6). In a following step the collagen fibres form cross-links between lysin residues. These fibres can withstand great tensile stresses and are responsible for the elasticity of e.g. skin tissue.

Source and Sample Preparation

Collagen type I was ordered from Nutacon (ultra pure bovine collagen 99.9 %), with an initial concentration of 3 mg/ml. The collagen was diluted in 10x-DMEM-buffer (PAA, Pasching, Austria) and Hepes-buffer (1M) to a concentration of 2.6 mg/ml. When the color of the medium switches from yellow to red a pH value of 7 is reached. The pH value was adjusted to physiological conditions for cells with 1 M NaOH (2.5 %). Subsequently the collagen was diluted with Hepes-buffer reaching the required concentrations (see. app. 6.8). As the amount of the material was not a limiting factor 450 μl sample volume were used for the measurements. They were performed using a plate with diameter of 5 cm and a gap width of 160 μm. After mounting the sample on the rheometer the collagen was heated from 21 to 37°C, in order to induce gelation.

Properties of Collagen Gels

Collagen gel formation depends strongly on the temperature. Formation of collagen fibres and networks seem to be an irreversible process in dependence of temperature T (fig. 6.7A). G' stays constant once the temperature has reached 37°C, implying that formed fibres of tropocollagen are stable. The second observation is that collagen strain-hardens under a constant shear (cf. fig. 6.7B). This can be explained by assuming that collagen fibres are cross-linked among each other. Furthermore, shearing the sample to 1000 % strain leads to irreversible changes in the network. These are plastic deformations of the fibre network e.g. irreversible cross-link detachment or fibre breakage (red-dotted area). Consequently the following second and third shear cycle show a clear strain weakening. This behavior is also observed for entangled and cross-linked actin networks. The remaining hysteresis effect (red shaded area) of the second and third cycle shown in the inset of fig. 6.7 belongs to transient deformations in the network and are reversible.
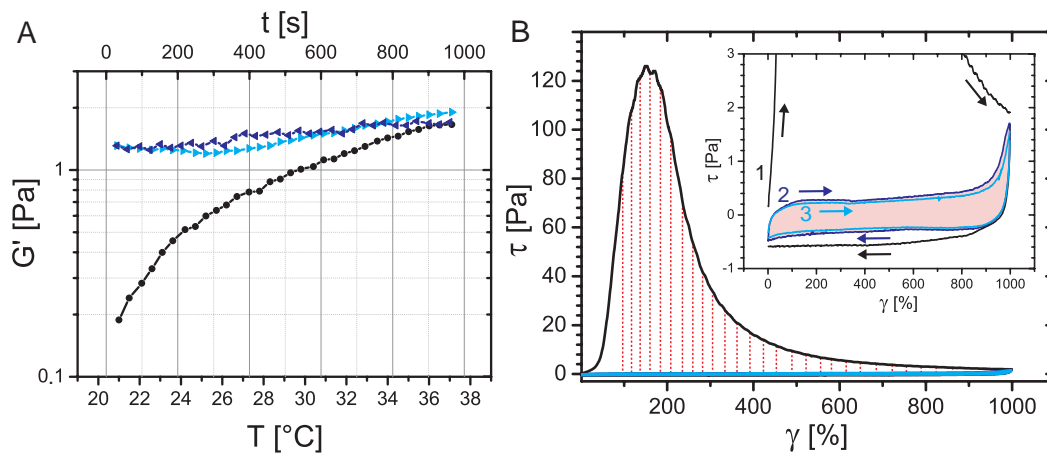
Figure 6.7: (A) Polymerization behavior (G' recorded at 0.5 Hz) of a collagen gel (c = 0.94 mg/ml) measured during a temperature cycle (black dots: 21°C → 37°C, blue left arrows: 37°C → 21°C, cyan right arrows: 21°C → 37°C). (B) Constant shear rate experiment ($\dot{\gamma} = 12.5$ %/s) for a collagen network with c = 1.25 mg/ml. The inset shows a magnification of the subsequently performed cycles from 0 to 1000 % strain (1. black, 2. blue, 3. cyan).
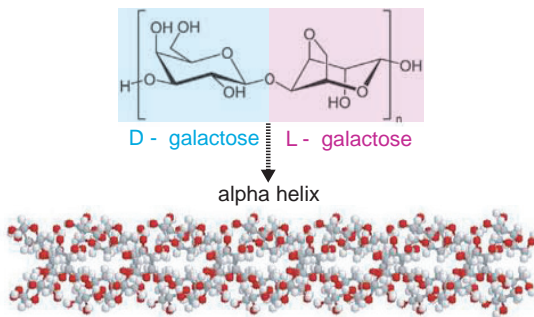
Figure 6.8: Chemical structure of the polysaccharide subunit of agarose. Two extended strands form an α-helical structure.

Agarose

Occurrence in Nature and Physical Properties

The biopolymer agarose occurs as a structural component in the cell wall of the dulse genuses Gelidium, Gracilaria or Sphaerococcus euchema (seaweed). Agarose is a main component of agar, which is derived from red algae. It is a polysaccharide of dimers of d-galactose and 3,6-anhydro-l-galactose, linked via glycosidic bonds (fig. 6.8). In addition two polysaccharide strands wind up to an alpha-helix as shown in fig. 6.8. Easily soluble in water agarose forms strong gels below 40°C, known as gelatine.

Source and Sample Preparation

Agarose was purchased from sigma aldrich (pnr 05055 Fluka BioChemika). The desired amount of agarose powder was dissolved in ddH$_2$O and boiled for one min (800 W in the microwave oven). Concentrations of 1.25, 2.5, 5, 10, 20 mg/ml w/v were used. A volume of 90 μl was mounted on the bottom plate of the rheometer after the solution hah cooled down to about 37°C (body temperature). The initial temperature for the measurements was 25°C. The measurements were performed using a PP25 and a gap width of 120 μm.

NSP1

Occurrence in Nature and Physical Properties

The cell nucleus is surrounded by the nuclear envelope which separates the inner nucleus from the cytoplasm. Since protein synthesis takes place in the cytoplasm and tRNA, mRNA as well as ribosomes are produced inside the nucleus, molecular exchange between the nucleus and the cytoplasm is required. Nuclear pore complexes (NPCs) which are large aqueous channels (up to 125MDa) connecting the cytoplasm with the nucleoplasm [Adam, 2001] allow diffusion of inert molecules up to 30 kDa across the nuclear envelope. Molecules larger than 30 kDa have to be transported by nuclear transport receptors (NTRs) through the NPC. The interior of the NPC comprises more than 30 different nucleoporins (NUPs) [Ball & Ullman, 2005]. Inside the NPC, these proteins contain clusters of up to 50 highly hydrophobic FG-amino acids repeats which alternate with hydrophilic aa sequences [Frey & Görlich, 2007]. In the selective phase model proposed by [Ribbeck & Görlich, 2001] the NUPs form a sieve-like network due to pairwise interactions of the hydrophobic FG-repeat domains. The resulting meshsize of the network is supposed to set the barrier for molecules exceeding 30kDa [Frey & Görlich, 2007].
NSP1 (nucleocytoskeletal protein 1), a synthetic nucleoporin, contains 55 phenylalanines which corresponds to 10 % of the overall 601 aa (supplement [Frey et al., 2006]). Concentrated solutions of NSP1 form strong hydrogels, whereas F→S mutants stay more or less liquid [Frey et al., 2006].

Source and Sample Preparation

The NSP1 was expressed and purified by Steffen Frey (center for Molecular Biology of the University of Heidelberg) and dried following [Frey et al., 2006]. The dried NSP1 was kept under low humidity at room temperature for several weeks. 80 μl of the basic buffer (app. 6.8) was added to the required amount of dried protein. In order to solve the protein in this buffer the solution was sonicated (till solved) first, then vortexed (some seconds) and at last centrifuged for 20 s. Neutralization of the solution by addition of 20 μl of the neutralization buffer (app. 6.8) initiates the gelation process. Immediately afterwards, the sample was mixed once with the pipette and 90 μl of the sample were mounted on the rheometer. The measurements were executed with a PP25 and a gap width of 120 μm at 21°C.

Comparison of Viscoelastic Properties of Investigated Aqueous Gels

In various cases nature uses biopolymer networks for retaining shape and elasticity. For example the cytoskeleton of cells and the extracellular matrix (ECM) are viscoelastic materials consisting of biopolymer networks. The cell walls of plants which augment the cell membrane are made of a biopolymer networks (cellulose fibrils, agarose). Furthermore compartments of the nuclear envelope also contain mesh-like protein assemblages which form hydrogels *in vitro*.

The biological materials agarose, NSP1, collagen and actin have one thing in common: Their subunits form biopolymers which arrange in three dimensional networks. By comparison of the four biopolymer networks the following questions are discussed: First, how strong are gels made of cell wall material (agarose) or membrane channel proteins (NSP1) in respect to a constitutive of the cytoskeleton (actin) or ECM (collagen)? Secondly, are there important parameters which determine the elasticity of the compared networks composed of the different materials?

The elasticity of the biopolymer networks can be varied between 1-10^4 Pa by changing the concentration . The stiffness of whole cells under an applied stress ranges between 1-30 kPa (e.g. fibroblasts, [Fernández et al., 2006]) similar to G' at polymer concentrations larger than 5 mg/ml. The concentrations of cytoskeletal polymers are reported to be in the range of 1-5 mg/ml [Boal, 2006]. For reaching the purpose as a molecular sieve the NSP1 networks must have the same elasticity as networks consisting of membraneous material, but with higher densities and consequently a smaller meshsize
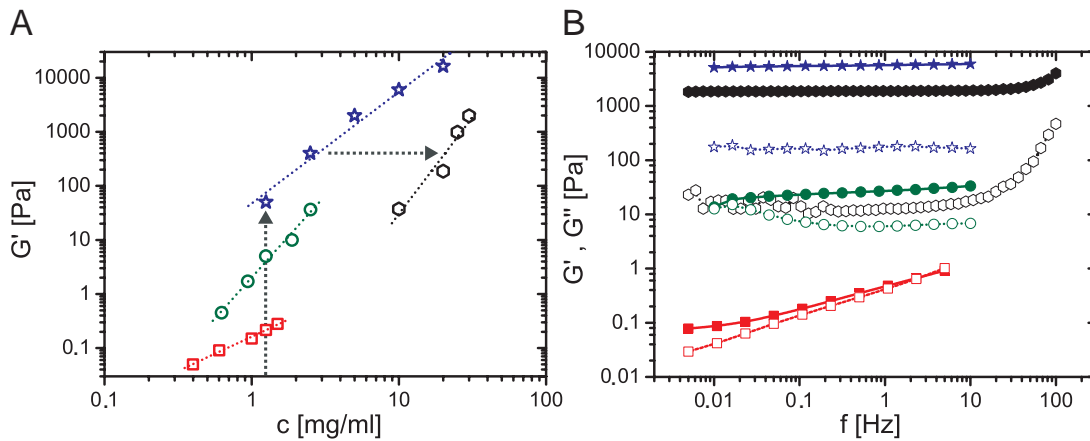
Figure 6.9: (A) Concentration dependency of G' of the four materials at a constant frequency (actin: $f = 0.04$ Hz, collagen: $f = 0.5$ Hz, NSP1: $f = 0.2$ Hz and agarose: $f = 0.2$ Hz). Actin values were taken from measurements with the TDR. (B) Comparison of the frequency behavior of viscoelastic properties of various aqueous gels (red squares: $c_a = 0.4$ mg/ml, green circles: $c_{collagen} = 1.88$ mg/ml, black hexagons: $c_{NSP1} = 30$ mg/ml and blue stars: $c_{agarose} = 10$ mg/ml) measured with the MCR.

(rightward pointing arrow in fig. 6.9A).

Measurements based on ECM preparations of 9.1 mg/ml (with an estimated collagen content of 30 %) resulted in an elasticity of about 10 Pa [Lieleg, 2005]. These results are in good agreement with the pure collagen measurements shown in fig. 6.9A. By extrapolation of the collagen data, one ends up with the same elasticity as for the agarose gels and the NSP1 gels (fig. 6.9A). Actin networks are 100 times lower and represent the weakest investigated gels. Cross-linked actin networks yield the elasticity range of other biopolymer networks (upward pointing arrow in fig. 6.9A). They are as stiff as the surrounding collagen gels which are linked via proteins in the separating membrane *in vivo*. Since the collagen networks reach a higher elasticity than pure actin filaments, the collagen bundles are supposed to be cross-linked. This can be explained by the huge length to diameter ratio of actin filaments ($\frac{L}{d} = 10^3$) and the huge thickness of collagen fibres which are thicker than 500 nm. The agarose alpha helix ($d \approx$ 1.5 nm) and NSP1 filamentous structures are roughly 1000 times thinner than collagen fibres. The only explanation for their huge elasticity is the very small subunit length and therefore the small length to cross-linker-distance ratio ($\frac{L}{L_c}$) which dominates the network system. From the G' measured for a certain concentration one could interpolate the ratio ($\frac{L}{d}$) for collagen and agarose to be 100 and 10 respectively. Overall, the elasticity of biopolymer gels can be tuned covering four orders of magnitude by

varying the concentration (see fig. 6.9A) which in turn defines the meshsize of the network (see eq. 1.20). Beside the concentration two additional parameters determine the viscoelastic behavior of the compared gels. Firstly, $(\frac{L}{d})$ which corresponds to the persistence length of a polymer thread and secondly the number of cross-links per filament $(\frac{L}{L_c})$.

Furthermore the differences of the biopolymer networks outcrop in the time dependence of the viscoelastic behavior (compare fig. 6.9B). Agarose and NSP1 gels are elastically dominated for more than three orders of magnitude of frequency, i.e. from 10 Hz to 5 mHz. In contrast the actin network elasticity dominates for frequencies lower than 5 mHz and the collagen network elasticity for frequencies higher than 0.1 Hz.

All in all the weakest constitutive, the actin network, dominates the viscoelastic behavior compared to the more elastic collagen gels. On the one hand cells have to be mobile on the other hand and have to be able to stiffen fast while exploring their surrounding. Consequently, beside the essential static properties of cells dynamic cross-linking is involved in the preservation of the vital functions of the cell.

Influence of Evaporation and Air Humidity on Rheological Experiments of Aqueous Gels

One big problem of the macrorheological measurement technique is the unsealed air water interface of the sample in contrast to cells, where the polymer network solution is surrounded by a lipid bilayer. In fig. 6.10A, one can see that G' for a NSP1 gel (gray color) or a collagen gel (filled light green circles) suddenly increases after a certain time (indicated by downward black arrows). Rim effects at the measuring tool or variations of the surface tension of the gap are possible effects influencing G'. Therefore, drying of the aqueous solutions with evolving time seems to gives rise to G'. In general the mechanical properties of a sample have to be determined after the polymerization process is completely finalized. Trying to keep the air humidity high prolonged the time until drying effects became apparent (compare black curve in fig. 6.10A). An easier and less costly way is putting silicon oil above the air water interface sealing the sample against evaporation of water. This was done[1] exemplarily for a collagen network (open dark green circles in fig. 6.10A).

---

[1]measurement was performed by Pablo Fernandez
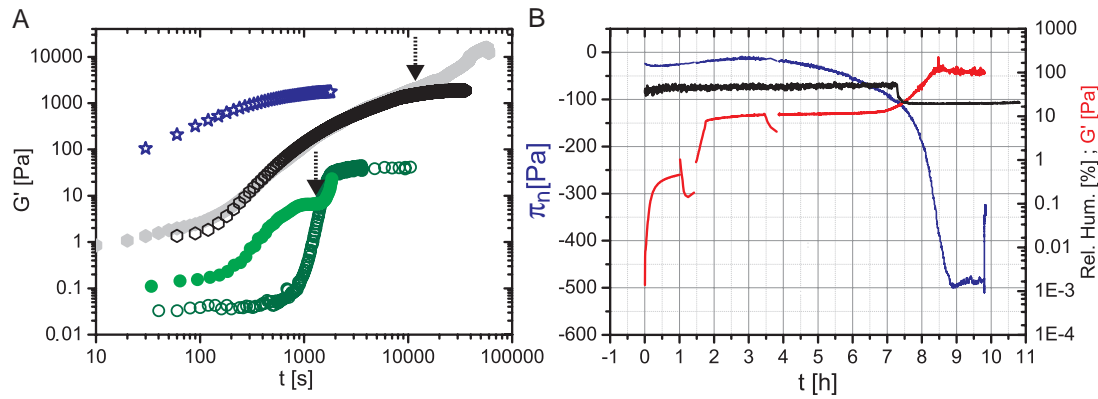
Figure 6.10: (A) *Time dependence of* G' *at constant frequency* (*same as in fig. 6.9*). *Measurement of NSP1* (*gray color, c = 30 mg/ml*) *collagen* (*filled light green circles, c = 1.25 mg/ml*) *with drying artefacts. No drying effects influenced the NSP1 measurement* (*black color, c = 30 mg/ml*) *at a constant surrounding air humidity of 50 %. Collagen* (*open dark green circles, c = 2.6 mg/ml*) *measurement with silicon oil against evaporation of water.* (B) *Normal pressure* (*blue line*), G' (*red line*) *and surrounding air humidity* (*black line*) *plotted versus time for a cross-linked actin network* (c_a = 9.5 *μM,* $< l >$ = 21 *μm and* $R_{actin/HMM}$ = 16), *measured with the MCR.*

Beside the viscoelastic moduli G' and G'' a normal stress ($\pi_n \equiv \frac{F_N}{A}$) is observed for biopolymer network which is perpendicular to the shear solutions [Janmey et al., 2007]. F_N is the measured normal force and A is the surface of the measuring tool. Exemplarily in fig. 6.10B π_n, the corresponding G' and the surrounding air humidity (measured with an combined humidity and temperature sensor, SMD RS232, Conrad Electronics, Germany) is plotted over time for an actin network cross-linked with HMM. The humidity was kept constant at roughly 50 % for about 7 h and was then reduced by a factor of 2.5 to 20 %. After the polymerization of the actin π_n is about 50 times higher than G' with active HMM cross-links. Reaching the rigor state of the HMM, G' rises up a factor of 20 to about 10 Pa. Passing 3.5 h π_n starts dropping down slowly, while G' still stays constant as well as the air humidity. With the sudden decrease of the air humidity, π_n drops down fast by a factor of 5 to -500 Pa and coincidentally G' rises again about the same factor as π_n to 100 Pa. The question arises whether the drop of π_n and the second increase of G' coincides with evaporation of water at the air water interface of the sample or not? Moreover, do biopolymer gels respond to external pressure? Daily variations in the air pressure are in the per mille regime. Are variations in the range of some hundred Pa already affecting the cytoskeleton of cells? Further measurements have to be done to elucidate these questions. The

largest known air pressure deviations are about 15 % of the standard air pressure corresponding to 15000 Pa. This is in the range of the strongest gels measured in this chapter and in accordance to the overall stiffness of cells. Varying the surrounding pressure in the percent regime of the standard air pressure should be sufficient to reveal a dependency of the elasticity or the normal pressure on the surrounding pressure.
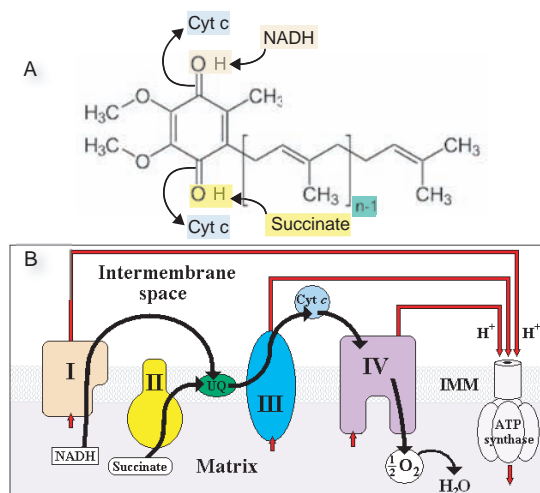
Figure 6.11: (A) *Chemical structure of coenzyme Q* (M_w = 863,4 *Da*). (B) *Ubiquinone* (*green*) *is reduced by NADH* (*skin color*) *and succinate* (*yellow*) *to hydrochinol* (QH_2). QH_2 *functions as a proton carrier and reduces the iron atom in the cytochrome c* (*blue*).

6.3   Rheology of Coenzyme Q10

Occurrence in Nature

Coenzyme Q also known as ubiquinone is abundant in all organisms. It is structurally related to the vitamins K or E. The coenzyme Q10 (Q10) exists in all vertebrate and is essential for life. Without Q10 the respiratory chain would be interrupted and the synthesis of ATP, the most important energy supplier in vertebrates would fail. The vital prerequisite for vertebrates makes Q10 attractive for all kind of investigations.

Source and Physical Properties

For the measurements with the MCR in plate plate (50 mm diameter) geometry at a gap width of 160 μm, pure Q10 from Kyowa Hakko Kogyo (Japan) was used. At room temperature Q10 occurs as a yellow to orange solid powder. It is lipophil and melts at 49° C. The boiling point lies beyond 200° C. Q10 can be supercooled down to 10° C, when recrystallization sets in and the melt solidifies again.

Measurements and Results

fig. 6.12A shows that the melt of Q10 is a newtonian liquid because the viscosity stays constant over three decades of increased shear rate $\dot{\gamma}$. At 60° C Q10 has a viscosity which is about 50 times larger than the viscosity of water (1 mPa·s at 25° C). Therefore, it can be measured far above the resolution limit. Since evaporation is neglectable for some hours the melt is easy to handle. The recorded viscosity of the Q10 melt increases
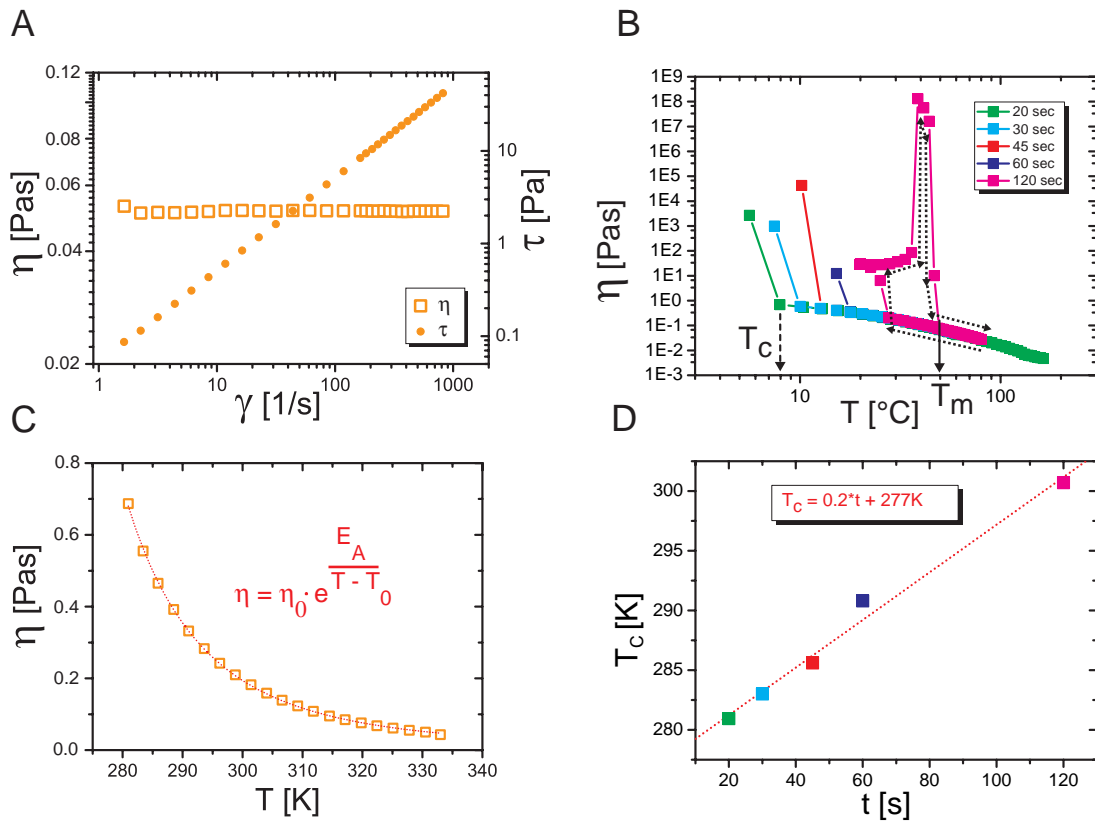
Figure 6.12: (A) *Orange open squares are the symbols for the measured viscosity η, filled dots depict the recorded stress τ. (B) Temperature cycle of η for different data point measuring times. (C) Viscosity increase with temperature of the supercooled Q10 melt (measuring time per data point is 20 seconds). The Vogel-Fulcher-Tammann (VFT) eq. is set in red color into the graph [Schneider, 2002]. (D) Time dependence of the critical temperature. The different colors corresponds to the temperature cycles in the upper graph.*

with decreasing temperature till it reaches a critical temperature T_c. At this temperature the viscosity of the supercooled melt jumps up due to recrystallization (see fig. 6.12B). With adjoining temperature increase back to the initial temperature the viscosity first increases further because more and more crystals are formed. After passing the melting temperature T_m the Q10 fluidises again completely and the viscosity perfectly matches the first measuring points (magenta filled data points in fig. 6.12B). With a linear regression to zero time one obtains: $T_c(0) = 277$ K ($4°$ C) (fig. 6.12D). The results from fitting the viscosity temperature curves for the different measuring times with the VFT eq. (fig. 6.12 C) are listed in tab. 6.1. The three variables are the zero temperature T_0, the activation energy E_A and the zero viscosity η_0.

TIME $[s]$	T_0 $[K]$	E_A $[K]$	η_0 $[Pas]$
20	184 ± 4.3	745 ± 60	3.2E-4 $\pm$ 9E-5
30	173 ± 1.6	870 ± 23	2.2E-4 $\pm$ 2E-5
45	172 ± 1.9	889 ± 27	2E-4 $\pm$ 2E-5
60	162 ± 3.4	1021 ± 49	1.2E-4 $\pm$ 2E-5

Table 6.1: Fit parameters following from the eq of fig. 6.12C

Discussion

For glassy polymers an arrhenius-like behavior is not adequate. Therefore the viscosity temperature dependence was fitted with the Vogel-Fulcher-Tammann equation. With a linear fit to the parameters of tab. 6.1 the following results are obtained:
The zero viscosity of Q10 is lower than the viscosity of pure water and the zero tem-

$T_0(0)$	184 K
$E_A(0)$	712 K
$\eta_0(0)$	0.4 mPas

Table 6.2: Extrapolated fit parameters for t = 0.

perature results in 184 K. Generally the glass temperature can be defined as $\frac{2}{3} \cdot T_m$ which gives 215 K for Q10. Another definition for the glass temperature at a viscosity of 10^{12} Pa·s results in 204 K from the VFT fit. In this model T_0 has to lie below the glass temperature. Here, this requirement is fulfilled. Using the values of tab. 6.2 the diffusion constant can be calculated. Therefore, the dimensions of the Q10 molecule is estimated from the crystal structure. The tail of the single Q10 molecules are approximately 3 Å thick and 22 Å long. The benzoquinone ring has a diameter of approximately 7 Å. Assuming a length of about 30 Å the diffusion constant D of Q10 at T_0 is:

$$D_{184K} = \frac{k_B \cdot T_0}{6 \cdot \pi \cdot \eta_0 \cdot l} = \frac{1.38 \cdot 10^{-23} \frac{J}{K} \cdot 184K}{6 \cdot \pi \cdot 0.0004 Pa \cdot s \cdot 30 \cdot 10^{-10} m} = 112 \frac{\mu m^2}{s} \quad (6.3)$$

This value is similar to the diffusion constant of a protein with a diameter of 3nm at body temperature ($D_{protein} = 108$ μm^2/s with $\eta = 0.7$ mPas [Howard, 2001]). At body temperature (37° C) the diffusion constant for Q10 results to 0.6 μm^2/s which is 200 times smaller than at T_0.
Recently emulsions of liquid oils were investigated for being applied as drug carrier. Analogously, Q10 could be used as a carrier for drugs because Q10 has interesting

properties. Beside the high supercooling possibility (the molten Q10 can be super-cooled by a factor of 1.2 in temperature.) Q10 is biologically compatible. For example nanodrops of Q10 in a water emulsion could be used for carrying liposoluble drugs.

6.4   Sample Preparation

Actin Sample Preparation

Standard G-actin from Rabbit Smooth Skeletal Muscle
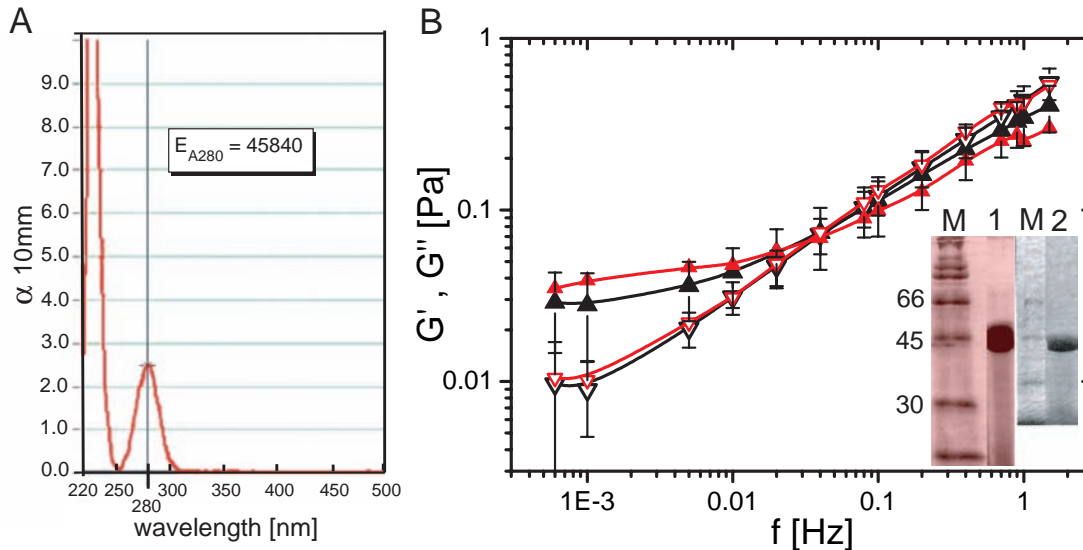
Figure 6.13: (A) *Characteristic 280 nm absorbance* (α) *peak* (*red*) *of ultra pure G-actin.* (B) *Comparison of actin prepared from rabbit and chicken muscle tissue.* G' *and* G'' (*defined in chap. 2.2.1*) *of chicken actin* (*red lines*) *lies in the error bar range of rabbit actin* (*black lines*). *Values were measured with the torsional disc rheometer* (*TDR, see chap. 2.2.3*). *Inset: Both SDS gels show no markable impurities. Columns of gel: marker* (*M*), *rabbit actin* (*1*), *chicken actin* (*2*).

Actin was obtained from rabbit smooth skeletal muscle according to the preparation of [Spudich & Watt, 1971]. Residuals of ABPs were removed by chromatography on a sephacryl S-300 column. The pure monomeric actin was sterile filtrated and divided into aliquots. A part of the G-actin solution was constrained in sucrose and stored in lyophilized form at -21° C [Goddette & Frieden, 1986]. Lyophilized actin was dissolved in ddH$_2$O and dialyzed against fresh G-buffer (app. 6.8) for 24 h. The actin solution was spun at 4° C with 38 k rotations per minutes (rpm) for 90 minutes (min) in an ultracentrifuge (L-90k, Beckman and Coulter) in order to remove actin oligomers. The actin concentration was photometrically determined with a spectral photometer (ND-1000, PeQLab Biotechnologie GmbH) at a wavelength of 280 nm and an extinction coefficient $\epsilon_{A,280} = 45840 \ \mathrm{M}^{-1} \cdot \mathrm{cm}^{-1}$ (fig. 6.13A). The G-actin

was stored max. 14 days on ice. Polymerization was initiated by adding one tenth of the sample volume of 10x-F-buffer (app. 6.8).

Standard G-actin from Chicken Muscle Tissue

It is also feasible to use other vertebrate muscle tissue for the preparation of highly pure actin. fig. 6.13B illustrates that the same rheological results were obtained with actin prepared from chicken breast muscle. Since the actin gain is lower from chicken muscle tissue the overall costs are higher and therefore the preparation from rabbit muscle is more economical and recommended.

Biotinylated G-actin

[1]

Lyophilized actin was dialyzed against 50 mM borat buffer with pH 8.0 at 4° C for 12 h. Afterwards the actin was polymerized for 1 h at room temperature by adjusting the salt concentration in the solution to 100 mM KCl and 2 mM $MgCl_2$. The polymerized actin was covalently modified with an biotin-NHS-ester in 2 x excess for 1 h. The reaction was quenched with sodium glutamate in 100 x excess for 15 min at room temperature. Subsequently, the biotinylated actin was depolymerized by centrifuging with 38 k rpm for 1.5 h at 4° C. Adjoining, the pellet was resolved in G-buffer. The resulting solution was purified by dialyzing against G-buffer for 12 h at 4° C followed by centrifugation with 38 k rpm for 1 h at 4° C. The concentration of the supernatant was determined as for the standard G-actin. The biotinylation grade β was determined by performing a displacement reaction with the dye $4-$Hydroxyazobenzene$-2-$carboxylic acid (HABA), which is bound to avidin (Sigma Aldrich, pnr H2153). HABA is displaced by biotin binding to avidin. With this displacement the absorbance of the dye α_{HABA} is changed stoichiometrically and can be measured photometrically (ND1000).

$$\beta = \frac{x_1}{\varepsilon} \cdot \frac{(x_2 \cdot \alpha_{HABA}) - \alpha_{HABA+sample}}{c_{sample}} \tag{6.4}$$

The extinction coefficient ε is 34 mM at 500 nm. x_1 is the dilution factor of the sample into the cuvette and x_2 is the dilution factor of HABA/avidin upon addition.

---

[1]Courtesy of Melanie Reisinger

Mixtures of Biotinylated and Standard G-actin
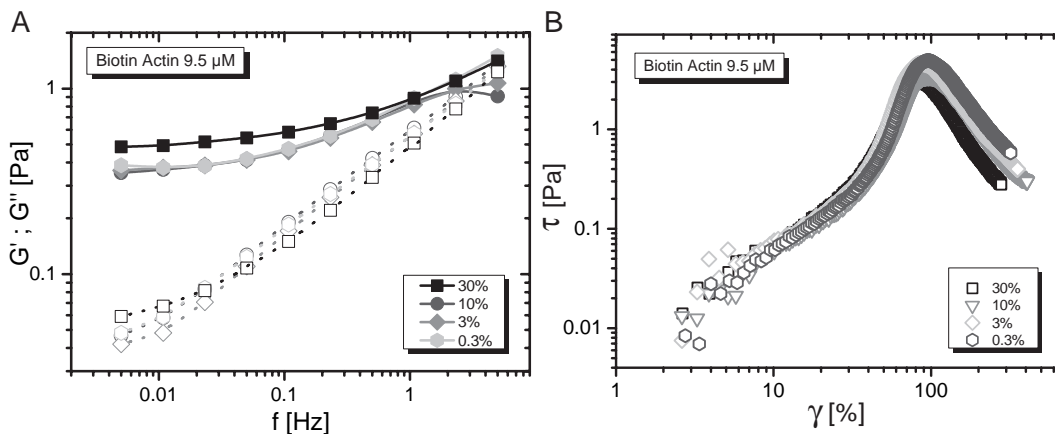
Figure 6.14: (A) *The graph represents the G' and G'' frequency dependence for mixtures of actin and biotinylated actin (chap. 1.1.1.) networks. They appear similar in the linear response regime.* (B) *Also no differences are resolvable in the nonlinear behavior ($\dot{\gamma} = 12.5$ %/s) which is shown for the same concentrations in the right figure.*

The effects of mixtures of biotinylated and normal actin were studied in the linear frequency regime of G' and G'' as well as the nonlinear response. As can be seen from fig. 6.14 the frequency behavior of G' and G'' stays the same and the stress strain curves are apparently not changed for biotin actin amounts of 0.3 up to 30 %. Therefore mixtures of biotinylated and normal actin are suited to investigate the effect of additional cross-linkers. Consequently mixtures of biotinylated actin are well suited to study the influence of neutravidin based cross-linkers on the actin network properties.

Actin Binding Proteins

Gelsolin

Gelsolin was prepared from bovine plasma serum following [Cooper et al., 1987] and stored in solution at -80° C. For the measurements the gelsolin was diluted in G-buffer and added to the sample before the addition of actin. Equation 1.1 was used to adjust the mean filament length for all measurements in this work.

Neutravidin

Neutravidin, provided in lyophilized form from Molecular Probes (pnr A2666), was dissolved in 10 mM phosphate buffer at pH 7.4 (Phosphate buffered saline, PBS, from

Sigma Aldrich, pnr P4417), then divided into aliquots and finally stored at -80° C. Thawed aliquots were used within one week performing the measurements.

Filamin

ggFln was prepared from chicken gizzard following [Shizuta et al., 1976] and stored in aliquots at -80° C. ddFln was a gift of M. Schleicher and was also stored in aliquots at -80° C.

Synthetic Cross-linkers with Hisactophilin

HisAc-S-S-HisAc, HisAc-D5-6 and HisAc-D2-6 were cloned, expressed and purified as described in the supplemental information of [Wagner et al., 2006] (for sequence alignment see chap. 6.6). The purified proteins were stored in 50 mM potassium phosphate buffer of pH 8.0. They were stable for several months at 4° C.

Cortexillin

Expression vectors were kindly provided by G. Gerisch. Two recombinant proteins, the full length construct CI1-444 and the CI227-444, which lacks the N-terminal ABD domains, were expressed and purified according to [Stock, 1999]. The cleavage of the N-terminal His-tag, which is necessary for the purification, is a difficult step in the purification process. The correct protease specie and the appropriate molar ratio of the protease to protein is crucial for this step. Within this work histidine-tagged proteins were used (Result of purification: see fig. 1.7 on the right). Both proteins, CI1-444 and CI227-444, were stored in aliquots at -80° C.

Myosin II and Subfragments

Myosin II and the subfragment HMM were prepared as described in [Uhde, 2004]. 35 % w/v sucrose and 10 mM Dithiothreitol (DTT) were added to the solution of the proteins. The protein solution was stored at -80° C.

Polyethers

PEO218k was purchased from Sigma Aldrich Germany (pnr 81206) and stored dissolved in 2 ml ddH$_2$O reaching a concentration of 20 % w/w. The concentration was

determined by lyophilizing 200 μl of the solution and weighing of the remaining powder. PEG6k was ordered from Merck KGaA Germany (pnr 8170071000). It was dissolved in ddH$_2$O reaching a final concentration of about 40 % w/w and used within two weeks.

The PEG solution was added to the actin samples before protein addition.

6.5 Cryo Electron Microscopy

With a higher resolution as with the confocal microscope one can obtain 3D reconstructions of unstained and unfixed biopolymer networks imbedded in amorphous ice. For visualization of actin networks EMs with 200kV or 300kV high voltage were used.

Sample Preparation

Actin was polymerized in low salt buffer reducing crystal formation during freezing (app. 6.8). A sample volume of 3-4 μl was adsorbed (30-60 s) to previously glow-discharged (60 s), holey-carbon-formvar films coated on copper grids. The grids were washed in a drop of 20 μl of ddH$_2$0 (60 s) and 4 μl of a colloidal gold particle solution was added on top of the droplet (with a mean diameter of 10 nm of the particles (G-1527, sigma aldrich). The gold particle solution was sonicated (for at least 5 min) preventing aggregation of particles in the solution before addition to the sample. After waiting another 60 s, the grids were immediately blotted by hand from backside with a filter paper and were plunged via a guillotine mechanism in liquid ethane [Tharmann, 2006].
Due to the blotting, the actin sample shrinks about a factor of 1000 to a mean ice thickness of 300 nm. Neither blotting from the front side nor blotting from back with a holey filter paper could improve the thickness of the ice, so that it would have been still possible to penetrate the ice without burning of the sample.

Vitrobot

In a vitrobot the blotting time, the time before plunging and the vitrifying time in liquid ethane can be varied systematically. In the vitrobot chamber temperature and air humidity are kept constant. For blotting from both sides the best blotting time for an actin concentration of 0.2 mg/ml and long filaments of around 21 μm resulted in 2.5 seconds.

Cryo Sectioning

One can get rid of the shrinking artefact of blotting, using the cryo sectioning method [Tharmann, 2006]. For this purpose, the samples were polymerized in cryo copper

tubes, which were laid in closed small reagent tubes containing a small amount of the freshly prepared sample (20 μl) as an evaporation protection. After polymerizing the actin for at least 1 h the samples were shock frozen under a constant pressure. The laser cut 250 μm thick slides of actin were transferred on grids at liquid nitrogen temperature. The following tested samples did not result in amorphous and coincidentally robust ice for laser cutting:

c_a [mg/ml]	$\langle l \rangle$ [μm]	buffer [app. 6.8]	cryo protection	polimerization time [h]
0.2	22	10x-F	sucrose 15 %	2, 4
0.4	2	10x-F	glycerol 15 %	1
0.6	21	10x-F,	sucrose 10 %,	2, 4
0.6	21	low salt	sucrose 15 %	2, 4
0.6	21, 1	10x-F, low salt	glycerol 8 %	2, 4
0.8	2	10x-F	glycerol 20 %	1
1.0	2	10x-F	glycerol 10 %	1

Table
6.3: Sample parameters which resulted not in amorphous and stable ice for laser cutting.

Once the right sample parameters are found, the cryosectioning method would be a sophisticated technique to record 3D images of non-shrunken, native actin filamentous networks without any dye or contrast agent which broaden and alter the filaments.

6.6   Summary of Actin Binding Proteins

ABP	M_w [**kDa**]	**aa** [**#**]	**D** [**#**]	L [**nm**]	K_D [**M**]	ΔG $[k_B \cdot T]$
AVIDIN (Av)	60	512	2	6	$1 \cdot 10^{-15}$	35
GELSOLIN	82	755	6	9	$4.5 \cdot 10^{-12}$ (G-Act.) $2.5 \cdot 10^{-8}$ (F-Act.)	26 18
HISACTOPHILIN (HisAc)	17	118	1	4	$1 \cdot 10^{-7}$	16
FASCIN (Fas)	55	486	2	12	$7 \cdot 10^{-7}$	14
dd FILAMIN (ddFln)	120	857	7	35	$\approx 10^{-7}$	16
gg FILAMIN (ggFln)	280	2469	4	160	$5 \cdot 10^{-7}$	15
CORTEXILLIN I (CI)	50.5	444	3	27	$2.3 \cdot 10^{-7}$	15
MYOSIN II (MyoII)	257	2245	5	160	$5 \cdot 10^{-7}$ (wo ATP) $5 \cdot 10^{-6}$ (w ADP) $1 \cdot 10^{-3}$ (w ADP+Pi) 5 (w ATP)	15 12 7 -2

In stated order the values of K_D follow: [Donald J. Voet, 2004], [Bryan, 1988], [Scheel et al., 1989], [Ono et al., 1997], [Hanein et al., 1997], [Limozin & Sackmann, 2002], [Faix et al., 1996], [Howard, 2001]. $\Delta G = k_B \cdot T \cdot \ln(K_D^{-1})$ [Claessens et al., 2008].

AVIDIN

GELSOLIN
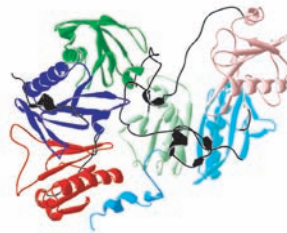
HISACTOPHILIN

FASCIN

dd FILAMIN

Rod domains

Actin binding site

gg FILAMIN

N - terminal Actin binding site

Rod domain 1

Rod domain 2

C - terminal dimer binding site

CORTEXILLIN I

N-terminal actin binding sites

C-terminal actin binding sites

1   227   444

MYOSIN II

LMM

HMM
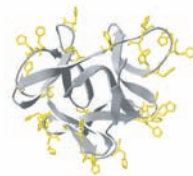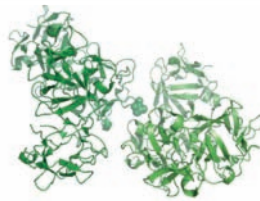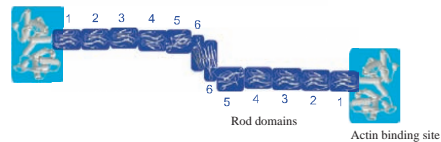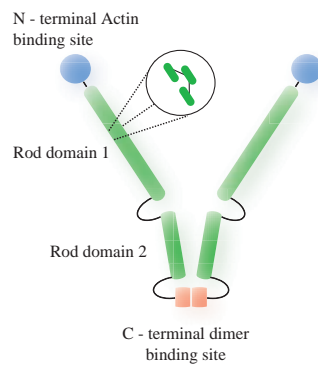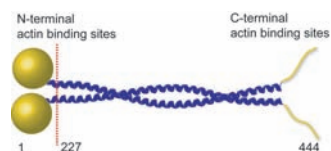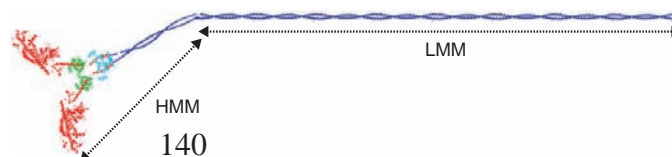
```
HisAc-HisAc   ------------------------------------------------------------MGN
HisAc         ------------------------------------------------------------
HisAc-C       ------------------------------------------------------------
HisAc-woC     ------------------------------------------------------------
HisAc-D5-6    ------------------------------------------------------------
HisAc-D4-6    ------------------------------------------------------------
HisAc-D3-6    ------------------------------------------------------------
HisAc-D2-6    ------------------------------------------------------------
HisAc-D1-6    ------------------------------------------------------------
DDFLN         ------------------------------------------------------------
Biotin-D2-6   ------------------------------------------------------------

HisAc-HisAc   RAFKSHHGHFLSAEGEAVKTHHGHHDHHTHFHVENHGGKVALKTHCGKYLSIGDHKQVYL
HisAc         ------------------------------------------------------------
HisAc-C       ------------------------------------------------------------
HisAc-woC     ------------------------------------------------------------
HisAc-D5-6    ------------------------------------------------------------
HisAc-D4-6    ------------------------------------------------------------
HisAc-D3-6    ------------------------------------------------------------
HisAc-D2-6    ------------------------------------------------------------
HisAc-D1-6    ------------------------------------------------------------
DDFLN         MAAAPSGKTWIDVQKKTFTGWANNYLKERILKIEDLATSLEDGVLLINLLEIISSKKILK
Biotin-D2-6   ------------------------------------------------------------

HisAc-HisAc   SHHLHGDHSLFHLEHHGGKVSIKGHHHHYISADHHGHVSTKEHHDHDTTFEEIIIGSGGS
HisAc         ------------------------------------------------------------
HisAc-C       ------------------------------------------------------------
HisAc-woC     ------------------------------------------------------------
HisAc-D5-6    ------------------------------------------------------------
HisAc-D4-6    ------------------------------------------------------------
HisAc-D3-6    ------------------------------------------------------------
HisAc-D2-6    ------------------------------------------------------------
HisAc-D1-6    ------------------------------------------------------------
DDFLN         YNKAPKIRMQKIENNNMAVNFIKSEGLKLVGIGAEDIVDSQLKLILGLIWTLILRYQIQM
Biotin-D2-6   ------------------------------------------------------------

HisAc-HisAc   SGNRAFKSHHGHFLSAEGEAVKTHHGHHDHHTHFHVENHGGKVALKTHSGKYLSIGDHKQ
HisAc         MGNRAFKSHHGHFLSAEGEAVKTHHGHHDHHTHFHVENHGGKVALKTHCGKYLSIGDHKQ
HisAc-C       MGNRAFKSHHGHFLSAEGEAVKTHHGHHDHHTHFHVENHGGKVALKTHSGKYLSIGDHKQ
HisAc-woC     MGNRAFKSHHGHFLSAEGEAVKTHHGHHDHHTHFHVENHGGKVALKTHSGKYLSIGDHKQ
HisAc-D5-6    MGNRAFKSHHGHFLSAEGEAVKTHHGHHDHHTHFHVENHGGKVALKTHSGKYLSIGDHKQ
HisAc-D4-6    MGNRAFKSHHGHFLSAEGEAVKTHHGHHDHHTHFHVENHGGKVALKTHSGKYLSIGDHKQ
HisAc-D3-6    MGNRAFKSHHGHFLSAEGEAVKTHHGHHDHHTHFHVENHGGKVALKTHSGKYLSIGDHKQ
HisAc-D2-6    MGNRAFKSHHGHFLSAEGEAVKTHHGHHDHHTHFHVENHGGKVALKTHSGKYLSIGDHKQ
HisAc-D1-6    MGNRAFKSHHGHFLSAEGEAVKTHHGHHDHHTHFHVENHGGKVALKTHSGKYLSIGDHKQ
DDFLN         SESDNSPKAALLEWVRKQVAPYKVVVNNFTDSWCDGRVLSALTDSLKPGVREMSTLTGDA
Biotin-D2-6   ------------------------------------------------------------

HisAc-HisAc   VYLSHHLHGDHSLFHLEHHGGKVSIKGHHHHYISADHHGHVSTKEHHDHDTTFEEIIIGS
HisAc         VYLSHHLHGDHSLFHLEHHGGKVSIKGHHHHYISADHHGHVSTKEHHDHDTTFEEIIIGS
HisAc-C       VYLSHHLHGDHSLFHLEHHGGKVSIKGHHHHYISADHHGHVSTKEHHDHDTTFEEIIIGS
HisAc-woC     VYLSHHLHGDHSLFHLEHHGGKVSIKGHHHHYISADHHGHVSTKEHHDHDTTFEEIIIGS
HisAc-D5-6    VYLSHHLHGDHSLFHLEHHGGKVSIKGHHHHYISADHHGHVSTKEHHDHDTTFEEIIIGS
HisAc-D4-6    VYLSHHLHGDHSLFHLEHHGGKVSIKGHHHHYISADHHGHVSTKEHHDHDTTFEEIIIGS
HisAc-D3-6    VYLSHHLHGDHSLFHLEHHGGKVSIKGHHHHYISADHHGHVSTKEHHDHDTTFEEIIIGS
HisAc-D2-6    VYLSHHLHGDHSLFHLEHHGGKVSIKGHHHHYISADHHGHVSTKEHHDHDTTFEEIIIGS
HisAc-D1-6    VYLSHHLHGDHSLFHLEHHGGKVSIKGHHHHYISADHHGHVSTKEHHDHDTTFEEIIIGS
DDFLN         VQDIDRSMDIALEEYEIPKIMDANDMNSLPDELSVITYVSYFRDYALNKEKRDADALAAL
Biotin-D2-6   ------------------------------------------------------------
```

```
HisAc-HisAc    GGSG■-------------------------------------------------------
HisAc          GGSG■-------------------------------------------------------
HisAc-C        GGSGC-------------------------------------------------------
HisAc-woC      GGSG--------------------------------------------------------
HisAc-D5-6     GGSG--------------------------------------------------------
HisAc-D4-6     GGSG--------------------------------------------------------
HisAc-D3-6     GGSG--------------------------------------------------------
HisAc-D2-6     GGSG--------------------------------------------------------
HisAc-D1-6     GGSGRETSDASKVEVYGPGVEGGFVNKSADFHIKAVNYYGEPLANGGEGFTVSVVGADGV
DDFLN          EKKRRETSDASKVEVYGPGVEGGFVNKSADFHIKAVNYYGEPLANGGEGFTVSVVGADGV
Biotin-D2-6    ------------------------------------------------------------

HisAc-HisAc    ------------------------------------------------------------
HisAc          ------------------------------------------------------------
HisAc-C        ------------------------------------------------------------
HisAc-woC      ------------------------------------------------------------
HisAc-D5-6     ------------------------------------------------------------
HisAc-D4-6     ------------------------------------------------------------
HisAc-D3-6     ------------------------------------------------------------
HisAc-D2-6     -----------------------------------------------IDGSDAQHSNAYGPG
HisAc-D1-6     EVPCKLVDNKNGIYDASYTATVPQDYTVVVQLDDVHCKDSPYNVKIDGSDAQHSNAYGPG
DDFLN          EVPCKLVDNKNGIYDASYTATVPQDYTVVVQLDDVHCKDSPYNVKIDGSDAQHSNAYGPG
Biotin-D2-6    ----------------------MAGGLNDIFEAQKIEWHEDTGIDGSDAQHSNAYGPG

HisAc-HisAc    ------------------------------------------------------------
HisAc          ------------------------------------------------------------
HisAc-C        ------------------------------------------------------------
HisAc-woC      ------------------------------------------------------------
HisAc-D5-6     ------------------------------------------------------------
HisAc-D4-6     ------------------------------------------------------------
HisAc-D3-6     ------------------------------------------------------------
HisAc-D2-6     LEGGKVGVPAAFKIQGRNKDGETVTQGGDDFTVKVQSPEGPVDAQIKDNGDGSYDVEYKP
HisAc-D1-6     LEGGKVGVPAAFKIQGRNKDGETVTQGGDDFTVKVQSPEGPVDAQIKDNGDGSYDVEYKP
DDFLN          LEGGKVGVPAAFKIQGRNKDGETVTQGGDDFTVKVQSPEGPVDAQIKDNGDGSYDVEYKP
Biotin-D2-6    LEGGKVGVPAAFKIQGRNKDGETVTQGGDDFTVKVQSPEGPVDAQIKDNGDGSYDVEYKP

HisAc-HisAc    ------------------------------------------------------------
HisAc          ------------------------------------------------------------
HisAc-C        ------------------------------------------------------------
HisAc-woC      ------------------------------------------------------------
HisAc-D5-6     ------------------------------------------------------------
HisAc-D4-6     ------------------------------------------------------------
HisAc-D3-6     -----------------------ILNSDSQNSYCDGPGFEKAQAKRPTEFTIHSVGAD
HisAc-D2-6     TKGGDHTVEVFLRGEPLAQGPTEVKILNSDSQNSYCDGPGFEKAQAKRPTEFTIHSVGAD
HisAc-D1-6     TKGGDHTVEVFLRGEPLAQGPTEVKILNSDSQNSYCDGPGFEKAQAKRPTEFTIHSVGAD
DDFLN          TKGGDHTVEVFLRGEPLAQGPTEVKILNSDSQNSYCDGPGFEKAQAKRPTEFTIHSVGAD
Biotin-D2-6    TKGGDHTVEVFLRGEPLAQGPTEVKILNSDSQNSYCDGPGFEKAQAKRPTEFTIHSVGAD

HisAc-HisAc    ------------------------------------------------------------
HisAc          ------------------------------------------------------------
HisAc-C        ------------------------------------------------------------
HisAc-woC      ------------------------------------------------------------
HisAc-D5-6     ------------------------------------------------------------
HisAc-D4-6     ------------------------------------------------------------
HisAc-D3-6     NKPCAAGGDPFQVSISGPHPVNVGITDNDDGTYTVAYTPEQPGDYEIQVTLNDEAIKDIP
HisAc-D2-6     NKPCAAGGDPFQVSISGPHPVNVGITDNDDGTYTVAYTPEQPGDYEIQVTLNDEAIKDIP
HisAc-D1-6     NKPCAAGGDPFQVSISGPHPVNVGITDNDDGTYTVAYTPEQPGDYEIQVTLNDEAIKDIP
DDFLN          NKPCAAGGDPFQVSISGPHPVNVGITDNDDGTYTVAYTPEQPGDYEIQVTLNDEAIKDIP
Biotin-D2-6    NKPCAAGGDPFQVSISGPHPVNVGITDNDDGTYTVAYTPEQPGDYEIQVTLNDEAIKDIP
```

```
HisAc-HisAc    ------------------------------------------------------------
HisAc          ------------------------------------------------------------
HisAc-C        ------------------------------------------------------------
HisAc-woC      ------------------------------------------------------------
HisAc-D5-6     ------------------------------------------------------------
HisAc-D4-6     -----KPAADPEKSYAEGPGLDGGECFQPSKFKIHAVDPDGVHRTDGGDGFVVTIEGPAP
HisAc-D3-6     KSIHIKPAADPEKSYAEGPGLDGGECFQPSKFKIHAVDPDGVHRTDGGDGFVVTIEGPAP
HisAc-D2-6     KSIHIKPAADPEKSYAEGPGLDGGECFQPSKFKIHAVDPDGVHRTDGGDGFVVTIEGPAP
HisAc-D1-6     KSIHIKPAADPEKSYAEGPGLDGGECFQPSKFKIHAVDPDGVHRTDGGDGFVVTIEGPAP
DDFLN          KSIHIKPAADPEKSYAEGPGLDGGECFQPSKFKIHAVDPDGVHRTDGGDGFVVTIEGPAP
Biotin-D2-6    KSIHIKPAADPEKSYAEGPGLDGGECFQPSKFKIHAVDPDGVHRTDGGDGFVVTIEGPAP

HisAc-HisAc    ------------------------------------------------------------
HisAc          ------------------------------------------------------------
HisAc-C        ------------------------------------------------------------
HisAc-woC      ------------------------------------------------------------
HisAc-D5-6     ---------------------------------------------KPAPSAEHSYAEGEG
HisAc-D4-6     VDPVMVDNGDGTYDVEFEPKEAGDYVINLTLDGDNVNGFPKTVTVKPAPSAEHSYAEGEG
HisAc-D3-6     VDPVMVDNGDGTYDVEFEPKEAGDYVINLTLDGDNVNGFPKTVTVKPAPSAEHSYAEGEG
HisAc-D2-6     VDPVMVDNGDGTYDVEFEPKEAGDYVINLTLDGDNVNGFPKTVTVKPAPSAEHSYAEGEG
HisAc-D1-6     VDPVMVDNGDGTYDVEFEPKEAGDYVINLTLDGDNVNGFPKTVTVKPAPSAEHSYAEGEG
DDFLN          VDPVMVDNGDGTYDVEFEPKEAGDYVINLTLDGDNVNGFPKTVTVKPAPSAEHSYAEGEG
Biotin-D2-6    VDPVMVDNGDGTYDVEFEPKEAGDYVINLTLDGDNVNGFPKTVTVKPAPSAEHSYAEGEG

HisAc-HisAc    ------------------------------------------------------------
HisAc          ------------------------------------------------------------
HisAc-C        ------------------------------------------------------------
HisAc-woC      ------------------------------------------------------------
HisAc-D5-6     LVKVFDNAPAEFTIFAVDTKGVARTDGGDPFEVAINGPDGLVVDAKVTDNNDGTYGVVYD
HisAc-D4-6     LVKVFDNAPAEFTIFAVDTKGVARTDGGDPFEVAINGPDGLVVDAKVTDNNDGTYGVVYD
HisAc-D3-6     LVKVFDNAPAEFTIFAVDTKGVARTDGGDPFEVAINGPDGLVVDAKVTDNNDGTYGVVYD
HisAc-D2-6     LVKVFDNAPAEFTIFAVDTKGVARTDGGDPFEVAINGPDGLVVDAKVTDNNDGTYGVVYD
HisAc-D1-6     LVKVFDNAPAEFTIFAVDTKGVARTDGGDPFEVAINGPDGLVVDAKVTDNNDGTYGVVYD
DDFLN          LVKVFDNAPAEFTIFAVDTKGVARTDGGDPFEVAINGPDGLVVDAKVTDNNDGTYGVVYD
Biotin-D2-6    LVKVFDNAPAEFTIFAVDTKGVARTDGGDPFEVAINGPDGLVVDAKVTDNNDGTYGVVYD

HisAc-HisAc    ------------------------------------------------------------
HisAc          ------------------------------------------------------------
HisAc-C        ------------------------------------------------------------
HisAc-woC      ------------------------------------------------------------
HisAc-D5-6     APVEGNYNVNVTLRGNPIKNMPIDVKCIEGANGEDSSFGSFTFTVAAKNKKGEVKTYGGD
HisAc-D4-6     APVEGNYNVNVTLRGNPIKNMPIDVKCIEGANGEDSSFGSFTFTVAAKNKKGEVKTYGGD
HisAc-D3-6     APVEGNYNVNVTLRGNPIKNMPIDVKCIEGANGEDSSFGSFTFTVAAKNKKGEVKTYGGD
HisAc-D2-6     APVEGNYNVNVTLRGNPIKNMPIDVKCIEGANGEDSSFGSFTFTVAAKNKKGEVKTYGGD
HisAc-D1-6     APVEGNYNVNVTLRGNPIKNMPIDVKCIEGANGEDSSFGSFTFTVAAKNKKGEVKTYGGD
DDFLN          APVEGNYNVNVTLRGNPIKNMPIDVKCIEGANGEDSSFGSFTFTVAAKNKKGEVKTYGGD
Biotin-D2-6    APVEGNYNVNVTLRGNPIKNMPIDVKCIEGANGEDSSFGSFTFTVAAKNKKGEVKTYGGD

HisAc-HisAc    ------------------------------------------------------------
HisAc          ------------------------------------------------------------
HisAc-C        ------------------------------------------------------------
HisAc-woC      ------------------------------------------------------------
HisAc-D5-6     KFEVSITGPAEEITLDAIDNQDGTYTAAYSLVGNGRFSTGVKLNGKHIEGSPFKQVLGNP
HisAc-D4-6     KFEVSITGPAEEITLDAIDNQDGTYTAAYSLVGNGRFSTGVKLNGKHIEGSPFKQVLGNP
HisAc-D3-6     KFEVSITGPAEEITLDAIDNQDGTYTAAYSLVGNGRFSTGVKLNGKHIEGSPFKQVLGNP
HisAc-D2-6     KFEVSITGPAEEITLDAIDNQDGTYTAAYSLVGNGRFSTGVKLNGKHIEGSPFKQVLGNP
HisAc-D1-6     KFEVSITGPAEEITLDAIDNQDGTYTAAYSLVGNGRFSTGVKLNGKHIEGSPFKQVLGNP
DDFLN          KFEVSITGPAEEITLDAIDNQDGTYTAAYSLVGNGRFSTGVKLNGKHIEGSPFKQVLGNP
Biotin-D2-6    KFEVSITGPAEEITLDAIDNQDGTYTAAYSLVGNGRFSTGVKLNGKHIEGSPFKQVLGNP
```

```
HisAc-HisAc      ----------------
HisAc            ----------------
HisAc-C          ----------------
HisAc-woC        ----------------
HisAc-D5-6       GKKNPEVKSFTTTRTAN
HisAc-D4-6       GKKNPEVKSFTTTRTAN
HisAc-D3-6       GKKNPEVKSFTTTRTAN
HisAc-D2-6       GKKNPEVKSFTTTRTAN
HisAc-D1-6       GKKNPEVKSFTTTRTAN
DDFLN            GKKNPEVKSFTTTRTAN
Biotin-D2-6      GKKNPEVKSFTTTRTAN
```

6.7 Network Parameters
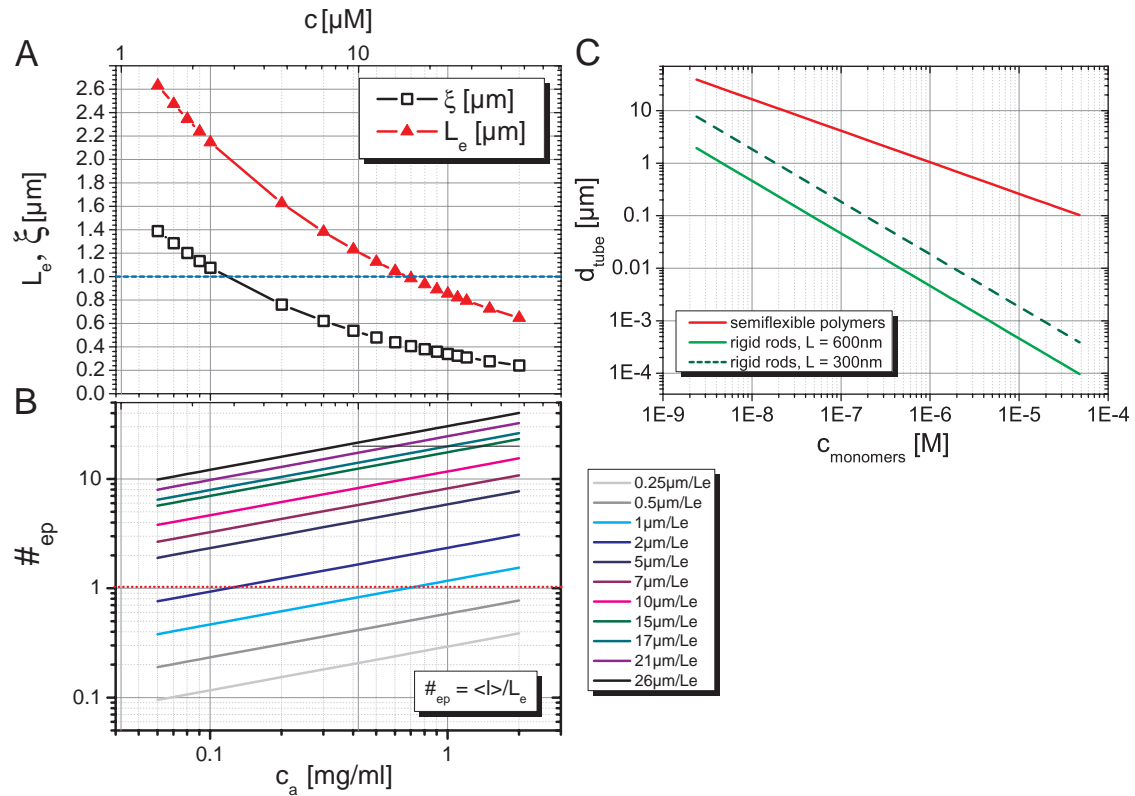
Figure 6.16: (A) Plot of the calculated entanglement length (cf. eq. 1.15 with prefactor $b = 2^{\frac{1}{5}}$) and meshsize (cf. eq. 1.21) in dependence of the actin filament concentration. At a concentration of $c_a = 0.75$ mg/ml an entanglement point density $\#_{e.p.}$ of $\frac{1}{(\mu m)^3}$ is reached. (B) Calculated number of the entanglement points in dependence of the actin concentration and filament length using eq. 3.1. The theoretical entanglement crossover for $c_a = 0.4$ mg/ml lies between 1-2 μm of filament length and is indicated by the red dashed line. (C) Plot of the calculated tube diameter (for semiflexible filaments e.g actin the calculation followed eq.1.14, and for stiff polymer filaments [Doi & Edwards, 1989]) in dependence of the filament concentration. $c_{monomers}$ corresponds to $c^{\star\star}$ if $d_{tube} = d_{rod}$.

6.8   Used Buffers

G-buffer (**Tris**) **pH** $= 8.0$

SUBSTANCE	MOLAR MASS IN [mg/mmol]	CONCENTRATION [mM]
Tris	121.1	2
$CaCl_2$	147	0.2
(ATP)	551.2	0.2
NaN_3	20%v solution	0.005%v
DTT	154.2	0.2

10x-F-buffer (**Tris**) **pH** $= 7.5$ **low salt concentrations**

SUBSTANCE	MOLAR MASS IN [mg/mmol]	CONCENTRATION [mM]
Tris	121.1	20
$MgCl_2$	203.3	10
ATP	551.2	5
(DTT)	154.2	2

10x-F-buffer (**Tris**) **pH** $= 7.5$

SUBSTANCE	MOLAR MASS IN [mg/mmol]	CONCENTRATION [mM]
Tris	121.1	20
$CaCl_2$	147	2
KCl	74.56	1000
$MgCl_2$	203.3	20
(ATP)	551.2	5
DTT	154.2	2

10x-F-buffer (**Mes**) **pH** $= 6.0$

SUBSTANCE	MOLAR MASS IN [mg/mmol]	CONCENTRATION [mM]
Mes	195.2	100
$CaCl_2$	147	2
KCl	74.56	1000
$MgCl_2$	203.3	20
ATP	551.2	5
(DTT)	154.2	2

10x-F-buffer (**Hepes**) **pH** $= 6.0, 6.5, 7.0, 7.5, 8.0$

SUBSTANCE	MOLAR MASS IN [mg/mmol]	CONCENTRATION [mM]
Hepes	238.3	100
$CaCl_2$	147	2
KCl	74.56	1000
$MgCl_2$	203.3	10
DTT	154.2	2

The 10x-G-Tris and 10x-F-Tris buffer was produced with or without ATP, if necessitated for measurements with HMM.

The 10x-F-Tris buffer contained 500 mM KCl for the experiments of chaps. 3.1, 3.1.2, 3.3.

The 10x-F-Mes buffer with or without DTT was used for measurements with the synthetic cross-links, if necessary.

10x-DMEM buffer

SUBSTANCE	MOLAR MASS IN [mg/mmol]	CONCENTRATION [mM]
D − Glucose	180.16	25
Phenol Red	354.4	22.6
NaN$_3$	20%v solution	0.005%v

Hepes buffer

SUBSTANCE	MOLAR MASS IN [mg/mmol]	CONCENTRATION [mM]
Hepes	238.3	20

Basic buffer pH = 12.0

SUBSTANCE	MOLAR MASS IN [mg/mmol]	CONCENTRATION [mM]
KOH	56.11	50
EDTA	372.24	1

Neutralization buffer pH = 7.5

SUBSTANCE	MOLAR MASS IN [mg/mmol]	CONCENTRATION [mM]
KOH	56.11	50
Acetic acid	60	250
K$_3$PO$_4$	212.28	250
EDTA	372.24	5

6.9   Abbreviations

aa	amino acid
ABP	actin binding protein
ABD	actin binding domain
app.	appendix
ADP	Adenosine-diphosphate
ATP	Adenosine-triphosphate
Av	Avidin
CI	Cortexillin I
chap	chapter
cryo	cryogenic
dd	Dictyostelium discoideum
ddFln	Dictyostelium discoideum Filamin
ddH_20	double de-ionized water
DSO	direct strain oscillation
DTT	Dithiothreitol
ECM	extra cellular matrix
EM	electron microscope
eq	equation
F-actin	filamenteous actin
Fas	Fascin
fig	figure
FFT	Fast Fourier Transformation
FJC	Freely Jointed Chain
G-actin	globular actin
ggFln	Gallus gallus Filamin
GWLC	Glassy Worm-Like Chain
HC	heavy chain
hisac	Hisactophilin
HMM	Heavy meromyosin
IC	ideal chain
Ig	Immunoglobuline
LAOS	large amplitude oscillatory shear
LC	light chain
LMM	Light Mero Myosin
MCR	MCR301 rheometer

MES	2-[N-Morpholino]ethane sulfonic acid
min	minute
MM	molecular motor
MT	Magnetic Tweezer
MTs	microtubules
MW	molecular weight
MyoII	Myosin II
NPC	nuclear pore complex
NSP1	nucleocytoskeletal protein 1
NTR	nuclear transport receptor
NUP	nucleoporin
PBS	phosphate buffered saline
PDB	Protein data bank
PEG	polyethylene glycol
PEO	polyethylene oxide
PIP_2	phosphatidylinositol bisphosphate
pnr	product number
POE	polyoxyethylene
Q10	coenzyme Q10
RC	real chain
rpm	rotations per minute
s	second
tab	table
TDR	Torsional Disc Rheometer
TEM	transmission electron microscopy
Tris	Tris $-$ (hydroxymethyl) aminomethan
TRITC	Tetramethyl rhodamin isothiocyanat
VFT	Vogel-Fulcher-Tammann
w	with
WLC	Worm-Like Chain
wo	without

6.10 Symbols

A	amplitude
A	area
α	absorbance
β	biotinylation grade
b	Kuhn segment length
c	concentration
$c^\star$	crossover concentration from dilute to semi-dilute regime
$c^{\star\star}$	crossover concentration from semi-dilute concentrated regime
c_c	critical concentration
c_a	actin concentration in solution
c_p	polymer concentration
c_0	initial concentration
χ	mean distance between rigid rods
δ	working distance
d	diameter
d_t	tube diameter
D	domain
D	diffusion coefficient
D_r	reptational diffusion coefficient
Da	Dalton [g/mol]
D_0	diameter of single filament
D_B	bundle diameter of actin filaments
η	static viscosity
η_0	zero shear rate viscosity
E_F	free energy
E_A	activation energy
f	frequency
f_e	euler force
ϵ	extinction coefficient
F	force
F_N	normal force
G	Youngs modulus
G'	storage modulus
G''	loss modulus
$G(t)$	relaxation modulus

G_L	secant modulus
G_M	tangent modulus
G_0	plateau modulus
$|G^*|$	absolute value of shear modulus
ΔG	free enthalpy
h	height
γ	strain
γ_c	critical strain
γ_d	drag coefficient
γ_{max}	maximum strain
$\dot{\gamma}$	shear rate
$J(t)$	creep compliance
κ	flexural rigidity
κ_b	bending rigidity
κ_s	stretching rigidity
k	spring constant
K	differential modulus
K'	differential modulus at constant frequency
K'_{lin}	linear differential modulus
K_D	dissociation constant
K_{max}	maximum differential modulus
$K_{tension}$	elastic stretching modulus
k_{ATPase}	ATPase rate
k_{off}	on rate (constant for detachment)
k_{on}	off rate (constant for attachment)
k_B	Boltzmann constant
l_c	cross linker distance
l_p	persistence length
l	end to end distance
l	diffusion length
λ_n	wavelength of eigenmode n
Λ_e	interaction length
$\langle l \rangle$	mean length
$\langle l \rangle_{crit}$	critical mean length
L	length
L_c	contour length
L_e	entanglement length

M_w	molar weight
M	molar [g/L]
n	number, order of eigenmodes
N_K	Number of Kuhn monomers
ν	dynamic viscosity
Pa	Pascal
p_d	path distance
P_i	Phosphate
P	probability
P_1	probability of single myosin head binding
π_N	normal force normalized on unit area
Φ	loss angle
r	duty ratio
ρ	density
ρ_l	line density
R_g	radius of gyration
$R_{A/G} = c_{actin}/c_{gelsolin}$	molar ratio of actin to gelsolin monomers
$R = c_{cross-link}/c_{actin}$	molar ratio of cross linker to actin monomers
$R^\star, R^{\star\star}$	crossover molar ratio
$\langle R^2 \rangle$	mean square end to end distance
S	entropy
σ	tension
σ_c	critical prestress
σ_{max}	maximum prestress
T	temperature
T_m	melting temperature
t	time
t_{drag}	drag time
t_{trans}	transition time
τ	stress
τ_{max}	maximum stress
τ_e	entanglement time
τ_n	relaxation time
τ_{on}	power stroke duration
τ_r	repation time
τ_{cycle}	cross bridge cycle duration
U	potential energy

V	volt
V	volume
ε	stretching parameter
φ	phase angle
ϱ	diameter to length ratio
v_{max}	maximum velocity
ξ	meshsize
ζ	drag coefficient of filament in tube
x	-fold
x	bundle scaling exponent
y	cross-linking scaling exponent
z	plateau modulus scaling exponent
% w	weight per weight percentage
#	count
$\#_{ep}$	number of entanglement points per filament

Bibliography

[Adam, 2001] Adam, S. A. (2001). The nuclear pore complex. *Genome Biology*, 2(9), 1s–6s.

[Agarkova & Perriard, 2005] Agarkova, I. & Perriard, J. (2005). The M-band: an elastic web that crosslinks thick filaments in the center of the sarcomer. *Trends in Cell Biology*, 15(9), 477s–485s.

[Alberts et al., 1995] Alberts, B., Bray, D., Lewis, J., Raff, M., Roberts, K., & Watson, J. D. (1995). *Molekularbiologie der Zelle*. D 68451 Weinheim: VCH Verlagsgesellschaft mbH, 3nd edition.

[Angelini et al., 2003] Angelini, T. E., Liang, H., Wriggers, W., & Wong, G. C. L. (2003). Like-charge attraction between polyelectrolytes induced by counterion charge density waves. *PNAS*, 100, 8634s–8637s.

[Bagshaw, 1993] Bagshaw, C. R. (1993). *Muscle contraction*. Chapman and Hall, 2-6 Boundary Row, London SE1 8HN, UK, 2 edition.

[Bakouche et al., 2006] Bakouche, F., Haviv, L., Groswasser, D., & Bernheim-Groswasser, A. (2006). Active gels: dynamics of patterning and self-organization. *Physical Biology*, 3, 264s–273s.

[Ball & Ullman, 2005] Ball, J. R. & Ullman, K. S. (2005). Versatility at the nuclear pore complex: lessons learned from the nucleoporin nup153. *Chromosoma*, 114(5), 319s–330s.

[Barton & Goldstein, 1996] Barton, N. R. & Goldstein, L. S. B. (1996). Going mobile: microtubule motors and chromosome segregation. *PNAS*, 93, 1735s–1742s.

[Bausch, 1999] Bausch, A. R. (1999). *Mikromechanische Untersuchung des Zytoplasmas, der Zellmembran und der Adhäsion mittels Magnetischer Pinzetten*. PhD thesis, E22, TUM.

[Bausch & Kroy, 2006] Bausch, A. R. & Kroy, K. (2006). A bottom-up approach to cell mechanics. *Nature Physics*, 2, 231s–238s.

[Bechinger et al., 1999] Bechinger, C., Grünberg, H., & Leiderer, P. (1999). Entropische Kräfte. *Physikalische Blätter*, 55(12), 53s–56s.

[Behrisch et al., 1995] Behrisch, A., Dietrich, C., Noegel, A. A., Schleicher, M., & Sackmann, E. (1995). The actin-binding protein hisactophilin binds in vitro to partially charged membranes and mediates actin coupling to membranes. *Biochemistry*, 34, 15182s–15190s.

[Bischofs & Schwarz, 2003] Bischofs, I. B. & Schwarz, U. S. (2003). Cell organization in soft media due to active mechanosensing. *PNAS*, 100, 9274s–9279s.

[Blanchoin & Pollard, 2002] Blanchoin, L. & Pollard, T. D. (2002). Hydrolysis of bound atp by polymerized actin depends on the bound divalent cation but not profilin. *Biochemistry*, 41, 597s–602s.

[Boal, 2006] Boal, D. (2006). *Mechanics of the cell*. USA, New York: Cambridge University Press, 4nd edition.

[Borukhov et al., 2005] Borukhov, I., Bruinsma, R. F., Gelbart, W. M., & Liu, A. J. (2005). Structural polymorphism of the cytoskeleton: a model of linker-assisted filament aggregation. *PNAS*, 102(10), 3673s–3678s.

[Brangwynne et al., 2007] Brangwynne, C. P., Koenderink, G. H., Barry, E., Dogic, Z., MacKintosh, F. C., & Weitz, D. A. (2007). Bending dynamics of fluctuating biopolymers probed by automated high-resolution filament tracking. *Biophysical Journal*, doi:10.1529/biophysj.106.096966.

[Brangwynne et al., 2008] Brangwynne, C. P., Koenderink, G. H., MacKintosh, F. C., & Weitz, D. A. (2008). Nonequilibrium microtubule fluctuations in a model cytoskeleton. *Physical Review Letters*, 100, 118104–1s–118104–4s.

[Bryan, 1988] Bryan, J. (1988). Gelsolin has three actin binding sites. *J. Cell Biol.*, 106, 1553s–1562s.

[Bullit et al., 1988] Bullit, E. S. A., Derosier, D. J., Coluccio, L. M., & Tilney, L. G. (1988). Three-dimensional reconstitution of an actin bundle. *J. Cell Biol.*, 104, 491s–501s.

[Carlier & Pantaloni, 1986] Carlier, M. F. & Pantaloni, D. (1986). Direct evidence for ADP-Pi-f-actin as the major intermediate in ATP-actin polymerization. Rate of dissociation of Pi from actin filaments. *Biochemistry*, 25, 7789s–7792s.

[Claessens et al., 2006a] Claessens, M., Bathe, M., Frey, E., & Bausch, A. (2006a). Actin-binding proteins sensitively mediate f-actin bundle stiffness. *Nature Materials*, 5, 748s–753s.

[Claessens et al., 2008] Claessens, M. M. A. E., Semmrich, C., Ramos, L., & Bausch, A. R. (2008). Helical twist controls the thickness of f-actin bundles. *PNAS*, 105(26), 8819s–8822s.

[Claessens et al., 2006b] Claessens, M. M. A. E., Tharmann, R., Kroy, K., & Bausch, A. R. (2006b). Microrheology of geometrically confined actin networks. *Nature Physics*, 2, 186s–189s.

[Cooper et al., 1987] Cooper, J. A., Bryan, J., 3d, B. S., Frieden, C., Loftus, D. J., & Elson, E. L. (1987). Macroinjection of gelsolin into living cells. *J. Cell Biol.*, 104, 491s–501s.

[Coppin & Leavis, 1992] Coppin, C. M. & Leavis, P. C. (1992). Quantitation in liquid-crystalline ordering in f-actin solutions. *Biophysical Journal*, 63, 794s.

[Cruz et al., 2000] Cruz, E. M. D. L., Mandinova, A., Steinmetz, M. O., Stoffler, D., Aebi, U., & Pollard, T. D. (2000). Polymerization and structure of nucleotide-free actin filaments. *J. Mol. Biol.*, 295, 517s–526s.

[de Gennes, 1979] de Gennes, P. G. (1979). *Scaling concepts in polymer physics*. Cornell University Press, London.

[Doi & Edwards, 1989] Doi, M. & Edwards, S. F. (1989). *Theorie of polymer dynamics*. Oxford Science Publications.

[Donald J. Voet, 2004] Donald J. Voet, J. G. V. (2004). *Biochemistry*. USA MA01923 Danvers 222 Rosewood Drive: John Wiley and Sons, Inc., 3rd edition.

[Ellis, 2001] Ellis, R. J. (2001). Macromolecular crowding: an important but neglected aspect of the intracellular environment. *Current Opinion in Structural Biology*, 11, 114s–119s.

[Ewoldt et al., 2007] Ewoldt, R. H., McKinley, G. H., & Hosoi, A. E. (2007). Fingerprinting soft materials: a framework for characterizing nonlinear viscoelasticity. *Cond. Soft Mat.*, arXiv:0710.5509, 1s–10s.

[Faix et al., 1996] Faix, J., Steinmetz, M., Boves, H., Kammerer, R. A., Lottspeich, F., Mintert, U., Murphy, J., Stock, A., Aebi, U., & Gerisch, G. (1996). Cortexillins, major determinants of cell shape and size, are actin-bundling proteins with a parellel coiled-coil tail. *The Cell*, 86, 631s–642s.

[Fernández et al., 2008] Fernández, P., Grosser, S., & Kroy, K. (2008). A unit-cell approach to the nonlinear rheology of biopolymer solutions. *submitted to Soft Matter*.

[Fernández et al., 2006] Fernández, P., Pullarkat, P. A., & Ott, A. (2006). A master relation defines the nonlinear viscoelasticity of single fibroblasts. *Biophysical Journal*, 90, 3796s–3805s.

[Ferry, 1980] Ferry, J. D. (1980). *Viscoelastic properties of polymers*. John Wiley and Sons Inc.

[Frey, 2001] Frey, E. (2001). *Physics in cell biology: actin as a model system for polymer physics*. Adv. in Solid State Physics.

[Frey & Görlich, 2007] Frey, S. & Görlich, D. (2007). A saturated fg-repeat hydrogel can reproduce the permeability properties of nuclear pore complexes. *The Cell*, 130, 512s–523s.

[Frey et al., 2006] Frey, S., Richter, R. P., & Görlich, D. (2006). Fg-rich repeats of nuclear pore proteins form a three-dimensional meshwork with hydrogel-like properties. *Science*, 314, 815s–817s.

[Fucini et al., 1999] Fucini, P., Köppel, B., Schleicher, M., Lustig, A., Holak, T. A., Müller, R., Stewar, M., & Noegel, A. A. (1999). Molecular architecture of the rod domain of the dictyostelium gelation factor abp120. *J. Mol. Biol.*, 291, 1017s–1023s.

[Furuike et al., 2001] Furuike, S., Ito, T., & Yamazaki, M. (2001). Mechanical unfolding of single filamin A (ABP-280) molecules detected by atomic force microscopy. *FEBS Letters*, 498, 72s–75s.

[Gardel et al., 2006a] Gardel, M. L., Nakamura, F., Hartwig, J., Stossel, J. C. C. T. P., & Weitz, D. A. (2006a). Prestressed f-actin networks cross-linked by hinged filamins replicate mechanical properties of cells. *PNAS*, 103(6), 1762s–1767s.

[Gardel et al., 2006b] Gardel, M. L., Nakamura, F., Hartwig, J., Stossel, J. C. C. T. P., & Weitz, D. A. (2006b). Stress-dependent elasticity of composite actin networks as a model for cell behavior. *Physical Review Letters*, 96, 088102–1s–088102–4s.

[Gardel et al., 2004a] Gardel, M. L., Shin, J. H., MacKintosh, F. C., Mahadevan, L., Matsudaira, P., & Weitz, D. A. (2004a). Elastic behavior of cross-linked and bundled actin networks. *Science*, 304, 1301s–1305s.

[Gardel et al., 2004b] Gardel, M. L., Shin, J. H., MacKintosh, F. C., Mahadevan, L., Matsudaira, P. A., & Weitz, D. A. (2004b). Scaling of f-actin network rheology to probe single filament elasticity and dynamics. *Physical Review Letters*, 93(18), 188102–1s–188102–4s.

[Gardel et al., 2003] Gardel, M. L., Valentine, M. T., Crocker, J. C., Bausch, A. R., & Weitz, D. A. (2003). Mikrorheology of entangled f-actin solutions. *Physical Review Letters*, 91(15), 158302–1s–158302–4s.

[Gittes & MacKintosh, 1998] Gittes, F. & MacKintosh, F. C. (1998). Dynamic shear modulus of a semiflexible polymer network. *Physical Review E*, 58(2), 1241s–1244s.

[Gittes et al., 1993] Gittes, F., Mickey, B., Nettleton, J., & Howard, J. (1993). Flexural rigidity of microtubules and actin filaments measured from thermal fluctuations in shape. *Journal of Cell Biology*, 120(4), 923s–934s.

[Glaser et al., 2008] Glaser, J., Hubert, C., & Kroy, K. (2008). Dynamics of sticky polymer solutions. *Proceedings of the 9th International Conference Path Integrals - New Trends and Perspectives*.

[Goddette & Frieden, 1986] Goddette, D. W. & Frieden, C. (1986). Actin polymerisation: the mechanism of action of cytoschalasin D. *J. Biol. Chem.*, 261, 15974s–15980s.

[Goff et al., 2002] Goff, L. L., Hallatschek, O., Frey, E., & Amblard, F. (2002). Tracer studies on f-actin fluctuations. *Physical Review Letters*, 89(25), 8101s–8105s.

[Hanein et al., 1997] Hanein, D., Matsudaira, P., & DeRosier, D. J. (1997). Evidence for a conformational change in actin induced by fimbrin N375 binding. *J. Cell Biol.*, 139(2), 387s–396s.

[Head et al., 2003] Head, D. A., Levine, A. J., & MacKintosh, F. C. (2003). Deformation of cross-linked semiflexible polymer networks. *Physical Review Letters*, 91(10), 108102–1s–108102–4s.

[Heussinger & Frey, 2006] Heussinger, C. & Frey, E. (2006). Floppy modes and nonaffine deformations in random fiber networks. *Physical Review Letters*, 97(10), 105501–1s–105501–4s.

[Hinner et al., 1998] Hinner, B., Tempel, M., Sackmann, E., Kroy, K., & Frey, E. (1998). Entanglement, elasticity and viscous relaxation of actin solutions. *Physical Review Letters*, 81(12), 2614s–2617s.

[Hinsch et al., 2007] Hinsch, H., Wilhelm, J., & Frey, E. (2007). Quantitative tube model for semiflexible polymer solutions. *European Physical Journal E*, 24, 35s–46s.

[Hodge & Cope, 2000] Hodge, T. & Cope, M. J. T. V. (2000). A myosin family tree. *J. Cell Science*, 113(19), 3353s–3354s.

[Hosek & Tang, 2004] Hosek, M. & Tang, J. X. (2004). Polymer-induced bundling of f-actin and the depletion force. *Physical Review E*, 69, 051907–1s–051907–9s.

[Hou et al., 1990] Hou, L., Phelps, K. L., & Lanni, F. (1990). Brownian motion of inert tracer macromolecules in polymerized and spontaneously bundled mixtures of actin and filamin. *J. Cell Biol.*, 110, 1645s–1654s.

[Howard, 2001] Howard, J. (2001). *Mechanics of motor proteins and the cytoskeleton*. 23 Plumtree Road, Sunderland, MA 01375 USA: Sinauer Associates, Inc.

[Howard & Ashmore, 1986] Howard, J. & Ashmore, J. F. (1986). Stiffness of sensory hair-bundles in the sacculus of the frog. *Hearing Res.*, 23, 93s–104s.

[Humphrey et al., 2002] Humphrey, D., Duggan, C., Saha, D., Smith, D., & Käs, J. (2002). Active fluidization of polymer networks through molecular motors. *Nature*, 416, 413s–416s.

[Huxley, 1969] Huxley, H. E. (1969). The mechanism of muscular contraction. *Science*, 164(886), 1356s–1365s.

[Isambert & Maggs, 1996] Isambert, H. & Maggs, A. C. (1996). Dynamics and rheology of actin solutions. *Macromolecules*, 29, 1036s–1040s.

[J. A. Åström et al., 2008] J. A. Åström, P. B. S. K., Vattulainen, I., & Karttunen, M. (2008). Strain hardening, avalanches and strain softening in dense cross-linked actin networks. *Physical Review E*, 77, 051913–1s–051913–6s.

[Janmey et al., 2007] Janmey, P. A., McCormick, M. E., Rammensee, S., Leight, J. L., Georges, P. C., & MacKintosh, F. C. (2007). Negative normal stress in semiflexible biopolymer gels. *Nature*, 6, 48s–51s.

[Janmey et al., 1986] Janmey, P. A., Peetermans, J., Zaner, K. S., Stossel, T. P., & Tanaka, T. (1986). Structure and mobility of actin filaments measured by quasielastic light scattering, viscosimetry and electron microscopy. *J. Biol. Chem.*, 261, 8357s–8362s.

[Kabsch et al., 1990] Kabsch, W., Mannherz, H. G., Suck, D., Pai, E. F., & Holmes, K. C. (1990). Atomic structure of the actin: DNase I complex. *Nature*, 347, 37s–44s.

[Kaufmann et al., 1992] Kaufmann, S., J., K., H., G. W., E., S., & G., I. (1992). Talin anchors and nucleates actin filaments at lipid membranes. *FEBS Letters*, 314, 203s–205s.

[Keller, 2003] Keller, M. (2003). *Aktive und passive Aktin-Myosin-Neztwerke*. PhD thesis, E22 TUM.

[Köhler et al., 2008] Köhler, S., Lieleg, O., & Bausch, A. R. (2008). Rheological characterization of the bundling transition in f-actin solutions induced by mehtylcellulose. *PLOS one*, 3(7, e236), 1s–5s.

[Kroy, 1998] Kroy, K. (1998). *Viskoelastizität von Lösungen halbsteifer Polymere*. PhD thesis, TUM.

[Kroy & Glaser, 2007] Kroy, K. & Glaser, J. (2007). The glassy wormlike chain. *New Journal of Physics*, 9, 416s–428s.

[Kulkarni et al., 2000] Kulkarni, A. M., Chatterjee, A. P., Schweizer, K. S., & Zukoski, C. F. (2000). Effects of polyethylene glycol on protein interactions. *Journal of Chemical Physics*, 113(21), 9863s–9873s.

[Kulp & Herzfeld, 1995] Kulp, D. T. & Herzfeld, J. (1995). Crowding-induced organization of cytoskeletal elements. III. spontaneous bundling and sorting of self-assembled filaments with different flexibilities. *Biophysical Chemistry*, 57(1), 93s–102s.

[Landau & Lifschitz, 1966] Landau, L. D. & Lifschitz, E. M. (1966). *Lehrbuch der Theoretischen Physik, Hydrodynamik*, volume 6. Akademie - Verlag Berlin.

[Lieleg, 2005] Lieleg, O. (2005). Untersuchung des Phasenverhaltens und der mikromechanischen Eigenschaften von Biopolymer-Netzwerken.

[Lieleg, 2008] Lieleg, O. (2008). *Model systems of the actin cortex*. PhD thesis, E27 TUM.

[Lieleg & Bausch, 2007] Lieleg, O. & Bausch, A. R. (2007). Cross-linker unbinding and self-similarity in bundled cytoskeletal networks. *Physical Review Letters*, 99, 158105–1s–158105–4s.

[Lieleg et al., 2007] Lieleg, O., Claessens, M. M. A. E., Heussinger, C., Frey, E., & Bausch, A. R. (2007). Mechanics of bundled semiflexible polymer networks. *Physical Review Letters*, 99, 088102–1s–088102–4s.

[Limozin & Sackmann, 2002] Limozin, L. & Sackmann, E. (2002). Polymorphism of cross-linked actin networks in giant vesicles. *Physical Review Letters*, 89(16), 168103–1s–168103–4s.

[Liu et al., 2006] Liu, J., Gardel, M. L., Kroy, K., Frey, E., Hoffman, B., Crocker, J. C., Bausch, A. R., & Weitz, D. A. (2006). Microrheology probes length scale dependent rheology. *Physical Review Letters*, 96, 118104–1s–118104–4s.

[Liu & Pollack, 2002] Liu, X. & Pollack, G. H. (2002). Mechanics of f-actin characterized with microfabricated cantilevers. *Biophysical Journal*, 83, 2705s–2715s.

[Liverpool, 2003] Liverpool, T. B. (2003). Anomalous fluctuations of active polar filaments. *Physical Review E*, 67, 031909–1s–031909–5s.

[Liverpool et al., 2001] Liverpool, T. B., Maggs, A. C., & Ajdari, A. (2001). Viscoelasticity of solutions of motile polymers. *Physical Review Letters*, 86(18).

[Liverpool & Marchetti, 2003] Liverpool, T. B. & Marchetti, M. C. (2003). Instabilities of isotropic solutions of active polar filaments. *Physical Review Letters*, 90, 138102s–138106s.

[Lodish et al., 2000] Lodish, H., Berk, A., Zipursky, S. L., Matsudaira, P., Baltimore, D., & Darnell, J. (2000). *Molecular Cell Biology*. USA 10010 New York: W. H. Freeman and Company, 4th edition.

[Lowey et al., 1969] Lowey, S., Slayter, H. S., Weeds, A. G., & Baker, H. (1969). Substructure of the myosin molecule: I. subfragments of myosin by enzymic degradation. *Journal of Molecular Biology*, 42, 1s–20s.

[Luan et al., 2008] Luan, Y., Lieleg, O., Wagner, B., & Bausch, A. R. (2008). Micro- and macrorheological properties of isotropically cross-linked actin networks. *Biophysical Journal*, 94, 1s–6s.

[MacKintosh & Käs, 1995] MacKintosh, F. C. & Käs, J. (1995). Elasticity of semiflexible biopolymer networks. *Physical Review Letters*, 75(24), 4425s–4428s.

[Madden & Herzfeld, 1993] Madden, T. L. & Herzfeld, J. (1993). Crowding-induced organization of cytoskeletal elements: I. spontaneous demixing of cytosolic proteins and model filaments to form filament bundles. *Biophysical Journal*, 65(3), 1147s–1154s.

[Marko & Siggia, 1995] Marko, J. F. & Siggia, E. D. (1995). Stretching DNA. *Macromolecules*, 28(26), 8759s–8770s.

[Mason et al., 2000] Mason, T. G., Gisler, T., Kroy, K., Frey, E., & Weitz, D. A. (2000). Rheology of f-actin solutions determined from thermally driven tracer motion. *Soc. of Rheol. , Inc.*, 44(4), 917s–928s.

[McCoy et al., 1999] McCoy, A. J., Fucini, P., Noegel, A. A., & Stewart, M. (1999). Structural basis for dimerization of the dictyostlium gelation factor (abp120) rod. *Nature*, 6(9), 836s – 841s.

[Medeiros et al., 2006] Medeiros, N. A., Burnette, D. T., & Forscher, P. (2006). Hydration of DMPC and DPPC at 4°C produces a novel subgel phase with convex-concave bilayer curvatures. *CPL*, 105, 149s–166s.

[Meyer & Aebi, 1990] Meyer, R. K. & Aebi, U. (1990). Bundling of actin filaments by α-actinin depends on its molecular length. *Journal of Cell Biology*, 110, 2013s–2024s.

[Ming et al., 2003] Ming, D., Kong, Y., Wu, Y., & Ma, J. (2003). Simulation of f-actin filaments of several microns. *Biophysical Journal*, 85, 27s–35s.

[Müller, 1991] Müller, O. (1991). *Entwicklung eines Rheometers zur Untersuchung viskoelastischer Eigenschaften membranassoziierter Aktinnetzwerke im verdünnten und halb-verdünnten Bereich.* PhD thesis, E22 TUM.

[Morse, 1998a] Morse, D. C. (1998a). Viscoelasticity of concentrated isotropic solutions of semiflexible polymers. 1. model and stress tensor. *Macromolecules*, 31, 7030s–7043s.

[Morse, 1998b] Morse, D. C. (1998b). Viscoelasticity of concentrated isotropic solutions of semiflexible polymers. 2. linear response. *Macromolecules*, 31, 7044s–7067s.

[Nédélec et al., 1997] Nédélec, F. J., Surrey, T., Maggs, A. C., & Leibler, S. (1997). Self-organization of microtubules and motors. *Nature*, 389(6648), 305s–308s.

[Niederman & Pollard, 1975] Niederman, R. & Pollard, T. D. (1975). Human platelet myosin. *Journal of Cell Biology*, 67, 72s–92s.

[Niranjan et al., 2001] Niranjan, P. S., Forbes, J. G., Greer, S. C., Freed, J. D., Freed, K. F., & Douglas, J. F. (2001). Thermodynamic regulation of actin polymerization. *J. of Chem. Phys.*, 114(24), 10573s–10576s.

[Odjik, 1983] Odjik, T. (1983). On the statistics and dynamics of confined or entagnled stiff polymers. *Macromolecules*, 16, 1340s–1344s.

[Odjik, 1995] Odjik, T. (1995). Stiff chains and filaments under tension. *Macromolecules*, 28, 7016s–7018s.

[Ono et al., 1997] Ono, S., Yamakita, Y., Yamashiro, S., Matsudaira, P. T., Gnarra, J. R., Obinata, T., & Matsumura, F. (1997). Identification of an actin binding region and a protein kinase c phosphorylation site on human fascin. *The Journal of Biological Chemistry*, 272(4), 2527s–2533s.

[Ott et al., 1993] Ott, A., Magnasco, M., Simon, A., & Libchaber, A. (1993). Measurement of the persistence length of polymerized actin using fluorescence microscopy. *Physical Review E*, 48(3), 1642s–1645s.

[Paar, 2004] Paar, A. (2004). *Physica MCRxx1 series: instruction manuel*. Anton Paar GmbH, Ostfildern, Germany.

[Passard et al., 1998] Passard, J., Njiwa, R. K., & Perré, P. (1998). Unsteady flow in cone and plate geometry: how computation can help rheometry. *Eur. Phys. J. AP*, 3, 321s–342s.

[Peppe & Drucker, 1979] Peppe, F. A. & Drucker, B. (1979). The myosin filament. *Journal of Molecular Biology*, 130, 379s–393s.

[Pollard, 1981] Pollard, T. D. (1981). Cytoplasmic contractile proteins. *J.Cell Biol.*, 91(3 Pt. 2), 156s–165s.

[Pollard & Borisy, 2003] Pollard, T. D. & Borisy, G. G. (2003). Cellular motility driven by assembly and disassembly of actin filaments. *The Cell*, 112, 453s–465s.

[Reisler et al., 1980] Reisler, E., Smith, C., & Seegan, G. (1980). Myosin minifilaments. *Journal of Molecular Biology*, 143, 129s–145s.

[Ribbeck & Görlich, 2001] Ribbeck, K. & Görlich, D. (2001). Kinetic analysis of translocation through nuclear pore complexes. *The EMBO Journal*, 20(6), 1320s–1330s.

[Rubinstein & Colby, 2003] Rubinstein, M. & Colby, R. H. (2003). *Polymer physics*. Oxford University Press Inc., New York, USA.

[Scheel et al., 1989] Scheel, J., Ziegelbauer, K., Kupke, T., Humbel, B. M., Noegel, A. A., Gerisch, G., & Schleicher, M. (1989). Hisactophilin, a histidine-rich actin-binding protein form dictyostelium discoideum. *J. Biol. Chem.*, 264(5), 2832s–2839s.

[Schleicher et al., 1995] Schleicher, M., André, B., Andréoli, C., Eichinger, L., Haugwitz, M., Hofmann, A., Karakesisoglou, J., Stöckelhuber, M., & Noegel, A. A. (1995). Structure/function studies on cytoskeletal proteins in dictyostelium amoebae as a paradigm. *FEBS Letters*, 369, 38s–42s.

[Schmidt, 1999] Schmidt, F. (1999). *Mikrorheologie von Netzwerken semiflexibler Biopolymere*. PhD thesis, E22 TUM.

[Schmoller, 2008] Schmoller, K. (2008). Composite actin networks. E27 TUM.

[Schneider, 2002] Schneider, S. (2002). *Viskositäten unterkühlter Metallschmelzen*. PhD thesis, Fakultät für Mathematik, Informatik und Naturwissenschaften der Rheinisch-Westfälischen Technischen Hochschule Aachen.

[Schwaiger et al., 2004] Schwaiger, I., Kardinal, A., Schleicher, M., Noegel, A. A., & Rief, M. (2004). A mechanical unfolding intermediate in an actin-crosslinking protein. *Nature Structural and Molecular Biology*, 11(1), 1s–5s.

[Selve & Wegner, 1987] Selve, N. & Wegner, A. (1987). Ph dependent rate of formation of the gelsolin actin complex from gelsolin and monomeric actin. *Eur. J. Biochem.*, 168, 111s–115s.

[Semmrich et al., 2008] Semmrich, C., Larsen, R. J., & Bausch, A. R. (2008). Nonlinear mechanics of entangled f-actin solutions. *Soft Matter*, 4, 1675s–1680s.

[Semmrich et al., 2007] Semmrich, C., Storz, T., Glaser, J., Merkel, R., Bausch, A. R., & Kroy, K. (2007). Glass transition and rheological redundancy in f-actin solutions. *PNAS*, 104(51), 20199s–20203s.

[Shin et al., 2004] Shin, J. H., Gardel, M. L., Mahadivan, L., Matsudaira, P., & Weitz, D. A. (2004). Relating microstructure to rheology of a bundled and cross-linked f-actin network in vitro. *PNAS*, 101(26), 9636s–9641s.

[Shizuta et al., 1976] Shizuta, Y., Shizuta, H., Gallo, M., Davies, P., & Pastan, I. (1976). Purification and properties of filamin, an actin binding protein from chicken gizzard. *Journal of Biological Chemistry*, 251(21), 6562s–6567s.

[Spudich & Watt, 1971] Spudich, J. A. & Watt, S. (1971). The regulation of rabbit skeletal muscle contraction. I: Biochemical studies of the interaction of the tropomyosin-troponin complex with actin and the proteolytic fragments of myosin. *J. Biol. Chem.*, 246(15), 4866s–4871s.

[Steinmetz et al., 1998] Steinmetz, M. O., Stock, A., Schulthess, T., Landwehr, R., Lustig, A., Faix, J., Gerisch, G., Aebi, U., & Kammmerer, R. A. (1998). A distinct 14 residues site triggers coiled-coil formation in cortexillin I. *The EMBO Journal*, 17(7), 1883s–1891s.

[Stock, 1999] Stock, A. (1999). Phd thesis.

[Stock et al., 1999] Stock, A., Steinmetz, M. O., Janmey, P. A., Aebi, U., Gerisch, G., Kammerer, R. A., Weber, I., & Faix, J. (1999). Domain analysis of cortexillin I: actin-bundling, PIP2-binding and the rescue of cytokinesis. *The EMBO Journal*, 18(19), 52745s – 5284s.

[Stoeckelhuber et al., 1996] Stoeckelhuber, M., Noegel, A. A., Eckerskorn, C., Köhler, J., Rieger, D., & Schleicher, M. (1996). Structure/function studies on the ph-dependent actin-binding protein hisactophilin in dictyostelium mutants. *Journal of Cell Science*, 109, 1825s–1835s.

[Storm et al., 2005] Storm, C., Pastore, J. J., MacKintosh, F. C., Lubensky, T. C., & Janmey, P. A. (2005). Nonlinear elastictiy in biological gels. *Nature*, 435, 191s–194s.

[Stossel et al., 2001] Stossel, T. P., Condeelis, J., Cooley, L., Hartwig, J. H., Noegel, A., Schleicher, M., & Shapiro, S. S. (2001). Filamins as integrators of cell mechanics and signalling. *Mac. Mag. ltd*, 2, 138s–145s.

[Sun et al., 1999] Sun, H. Q., Yamamoto, M., Mejillano, M., & l. Yin, H. (1999). Gelsolin, a multifunctional actin regulatory protein. *The Journal of Biological Chemistry*, 274, 33179s–33182s.

[Svitkina et al., 1997] Svitkina, T. M., Verkhovsky, A. B., McQuade, K. M., & Borisy, G. G. (1997). Analysis of the actin-myosin II system in fish epidermal keratocytes: mechanism of cell body translocation. *Journal of Cell Biology*, 139, 397s–415s.

[Takiguchi, 1990] Takiguchi, K. (1990). Heavy meromyosin induces sliding movements between antiparallel actin filaments. *Journal of Biochemistry*, 109, 520s–527s.

[Tanaka-Takiguchi et al., 2004] Tanaka-Takiguchi, Y., Kakei, T., Tanimura, A., Takagi, A., Honda, M., Hotani, H., & Takiguchi, K. (2004). The elongation and contraction of actin bundles are induced by double-headed myosins in a motor concentration-dependent manner. *Journal of Molecular Biology*, 109, 520s–527s.

[Tellam et al., 1983] Tellam, R. L., Sculley, M. J., & Nichol, L. W. (1983). The influence of poly(ehtylene glycol) 6000 on the properties of skeletal-muscle actin. *Biochemical Journal*, 213, 651s–659s.

[Tempel et al., 1996] Tempel, M., Isenberg, G., & Sackmann, E. (1996). Temperature-induced sol-gel transition and microgel formation in α-aktinin cross-linked actin networks: a rheological study. *Physical Review E*, 54(2), 1802s–1810s.

[Tharmann, 2006] Tharmann, R. (2006). *Mechanical properties of complex cytoskeleton networks*. PhD thesis, E22 TUM.

[Tharmann et al., 2006] Tharmann, R., Claessens, M., & Bausch, A. R. (2006). Micro- and macrorheological properties of actin networks effectively cross-linked by depletion forces. *Biophysical Journal*, 90, 2622s–2627s.

[Tharmann et al., 2007] Tharmann, R., Claessens, M., & Bausch, A. R. (2007). Viscoelasticity of isotropically cross-linked actin networks. *Physical Review Letters*, 98, 088103–1s–088103–4s.

[Trepat et al., 2008] Trepat, X., Lenormand, G., & Fredberg, J. J. (2008). Universality in cell mechanics. *Soft Matter*, 4, 1750s–1759s.

[Trinick & Elliott, 1979] Trinick, J. & Elliott, A. (1979). Electron microscope studies of thick filaments from vertebrate skeletal muscle. *Journal of Molecular Biology*, 131, 133s–136s.

[Tschoegl, 1989] Tschoegl, N. W. (1989). *The phenomenological theory of linear viscoelastic behavior*. Springer Verlag Berlin, Heidelberg, New York, London, Paris, Tokyo.

[Tseng & Wirtz, 2001] Tseng, Y. & Wirtz, D. (2001). Mechanics and multiple-particle tracking microheterogeneitiy of α-actinin-cross-linked actin filament networks. *Biophysical Journal*, 81, 1643s–1656s.

[Uhde, 2004] Uhde, J. (2004). *Mikrorheometrie passiver und aktiver Aktinnetzwerke*. PhD thesis, E22 TUM.

[Uhde et al., 2004] Uhde, J., Keller, M., Sackmann, E., Parmeggiani, A., & Frey, E. (2004). Internal motility in stiffening actin-myosin networks. *Physical Review Letters*, 93(26).

[v. Olshausen, 2007] v. Olshausen, P. (2007). Einfluß entropischer Kräfte auf die Struktur und Mechanik spezifisch gebündelter Aktinnetzwerke.

[v. Teeffelen, 2004] v. Teeffelen, S. (2004). Theorie effektiver Potentiale semiflexibler Polymer-Lösungen.

[Verkhovsky et al., 1997] Verkhovsky, A. B., Svitkina, T. M., & Borisy, G. G. (1997). Polarity sorting of actin filaments in cytochalasin-treated fibroblasts. *Journal of Cell Science*, 110, 1693s–1704s.

[Vorobiev et al., 2003] Vorobiev, Strokopytov, B., Drubin, D. G., Frieden, C., Ono, S., Condeelis, J., Rubenstein, P. A., & Almo, S. C. (2003). The structure of non-vertebrate actin: implications for the ATP hydrolytic mechanism. *PNAS*, 100(10), 5760s–5765s.

[Wachsstock et al., 1993] Wachsstock, D. H., Schwarz, W. H., & Pollard, T. D. (1993). Affinity of α-actinin for actin determines the structure and mechanical properties of actin filament gels. *Biophysical Journal*, 65, 205s–214s.

[Wachsstock et al., 1994] Wachsstock, D. H., Schwarz, W. H., & Pollard, T. D. (1994). Cross-linker dynamics determine the mechanical properties of actin gels. *Biophysical Journal*, 66, 801s–809s.

[Wagner, 2004] Wagner, B. (2004). Rheologische Charakterisierung der Struktur-Funktionsbeziehung von Aktinvernetzerproteinen.

[Wagner et al., 2006] Wagner, B., Tharmann, R., Haase, I., Fischer, M., & Bausch, A. R. (2006). Cytoskeletal polymer networks: the molecular structure of cross-linkers determines macroscopic properties. *PNAS*, 103(38), 13974s–13978s.

[Weber et al., 1999] Weber, I., Gerisch, G., Heizer, C., Murphy, J., Badelt, K., Stock, A., Schwartz, J.-M., & Faix, J. (1999). Cytokinesis mediated through the recruitment of cortexillins into the cleavage furrow. *The EMBO Journal*, 18(3), 586s–594s.

[Weber et al., 2000] Weber, I., Neujahr, R., Du, A., Köhler, J., Faix, J., & Gerisch, G. (2000). Two-step positioning of a cleavage furrow by cortexillin and myosin II. *Current Biology*, 10, 501s–506s.

[Wegner, 1976] Wegner, A. (1976). Head to tail polymerization of actin. *J. Mol. Biol.*, 108(1), 139s–150s.

[Weitz, 2004] Weitz, P. A. J. D. A. (2004). Dealing with mechanics: mechanisms of force transduction in cells. *Trends in Biochemical Sciences*, 29(7), 364s–369s.

[Wick, 1999] Wick, M. (1999). Filament assembly properties of the sarcomeric myosin heavy chain. *Poultry Science*, 78(5), 735s–742s.

[Wilhelm & Frey, 2003] Wilhelm, J. & Frey, E. (2003). Elasticity of stiff polymer networks. *Physical Review Letters*, 91(10), 108103–1s–108103–4s.

[Wilhelm et al., 1998] Wilhelm, M., Maring, D., & Spiess, H. W. (1998). Fourier-transform rheology. *Rheology Acta*, 37, 399s–405s.

[Wrobel et al., 2002] Wrobel, L. K., Fray, T. R., Molloy, J. E., Adams, J. J., Armitage, M. P., & Sparrow, J. C. (2002). Contractility of single human dermal myofibroblasts and fibroblasts. *Cell. Motil. Cytoskeleton*, 52, 82s–90s.

[Xu et al., 1998] Xu, J., Wirtz, D., & Pollard, T. D. (1998). Dynamic cross-linking by α-actinin determines the mechanical properties of actin filament networks. *Journal of Biological Chemistry*, 273(16), 9570s–9576s.

[Yildiz et al., 2003] Yildiz, A., Forkey, J. N., McKinney, S. A., Ha, T., Goldman, Y. E., & Selvin, P. R. (2003). Myosin V walks hand-over-hand: single fluorophore imaging with 1.5-nm localization. *Science*, 300, 2061s–2065s.

[Yin & Stossel, 1979] Yin, H. L. & Stossel, T. P. (1979). control of cytoplasmic actin gel-sol transformation by gelsolin, a calcium-dependent regulatory protein. *Nature*, 281(5732), 583s–586s.

[Ziemann, 1994] Ziemann, F. (1994). *Aufbau eines neuartigen Magnetkugel-Mikrorheometers zur lokalen Messung viskoelastischer Parameter weicher Polymernetzwerke und zur Kraftmessung im Femtonewtonbereich*. PhD thesis, E22 TUM.

[Zimmerle & Freiden, 1988] Zimmerle, C. T. & Freiden, C. (1988). Effect of ph on the mechanism of actin polymerization. *Biochemistry*, 27, 7766s–7772s.

Last but not least, i've survived!

Curriculum Vitae

Personal Data

Name	Bernd Wagner
Address	Waldrebenstraße 10 80935 München
Email	bwagner@ph.tum.de
Day of Birth	13.09.1978
Place of Birth	Donauwörth, Deutschland
Nationality	German
Personal status	Single

Studies and Doctorate

since 04 / 2005	PhD at Department for Biophysics E22/27 of Technical University of Munich (TUM) Supervision of Advanced Practical Course „Enzyme Kinetics and Molecular Motors" for Physicists
11 / 1998 – 12 / 2004	Studies of General Physics at Technical University of Munich Degree: Dipl. Phys. Univ. (Grade 1.6) Major Subject: Energy Sciences and Astrophysics Minor Subject: Medical Radiation Physics
12 / 2003 – 12 / 2004	Diploma Thesis in Biophysics, Supervision of School Student and Working Student

School Education

09 / 1989 – 06 / 1998	Secondary School: "Gymnasium Donauwörth" Degree: General Matriculation Standard

Further education

10 / 07 - 03 / 08	Coaching Certificate "B - Licence" at the distance learning institue "IST"

Language skills

English	Business fluent
French	Good
Spanish	Basic

Scholarships

06 / 2006 – up to now	Efellows.net Scholarship
10 / 2006 – 12 / 2007	Readers scholarship "Die Welt"

Publications

09 / 2006, PNAS (first author)	„Cytoskeletal polymer networks: molecular structure of cross-linkers determine macroscopic properties"
09/ 2007, Biophys.J. (co-author)	Micro- and macrorheological properties of isotropically cross-linked actin networks
06/2008, Macromol. (co-author)	Methyl group dynamics in polycrystalline, glassy, supercooled, and molten coenzyme Q10 studied by quasielastic neutron scattering